Synthesis and Characterization of Nanostructured ZnO and SnO_x for VOC Sensor Devices

by

Hosang Ahn

A dissertation submitted to the Graduate Faculty of
Auburn University
in partial fulfillment of the
requirements for the Degree of
Doctor of Philosophy

Auburn, Alabama
December 12, 2011

Keywords: ZnO nanorod, SnO_2 thin film, SnO thin film, transition metal,
UV activation, gas sensor, flexible electronics

Approved by

Dong-Joo Kim, Chair, Associate Professor of Materials Engineering
Jeffrey W. Fergus, Professor of Materials Engineering
Zhongyang Cheng, Professor of Materials Engineering
Minseo Park, Associate Professor of Physics

Abstract

In this dissertation, nanostructured ZnO and SnO_x with various forms of thin films, particles and rods were deposited and synthesized by combination of sputtering, thermolysis assisted chemical solution method, and/or dc applied electrodeposition. Different substrates such as alumina, silicon dioxide, and polyimide films were used to grow nanostructured materials in order to fabricate highly sensitive and selective VOC sensor devices. Synthesized ZnO and SnO_x materials were characterized by FE-SEM, XRD, EDS, Raman spectroscopy and Keithley 2400 sourcemeter to examine the surface morphology, crystalline phase, atomic composition and electrical resistance change. Gas sensing properties of nanostructured metal oxides were studied as functions of the structural and compositional changes. Three different gases: acetone, ethanol, and ethylene, mixed with synthetic air were tested in a closed chamber by continuously flowing gases.

SnO_2 thin films were deposited by rf sputtering from a SnO_2 ceramic target under different argon-to-oxygen ratios to investigate the effects of oxygen stoichiometry on ethylene sensing properties. Thin film sensors exhibited higher sensitivity compared with bulk from SnO2 sensors. Post-annealing of the fabricated thin films influenced gas sensitivity while the control of argon-to-oxygen ratio during the film deposition did not affect the properties significantly due to the effective formation SnO_2 by a post-annealing process. An ethylene sensing mechanism for the SnO_2 thin film sensor was also newly suggested.

Significant compositional effects of tin oxide were investigated by sputter deposition from a metallic tin target. Post-annealing of the films resulted in SnO and/or SnO_2 phases depending on annealing temperature. Combinatorial phases of SnO_x, i.e. gradual distribution of SnO and SnO_2 on the sample substrate, were fabricated by co-sputtering of tin metal and tin oxide ceramic targets. Gas sensing properties of the films were investigated with an emphasis on tin phases and microstructure. Although SnO is a p-type semiconductor and SnO_2 is a n-type semiconductor, the data on sensitivity using three different gases were similar except for the direction of resistance changes during the detection of the gases. Such a combinatorial approach would enhance the selectivity of a VOC sensor by merging two different types of semiconducting materials.

Geometric effects of the oxides on the gas sensing properties were investigated by constructing ZnO nanorods on ZnO thin film seed layers. A series of devices were prepared with seed layers of different thickness upon which nanorods with tuned density were grown. Quantitative analysis of the sensing mechanism shows that volumetric geometry of the nanorods such as diameter and length is a more critical factor than the thickness of the seed layer. In addition to control of the nanorod structure, the transition metal ions such as nickel, cobalt, and copper were doped into ZnO nanorods during electrodeposition. Such doping can provide the ability to operate at room temperature and to use flexible polymer substrates. Nickel was successfully doped *in-situ* into ZnO nanorods in aqueous solution. A doped concentration of 6% nickel revealed the most enhanced sensing property at room temperature under UV illumination. A mechanism is proposed to explain how the transition metal ions in zinc oxide play an important role in the gas sensitivity under UV illumination.

Acknowledgments

It is with my sincerest appreciation to Dr. Dong-Joo Kim to whom this dissertation could not have completed without his encouragement and support. He not only guided me throughout the research effort but also encouraged me over the course of the Ph.D. pursuit and in overcoming personal obstacles since joining his research group. He is one of my role models not only in science and research field but also in life with regard to the attitudes towards people as well as organizations.

I would like to express my deepest gratitude to my committee members, Dr. Jeffery W. Fergus, Dr. Zhongyang Cheng, and Dr. Minseo Park for their valuable suggestions and guidance. I also would like to show thanks to my group alumni and members, Dr. Howard Clyde Wikle, Dr. Sang H. Yoon, Dr. Young Ho Kim, Dr. Jung-Hyun Park, Dr. Dan Liu, Mr. Chiwon Kang, Mr. Seon-Bae Kim, Mr. Jaeyoung Jeong, Ms. Hyejin Park, Ms. Yoonsung Chung, for their co-work and help during the last four and a half years.

In testing the gas sensors, I would like to give my thanks to Dr. Joo Hyon Noh for his valuable discussions, suggestions and in setting up the equipment to measure the gas sensing properties. Your Lab VIEW based gas flowing system really saved me considerable time and made the experiments much easier.

During my time in Auburn, it was my pleasure to have many meaningful conversations with the Bishop family: Jim, Roxane, and Jon Bishop; Christy Kilpatrick Williams, now wife of Mr. Mike L. Williams; other colleagues: Mr. Hoonsuk Rho and Mr. Yaqi Wang.

Lastly, my family is the reason why I live and study here in U.S. I would like to say to my parents: Young Hong Ahn and Soon Sun Baek; my wife and son: Hyunhee Kim and Travis Ahn; my sister: Jee Eun Ahn that I love you. Without their love and support during my study, I could have not reached this point.

Table of Contents

List of Tables

List of Figures

List of Abbreviations

ZnO	Zinc Oxide
SnO	Tin monoxide
SnO_2	Tin dioxide
TFTs	Thin Film Transistors
DSSC	Dye-Sensitized Solar Cells
CVD	Chemical Vapor Deposition
PLD	Pulsed Laser Deposition
DC	Direct Current
RF	Radio Frequency
FE-SEM	Field Emission- Scanning Electron Microscopy
XRD	X-Ray Diffraction
EDS	Energy Dispersive X-ray Spectroscopy
VOC	Volatile Organic Compound
UV	Ultra Violet
LED	Light Emitting Diode
HMT	Hexamethylenetetramine
TEA	Trethanolamine
EN	Ethylene Diamine
DAP	DiAmino-1, 2 Propane,

GaN	Gallium Nitride
PDADMAC	Poly (diallyldimethylammonium chloride)
PSS	Poly (styrenesulfonate),

CHAPTER 1 INTRODUCTION

1.1 Motivation and background

Nanostructured metal oxides, such as ZnO and SnO_x have attracted more attention recently due to their good semiconducting, optical, magnetic and electrical properties. In gas sensor applications, the fabrication of ZnO nanostructure has been used to develop a highly sensitive electronic nose system. The higher surface area to volume ratios of nanostructures enables the sensor to detect volatile organic compounds (VOC) in the sub-ppm range [1]. Such a modulation of surface to volume ratio is also known to influence the photocatalytic property and power conversion efficiency in dye sensitized solar cell applications [2]. In battery applications, ZnO has been investigated as both an anode material and a coating material for LiNiMnO, LiV_3O_8 cathodes in lithium-ion and Ni/Zn secondary batteries [3-5]. Unlike ZnO, tin oxides have different stoichiometric compounds such as SnO, SnO_2 and Sn_2O_3. Among these compounds, tin dioxide (SnO_2) and tin monoxide (SnO) have been widely researched for engineering applications. Tin dioxide is an anode material applicable to high capacity lithium ion batteries [6]. The excellent photostability and high charge carrier mobility of SnO_2 has expanded its usage for dye-sensitized solar cells (DSSC) [7]. SnO_2 has been widely researched for gas sensor applications because of its relatively high resistance change at sensing temperature for various gas species [8]. Tin monoxide has not been as widely researched, but its native p-type semiconducting property with high hole mobility and charge transport rate has recently attracted attention for fast thin film transistors (TFTs) [9]. To apply these oxides for the applications mentioned above, including VOC sensors, critical factors for investigation include micro/nano structural modulation such as surface to volume ratio and crystalline phase, and composition modification such as doping and stoichiometry.

Structural and compositional control of the oxide materials can be accomplished by modifying process parameters during fabrication. Several technologies such as CVD, PLD, sputtering, sol-gel spin coating, electrochemical deposition, and hydrothermal chemical solution methods have been investigated to prepare films and grow nanostructured materials. Among these technologies, three methods were used for this research: sputtering, sol-gel coating and electrochemical deposition. Sputtering is a widely used methodology for depositing thin films due to its ease in controlling parameters, reproducibility and long term stability [10]. Sputtering can be performed via two operating modes: direct current (dc) field assisted power and radio frequency (rf) assisted power depending on the types of target material. The micro/nano structure and stoichiometry of the metal oxide thin films can be adjusted by varying process parameters such as power density, gas mixture during plasma generation, and heating temperature. The sol-gel method has unique advantages in film deposition. Film thickness can be easily controlled by adjusting the spin-coating conditions and/or the viscosity of solution. The composition of films can be controlled by adjusting the mixing ratios of raw chemicals in the solution. Relatively uniform films can be deposited on a large scale substrate at low cost. A similar solution approach can be used to grow nanostructured oxides at low temperature. Since Lionel Vayssieres introduced the concept of a chemical solution method for low temperature synthesis of oxides, a great quantity of literatures has been published on the subject [11]. Various shapes of nanostructures can be fabricated by simple changes in parameters such as salt concentration, deposition time, and pH, can derive shape modification [12]. In spite of the many articles, there are still several limitations in growing nanostructure when introducing doping elements into the nanostructure. The application of an electric field during solution growth can provide the additional impetus necessary to promote the incorporation of chemical species into the structure [13].

Gas sensing properties of metal oxides are known to depend on the structure, composition, sensing temperature and gas species [14]. Much research has been carried out to improve the selectivity and sensitivity and to lower the sensing temperature for long-term reliable operation with reduced energy consumption. Modulation of a material’s structure has been performed by forming nanostructures such as nanorods, nanowires, nanoflowers, and nanotubes to achieve higher specific surface area [15-18]. Recently, more complicated structures to fully utilize surface area such as hierarchical nanostructured oxides have been attempted by repeating growth on as-synthesized structures or by combining two or more different methodologies to fully utilize the surface area [19-20]. Modification of the metal oxide’s composition has been performed by doping elements such as noble metals and transition metals to enhance the gas sensitivity. Since thin film and nanostructure fabrication often use non-thermodynamic conditions, the stoichiometry of metal oxide has been controlled by adjustment of the synthesis atmosphere for oxide growth and by controlled heating such as post-annealing. Because elevated operation temperature is considered as a potential limit of metal oxide gas sensor, there have been efforts to lower operation temperature by both structural and compositional modification and/or by adopting other energy sources such as ultraviolet (UV) and xenon lights [21-24].

Although numerous experiments regarding oxide gas sensors have been performed, few researchers have addressed the sensing mechanism to correlate two dimensional film structures with three dimensional nanostructures under the same experimental conditions. Furthermore, the approaches investigated here to improve the selectivity of sensors by utilizing combinatorial phases of oxides and to lower sensing temperature by combination of UV and transitional metals are rarely reported. Room temperature sensing can allow one to use soft polymer substrates for more flexible gas sensing devices.

1.2 Research Objectives

The objective of this research is to develop a highly sensitive and selective metal oxide based VOC sensor working at room temperature to detect sub-ppm range gas concentrations. The investigation is also to advance understanding the relationship between oxides' structural and compositional changes and their gas sensing properties. The results of this effort will be applicable to future, flexible, E-nose devices.

The following approaches were taken to achieve the objectives of this research:

1. To control the structure of ZnO and SnO_x metal oxide materials and to understand their growth mechanisms: The effects of processing parameters on the 2D (thin film) and 3D (nanorods and nanotrees) structures, and their resulting effects, on the gas sensing properties of the sensors are studied.
2. To control the composition of ZnO and SnO_x metal oxide materials and to understand its effects on the structural and electrical properties: Electrical and optical properties of metal oxide materials can be adjusted by doping with noble and transition metals, and

through control of the crystalline phase. Gas sensing properties of the sensors are studied with regards to doping and crystalline phase.

3. To investigate the gas sensing mechanism under various structural and operation conditions. An alternative energy source (UV light) is employed to sense gas molecules at room temperature by investigating sensing mechanisms in terms of microstructure and composition.

1.3 Dissertation structure

Chapter 1 introduces this dissertation, providing the motivation, research objectives, and dissertation structure.

Chapter 2 covers the background of this research: nanostructured ZnO and SnOx materials, principle of metal oxide based gas sensors, and nanostructured ZnO and SnOx based gas sensor research.

Chapter 3 describes the details of experiments. Processes to fabricate the sensor devices on different substrate and procedures to measure the gas sensing properties are explained.

Chapter 4 describes the investigation of 2D structured thin films of ZnO and SnO_x deposited by rf/dc sputtering and the effects of processing parameters on the electrical properties and preferred crystalline phase of the materials. The relationship between the gas sensing properties and the electrical properties and crystalline phase are discussed.

Chapter 5 describes the investigation of SnO_2 thin films deposited by rf sputtering and its materials properties as a result of argon-to-oxygen ratios and post annealing treatments. Ethylene sensing properties of SnO_2 thin film sensors, fabricated under different conditions, are studied.

Chapter 6 describes the investigation of ZnO thin films deposited by rf sputtering. On the deposited thin films, ZnO nanorods were grown by a thermolysis assisted chemical solution method. Geometric factors such as film thickness, length, and diameter of nanorods on ethanol gas sensing properties of the sensor are discussed.

Chapter 7 describes the investigation to modulate the composition of ZnO by *in-situ* doping of transition metal ions into ZnO nanorods by electrodeposition.

Chapter 8 describes the investigation of nickel-doped ZnO nanorods, chosen based on optimal results from *in-situ* doping, for the fabrication of flexible VOC sensor devices. Room temperature gas sensing properties of nickel-doped ZnO nanorods sensors are studied in terms of nickel concentration and sensitivity enhancement under UV illumination.

Chapter 9 summarizes the achievements attained over the course of this effort and future research directions that may further advance the field.

References

1. S. Kanan, O. El-Kadri, I. Abu-Yousef, andM. Kanan, "Semiconducting Metal Oxide Based Sensors for Selective Gas Pollutant Detection," *Sensors,* **9**[10] 8158-96 (2009).
2. S. H. Ko, D. Lee, H. W. Kang, K. H. Nam, J. Y. Yeo, S. J. Hong, C. P. Grigoropoulos, and H. J. Sung, "Nanoforest of Hydrothermally Grown Hierarchical ZnO Nanowires for a High Efficiency Dye-Sensitized Solar Cell," *Nano Letters,* **11**[2] 666-71 (2011).
3. Y. K. Sun, Y. S. Lee, M. Yoshio, andK. Amine, "Synthesis and Electrochemical Properties of ZnO-Coated LiNi[sub 0.5]Mn[sub 1.5]O[sub 4] Spinel as 5 V Cathode Material for Lithium Secondary Batteries," *Electrochemical and Solid-State Letters,* **5**[5] A99-A102 (2002).

4. X. Li, P. Li, M. Luo, X. Chen, andJ. Chen, "Controllable solvo-hydrothermal electrodeposition of lithium vanadate uniform carnation-like nanostructure and their electrochemical performance," *Journal of Solid State Electrochemistry,* **14**[7] 1325-32 (2010).
5. M. Geng and D. O. Northwood, "Development of advanced rechargeable Ni/MH and Ni/Zn batteries," *International Journal of Hydrogen Energy,* **28**[6] 633-36 (2003).
6. S. Han, B. Jang, T. Kim, S. M. Oh, andT. Hyeon, "Simple Synthesis of Hollow Tin Dioxide Microspheres and Their Application to Lithium-Ion Battery Anodes," *Advanced Functional Materials,* **15**[11] 1845-50 (2005).
7. H. Tian, P.-H. Liu, W. Zhu, E. Gao, D.-J. Wu, andS. Cai, "Synthesis of novel multi-chromophoric soluble perylene derivatives and their photosensitizing properties with wide spectral response for SnO nanoporous electrode," *Journal of Materials Chemistry,* **10**[12] 2708-15 (2000).
8. Y. Liu, E. Koep, andM. Liu, "A Highly Sensitive and Fast-Responding SnO2 Sensor Fabricated by Combustion Chemical Vapor Deposition," *Chemistry of Materials,* **17**[15] 3997-4000 (2005).
9. R. E. Presley and et al., "Tin oxide transparent thin-film transistors," *Journal of Physics D: Applied Physics,* **37**[20] 2810 (2004).
10. M. Fleischer and H. Meixner, "Sensing reducing gases at high temperatures using long-term stable Ga2O3 thin films," *Sensors and Actuators B: Chemical,* **6**[1-3] 257-61 (1992).
11. L. Vayssieres, "Growth of Arrayed Nanorods and Nanowires of ZnO from Aqueous Solutions," *Advanced Materials,* **15**[5] 464-66 (2003).

12. Y. Tak and K. Yong, "Controlled Growth of Well-Aligned ZnO Nanorod Array Using a Novel Solution Method," *The Journal of Physical Chemistry B,* **109**[41] 19263-69 (2005).
13. J. Rousset, E. Saucedo, andD. Lincot, "Extrinsic Doping of Electrodeposited Zinc Oxide Films by Chlorine for Transparent Conductive Oxide Applications," *Chemistry of Materials,* **21**[3] 534-40 (2009).
14. H. Meixner and U. Lampe, "Metal oxide sensors," *Sensors and Actuators B: Chemical,* **33**[1-3] 198-202 (1996).
15. Z. R. Tian, J. A. Voigt, J. Liu, B. McKenzie, andM. J. McDermott, "Biomimetic Arrays of Oriented Helical ZnO Nanorods and Columns," *Journal of the American Chemical Society,* **124**[44] 12954-55 (2002).
16. L. E. Greene, M. Law, J. Goldberger, F. Kim, J. C. Johnson, Y. Zhang, R. J. Saykally, andP. Yang, "Low-Temperature Wafer-Scale Production of ZnO Nanowire Arrays," *Angewandte Chemie International Edition,* **42**[26] 3031-34 (2003).
17. C. Y. Jiang, "Improved dye-sensitized solar cells with a ZnO-nanoflower photoanode," *Appl. Phys. Lett.,* **90**[26] 263501 (2007).
18. A. B. F. Martinson, J. W. Elam, J. T. Hupp, andM. J. Pellin, "ZnO Nanotube Based Dye-Sensitized Solar Cells," *Nano Letters,* **7**[8] 2183-87 (2007).
19. B. Li and Y. Wang, "Facile Synthesis and Enhanced Photocatalytic Performance of Flower-like ZnO Hierarchical Microstructures," *The Journal of Physical Chemistry C,* **114**[2] 890-96 (2009).
20. M. Raula, M. H. Rashid, T. K. Paira, E. Dinda, andT. K. Mandal, "Ascorbate-Assisted Growth of Hierarchical ZnO Nanostructures: Sphere, Spindle, and Flower and Their Catalytic Properties," *Langmuir,* **26**[11] 8769-82 (2010).

21. A. Wei and et al., "Room-Temperature NH 3 Gas Sensor Based on Hydrothermally Grown ZnO Nanorods," *Chinese Physics Letters,* **28**[8] 080702 (2011).
22. X. Jia, H. Fan, M. Afzaal, X. Wu, andP. O'Brien, "Solid state synthesis of tin-doped ZnO at room temperature: Characterization and its enhanced gas sensing and photocatalytic properties," *Journal of Hazardous Materials,* **193**[0] 194-99 (2011).
23. S. Fan, "UV-activated room-temperature gas sensing mechanism of polycrystalline ZnO," *Appl. Phys. Lett.,* **95**[14] 142106 (2009).
24. L. Peng, Q. Zhao, D. Wang, J. Zhai, P. Wang, S. Pang, andT. Xie, "Ultraviolet-assisted gas sensing: A potential formaldehyde detection approach at room temperature based on zinc oxide nanorods," *Sensors and Actuators B: Chemical,* **136**[1] 80-85 (2009).

CHAPTER 2 BACKGROUND AND LITERATURE REVIEW

2.1 Nanostructured Zinc oxide (ZnO) and its doping

ZnO is a semiconducting material with high band gap energy of 3.37 eV and exciton binding energy of 60 meV and has an intrinsic n-type property [1]. Due to its nature, lot of applications such as gas sensors [2], solar cells [3], field effect transistors [4], and optoelectric devices [5] utilizing ZnO materials have been researched to investigate the optimum material property for the best operations. As a material property of ZnO is much dependent on its structural difference, several technologies including MOCVD, hydrothermal, and chemical bath deposition [6-8] to synthesize various shapes of nanostructures have been reported. Since a chemical aqueous solution method to grow nanorods or nanowires was first reported by Lionel Vayssieres in 2003 [9], a chemical solution method has been widely utilized because it can originate different nanostructures at low temperature on various substrates in a large scale with easiness in controlling parameters. Wet chemical solution method can be generally divided into two categories depending on the temperature for the dissolved ions to be precipitated. At relatively high temperature such as 100-300 ℃, which is higher than the boiling point of water at standard pressure, dissolved ions initiate to nucleate and grow. Hydrothermal deposition includes direct precipitation of powders by changing the limit of solubility [10]. Chemical solution method assisted by thermal decomposition, or thermolysis is a relative low temperature process, which is operated less than 100 ℃. In determining the nucleation rate and growth rate, chemical balance between cat ions and anions in solution is primary factor to govern the process rather than the temperature of hydrothermal deposition [11]. In figure 2.1, two main parameters to determine the direction of reactions between dissolved ions according to the solubility limit. Line a represents the solubility line of zinc oxide. The solubility of zinc hydroxide is drawn as a dashed line b. Line C is a solubility line of metastable ZnO nuclei in the solution for homogeneous nucleation.

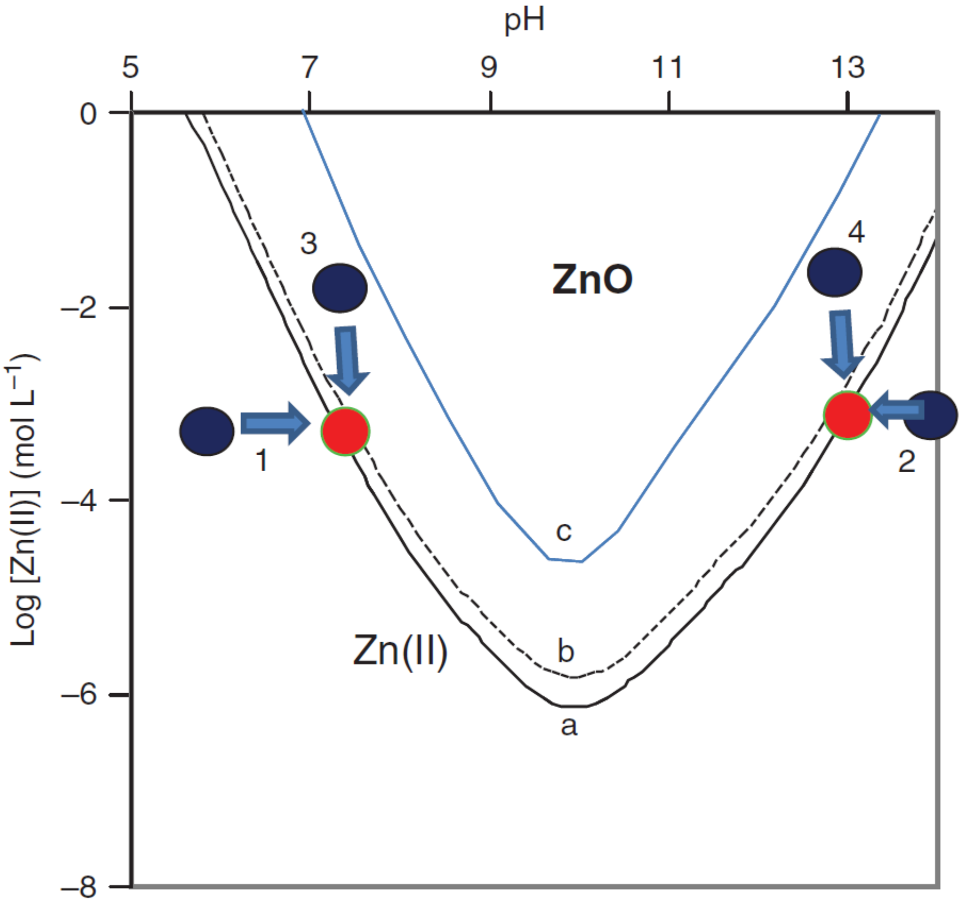

Figure 2.1 Thermodynamic equilibrium diagram of ZnO chemical solution deposition at room temperature. Line (a) and (b) are the solubility limits of zinc oxide and zinc nitrate, respectively. Line C is a guide line of metastable solution [12].

Under curves, ZnO is not precipitated on the substrate. Under specific conditions depending on pH, concentration of zinc ion, as denoted in the curve as blue circle 1, 2, 3, and 4, ZnO nanostructures can be nucleated heterogeneously on the substrate and grown by moving the conditions onto the line a. In cases of conditions 1 and 2, change in pH associated with concentration of zinc ions and hydroxy ions can deliver the zinc oxide nucleation. In cases of 3 and 4, system is on metastable region between solid Zn(OH)2 and solid ZnO status. Supersaturation of solution can derive the heterogeneous nucleation of ZnO under these conditions.

Heterogeneous nucleation and growth on the substrate is expressed by the chemical reactions as shown in below. First, zinc cat ions released from raw chemicals such as zinc nitrate, zinc chloride, and zinc acetate, reacts with hydroxide ions supplied by HMT (hexamethylenetetramine) and urea from the thermal decomposition in water. Then, solid zinc hydroxide is heterogeneously nucleated on preferred sites of the substrate. Table 2.1 gives the summarized data of stability constants of several different ligands, which was released from counting chemicals, such as formate, ethylenediamine, chloride, acetate, hexamethylenetetramine, in solution. When ionic precursors react with each other to produce ZnO, the amount of soluble ZnO in solution reaches to its maximum limitation as time increases. Then, insoluble ZnO are precipitated on the substrate. The relationship between K_1 for soluble ZnO and K_2 for precipitated ZnO are described in equation 1 and 2 to make a thermodynamic equilibrium.

$$K_1 = \left[Zn^{2+}\right]\left[OH^-\right]^2 \qquad (1)$$

$$K_1 = K_2 \qquad (2)$$

Table 2.1 List of stability constants of ligands participating in ZnO formation with zinc cat ions in aqueous solution at 25 ℃ TEA: trethanolamine, EN: ethylene diamine, HMT: hexamethylenetetramine, DAP: diamino-1,2 propane, Citrate: citric acid ($C_3H_4(OH)(COOH)_3$) [12]

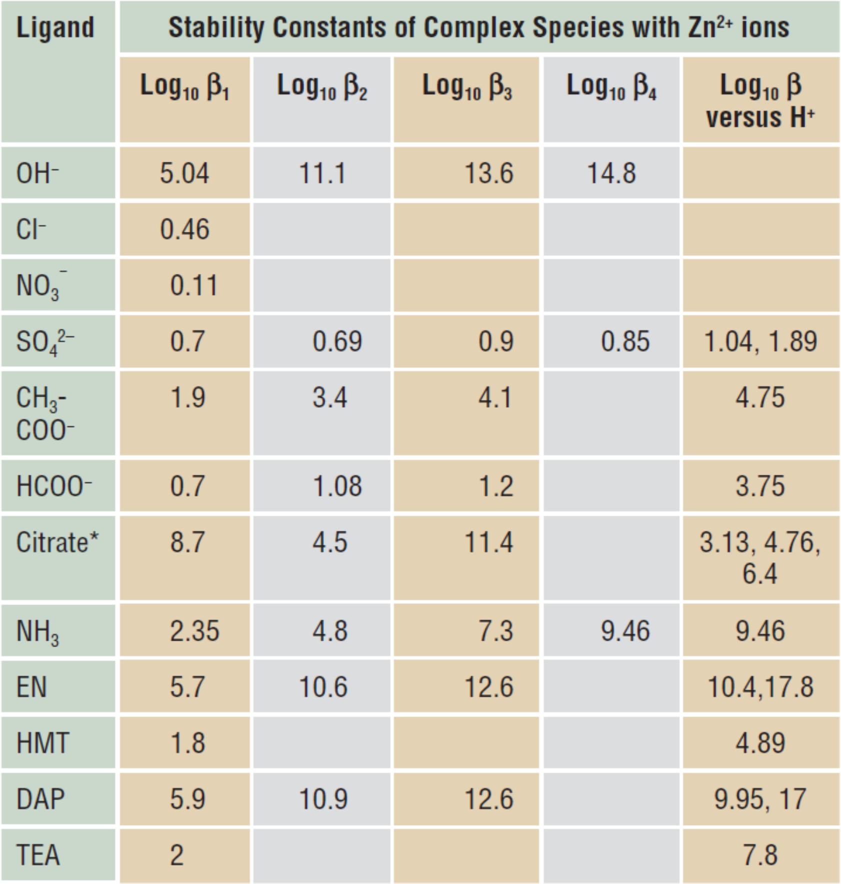

Ligand	Stability Constants of Complex Species with Zn^{2+} ions				
	$Log_{10}\ \beta_1$	$Log_{10}\ \beta_2$	$Log_{10}\ \beta_3$	$Log_{10}\ \beta_4$	$Log_{10}\ \beta$ versus H^+
OH^-	5.04	11.1	13.6	14.8	
Cl^-	0.46				
NO_3^-	0.11				
SO_4^{2-}	0.7	0.69	0.9	0.85	1.04, 1.89
CH_3-COO^-	1.9	3.4	4.1		4.75
$HCOO^-$	0.7	1.08	1.2		3.75
Citrate*	8.7	4.5	11.4		3.13, 4.76, 6.4
NH_3	2.35	4.8	7.3	9.46	9.46
EN	5.7	10.6	12.6		10.4,17.8
HMT	1.8				4.89
DAP	5.9	10.9	12.6		9.95, 17
TEA	2				7.8

To make an initial nucleation of Zn $(OH)_2$ happen, external energy such as thermal energy should be supplied to the solution to overcome the surface energy between the solution and the solid product. In the case of growing on the substrate, net surface energy to form the ionic product is reduced as much as that of substrate. Consequently, ZnO formation can be preceded under lower supersaturation limit, which controls the precipitation of nucleus [13]. This is one of reason to use chemicals releasing hydroxide ions to control the reaction slowly. As summarized in table 2.1, several different chemicals to provide zinc ions and anions to from nanostructured ZnO were utilized. Controlling parameters such as degree of saturation, control of growth site, and control of preferred growth direction, resulted in morphology changes as depicted in figure 2.2.

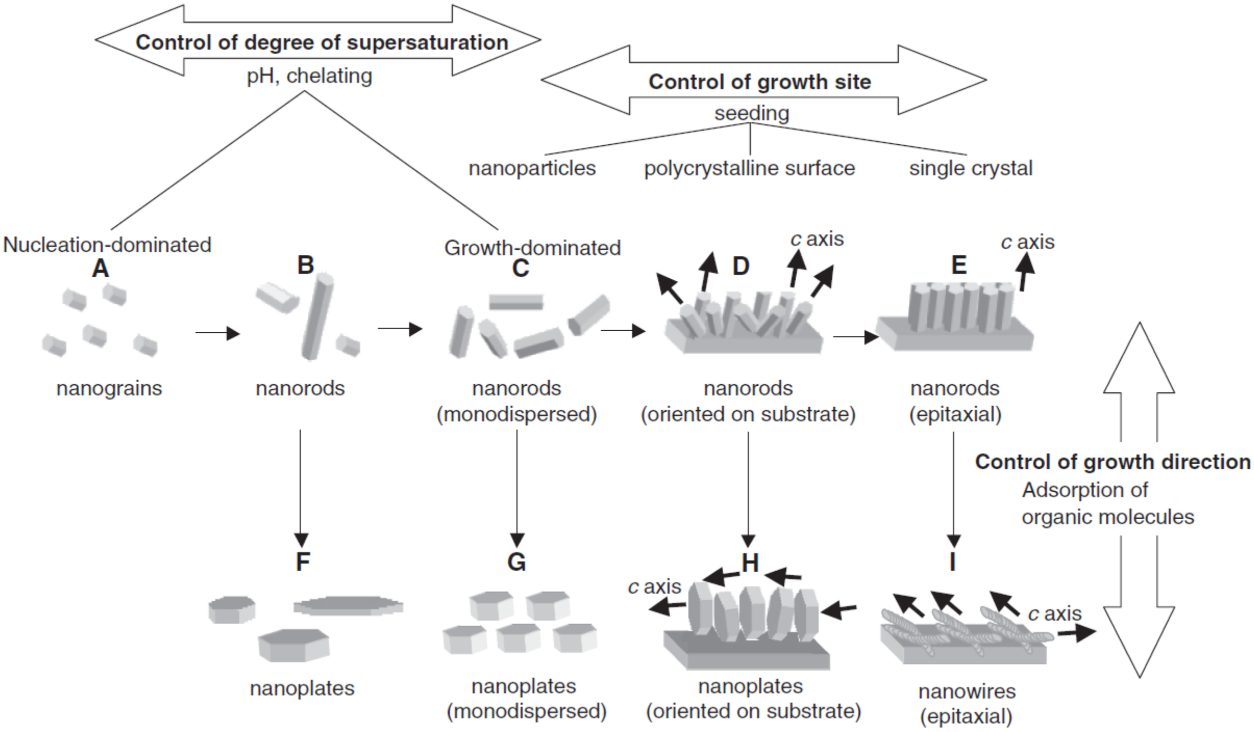

Figure 2.2 Schematic drawings to describe the role of parameters on the ZnO nanostructure formation [14]

ZnO nanograins or nanoparticles was synthesized using zinc sulfate heptahydrate ($ZnSO_4 \cdot 7H_2O$) and NaOH in different molar ratio to have pH 5.6 and 13.6, respectively. The growth and nucleation rate was only controlled by pH value. It was observed that much higher amount of ZnO nuclei could be generated at low pH value due to a low solubility of ZnO in the solution. Thus, ZnO precursors are precipitated to the nanoparticles [15-16]. Other than chemical solution method, ZnO nanorods can be grown in different ways depending on parameters. As discussed in previous paragraph, high pH values, on the contrary, was deducted in low nucleation rate. Limited numbers of nuclei are forced to grow to have high aspect ratio forming nanorods [17].

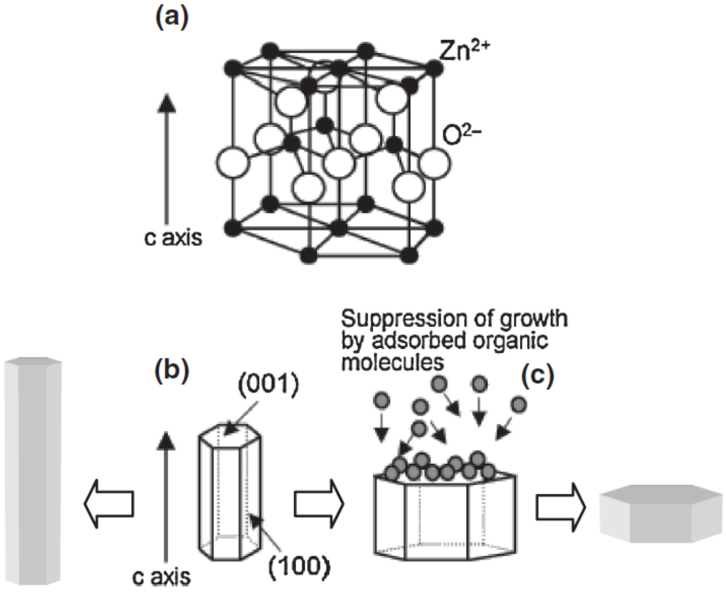

Figure 2.3 (a) Wurtzite ZnO structure unite cell (b) example of vertical growth of unit cell (c) example of lateral growth of unit cell [14]

In terms of chemical balance of solution, a high aspect ratio to have a rod type of ZnO can be achieved by lowering overall concentration of zinc salts while maintaining initial 1:1 ratio of zinc salt with HMT [9]. The unique role of HMT compared with other chemical is to supply both OH^- and NH^{4+}, which gradually increase pH value without other base chemicals. Vertical orientation of nanorods can be easily controlled by growing on seed layers such as thin films and nanoparticles deposited on the substrate.

Table 2.2 Hierarchical ZnO nanostructures according to deposition method, chemicals, and experimental conditions (researches from 2009 to 2011) [25-61]

	Method	Materials	Conditions	morphology	year
Chemical Solution Method	Hydrothermal	ZnCl2, NaOH	30ml water, 80C 24hr, sealed glass bottle	Flower like microparticles	2010
	Hydrothermal	ZnOH42-, NaOH	37ml water, 100C 10hr, Teflon autoclave	brush like nanowires	2009
	Hydrothermal	zinc acetate+ethylene glycol	4ml water, 60ml EG 150C 3-5hr, autoclave	Hollow spheres	2009
	Hydrothermal	zinc nitrate, zinc acetate, EG, water	zinc foil, 150C 15-20hr, autoclave	nanowire, urchin,	2010
	Hydrothermal	zinc acetate+HMT, NaOH	95C 6-60hr, autoclave	multipod, flower like nanorods	2010
	Hydrothermal	zinc acetate, NaOH	90C 10hr, autoclave	nanobrush, flower like, needle like, nanoplates	2009
	Hydrothermal+delectrodeposition	zinc nitrate, KOH	zinc foil, R.T. 10-12hr, autoclave, 2nd step(1V, AuCl4)	Flower like nanostructure	2011
	Hydrothermal+photodeposition	zinc acetate, HMT, copper sulfide	95C, 10hr, glass bottle, 365nm black light, overnight	Corn like Cu doped ZnO nanorod	2011
	Hydrothermal+electrodeposition	zinc nitrate, KCl, HMT	1.1V on ITO 30min, 50C, 90C 4hr for CBD	1st nanosheet+2nd nanowires	2010
	Hydrothermal+pyrolysis	zinc carbonate, HMT, ethanol	160C 8hr,Teflon autoclave	ZnO nanosheets	2009
	Hydrothermal+ultrasonication	zinc acetate, diethanolamine, ethanol, Zinc nitrate, HMT, sodium citrate	ZnO seeded FTO glass, 90C 6hr, 60min ultra	1st nanorod+2nd tube	2011
	microwave irradiation	zinc nitrate, MDBF4	water,900W 20% power, 2hr	ZnO nanobelts	2009
	Solvothermal	zinc nitrate, HMT, ethanol, NaOH	1st 85C, 5h, 2nd water+ethanol	sphere shape nanorods, urchin	2010
	Solvothermal	zinc acetylacetonate, THF, decane, ethanol	120C, 20hr	different shape depending on solvent type,	2009
	sonochemical	zinc acetate, dimethyl sulfoxide, water	ultrasound horn, less than 1hr,	Hollow spheres	2010
	electrospinning+hydrothermal	Zinc acetate, PVA, zinc nitrate, HMT	20KV,15cm, 10C/min, 85C, 4hr	nanorods on nanowires	2010
	Hydrothermal+ chemical additives	Zinc nitrate, EDA, HMT	80C, 0.5hr to 6hr, FTO,	nanorods on nanorods	2010
	Hydrothermal+ chemical additives	Zinc acetate, nitrate, sulfate, NaOH, ascorbic acid, etc	30 to 90C	flower, spindle, sphere, etc	2010
	Hydrothermal+ chemical additives	Zinc acetate, ethanolamine, NaOH	140C, 12hr, 60C, 4hr	flowerlike, spindle, sword, umbrella	2011
	Hydrothermal+ chemical additives	zinc nitrate, HMT, diaminopropane	90C 6hr, 60C 6hr	branched nanorod, nanowire array	2011

	Hydrothermal+ chemical additives	zinc acetate,	88C 1hr, 65C additional time (days)	Bunched Roselike and Core-Shell-like	2010
	Hydrothermal+ chemical additives	zinc nitrate, PVP, NaOH,	105C, 2hr	flower with nanosheets	2009
	Hydrothermal+ chemical additives	zinc nitrate, SDBS, NaOH, ethanol, water	constant temperature, several hours.	hexagonal disks	2009
	Hydrothermal+ chemical additives	zinc nitrate, HMT, trisodium citrate	90C, 3hr	flower with nanosheets	2011
	Hydrothermal+ chemical additives	zinc nitrate, HMT, trisodium citrate	60C, 24hr, 130C 24hr,	nanosheets on rod, microrods	2011
	Hydrothermal+ chemical additives	zinc acetate, carboxymethyl cellulose, ammonia	120C, 2hr, Teflon autoclave	double cage connected nanoshells	2010
	Hydrothermal+ chemical additives	zinc acetate, sodium dodecyl sulfate, hexane, hexanol, NaOH	120-180C , 10hr, Teflon autoclave	nanosheets, thorn on nanorods	2009
	Hydrothermal+ chemical additives+ seed layer	zinc acetate, sammonium hydroxide, PEI	90C , 10hr, Teflon autoclave	very long nanorods	2010
	Hydrothermal+ chemical additives	zinc acetate, PEG		short nanodisks, large diameter	2009
	precursor controlled	aniline coated Au seed, zinc acetate, NaOH, tetrachkiriauric acid trihydrate	80c 5min, 10min, 60C	star shape, microflower	2009
	precursor controlled	zinc acetate, ammonia, water, citrate family	90C 1hr, 90C 1hr	various shape	2009
CVD	CVD+supersaturation	1g of zinc powder	100sccm argon, 1% oxygen, 520C, 20min heating	nanorod with changing diameter	2010
	CVD+template	0.6g of zinc powder	240sccm argon, 60sccm oxygen, 550C, 120min heating	lotus leaf like ZnO nanostructures	2008
electrochemical deposition	electrochemical	zinc acetate, dimethyl sulfoxide(solvent), water,	70C 1hr, different DMSO volume	nanorod with changing diameter	2009
	two step electrochemical on spin coated seed	zinc acetate, dimethyl sulfoxide(solvent), water,	80C -1V, 2h, 4h, 8h, 2nd step: 0.25h, 1h	nanorods with nanorods	2011
	electrochemical	zinc chloride, KCl	90C, 45min	microrods on nanosheets	2011
	electrochemical	zinc chloride, KCl	KCl etching, PS template	urchin like nanorods	2011

Seed layers play a role of preferred nucleation sites for the heterogeneous ZnO growth. Sol-Gel spin coating and ZnO sputtering are generally used methods to prepare seed layers [18-19]. In some cases, single crystalline substrates such as (001) plane of ZnO substrate, alumina (0001) substrate with GaN layer, were utilized to grow vertically aligned ZnO nanorods [20-21]. ZnO nanowires are similar with nanorods in shape, but have a small diameter than nanorods. As described in nanorods, more dilute concentration of zinc salts with same ratio of HMT can make a smaller diameter of nanowire [22].

ZnO nanoplates are generally synthesized by controlling the preferred growth direction assisted by shape modifiers such as PDADMAC (poly (diallyldimethylammonium chloride), PSS (poly (styrenesulfonate), trisodium citrate [23]. As explained in previous paragraphs, anisotropic nature of growing ZnO along vertical direction derives into nanorods, nanowires formation. By selectively adsorbing on the (001) plane of ZnO, lateral growth can be promoted and deduced in nanoplates in larger diameter [24]. Each chemical additive has a different number of functional groups as well as different chemical structure. Due to these points, relative probability to be adsorbed in the specific planes varies and determines various shape modifications as shown in figure 2.3 [14]. To take a maximum advantage of nanostructured ZnO, recent researches have been focused on growing hierarchical nanostructure by repeating recipe to grow one dimensional nanostructures two or three times or combining at least two different methodologies. In table 2.2, details of experimental conditions and methodologies are summarized.

2.2 Nanostructured Tin oxide (SnO_x) and its doping

Tin dioxide (SnO_2) is another semiconducting metal oxide material, which as 3.6 eV of band gap energy at 300K [62].Its transparency in the range of visible light, SnO_2 is widely used in optoelectronic device [63] as well as transparent electrodes [64]. Nanostructured SnO_2 is reported to have a high surface to volume ratio and quantum confinement effects, which delivers enhanced electrical, optical and mechanical properties. Similar technologies as utilized in synthesizing ZnO nanostructures, such as hydrothermal, sol-gel spin coating, solvothermal, CVD (Chemical Vapor Deposition), sputtering, and electrospinning, were used for the synthesis of nanoparticles, nanowires, nanorods, nanotubes and hollow structure [65-69].

To synthesize SnO_2 nanowires, pulsed vapor solid synthesis method was used by evaporating tin monoxide [70]. Thermal evaporation is another method to grow large amount of SnO_2 nanowires. In the atmosphere of argon and oxygen gas mixture, SnO_2 nanowires were obtained via carbothermal synthesis. Guo et al used a hydrothermal method at low temperature and successfully synthesized controlled morphology of SnO_2 nanorods. In their experimental conditions, CTAB (cetyltrimethyl ammonium bromide) power was a key playing chemical additive in $SnCl_4$ and NaOH chemical solution by forming an intermediate ions CTA^+- $Sn(OH)^{2-}$. Diameter of SnO_2 nanorods was dependent on the concentration of $SnCl_4$. Balances between $SnCl_4$ and CTAB and electrostatic repulsion forces of intermediate ions could induce the controlled synthesis of SnO_2 nanostructures [71]. Vayssieres et al suggested chemical aqueous solution method for highly ordered SnO_2 nanorods growth on a Fluorine-SnO_2 glass substrate at 95 ℃ for 2 days. $SnCl_4{\cdot}5H_2O$ and $(NH_2)_2CO$ with adding HCl were used as raw materials. Experimental parameters, such as pH, ionic strength, and dissolved ions, determine the highest surface energy of facet to grow the tailored nanorods. Similar with the growth mechanism in ZnO, the nucleation and growth rate during process govern the overall morphology [72]. Consequently, SnO_2 nanorods were grown along the vertical direction; (001) plan, the highest surface energy, to the substrate.

Improvement in electrical and optical property of SnO_2 was observed when doped with additives, such as noble metals, transition metals, and other elements such as antimony, fluorine. The key roles of additives in properties of pure SnO_2 are to allow catalytic reactions on the surface, modulate the Debye length, locate additional level in energy band, and control the grain growth in thermal treatment [73]. Sb doped SnO_2 thin films by e-beam evaporation were studied depending on different amount of antimony. Antimony could be incorporated in SnO_2 as Sb^{5+}, Sb^{4+}, and Sb^{3+} depending on the amount and oxygen vacancies in SnO_2 and contributed as donor or acceptor, respectively. In addition to, Sb ions work as a glass network modifier to influence electrical and optical properties due to a shift in the Fermi level [74]. Nobel metals such as Pd, Au, and Pt, are studied widely to modulate the properties of pure SnO_2. The existence of noble metals influences the grain growth and defects formation in intrinsic tin dioxide during calcinations. Thus, grain size at specific calcinations temperature was controlled by altering doping element and its amount [75]. Transition metal, copper ions was mixed into SnO_2 nanopowder and sol-gel spin coated. By the substitution of Sn^{4+} into Cu^{2+} might increase the amount of oxygen vacancy, which causes a resistance drop or decrease its concentration as positioning at interstitial site, which results in a resistance increase. Overall impact of copper, however, may be governed by substitutional doping due to a relative small ionic radius of Cu^{2+} than Sn^{4+}. Challenge in doping transition metal ions is that it may make readily a secondary oxide phase, which might deteriorate the intrinsic property of metal oxide [76]. Another doping element, fluorine is utilized to modify the property of SnO_2 due to high conductivity and transparency. Fluorine ions can be corporate into oxygen vacancy easily because ionic radius of fluorine is similar with that of oxygen and also binding energy between tin atom and oxygen atom is similar with that between tin atom and fluorine atom [77]. Due to this, crystallinity of SnO_2 to (002) direction was enhanced. Charge carrier concentration and resistivity are reported to be dependent on the doping concentration, but mobility of charge carrier does not show dependence on fluorine doping [78]. Chen et al reported calcination assisted SnO_2 nanorods synthesis in bulk scale. Mixed power of sodium chloride, sodium carbonate, and stannic chloride, was used as precursors. Ostwald ripening to form large size particles from dissolved small particles was primary mechanism to grown SnO_2 nanorods. The controlled viscosity and mobility by chemical additives, such as NaCl, depending on calcination temperature, enabled the nucleation and growth of nanorods [79]. Vapor phase transport method was used to growth the patterned SnO_2 nanowires on a gold catalyst coated silicon substrate. SnO_2 and graphite powder in same ratio were mixed as precursor and located in heated furnace under argon and oxygen gas atmosphere. Initial reaction between carbon and SnO_2 make a formation of SnO phase. At 600 ℃, metastable SnO phase decomposed into tin and tin dioxide phases. Liquid tin phase adsorbed on the gold catalyst and make a tin-gold alloy and SnO phase. At elevated temperature, 800 ℃, adsorbed Sn and SnO are transformed into SnO_2 nanowires completely after 1hr. Depending on furnace temperatures, morphology of nanowires and continuity were changed [80]. SnO_2 nanorods were grown by high pressure pulsed laser deposition using SnO_2 target on a single crystalline (001) silicon wafer. In this study, structure and morphology of SnO_2 were characterized according to chamber pressure. Kinetic energy between plume and gas species influences the nucleation of SnO_2 and growth mechanism. Favored growth of nanorods was achieved when epitaxial growth was inhibited [81].

2.3 Principle of metal oxide gas sensors and its limitation

Monitoring and controlling atmosphere has become critical in various industrial fields, e.g., agriculture, medical care, manufacturing and bio-safety. In the system to control atmosphere into desired level, quick and accurate information acquisition from the field and signal processing to comprehend the condition of environment are required. The gas sensors, especially based on solid state metal oxide materials have several advantages; applicability to various gases, inexpensive fabrication and simple operation. Because of these strong points, metal oxide based gas sensors have been widely used for atmosphere monitoring sensor. On the contrary, metal oxide based gas sensors still have limitations; high working temperature, dull discrimination among similar gas species and impropriety to inflammable gas and, biomedical applications [82-84]. Metal oxide materials; ZnO, SnO_2, WO_3, In_2O_3 and etc., are reported to react with various types of gases. It shows different sensitivity depending on its concentration and types of gas. Generally, temperatures below 400℃ are known to working temperature for metal oxide to have gaseous molecule reaction (desorption and adsorption) on the surface of oxide. When the surface of oxide is heated, four different types of oxygen molecules and/or atomic species are involved into reaction with oxide material. Yamazoe et al. [85] reported that O_2 desorbs from the oxide surface at 80 ℃, O_2^- at 150 ℃, O^- and/or O^{2-} at 560 ℃, respectively by using TPD (Temperature Programmed Desorption) chromatograms analysis of oxygen adsorbed on SnO_2 powder. Among four different types of oxygen species, dominant species concerning resistance change on oxide surface is O^- in conventional working temperature of metal oxide sensors. From the reaction between O_2 and metal oxide; ZnO or SnO_2, at above temperature 300 ℃, oxygen absorb free electrons from the surface of metal oxide and becomes O^- as shown in below equation.

$$O_2\,(\text{gas}) + 2e = 2O^-\,(\text{surface})$$

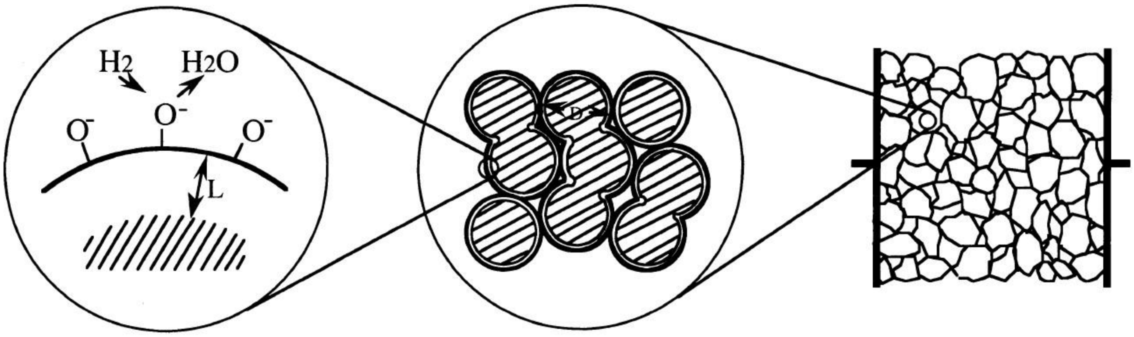

(a) Surface
(Receptor function)

(b) Microstructure
(Transducer function)

(c) Element
(Output resistance change)

Figure 2.4 Dimensional functions of structures in gas sensing of metal oxide materials [85]

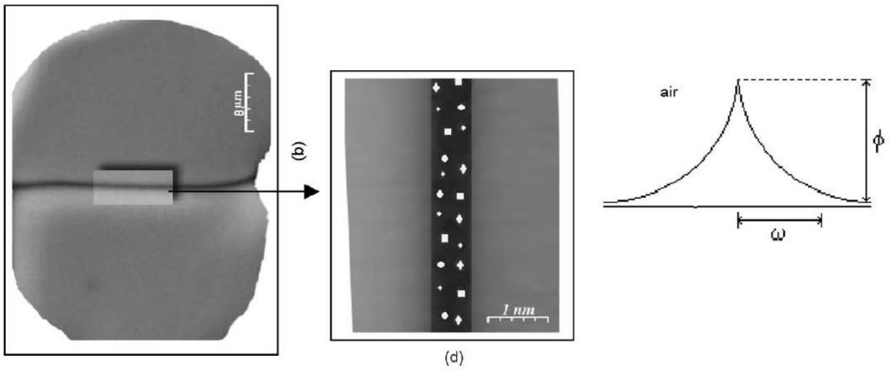

Figure 2.5 Sequential zoomed-in image of potential barrier at grain boundary of metal oxide material exposed in air [85].

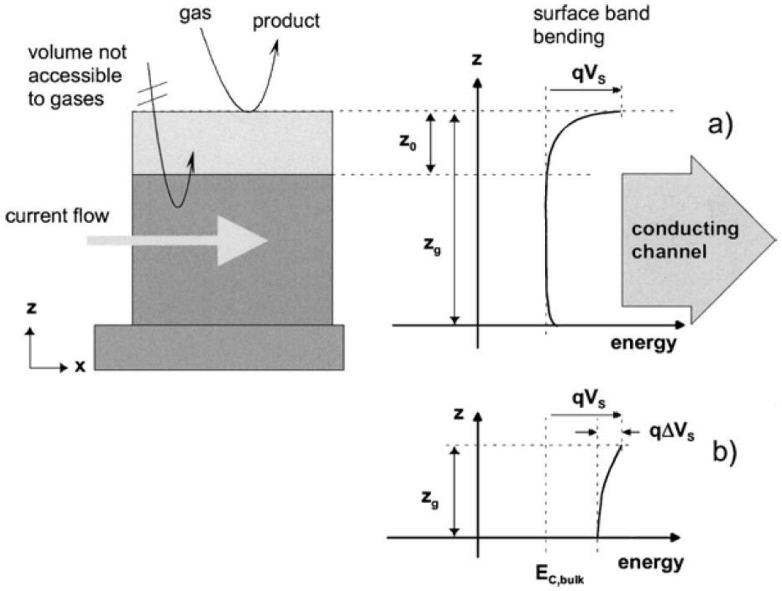

Figure 2.6 Schematic diagram of sensing mechanism of compact thin film layer in gas response.
a) energy band bending for relatively thick compact films and shows a partially depleted status
b) energy band bending for relatively thin compact films and shows a completely depleted status

As shown in above figure 2.7, several types of oxygen molecules can be adsorbed on the grain boundary depleting the free electrons and induces potential barriers with width of ω. In the case of compact thin layer as described in below figure 3, only surface of films participate in gas response reaction. Depending on relevant thickness of thin films to the Debye length λ_D, gas reaction on the surface can completely deplete the entire conduction layer when thickness of film become close to the Debye length. However, relatively thicker film that the Debye length, gas reaction do not completely participate in conduction change as shown in figure 3b). For thick porous film, conduction mechanism occurs in somewhat different ways depending on grain sizes as represented in figure 4. In case of thick films with large grains, volumetric space of films influences overall conduction change. Therefore, a participating surface becomes larger than actual geometry of films [86]. If the grain size is smaller than Debye length, mean free path of free electrons corresponds with grain size and surface of film also contributes to the overall resistance as similar with compact thin films. It is because charge carriers have collisions on the surface of materials as much as collisions in bulk of the grain [87].

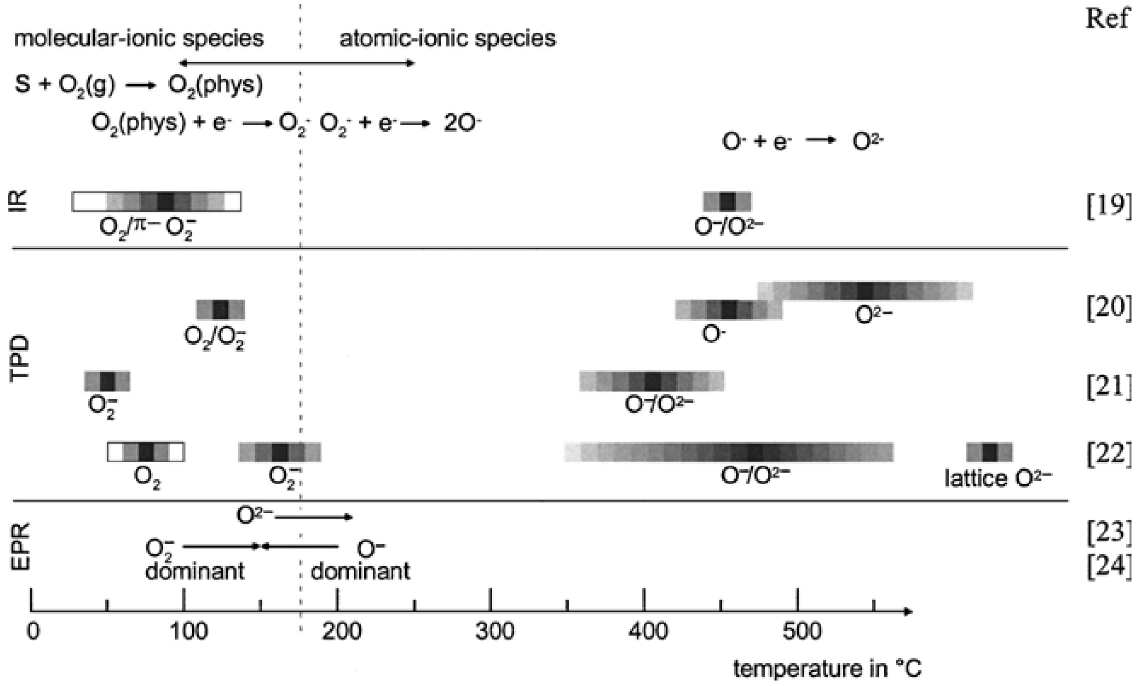

Figure 2.7 Types of oxygen species can be adsorbed on the metal oxide surface [87]

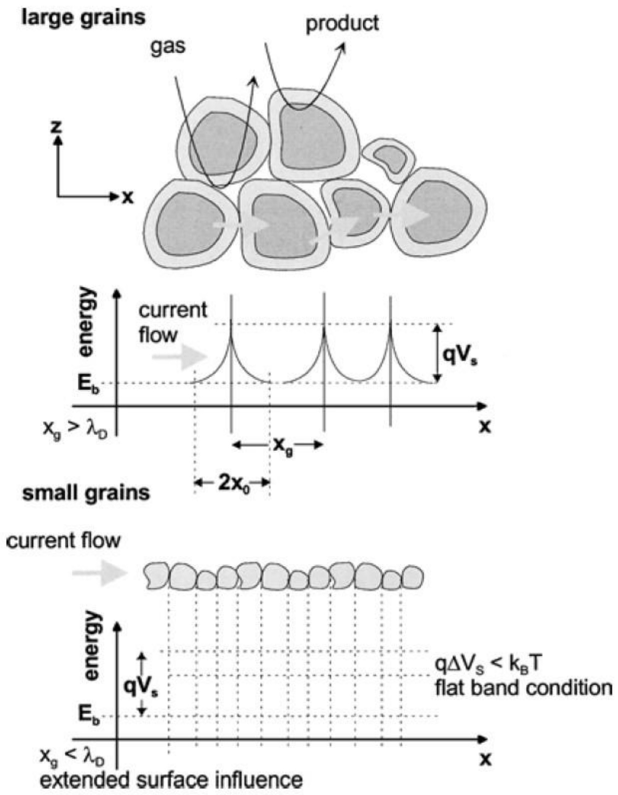

Figure 2.8 Schematic explanation of the reaction between gas molecule and porous thick film of metal oxide layer depending on its grain size and related change in energy band

Xg: Grain size, X_0: Depth of depletion layer, λ_D: The Debye length [87]

Working temperature is another key factor influencing sensing mechanism in metal oxide based gas sensors. From the literature reviews, reducing or oxidizing gases detected by ZnO or SnO_2 sensors, optimized temperature showing the best sensitivity for specific gases are different. It can be explained that concentration of charge carriers increases as temperature are elevated and consequently decreases a value of the Debye length. On the contrary, under lower temperature, semiconducting materials are eager to work as insulators rather than semiconductors. It makes hard for metal oxide to react with gas molecules to show resistance change [83].

2.4 Nanostructured metal oxide for gas sensor applications

Several different types of metal oxide materials, e.g., zinc oxide, tin oxide, indium oxide and so on, have been utilized for chemical gas sensor. In below figure 2.9, researches on tin oxide materials are dominant in numbers compared with other oxides. Second portion in number of researches is hold by mixed metal oxides. Other materials, e.g., zinc oxide, tungsten oxide and titanium oxide are also researched for gas sensors next to tin oxide.

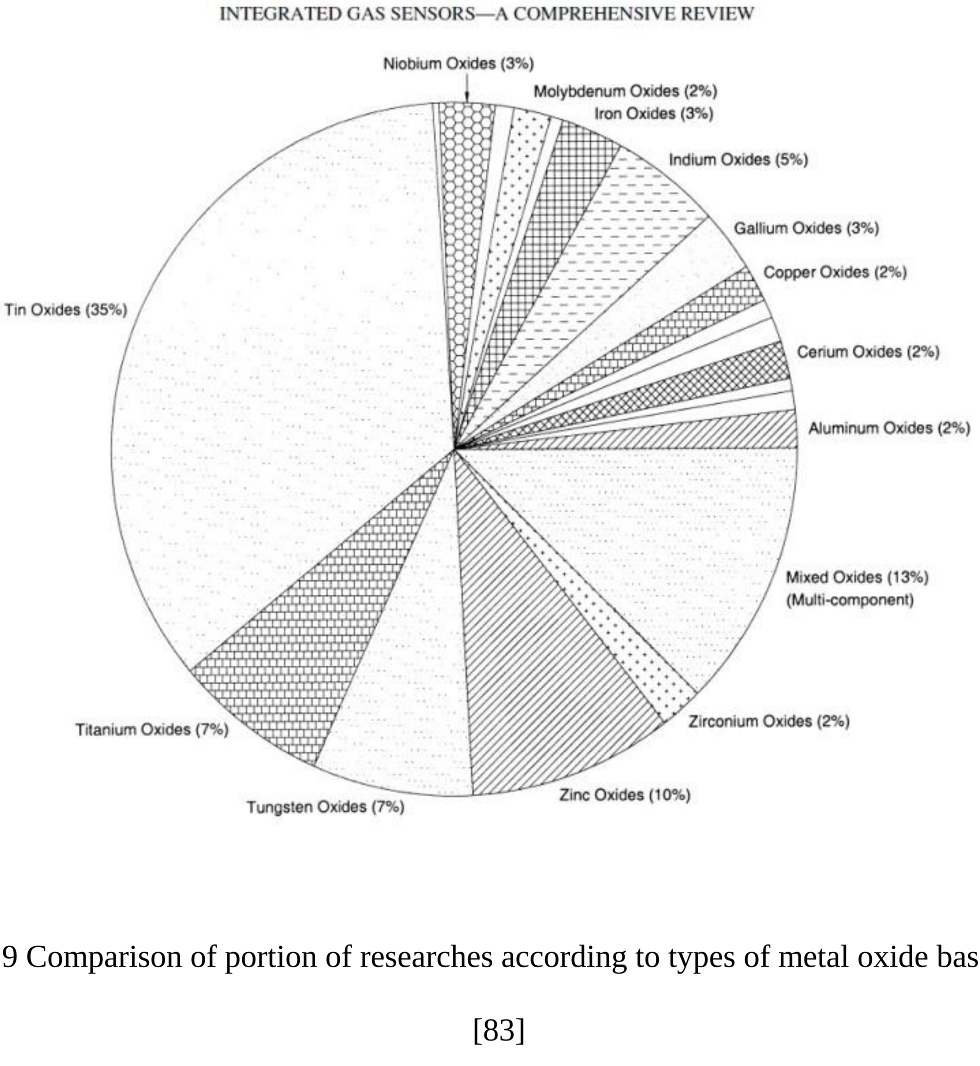

Figure 2.9 Comparison of portion of researches according to types of metal oxide based sensors [83]

As a pure form of tin oxide materials are used to detect several different types of gases, e.g., H_2, C_2H_5OH, CO, NO_x, CH_4, SO_2, H_2S, and CO_2 in the level of ppb or ppm in air atmosphere. Depending on type of gases, working temperatures for sensors are also different from 25°C to 650°C. Zinc oxides are used for gas sensor application. ZnO is reported that it shows good response to gases of ammonia family, CO, O_2, O_3 and H_2 [9].

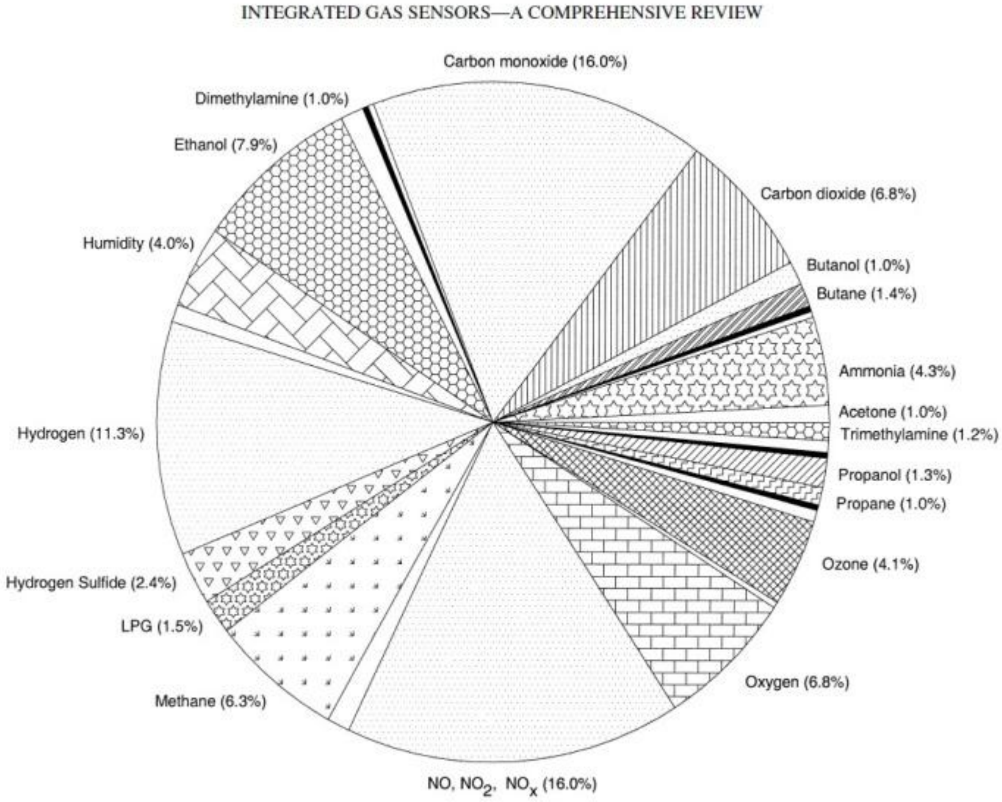

Figure 2.10 Diagram showing types of gases researched on the base of metal oxide material gas sensor [83].

Table 2.3 Nanostructured ZnO applied for chemical sensors and detectable gas species [88-104]

Material	Structure	Method	gas	Conditions
ZnO	nanowire	Selective growth on chip	NO_2	0.5~3ppm S:10~90 @225 ℃
ZnO	nanorod	Hydrothermal solution method	Acetone, ethanol, toluene, CO, etc	100ppm, S:2~3 @300 ℃
ZnO, Sn-doped, Ni-doped ZnO	thin film	Successive ionic layer adsorption and reaction method	Ammonia, NO_2	100ppm, S:1~6 @250 ℃
ZnO	nanoflake, nanowire	Sputtering+ local oxidation	ethanol	50ppm, 100 ℃ S~1.6
Ga-ZnO,	nanowire	Zinc powder, evaporization	ethanol	1500ppm, 300 ℃, S~1.6
ZnO	dumbbell-like	Aqueous solution	acetone, ethanol	50ppm, 300 ℃, S~8,16
Au-ZnO, ZnO	nanowire	Zinc power, oxidation	ethanol	1000ppm, 280 ℃, S~23
ZnO	nanoparticles, nanosolids	Zinc power paste coating	Ethanol, acetone, benzene, toluene, xyylene	3000ppm 370 ℃, 420 ℃, S:1~20
ZnO Pt-ZnO	nanorods, nanowires, nanotubes	Electrophoretic deposition with template, chemical synthesis with powder	Hydrogen, ethanol	100ppm, 200 ℃, S:32~80 S:800 for H_2
ZnO	nanobelts	Sputtering,	ethanol	50ppm, S:7, 220 ℃
ZnO, ZnO-Au ZnO-Ga	nanowire	Zn powder, vaporization, oxidation	acetone	200ppm, S:1.2~1.8, 300 ℃
ZnO	nanowire	Thermal evaporation, MEMS	ethanol	1~200ppm, S:45, 300 ℃
ZnO - InSb	nanorod	Hydrothermal	acetone	500ppm, S:5, 300 ℃
ZnO	nanowire	Thermal evaporation	Acetone, CO, ethanol,	1~500ppm, S:1~64, 400 ℃
ZnO-Sb	nanoparticles	Vapor condensation	Benzene, acetone, ethyl alcohol, toluene, xylene	100ppm, S7.5~40, 200~500 ℃
ZnO	nanorods	Chemical solution method	Benzene, ethanol, toluene, acetone	100ppm, S:10~120, 300 ℃
ZnO	nanorods	Reactive vapor deposition, Zn powder	Ethanol, hydrogen sulfide	100ppm, S:2.5~6.5, 100 ℃

Table 2.4 Nanostructured SnO_2 applied for chemical sensors and detectable gas species [105-126]

Material	Structure	Method	gas	Conditions
SnO_2-Sb	thin film, porous, dense	Thermal evaporation	Ethanol	3200ppm, S:2.0, 200 ℃
SnO_2	thin film	PECVD	Ethanol	10-50ppm, S:45 , 450 ℃
SnO_2	nanobelts	Thermal evaporation	Co, NO_2	50-500ppm,S: 10 , 200-450℃
SnO_2	nanowhiskers	Thermal evaporation	Ethanol	50ppm, S:23, 300 ℃
SnO_2	nanorods	Hydrothermal	Ethanol	10-300ppm, S:4-30, 300 ℃
SnO_2	nanorods	Hydrothermal	Ethanol	10-300ppm, S:8-82, 300 ℃
SnO_2/MWCNT	coreshell	Wet chemical method	Ethanol	50ppm, S:24.5, 300 ℃
SnO_2-Pd	thin film	RGTO technique	Hydrogen, Ethanol	1000ppm, S:10 , 350 ℃
SnO_2-Pt, Pd, Co	thin film	sputtering	CO, CH_4,	10000ppm, S:1-12 , 350 ℃
SnO_2	hollow spheres	Heat treatment of $SnCl_4$, Carbon	Ethanol	1000ppm, S:8, 300 ℃
SnO_2-Pt	thick film	Thermal oxidation	Ethyne, Hydrogen, NO_2	150sccm of gas, S:2.3, 440 ℃
SnO_2	nanoparticulate	rf. sputtering	NO_2	5ppm of gas, S:2.5, 130 ℃
Silver-SnO_2	thin film	Sol-gel spin coating	H_2S	10ppm, S:50-120, 70 ℃
SnO_2-Mo	thin film	Sol paste- calcination	Ethyl alcohol, CO, NO_2	500ppm, S: 10, 100-500 ℃
SnO_2	thin film	rf. sputtering	CO	25-400ppm, S:1.2- 2.2, 560K
SnO_2	thin film	MOCVD	H_2S, CH_4, NO_2	2ppm, S:1.1, 350 ℃
SnO_2	nanorods, hollow microspheres	Hydrothermal	Ethanol, methanol	100-900ppm, S:5-53, at room temperature, 300 ℃
SnO_2	nanorods	Solid-state reaction	ethanol	10-2000ppm, S:120, 300 ℃
SnO_2-Au	thin film	RGTO technique	CO	100-500ppm, S:3-11, 350 ℃
SnO_2-Pd	thick film	Ceramic power process	CO, methane, propane, ethanol	250-1000ppm, S:2.5-3.5, 500 ℃
SnO_2	nanowire	Hydrothermal	acetone	20-500ppm, S: 1-15, 285 ℃

As stated earlier, specific gas are detectable by certain type of metal oxide material. In figure 2.10, various types of gases utilized for metal oxide bases gas sensor application and summarized into the percentage. As described in figure, carbon monoxide and nitrogen oxides occupies 16% respectively with highest portion, 11% of research for hydrogen, ethanol and carbon dioxide follows next with 8% and 7% respectively. Other gases, e.g., methane and ozone are also explored [83]. Thanks to the advantage of nanostructured metal oxide as discussed in previous chapters, nanostructured ZnO and SnO_2 have been applied to develop highly sensitive and fast response chemical gas sensors. Several forms of ZnO nanostructures such as nanorods, nanowires, and polycrystalline films have been applied to detect ethanol, acetone, nitrogen oxide and etc as summarized in table 2.3.

Most researches have been performed to improve sensitivity to specific gas species by adapting various nanostructures such as thin film, nanorod, nanorod, and nanoparticles. It was found that synthesis of nano-scale structure and its modulation were highly dependent of process parameters of technologies. However, rare researches to investigate the relationship between nanostructures in controlled geometry and gas sensing property have been performed. Details of experimental design will be explained in later chapter. Nanostructured SnO_2 is also widely utilized to develop high-performance chemical sensors. Though it is relatively hard to modulate its shape than ZnO, higher sensitivity to various gas species spurred to develop chemical sensors based on nanostructured SnO_2.

As shown in table 2.4, nanostructured SnO_2 based gas sensor studies utilized different technologies to synthesize and deposit nanowire, nanorods, hollow spheres and thin films. Compared to ZnO related researches, researches utilizing SnO_2 nanorods, nanowires are relatively rarely studied. It is thought that relative stability of crystalline facets of SnO_2 in terms of surface energy is observed to have similar growth rates in each facet [126]. To determine preferred growth rate, process conditions to change the relative surface energy is necessary, but it is quite difficult to control parameters to obtain designed nanostructures experimentally. In case of SnO_2 thin films, no systematic parametric studies have been performed to determine structural change including microstructure and tin phases according to process parameters in sputtering, sol-gel, and CVD.

In this study, both nanostructured ZnO and SnO_2 in various structures such as nanorods, thin films are approached using sputtering, thermolysis assisted chemical solution method and electrodeposition. Synthesized or deposited ZnO and SnO_2 will be fabricated to gas sensors to investigate the structural changes according to process parameters and gas sensing properties.

For ZnO, thin films will be deposited varying argon to oxygen ratio to determine the optimum conditions for gas sensor fabrication. Then, ZnO nanorods will be synthesized on the optimized thin film providing the preferred nucleation sites. Geometric effects of thin films and nanorods on gas sensing properties of ZnO nanorods sensors and its role of thin films and nanorods will be investigated and suggested in later chapter. In addition to, study for gas sensor development on flexible substrate is also rarely reported. In engineering aspects, gas sensing property of metal oxide thin film and nanorods sensors integrated on flexible substrates will be studied investigate the substrate effect on the structure of metal oxide and related gas sensing properties. For SnO_x, thin films will be deposited by both rf and dc sputtering to control the ratio of Sn and O. In rf sputtering, argon to oxygen ratios will be varied to determine the SnO_2 phases. Post annealing will be carried out on dc sputtered SnOx films to find out the optimum temperatures to have different SnO, Sn_2O_3, SnO_2 phases. Similar with the approach to ZnO, SnO_2 nanorods will be attempted to synthesize by chemical solution method to take advantage of high specific surface area.

References

1. M. H. Huang, S. Mao, H. Feick, H. Yan, Y. Wu, H. Kind, E. Weber, R. Russo, andP. Yang, "Room-Temperature Ultraviolet Nanowire Nanolasers," *Science*, **292**[5523] 1897-99 (2001).
2. J. Xu, Q. Pan, Y. a. Shun, andZ. Tian, "Grain size control and gas sensing properties of ZnO gas sensor," *Sensors and Actuators B: Chemical*, **66**[1-3] 277-79 (2000).
3. K. Keis, E. Magnusson, H. Lindström, S.-E. Lindquist, andA. Hagfeldt, "A 5% efficient photoelectrochemical solar cell based on nanostructured ZnO electrodes," *Solar Energy Materials and Solar Cells*, **73**[1] 51-58 (2002).
4. P. F. Carcia, R. S. McLean, M. H. Reilly, andG. Nunes, "Transparent ZnO thin-film transistor fabricated by rf magnetron sputtering," *Applied Physics Letters*, **82**[7] 1117-19 (2003).
5. R. Vispute, "Heteroepitaxy of ZnO on GaN and its implications for fabrication of hybrid optoelectronic devices," *Appl. Phys. Lett.*, **73**[3] 348 (1998).
6. Y. Liu, C. Gorla, S. Liang, N. Emanetoglu, Y. Lu, H. Shen, andM. Wraback, "Ultraviolet detectors based on epitaxial ZnO films grown by MOCVD," *Journal of Electronic Materials*, **29**[1] 69-74 (2000).
7. B. Liu and H. C. Zeng, "Hydrothermal Synthesis of ZnO Nanorods in the Diameter Regime of 50 nm," *Journal of the American Chemical Society*, **125**[15] 4430-31 (2003).

8. T. Saeed and P. O'Brien, "Deposition and characterisation of ZnO thin films grown by chemical bath deposition," *Thin Solid Films*, **271**[1-2] 35-38 (1995).
9. L. Vayssieres, "Growth of Arrayed Nanorods and Nanowires of ZnO from Aqueous Solutions," *Advanced Materials,* **15**[5] 464-66 (2003).
10. D. Andeen, L. Loeffler, N. Padture, andF. F. Lange, "Crystal chemistry of epitaxial ZnO on MgAl2O4 produced by hydrothermal synthesis," *Journal of Crystal Growth*, **259**[1-2] 103-09 (2003).
11. X. Gao, X. Li, andW. Yu, "Flowerlike ZnO Nanostructures via Hexamethylenetetramine-Assisted Thermolysis of Zinc−Ethylenediamine Complex," *The Journal of Physical Chemistry B,* **109**[3] 1155-61 (2005).
12. D. Lincot, "Solution growth of functional zinc oxide films and nanostructures," *MRS Bulletin*, **35**[10] (2010).
13. K. Govender, D. S. Boyle, P. B. Kenway, andP. O'Brien, "Understanding the factors that govern the deposition and morphology of thin films of ZnO from aqueous solution," *Journal of Materials Chemistry,* **14**[16] 2575-91 (2004).
14. T. Kawano and H. Imai, "Nanoscale morphological design of ZnO crystals grown in aqueous solutions," *Journal of the Ceramic Society of Japan,* **118**[1383] 969-76 (2010).
15. T. Kawano and H. Imai, "Fabrication of ZnO Nanoparticles with Various Aspect Ratios through Acidic and Basic Routes," *Crystal Growth & Design*, **6**[4] 1054-56 (2006).
16. T. Kawano and H. Imai, "A simple preparation technique for shape-controlled zinc oxide nanoparticles: Formation of narrow size-distributed nanorods using seeds in aqueous solutions," *Colloids and Surfaces A: Physicochemical and Engineering Aspects,* **319**[1-3] 130-35 (2008).

17. Z. Zhou and Y. Deng, "Kinetics Study of ZnO Nanorod Growth in Solution," *The Journal of Physical Chemistry C,* **113**[46] 19853-58 (2009).
18. S. J. Kwon, "Patterned growth of ZnO nanorods by micromolding of sol-gel-derived seed layer," *Appl. Phys. Lett.,* **87**[13] 133112 (2005).
19. J. Song and S. Lim, "Effect of Seed Layer on the Growth of ZnO Nanorods," *The Journal of Physical Chemistry C,* **111**[2] 596-600 (2006).
20. G. She, "Controlled synthesis of oriented single-crystal ZnO nanotube arrays on transparent conductive substrates," *Appl. Phys. Lett.,* **92**[5] 053111 (2008).
21. I. Levin, "Growth habits and defects in ZnO nanowires grown on GaN/sapphire substrates," *Appl. Phys. Lett.,* **87**[10] 103110 (2005).
22. Y. Tak and K. Yong, "Controlled Growth of Well-Aligned ZnO Nanorod Array Using a Novel Solution Method," *The Journal of Physical Chemistry B,* **109**[41] 19263-69 (2005).
23. S. P. Garcia and S. Semancik, "Controlling the Morphology of Zinc Oxide Nanorods Crystallized from Aqueous Solutions: The Effect of Crystal Growth Modifiers on Aspect Ratio," *Chemistry of Materials,* **19**[16] 4016-22 (2007).
24. L. P. Bauermann, J. Bill, andF. Aldinger, "Bio-friendly Synthesis of ZnO Nanoparticles in Aqueous Solution at Near-Neutral pH and Low Temperature," *The Journal of Physical Chemistry B,* **110**[11] 5182-85 (2006).
25. B. Li and Y. Wang, "Facile Synthesis and Enhanced Photocatalytic Performance of Flower-like ZnO Hierarchical Microstructures," *The Journal of Physical Chemistry C,* **114**[2] 890-96 (2009).

26. Y. Zhang, J. Xu, Q. Xiang, H. Li, Q. Pan, andP. Xu, "Brush-Like Hierarchical ZnO Nanostructures: Synthesis, Photoluminescence and Gas Sensor Properties," *The Journal of Physical Chemistry C,* **113**[9] 3430-35 (2009).
27. J. Yin, Q. Lu, Z. Yu, J. Wang, H. Pang, andF. Gao, "Hierarchical ZnO Nanorod-Assembled Hollow Superstructures for Catalytic and Photoluminescence Applications," *Crystal Growth & Design,* **10**[1] 40-43 (2009).
28. J. Wu and D. Xue, "Morphology-tuned growth of ZnO microstructures," *Materials Research Bulletin,* **45**[3] 300-04 (2010).
29. E.-S. Jang, J.-H. Won, Y.-W. Kim, Z. Cheng, andJ.-H. Choy, "Synthesis of porous and nonporous ZnO nanobelt, multipod, and hierarchical nanostructure from Zn-HDS," *Journal of Solid State Chemistry,* **183**[8] 1835-40 (2010).
30. W.-D. Zhang, W.-H. Zhang, andX.-Y. Ma, "Tunable ZnO nanostructures for ethanol sensing," *Journal of Materials Science,* **44**[17] 4677-82 (2009).
31. M. Ahmad, S. Yingying, A. Nisar, H. Sun, W. Shen, M. Wei, andJ. Zhu, "Synthesis of hierarchical flower-like ZnO nanostructures and their functionalization by Au nanoparticles for improved photocatalytic and high performance Li-ion battery anodes," *Journal of Materials Chemistry,* **21**[21] 7723-29 (2011).
32. H. Bai, Z. Liu, andD. D. Sun, "Hierarchical ZnO/Cu "corn-like" materials with high photodegradation and antibacterial capability under visible light," *Physical Chemistry Chemical Physics,* **13**[13] 6205-10 (2011).
33. F. Xu, M. Dai, Y. Lu, andL. Sun, "Hierarchical ZnO Nanowire−Nanosheet Architectures for High Power Conversion Efficiency in Dye-Sensitized Solar Cells," *The Journal of Physical Chemistry C,* **114**[6] 2776-82 (2010).

34. J. Zhang, S. Wang, M. Xu, Y. Wang, B. Zhu, S. Zhang, W. Huang, andS. Wu, "Hierarchically Porous ZnO Architectures for Gas Sensor Application," *Crystal Growth & Design,* **9**[8] 3532-37 (2009).
35. Q.-P. Luo, B.-X. Lei, X.-Y. Yu, D.-B. Kuang, andC.-Y. Su, "Hiearchical ZnO rod-in-tube nano-architecture arrays produced via a two-step hydrothermal and ultrasonication process," *Journal of Materials Chemistry,* **21**[24] 8709-14 (2011).
36. L. Zhu, Y. Zheng, T. Hao, X. Shi, Y. Chen, andJ. Ou-Yang, "Synthesis of hierarchical ZnO nanobelts via Zn(OH)F intermediate using ionic liquid-assistant microwave irradiation method," *Materials Letters,* **63**[28] 2405-08 (2009).
37. Y. F. Zhu, G. H. Zhou, H. Y. Ding, A. H. Liu, Y. B. Lin, andN. L. Li, "Controllable synthesis of hierarchical ZnO nanostructures via a chemical route," *Physica E: Low-dimensional Systems and Nanostructures,* **42**[9] 2460-65 (2010).
38. F. Amano, O.-O. Prieto-Mahaney, Y. Terada, T. Yasumoto, T. Shibayama, andB. Ohtani, "Decahedral Single-Crystalline Particles of Anatase Titanium(IV) Oxide with High Photocatalytic Activity," *Chemistry of Materials,* **21**[13] 2601-03 (2009).
39. C.-X. He, B.-X. Lei, Y.-F. Wang, C.-Y. Su, Y.-P. Fang, andD.-B. Kuang, "Sonochemical Preparation of Hierarchical ZnO Hollow Spheres for Efficient Dye-Sensitized Solar Cells," *Chemistry – A European Journal,* **16**[29] 8757-61 (2010).
40. Y. Li, J. Gong, and Y. Deng, "Hierarchical structured ZnO nanorods on ZnO nanofibers and their photoresponse to UV and visible lights," *Sensors and Actuators A: Physical,* **158**[2] 176-82 (2010).

41. Y.-S. Fu, J. Sun, Y. Xie, J. Liu, H.-L. Wang, andX.-W. Du, "ZnO hierarchical nanostructures and application on high-efficiency dye-sensitized solar cells," *Materials Science and Engineering: B,* **166**[3] 196-202 (2010).
42. L. Guo, Y. L. Ji, H. Xu, P. Simon, andZ. Wu, "Regularly Shaped, Single-Crystalline ZnO Nanorods with Wurtzite Structure," *Journal of the American Chemical Society,* **124**[50] 14864-65 (2002).
43. X. Wang, Q. Zhang, Q. Wan, G. Dai, C. Zhou, andB. Zou, "Controllable ZnO Architectures by Ethanolamine-Assisted Hydrothermal Reaction for Enhanced Photocatalytic Activity," *The Journal of Physical Chemistry C,* **115**[6] 2769-75 (2011).
44. X. Fang, L. Peng, X. Shang, andZ. Zhang, "Controlled synthesis of ZnO branched nanorod arrays by hierarchical solution growth and application in dye-sensitized solar cells," *Thin Solid Films,* **519**[19] 6307-12 (2011).
45. X. Hu, Y. Masuda, T. Ohji, andK. Kato, "Dissolution−Recrystallization Induced Hierarchical Structure in ZnO: Bunched Roselike and Core−Shell-like Particles," *Crystal Growth & Design,* **10**[2] 626-31 (2009).
46. Y. Tong, J. Cheng, Y. Liu, andG. G. Siu, "Enhanced photocatalytic performance of ZnO hierarchical nanostructures synthesized via a two-temperature aqueous solution route," *Scripta Materialia,* **60**[12] 1093-96 (2009).
47. X. L. Zhang, R. Qiao, R. Qiu, J. C. Kim, andY. S. Kang, "Fabrication of Hierarchical ZnO Nanostructures via a Surfactant-Directed Process," *Crystal Growth & Design,* **9**[6] 2906-10 (2009).
48. H. Lu, S. Wang, L. Zhao, J. Li, B. Dong, andZ. Xu, "Hierarchical ZnO microarchitectures assembled by ultrathin nanosheets: hydrothermal synthesis and enhanced photocatalytic

activity," *Journal of Materials Chemistry,* **21**[12] 4228-34 (2011). Y. Yang, G. Du, X. Xin and B. Xu, Applied Physics A: Materials Science & Processing 104 (2011) 1229.

49. J. Yin, Q. Lu, Z. Yu, J. Wang, H. Pang, andF. Gao, "Hierarchical ZnO Nanorod-Assembled Hollow Superstructures for Catalytic and Photoluminescence Applications," *Crystal Growth & Design,* **10**[1] 40-43 (2009).
50. J. Zhang, S. Wang, M. Xu, Y. Wang, B. Zhu, S. Zhang, W. Huang, andS. Wu, "Hierarchically Porous ZnO Architectures for Gas Sensor Application," *Crystal Growth & Design,* **9**[8] 3532-37 (2009).
51. C. Xu, P. Shin, L. Cao, andD. Gao, "Preferential Growth of Long ZnO Nanowire Array and Its Application in Dye-Sensitized Solar Cells," *The Journal of Physical Chemistry C,* **114**[1] 125-29 (2009).
52. X. Liu, M. Afzaal, K. Ramasamy, P. O'Brien, andJ. Akhtar, "Synthesis of ZnO Hexagonal Single-Crystal Slices with Predominant (0001) and (000$\bar{1}$) Facets by Poly(ethylene glycol)-Assisted Chemical Bath Deposition," *Journal of the American Chemical Society,* **131**[42] 15106-07 (2009).
53. D. Krishnan and T. Pradeep, "Precursor-controlled synthesis of hierarchical ZnO nanostructures, using oligoaniline-coated Au nanoparticle seeds," *Journal of Crystal Growth,* **311**[15] 3889-97 (2009).
54. S. Cho, J.-W. Jang, S.-H. Jung, B. R. Lee, E. Oh, andK.-H. Lee, "Precursor Effects of Citric Acid and Citrates on ZnO Crystal Formation," *Langmuir,* **25**[6] 3825-31 (2009).
55. Y. Yan, L. Zhou, Z. Han, andY. Zhang, "Growth Analysis of Hierarchical ZnO Nanorod Array with Changed Diameter from the Aspect of Supersaturation Ratio," *The Journal of Physical Chemistry C,* **114**[9] 3932-36 (2010).

56. Y. Li, M. Zheng, L. Ma, M. Zhong, andW. Shen, "Fabrication of Hierarchical ZnO Architectures and Their Superhydrophobic Surfaces with Strong Adhesive Force," *Inorganic Chemistry*, **47**[8] 3140-43 (2008).
57. X.-H. Lu, D. Wang, G.-R. Li, C.-Y. Su, D.-B. Kuang, andY.-X. Tong, "Controllable Electrochemical Synthesis of Hierarchical ZnO Nanostructures on FTO Glass," *The Journal of Physical Chemistry C*, **113**[31] 13574-82 (2009).
58. J. Qiu, M. Guo, Y. Feng, andX. Wang, "Electrochemical deposition of branched hierarchical ZnO nanowire arrays and its photoelectrochemical properties," *Electrochimica Acta*, **56**[16] 5776-82 (2011).
59. H. Wang, Y. Liu, M. Li, H. Huang, H. Xu, andH. Shen, "Fabrication of three-dimensional ZnO with hierarchical structure via an electrodeposition process," *Applied Physics A: Materials Science & Processing*, **103**[2] 463-66 (2011).
60. J. Elias, J. Michler, L. Philippe, M.-Y. Lin, C. Couteau, G. Lerondel, andC. Lévy-Clément, "ZnO Nanowires, Nanotubes, and Complex Hierarchical Structures Obtained by Electrochemical Deposition," *Journal of Electronic Materials*, **40**[5] 728-32 (2011).
61. M. Law, H. Kind, B. Messer, F. Kim, andP. Yang, "Photochemical Sensing of NO2 with SnO2 Nanoribbon Nanosensors at Room Temperature," *Angewandte Chemie International Edition*, **41**[13] 2405-08 (2002).
62. I. Saadeddin, B. Pecquenard, J. P. Manaud, R. Decourt, C. Labrugère, T. Buffeteau, andG. Campet, "Synthesis and characterization of single- and co-doped SnO2 thin films for optoelectronic applications," *Applied Surface Science*, **253**[12] 5240-49 (2007).

63. M. Okuya, S. Kaneko, K. Hiroshima, I. Yagi, andK. Murakami, "Low temperature deposition of SnO2 thin films as transparent electrodes by spray pyrolysis of tetra-n-butyltin(IV)," *Journal of the European Ceramic Society,* **21**[10-11] 2099-102 (2001).

64. S. G. Ansari, P. Boroojerdian, S. R. Sainkar, R. N. Karekar, R. C. Aiyer, andS. K. Kulkarni, "Grain size effects on H2 gas sensitivity of thick film resistor using SnO2 nanoparticles," *Thin Solid Films,* **295**[1-2] 271-76 (1997).

65. Y. Wang, X. Jiang, andY. Xia, "A Solution-Phase, Precursor Route to Polycrystalline SnO2 Nanowires That Can Be Used for Gas Sensing under Ambient Conditions," *Journal of the American Chemical Society,* **125**[52] 16176-77 (2003).

66. D. F. Zhang, L. D. Sun, J. L. Yin, andC. H. Yan, "Low-Temperature Fabrication of Highly Crystalline SnO2 Nanorods," *Advanced Materials,* **15**[12] 1022-25 (2003).

67. Y. Wang, J. Y. Lee, andH. C. Zeng, "Polycrystalline SnO2 Nanotubes Prepared via Infiltration Casting of Nanocrystallites and Their Electrochemical Application," *Chemistry of Materials,* **17**[15] 3899-903 (2005).

68. Y. Wang, F. Su, J. Y. Lee, andX. S. Zhao, "Crystalline Carbon Hollow Spheres, Crystalline Carbon−SnO2 Hollow Spheres, and Crystalline SnO2 Hollow Spheres: Synthesis and Performance in Reversible Li-Ion Storage," *Chemistry of Materials,* **18**[5] 1347-53 (2006).

69. Y. Lilach, J.-P. Zhang, M. Moskovits, andA. Kolmakov, "Encoding Morphology in Oxide Nanostructures during Their Growth," *Nano Letters,* **5**[10] 2019-22 (2005).

70. C. Guo, M. Cao, andC. Hu, "A novel and low-temperature hydrothermal synthesis of SnO2 nanorods," *Inorganic Chemistry Communications,* **7**[7] 929-31 (2004).

71. L. Vayssieres and M. Graetzel, "Highly Ordered SnO2 Nanorod Arrays from Controlled Aqueous Growth," *Angewandte Chemie,* **116**[28] 3752-56 (2004).

72. B. Thangaraju, "Structural and electrical studies on highly conducting spray deposited fluorine and antimony doped SnO2 thin films from SnCl2 precursor," *Thin Solid Films,* **402**[1-2] 71-78 (2002).

73. E. K. Shokr, M. M. Wakkad, H. A. Abd El-Ghanny, andH. M. Ali, "Sb-doping effects on optical and electrical parameters of SnO2 films," *Journal of Physics and Chemistry of Solids,* **61**[1] 75-85 (2000).

74. A. Cabot, J. Arbiol, J. R. Morante, U. Weimar, N. Bârsan, andW. Göpel, "Analysis of the noble metal catalytic additives introduced by impregnation of as obtained SnO2 sol–gel nanocrystals for gas sensors," *Sensors and Actuators B: Chemical,* **70**[1-3] 87-100 (2000).

75. S. Liu and M. Zuo, "Influence of Doping Methods on the Gas-Sensing Properties of CuO-SnO2 Sensors," *Advanced Materials Research,* **306** (2011).

76. A. Gamard, O. Babot, B. Jousseaume, M.-C. Rascle, T. Toupance, andG. Campet, "Conductive F-doped Tin Dioxide Sol−Gel Materials from Fluorinated β-Diketonate Tin(IV) Complexes. Characterization and Thermolytic Behavior," *Chemistry of Materials,* **12**[11] 3419-26 (2000).

77. H. Ohgi, T. Maeda, E. Hosono, S. Fujihara, andH. Imai, "Evolution of Nanoscale SnO2 Grains, Flakes, and Plates into Versatile Particles and Films through Crystal Growth in Aqueous Solutions," *Crystal Growth & Design,* **5**[3] 1079-83 (2005).

78. Z. W. Chen, J. K. L. Lai, andC. H. Shek, "Bulk-quantity SnO2 nanorods synthesized from simple calcining process based on annealing precursor powders," *Journal of Non-Crystalline Solids,* **351**[46-48] 3619-23 (2005).

79. Y.-D. Ko, "Self-supported SnO 2 nanowire electrodes for high-power lithium-ion batteries," *Nanotechnology,* **20**[45] 455701 (2009).

80. L. C. Tien, S. J. Pearton, D. P. Norton, andF. Ren, "Synthesis and characterization of single crystalline SnO<sub>2</sub> nanorods by high-pressure pulsed laser deposition," *Applied Physics A: Materials Science & Processing,* **91**[1] 29-32 (2008).

81. M. Batzill and U. Diebold, "The surface and materials science of tin oxide," *Progress in Surface Science,* **79**[2-4] 47-154 (2005).

82. L. G. P. Simões, M. R. Cássia-Santos, M. M. Oliveira, E. Longo, andJ. A. Varela, "Effect of La2O3 addition and O2 atmosphere on the electric properties of SnO2TiO2," *Materials Chemistry and Physics,* **90**[2-3] 234-38 (2005).

83. K. Ellmer, "Magnetron sputtering of transparent conductive zinc oxide: relation between the sputtering parameters and the electronic properties," *Journal of Physics D: Applied Physics,* **33**[4] R17 (2000).

84. N. Yamazoe, G. Sakai, andK. Shimanoe, "Oxide Semiconductor Gas Sensors," *Catalysis Surveys from Asia,* **7**[1] 63-75 (2003).

85. X. Gao, X. Li, andW. Yu, "Flowerlike ZnO Nanostructures via Hexamethylenetetramine-Assisted Thermolysis of Zinc−Ethylenediamine Complex," *The Journal of Physical Chemistry B,* **109**[3] 1155-61 (2005).

86. J. Gong, Q. Chen, M.-R. Lian, N.-C. Liu, R. G. Stevenson, andF. Adami, "Micromachined nanocrystalline silver doped SnO2 H2S sensor," *Sensors and Actuators B: Chemical,* **114**[1] 32-39 (2006).

87. M. W. Ahn, K. S. Park, J. H. Heo, D. W. Kim, K. J. Choi, andJ. G. Park, "On-chip fabrication of ZnO-nanowire gas sensor with high gas sensitivity," *Sensors and Actuators B: Chemical,* **138**[1] 168-73 (2009).
88. Y. Zeng, T. Zhang, M. Yuan, M. Kang, G. Lu, R. Wang, H. Fan, Y. He, andH. Yang, "Growth and selective acetone detection based on ZnO nanorod arrays," *Sensors and Actuators B: Chemical,* **143**[1] 93-98 (2009).
89. O. Lupan, S. Shishiyanu, L. Chow, andT. Shishiyanu, "Nanostructured zinc oxide gas sensors by successive ionic layer adsorption and reaction method and rapid photothermal processing," *Thin Solid Films,* **516**[10] 3338-45 (2008).
90. T.-J. Hsueh and C.-L. Hsu, "Fabrication of gas sensing devices with ZnO nanostructure by the low-temperature oxidation of zinc particles," *Sensors and Actuators B: Chemical,* **131**[2] 572-76 (2008).
91. T.-J. Hsueh, C.-L. Hsu, S.-J. Chang, andI. C. Chen, "Laterally grown ZnO nanowire ethanol gas sensors," *Sensors and Actuators B: Chemical,* **126**[2] 473-77 (2007).
92. Q. Qi, T. Zhang, L. Liu, X. Zheng, Q. Yu, Y. Zeng, andH. Yang, "Selective acetone sensor based on dumbbell-like ZnO with rapid response and recovery," *Sensors and Actuators B: Chemical,* **134**[1] 166-70 (2008).
93. N. Hongsith, C. Viriyaworasakul, P. Mangkorntong, N. Mangkorntong, andS. Choopun, "Ethanol sensor based on ZnO and Au-doped ZnO nanowires," *Ceramics International,* **34**[4] 823-26 (2008).
94. H. Xu, X. Liu, D. Cui, M. Li, andM. Jiang, "A novel method for improving the performance of ZnO gas sensors," *Sensors and Actuators B: Chemical,* **114**[1] 301-07 (2006).

95. C. S. Rout, S. Hari Krishna, S. R. C. Vivekchand, A. Govindaraj, andC. N. R. Rao, "Hydrogen and ethanol sensors based on ZnO nanorods, nanowires and nanotubes," *Chemical Physics Letters,* **418**[4-6] 586-90 (2006).
96. S. Choopun, N. Hongsith, P. Mangkorntong, andN. Mangkorntong, "Zinc oxide nanobelts by RF sputtering for ethanol sensor," *Physica E: Low-dimensional Systems and Nanostructures,* **39**[1] 53-56 (2007).
97. C. Shoou-Jinn, H. Ting-Jen, I. C. Chen, H. Shang-Fu, C. Sheng-Po, H. Cheng-Liang, L. Yan-Ru, andH. Bohr-Ran, "Highly Sensitive ZnO Nanowire Acetone Vapor Sensor With Au Adsorption," *Nanotechnology, IEEE Transactions on,* **7**[6] 754-59 (2008).
98. Q. Wan, "Fabrication and ethanol sensing characteristics of ZnO nanowire gas sensors," *Appl. Phys. Lett.,* **84**[18] 3654 (2004).
99. N. Kakati, S. H. Jee, S. H. Kim, H.-K. Lee, andY. S. Yoon, "Sensitivity Enhancement of ZnO Nanorod Gas Sensors with Surface Modification by an InSb Thin Film," *Japanese Journal of Applied Physics,* **48**[10] 105002 (2009).
100. E. Comini, G. Faglia, M. Ferroni, andG. Sberveglieri, "Gas sensing properties of zinc oxide nanostructures prepared by thermal evaporation," *Applied Physics A: Materials Science & Processing,* **88**[1] 45-48 (2007).
101. Y. Lv, L. Guo, H. Xu, andX. Chu, "Gas-sensing properties of well-crystalline ZnO nanorods grown by a simple route," *Physica E: Low-dimensional Systems and Nanostructures,* **36**[1] 102-05 (2007).
102. L. Liao, H. B. Lu, J. C. Li, H. He, D. F. Wang, D. J. Fu, C. Liu, andW. F. Zhang, "Size Dependence of Gas Sensitivity of ZnO Nanorods," *The Journal of Physical Chemistry C,* **111**[5] 1900-03 (2007).

103. S. Si, C. Li, X. Wang, Q. Peng, andY. Li, "Fe2O3/ZnO core–shell nanorods for gas sensors," *Sensors and Actuators B: Chemical,* **119**[1] 52-56 (2006).
104. T. Brousse and D. M. Schleich, "Sprayed and thermally evaporated SnO2 thin films for ethanol sensors," *Sensors and Actuators B: Chemical*, **31**[1-2] 77-79 (1996).
105. F. Hellegouarc’h, F. Arefi-Khonsari, R. Planade, andJ. Amouroux, "PECVD prepared SnO2 thin films for ethanol sensors," *Sensors and Actuators B: Chemical,* **73**[1] 27-34 (2001).
106. E. Comini, "Stable and highly sensitive gas sensors based on semiconducting oxide nanobelts," *Appl. Phys. Lett.,* **81**[10] 1869 (2002).
107. Z. Ying and et al., "SnO 2 nanowhiskers and their ethanol sensing characteristics," *Nanotechnology,* **15**[11] 1682 (2004).
108. Y. J. Chen, "Synthesis and ethanol sensing characteristics of single crystalline SnO2 nanorods," *Appl. Phys. Lett.,* **87**[23] 233503 (2005).
109. Y. J. Chen, "Linear ethanol sensing of SnO2 nanorods with extremely high sensitivity," *Appl. Phys. Lett.,* **88**[8] 083105 (2006).
110. C. Yujin and et al., "The enhanced ethanol sensing properties of multi-walled carbon nanotubes / SnO 2 core/shell nanostructures," *Nanotechnology,* **17**[12] 3012 (2006).
111. S. Giorgio, "Classical and novel techniques for the preparation of SnO2 thin-film gas sensors," *Sensors and Actuators B: Chemical,* **6**[1-3] 239-47 (1992).
112. S. H. Kim, K. T. Lee, S. Lee, J. H. Moon, andB.-T. Lee, "Effects of Pt/Pd Co-Doping on the Sensitivity of SnO2 Thin Film Sensors," *Japanese Journal of Applied Physics,* **41** (2002).

113. Y. Tan, C. Li, Y. Wang, J. Tang, andX. Ouyang, "Fast-response and high sensitivity gas sensors based on SnO2 hollow spheres," *Thin Solid Films,* **516**[21] 7840-43 (2008).

114. A. Helwig, G. Müller, G. Sberveglieri, andG. Faglia, "Gas response times of nano-scale SnO2 gas sensors as determined by the moving gas outlet technique," *Sensors and Actuators B: Chemical,* **126**[1] 174-80 (2007).

115. A. Karthigeyan, R. P. Gupta, K. Scharnagl, M. Burgmair, M. Zimmer, S. K. Sharma, andI. Eisele, "Low temperature NO2 sensitivity of nano-particulate SnO2 film for work function sensors," *Sensors and Actuators B: Chemical,* **78**[1-3] 69-72 (2001).

116. J. Gong, Q. Chen, M.-R. Lian, N.-C. Liu, R. G. Stevenson, andF. Adami, "Micromachined nanocrystalline silver doped SnO2 H2S sensor," *Sensors and Actuators B: Chemical,* **114**[1] 32-39 (2006).

117. M. Ivanovskaya, P. Bogdanov, G. Faglia, P. Nelli, G. Sberveglieri, andA. Taroni, "On the role of catalytic additives in gas-sensitivity of SnO2-Mo based thin film sensors," *Sensors and Actuators B: Chemical,* **77**[1-2] 268-74 (2001).

118. M. Di Giulio, G. Micocci, R. Rella, P. Siciliano, andA. Tepore, "Properties of reactively sputtered tin oxide films as CO gas sensors," *Sensors and Actuators B: Chemical,* **23**[2-3] 193-95 (1995).

119. J. R. Brown, P. W. Haycock, L. M. Smith, A. C. Jones, andE. W. Williams, "Response behaviour of tin oxide thin film gas sensors grown by MOCVD," *Sensors and Actuators B: Chemical,* **63**[1-2] 109-14 (2000).

120. S. Seal and S. Shukla, "Nanocrystalline SnO gas sensors in view of surface reactions and modifications," *JOM Journal of the Minerals, Metals and Materials Society,* **54**[9] 35-38 (2002).

121. H. Wang, J. Liang, H. Fan, B. Xi, M. Zhang, S. Xiong, Y. Zhu, andY. Qian, "Synthesis and gas sensitivities of SnO2 nanorods and hollow microspheres," *Journal of Solid State Chemistry,* **181**[1] 122-29 (2008).
122. H. Zhao, Y. Li, L. Yang, andX. Wu, "Synthesis, characterization and gas-sensing property for C2H5OH of SnO2 nanorods," *Materials Chemistry and Physics,* **112**[1] 244-48 (2008).
123. P. Nelli, G. Faglia, G. Sberveglieri, E. Cereda, G. Gabetta, A. Dieguez, A. Romano-Rodriguez, andJ. R. Morante, "The aging effect on SnO2–Au thin film sensors: electrical and structural characterization," *Thin Solid Films,* **371**[1-2] 249-53 (2000).
124. A. Ahmad and J. Walsh, "The influence of precursor powders and processing parameters on the properties of SnO<sub>2</sub>-based gas sensors," *Journal of Materials Science,* **38**[21] 4325-32 (2003).
125. Q. Lipeng and et al., "The template-free synthesis of square-shaped SnO 2 nanowires: the temperature effect and acetone gas sensors," *Nanotechnology,* **19**[18] 185705 (2008).

CHAPTER 3 DEVICE FABRICATION AND GAS SEISNG MEASUREMENT

3.1 Substrate preparation

Four different materials were used for substrate to characterize sensing materials and fabricate sensors to measure the gas sensing property. First, alumina plate was prepared by cleaning ultrasonically. Alumina is useful for the several applications as a substrate. As it has a good thermal conductivity and heat resistance, alumina are appropriate for devices working at high temperature. Stability in corrosive or flammable chemical is another advantage of alumina substrate. In electric device fabrication, electric insulation of alumina allows its usage to deposit electrodes on the plate to measure the accurate current by avoiding other interferences from substrates [1]. In table 3.1, basic mechanical and electrical property of alumina plate is summarized. In this research, 96% alumina plate was utilized. To separate each sensor from the plate easily, laser processing to draw cutting lines was performed. In figure 3.1(a), laser processed alumina plate is shown. Microstructure of alumina substrate before sensor fabrication was observed by FE-SEM. As shown in figure 3.1(b), surface morphology of alumina plate has a quite rough and somewhat porous. Due to this nature, rough alumina substrate can be utilized to grow ZnO nanostructures in random direction. Details of process and mechanism will be discussed in later chapter.

Secondly, one side polished, n-type of 4" silicon dioxide substrate was prepared. Silicon wafers were purchased from University wafer (South Boston, MA). Silicon dioxide layers were thermally oxidized to have a uniform thickness. Thickness of silicon dioxide was measured to have 500 nm. Thermally oxidized silicon dioxide layer has a tetrahedral structure as shown in figure 3.2. Atomic distances between Si atom and O atom, and O atom and O atom are 1.6 and 2.27 angstrom, respectively. General form of SiO_2 in nature is amorphous structure [3].

Table 3.1 Mechanical and electrical property of alumina [2]

Property		Unit	96% Al_2O_3	99.6% Al_2O_3
Appearance			White	White
Bulk Density		g/c.c	3.72	3.85
Water adsorption			Nil	Nil
Grain Size		μm	3~4	Less than 1.5
Thermal characteristics	Thermal conductivity	W/mK	22.3	29.5
	Coefficient of linear thermal expansion	x 10^{-6}/ ℃, RT~800 ℃	8.0	8.2
Mechanical characteristics	Flexure Strength	Mpa	350	500
Electrical Characteristics	Dielectric breakdown voltage	V/m	$14x10^{6}$	$18x10^{6}$
	Volume resistivity	Ohm·cm	$>10^{14}$	$>10^{14}$
	Dielectric constant	1MHZ	9.5	9.8
	Dielectric loss angle	1 MHZ (x10^{-4})	3	2

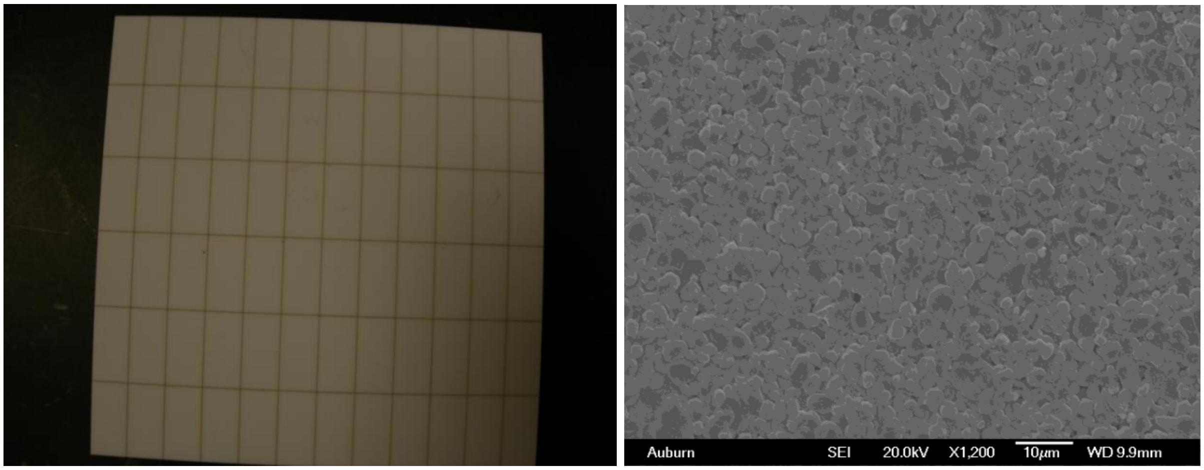

Figure 3.1 (a) Laser processed alumina plate, (b) FE-SEM picture of alumina plate at x1200 mag.

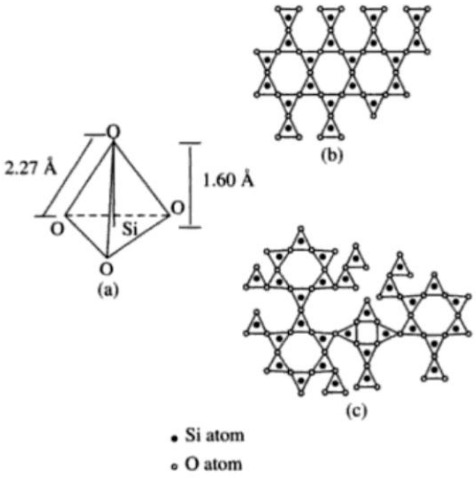

Figure 3.2 Crystal structure of thermally oxidized SiO_2 layer (a), structure of regularly ordered quartz (b), randomly ordered amorphous SiO_2 (c) for comparison [3]

Silicon dioxide is reported to have a good stability in silicon and dioxide interface, electrical and physical properties [4]. High melting point and chemical stability made silicon oxide to use as a great insulation material [5]. To clean the SiO_2/Si wafers, 100% reagent grade of acetone (fisher scientific, PA) was directly applied to the surface of wafers by immersing whole wafers in Pyrex® bowl. Pure nitrogen gas was sprayed to remove the residual acetone.

For flexible electronic device fabrication, two polyimide films, Kapton® and Cirlex® were purchased from McMaster Carr (Santa Fe Springs, CA) and thickness is compared in figure 3.3. Below table 3.2 shows the details of properties of Kapton® and Cirlex® films. Figure 6 and 7 shows mechanical property change in aging films at high temperature according to time change.

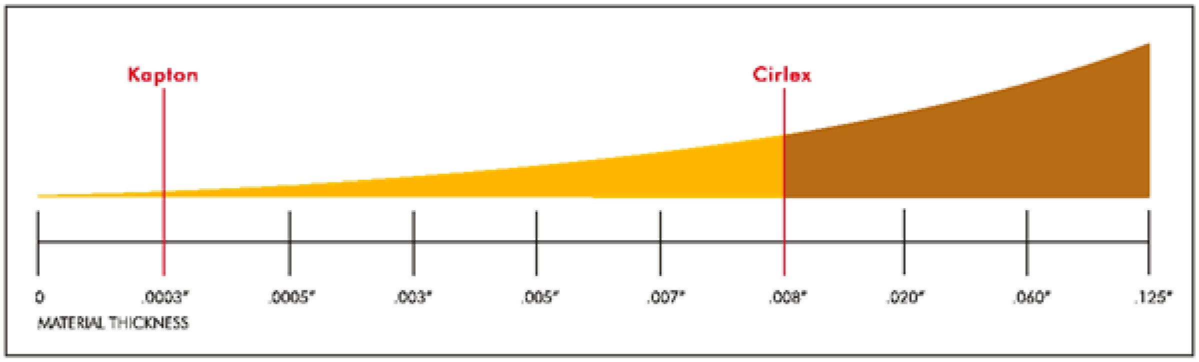

Figure 3.3 Thickness comparisons between typical Kapton® and Cirlex® films

Table 3.2 Thermal, electrical, and chemical property comparison between Cirlex® and Kapton® films [6]

	Cirlex®	Kapton®
Thermal property	Temperature range from -269 ℃ to 351 ℃	Temperature range from -269 ℃ to 400 ℃
Electrical property	2790 volts/mm for 0.23mm thickness	3000 volts/mm for 0.30mm thickness
Chemical property	Impermeable to organic chemicals, fuels and solvents	No known organic solvents to melt or burn

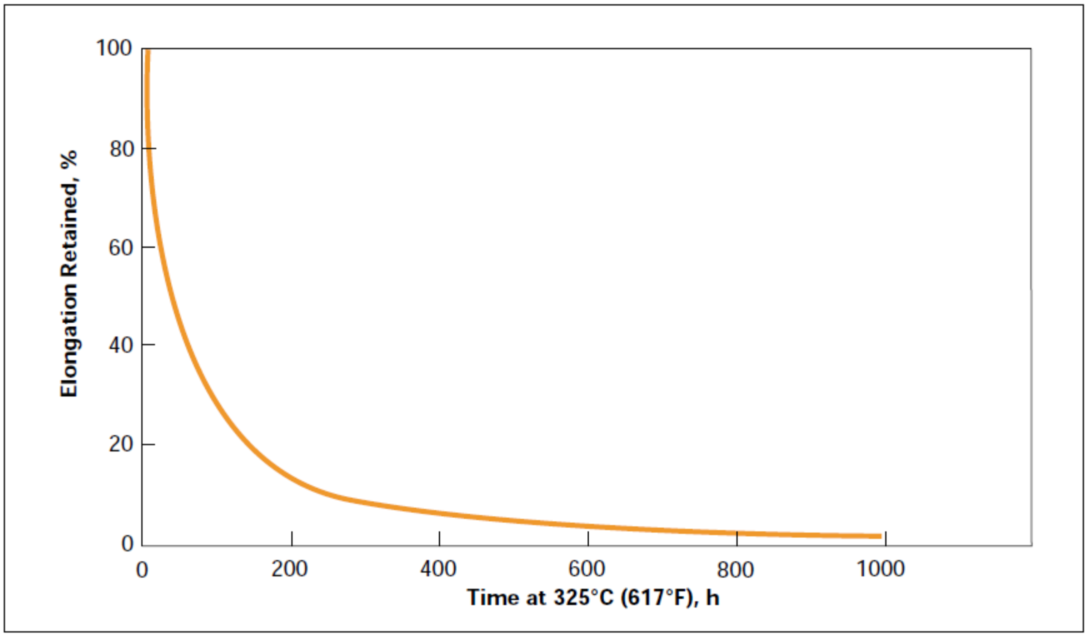

Figure 3.4 Elongation retained % according to time in aging in air at 325 ℃, 25 micron HN Kapton® film was tested

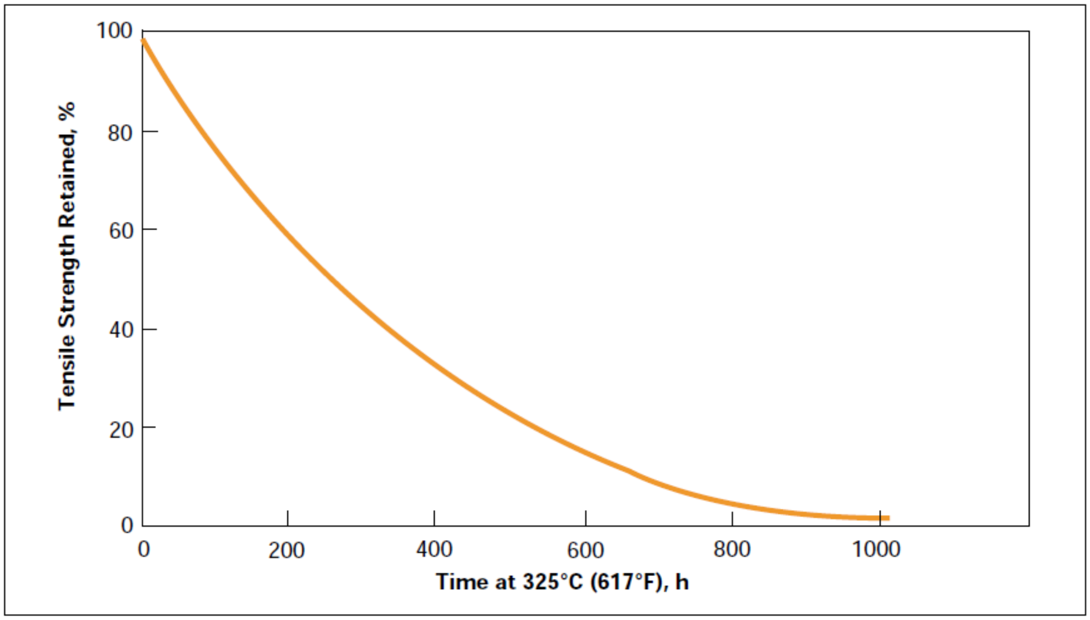

Figure 3.5 Tensile strength retained % according to time duration at 325 ℃ in air, 25 micron HN Kapton® film was tested

Overall thermal, electrical, and chemical property of Kapton® and Cirlex® films are similar, but judged on the mechanical property change of Kapton® at high temperature, Kapton® films appears to be not suitable for high temperature sensor application. To fabricate flexible sensor device applicable both at room temperature and high temperature, Cirlex® films are selected to use a substrate.

3.2 Bottom electrode deposition

Platinum electrode has several advantages in electric devices. In carrying current, resistance change depending on working temperature is quite linear. Chemical and mechanical stability in long term usage is also reliable [7]. Due to stability in high temperature and harsh conditions, platinum electrode is widely used in gas sensors, fuel cells, and transducers [8]. Prior to the deposition, mask to make a pattern are made into two types depending on the dimension of electrode. For simple and easy usage, stainless steel shadow mask is made by laser processing as depicted in figure 3.6. Width of electrode and finger distance was 400 µm, respectively. Drawing of electrode is shown in figure 3.7. For smaller electrodes` deposition, quartz mask was prepared due to a higher resolution than economic film mask. Dimension of electrode varied from 25 µm to 100 µm. Source design to make a quartz mask was prepared using AutoCAD® .

Electrodes ranging from 25 µm to 100 µm were patterned through photolithography process. First, image reversal photo resist (PR) AZ 5214-E was spin coated. Acceleration was 1000 rpm and coating was performed at 3000 rpm for 30 second. Both silicon dioxide and polyimide substrates were tested and PR was successfully coated on both substrates. Thickness of PR was measured by Alpha-step 200 profilometer (Tencor Instruments) and showed 1.5 µm. Coated substrates were heated on a hot plate at 105 ℃ for 1minute right after the PR deposition.

Double-sided mask aligned with UV light was utilized to perform a photolithography. Power of 345nm UV was set to 275W and exposed for 25sec. After the UV exposure, developing was followed using AZ300K solution. Solution was used as-received and substrates were emerged in a solution for 1.2 min. To remove residual chemicals and prevent further development, substrates were rinsed in flowing D.I water thoroughly. Next to washing, substrates were air blown to get rid of water droplets. Developed substrate was complete dried at room temperature for the next step, electrode deposition by sputtering. Platinum target was installed at dc cathode. Applied voltage was 300W. To deposit 100nm thick of electrode, it took 360 sec. Deposited platinum on the patterned substrate is shown in figure 3.8. The final step to remove the residual PR, lift-off process was carried out using 100% reagent grade acetone (fisher scientific) for 1hr. After 1hr lift-off, ultrasonication was followed physically to improve the lift-off speed. Patterned electrodes were observed by optical microscope to check the unresolved areas. Unless all electrodes were clearly patterned, lift-off process repeated one more time. For 400 µm electrode pattering, stain steel shadow mask was attached on the substrate. Advantages of using a shadow mask is to avoid bunch of photolithography processes, and to apply for any flat substrates, which are hard to use for photolithography, such as alumina or small size substrates to perform a PR coating. As shown in figure 3.9, from left to right, three pictures represent platinum bottom electrode patterned alumina substrate, silicon dioxide substrate, Cirlex® polyimide film, respectively.

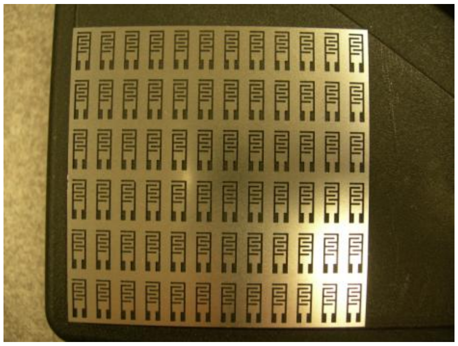

Figure 3.6 Laser processed stainless steel shadow mask, 400 µm width and finger distance

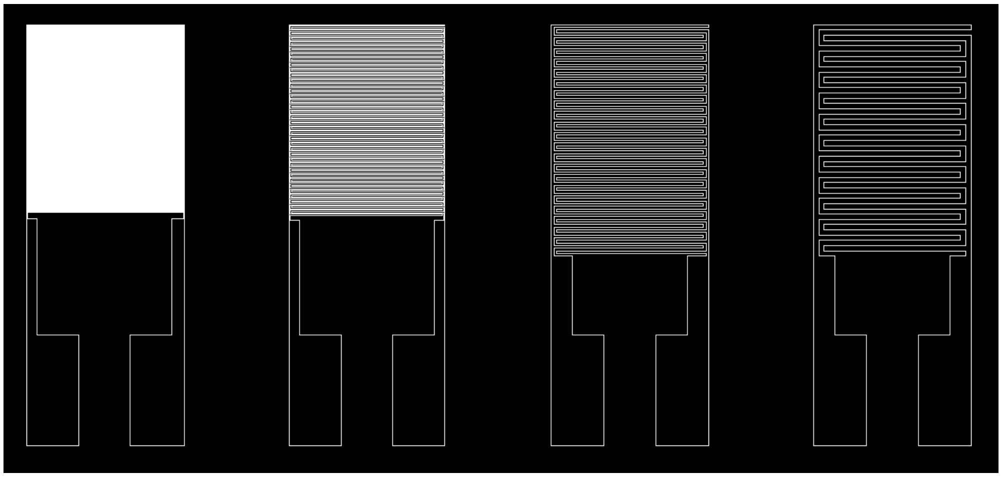

Figure 3.7 AutoCAD designs of interdigitated electrodes with 200, 100, 50, and 25 µm width and finger distance from right to left. Sensing area are designed to be same regardless electrodes` dimension

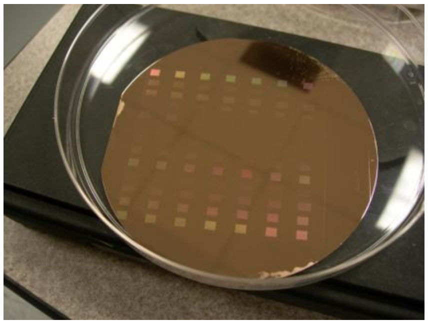

Figure 3.8 platinum deposited on a patterned silicon dioxide substrate by PR developing

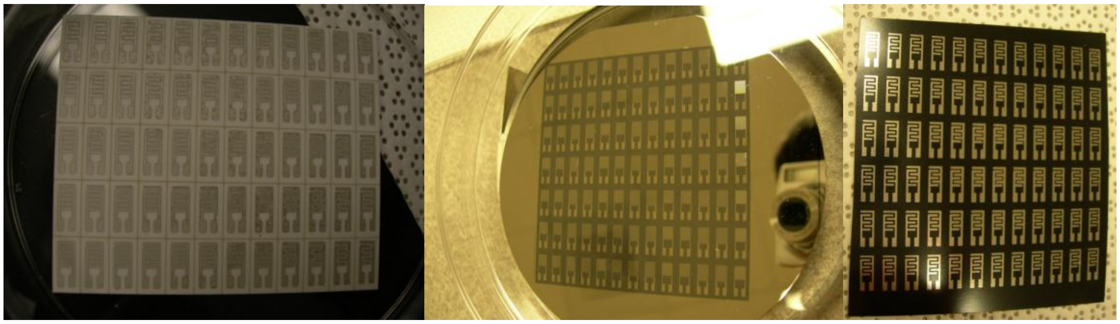

Figure 3.9 Platinum coated bottom electrodes on (a) alumina plate with shadow mask (b) silicon dioxide substrate after the lift-off (c) polyimide Cirlex® film with shadow mask

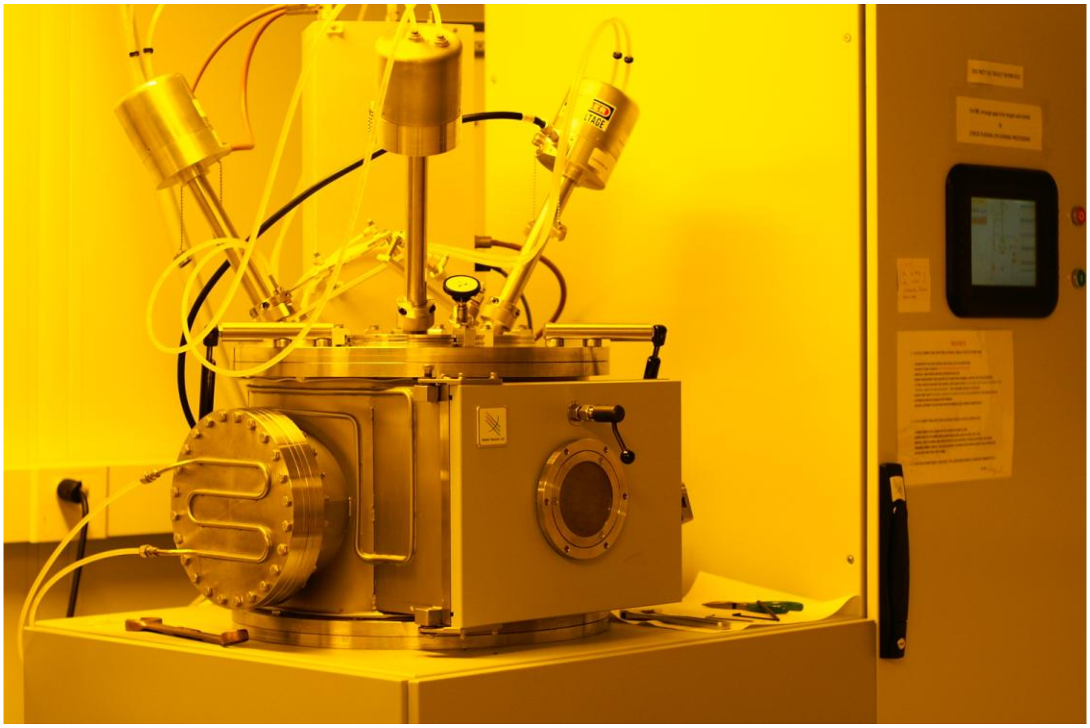

Figure 3.10 Denton Discovery 18 rf/dc sputtering system

3.3 Sensing layer deposition and growth

3.3.1 Sputtering

Rf/dc sputtering was performed by using Discovery 18 (Denton Vacuum) as shown in figure 3.10. The chamber inside require high vacuum environment to minimize the side-effect from other gas molecules, particles and water molecules in generating plasma and reaching target molecules to the substrate. Approximately $5X10^{-6}$ mTorr of vacuum level was achieved by turbo pump for 5 hrs` pumping down. Prior to the sputtering, argon and oxygen gas mixture was introduced into the chamber in the ratio of 20:2 to supply sufficient oxygen to achieve the stable and more stoichiometric ZnO films [9]. Generally, dielectric ceramic targets in sputtering require rf sputtering even deposition rate is quite slower than dc sputtering [transparent conductive zinc oxide: basics and applications in thin film]. 3" ZnO ceramic target was attached on rf cathode. 80W power was applied for 1500 sec. to deposit approximately 80nm thick ZnO films. Distance between cathode and bottom plate was 4". Schematic diagram of cathode and bottom plate is as drawn in figure 3.11. As shown in diagram, rf and dc cathode is located with an angle from the vertically elevated point. For uniform deposition, bottom plate is rotated in 50 rpm to compensate the difference between center and edge area.

In the case of SnO_x thin film deposition, both rf and dc sputtering were carried out using SnO_2 ceramic target and Sn metallic target. As explained before, rf sputtering using ceramic SnO_2 has advantage in obtaining more stoichiometric SnO_2 thin films. However, tin dioxide is relatively difficulty to achieve rather than ZnO due to various tin phases depending on the processing conditions such SnO, SnO_2, Sn_2O_3 [10].

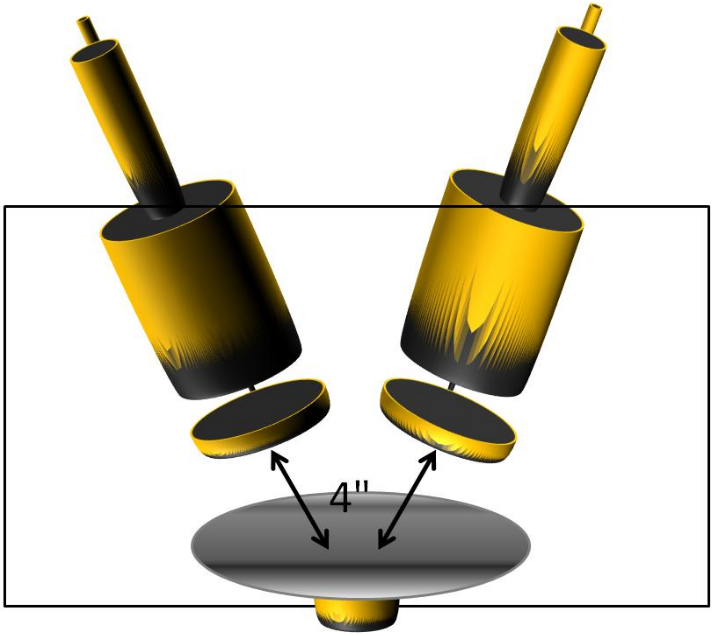

Figure 3.11 Schematic diagram of rf, dc cathodes and bottom plate

In following chapters, properties of SnO and SnO_2 thin films depending on structural and compositional changes were studied by different argon to oxygen ratios in gas mixture, post annealing temperature for both rf and dc sputtered films. As thickness of thin films varied according to the amount of argon and oxygen in gas mixtures, thickness of films were controlled to have 130nm by changing sputtering time. Each thickness of films was characterized by FE-SEM by observing cross section of films.

3.3.2 Sol-gel spin coating

Chemical solution deposition, known as sol-gel spin coating is widely used to deposit thin films. Solution was made by mixing two raw chemicals, zinc acetate dehydrate ($Zn(CH_3COO)_2 \cdot 2\ H_2O$, Aldrich) and 2-MOE (2-methoxyethanol, $CH_3OCH_2CH_2OH$, Aldrich). Additionally, chelating agents to help solubility of zinc salts and increase the stability to the humidity during the deposition [11-12], two types of agents, DEA (Diethanolamine, $HN(CH_2CH_2OH)_2$, Aldrich) and MEA (Monoethanolamine, $NH_2CH_2CH_2OH$, Aldrich) were utilized. Two solutions with different chelating agent were made and stirred at 80 ℃ for 1hr. Then, heated solution was cooled down at room temperature. By using a spin coater (WS-400-6NPP-LITE, Laurell Technologies Corporation) as shown in figure 3.12, approximately 27nm thick ZnO films were deposited under 3000 rpm and 30 sec deposition per one layer for 0.05M ZnO solution. Heat treatment to perform a pyrolysis was done at 300 ℃ and 250 ℃ for 10 min. for DEA and MEA, respectively. Every 5 times deposition, post annealing was carried out at 650 ℃ for 1hr.

Figure 3.12 Spin coater WS-400-6NPP-LITE (Laurell Technologies Corporation)

3.3.3 Aqueous chemical solution method

Nanostructured metal oxides such as ZnO and SnO_2 are widely grown by chemical solution method because structures can be easily modified at low temperature [13]. Based on the suggested method by Lionel Vayssieres in 2003, ZnO nanorods were grown on top of the ZnO seed layer in the manner described by Vayssieres [14]. A mixture of 0.01 mol of crystalline zinc nitrate hexahydrate (ACS Certified, Fisher Scientific, Pittsburgh, PA, USA) and 0.01 mol of HMT (hexamethylenetetramine, 99%, Sigma-Aldrich, St. Louis, MO, USA) were dissolved in 400 ml of deionized (DI) water. The aqueous solution was stirred at room temperature for 12 hr until all chemicals were completely dissolved. A hot water bath (IsoTemp 202, Fisher Scientific), as shown in figure 3.13, was used to accurately and digitally maintain a synthesis temperature of 85 ℃. Previously seeded substrates were placed into the solution with the seed layer pointing down and ZnO nanorods allowed growing for 4 hr as shown in figure 3.14. Nanostructure of ZnO was modified depending on heating temperatures from 75 ℃ to 95 ℃. Molar concentration of solution also varied from 0.001 mol of zinc nitrate hexahydrate and 0.1 mol of zinc salt by balancing same molar ratio of HMT. Details of study according to heating temperature and molar concentration of solution will be explained in later chapter.

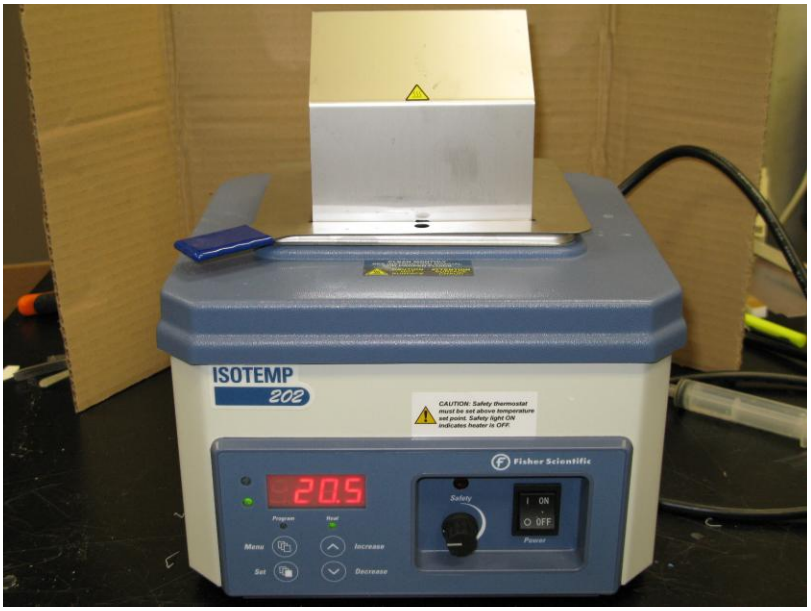

Figure 3.13 Hot water bath (IsoTemp 202, Fisher Scientific)

Figure 3.14 ZnO thin film coated substrates hang on the supporting bar by facing down

3.3.4 Electrodeposition

Electrodeposition was used to dope transition metal ions in aqueous solution and modify ZnO nanostructures via dc electric field. Generally, transition metal ions in aqueous solution prefer to stay in solutions as forming an aquo complex rather than incorporating into ZnO nanostructure [15]. External driving force such as dc electric field is necessary to draw dissolved ions into zinc lattices of substrate. In this study, ZnO thin film coated substrate with platinum electrode was used as an anode to compare the ZnO nanostructure grown assisted by dc electric field and chemically grown ZnO nanostructure without dc electric field. Morphology of ZnO nanostructure was highly influenced by dc electric field in terms of diameter, length and density. DC field was changed by increasing or decreasing voltage in the range of 1V to 5V. Material working as cathode was 304 stainless steel, which do not participate in chemical reaction. Distance between cathode and anode was fixed to be 1cm. Any additional acid or base was not added to modify the pH value. Chemical additives, which might influence the stability of solution was not used to focus on the effect of DC field. As described in previous aqueous chemical solution method, ZnO and platinum electrode coated substrate was immersed in a solution by deposited face down and cathode, stainless steel, was located in parallel. 0.01 mol of zinc nitrate hexahydrate and same concentration of HMT were made into a solution and deposition time was same as 4 hr.

3.4 Material characterization

The crystallinity and morphology of both the ZnO seeded substrates and the nanorod structures were examined using X-ray diffraction (XRD) and field emission scanning electron microscopy (FE-SEM). XRD samples were scanned from 20° to 80° 2-theta at the rate of 5° per minute under 40 kV and 40 mA power with a CuK-alpha radiation source (D/MAX B, Rigaku, Tokyo, Japan). Surface morphology was observed with FE-SEM (JSM-7000F, JEOL, Tokyo Japan). Composition and atomic ratio of materials are analyzed by EDS (Energy Dispersive X-ray Spectroscopy) equipped in FE-SEM (INCA system, Oxford Instruments) in Point & ID mode. For the analysis of transition metal doping, Raman spectroscopy (He-Cd laser, 80mW, Kimmon Electric with 441.6 nm line) was used to investigate the interaction of monochromic laser with crystal structure in vibration, rotation modes. Single crystal of ZnO grown along to the (001) plane was characterized to use as standard peaks. Two modes, A_1 (Transverse Optical) and E_1 (Longitudinal Optical), were used to study changes in Ni-doped ZnO nanorods. By observing and comparing the peak shift in two modes, influence of transition doping in ZnO nanostructure was studied.

3.5 Gas sensing property measurement

To test the gas sensing properties, sensors were loaded into a small test chamber connected with various gases controlled by a mass flow controller (MKS1179A, MKS Instruments, Andover, MA, USA) as shown in figure 3.15. Total gas flow was fixed at 100 sccm by combining three gases: pure nitrogen (MFC_1), pure oxygen (MFC_2) and 500 ppm of ethanol diluted in nitrogen gas (MFC_3). Oxygen flow was fixed at 20 sccm to produce a synthetic air with an ethanol concentration given by:

$$C_{ethanol}(ppm) = \frac{500 \times MFC_3}{MFC_1 + MFC_2 + MFC_3}$$

Sensor resistance was measured with a digital multimeter (Model 2400-LV SourceMeter, Keithley Instruments Inc., Cleveland, OH, USA). The surface temperature of the sensors was elevated by applying a dc voltage to the back side platinum heater. In this experiment, the temperature of the sensor was stabilized to 300 ℃ until its fluctuation was within 1% as measured with a thermocouple.

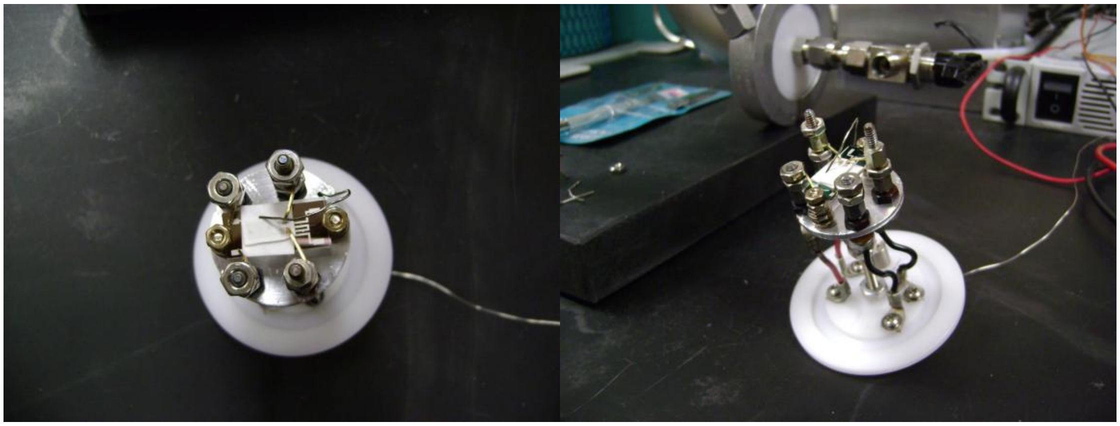

Figure 3.15 Hand-made apparatus to measure the resistance changes in a closed chamber.

VOC gases were purchased from Airgas South, Inc. (Atlanta, GA) in a sealed cylinder diluted in a nitrogen atmosphere with a concentration of 500ppm. Schematic diagram of gas flowing system and picture of configuration is shown in figure 3.16.

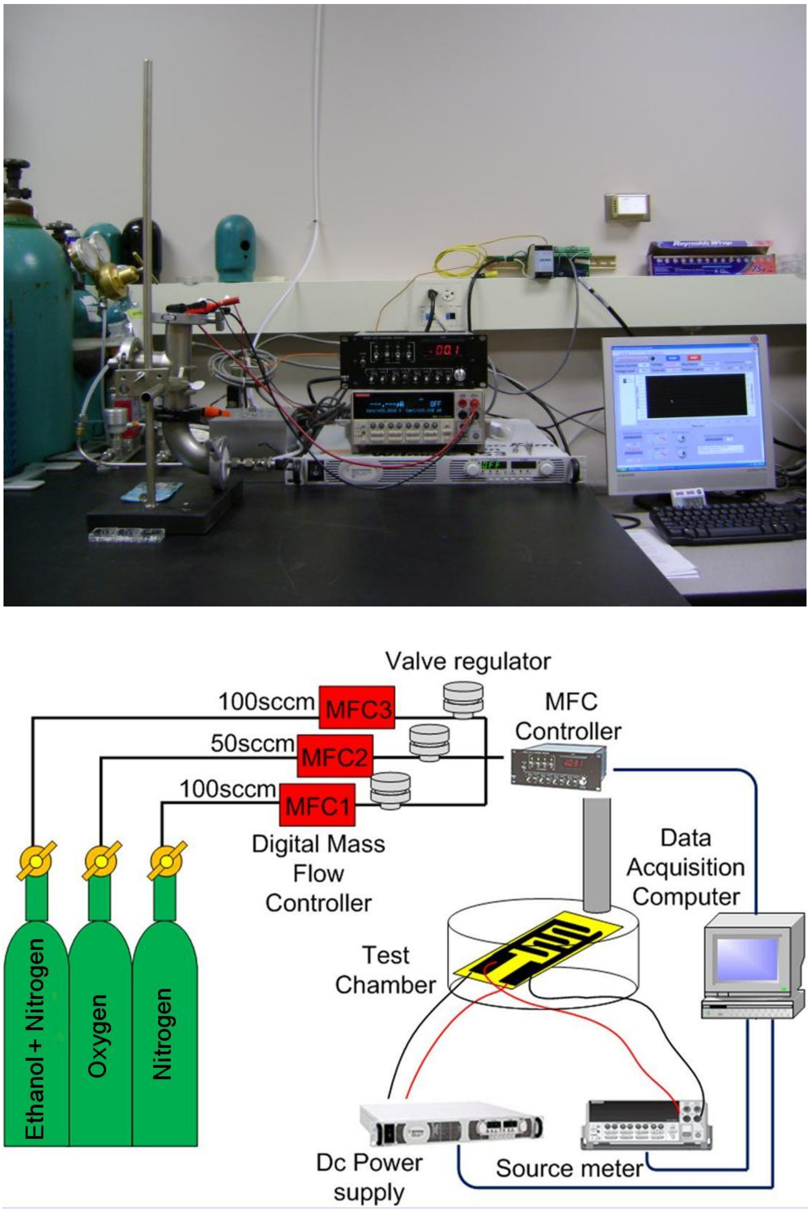

Figure 3.16 Gas sensing property measurement system and schematic diagram of configured parts, gas cylinders, DC power supply, test chamber, MFC (Mass Flow Controller), and data acquisition computer run by NI Lab VIEW

References

1. R. Martínez-Máñez, J. Soto, E. Garcia-Breijo, L. Gil, J. Ibáñez, andE. Llobet, "An “electronic tongue” design for the qualitative analysis of natural waters," *Sensors and Actuators B: Chemical*, 104[2] 302-07 (2005).
2. Leatec Fine Ceramics Co., LTD, Leader of Ceramic Materials Technology Industry
3. Microsensors, MEMS, and smart devices, p10-p12
4. 1972 annual report, conference on electrical insulation and dielectric phenomena, national academy sciences, p75
5. A single layer of grapheme formation of silicon oxide surface (001), p21
6. http://www.cirlex.com/technical.asp, www2.dupont.com/Kapton
7. http://www.sensorland.com/HowPage017.html
8. F. F. C. Duval, R. A. Dorey, R. H. Haigh, and R. W. Whatmore, "Stable TiO2/Pt electrode structure for lead containing ferroelectric thick films on silicon MEMS structures," *Thin Solid Films,* 444[1-2] 235-40 (2003).
9. J. Hinze, "In situ measurement of mechanical stress in polycrystalline zinc-oxide thin films prepared by magnetron sputtering," *J. Appl. Phys.*, 88[5] 2443 (2000).
10. A. M.-J. Matti and T. R. Tapio, "Possible structures of nonstoichiometric tin oxide: the composition Sn 2 O 3," *Modelling and Simulation in Materials Science and Engineering,* 12[1] 33 (2004).
11. Y. Ohya, H. Saiki, andY. Takahashi, "Preparation of transparent, electrically conducting ZnO film from zinc acetate and alkoxide," *Journal of Materials Science,* 29[15] 4099-103 (1994).

12. Y. Ohya, H. Saiki, T. Tanaka, andY. Takahashi, "Microstructure of TiO2 and ZnO Films Fabricated by the Sol-Gel Method," *Journal of the American Ceramic Society,* 79[4] 825-30 (1996).
13. R. Wahab, S. G. Ansari, Y. S. Kim, H. K. Seo, G. S. Kim, G. Khang, andH.-S. Shin, "Low temperature solution synthesis and characterization of ZnO nano-flowers," *Materials Research Bulletin,* 42[9] 1640-48 (2007).
14. L. Vayssieres, "Growth of Arrayed Nanorods and Nanowires of ZnO from Aqueous Solutions," *Advanced Materials,* 15[5] 464-66 (2003).
15. L. E. Greene, B. D. Yuhas, M. Law, D. Zitoun, andP. Yang, "Solution-Grown Zinc Oxide Nanowires," *Inorganic Chemistry,* 45[19] 7535-43 (2006).

CHAPTER 4 ZNO AND SNO$_X$ THIN FILMS BY SPUTTERING

4.1 Introduction

Zinc oxide (ZnO) is one of widely researched semiconducting material due to its wide band gap energy, 3.37 eV and transparency in range from 0.4 to 2 µm of optical wavelength. Chemical stability in reducing atmosphere expands its applications [1]. Tin dioxide (SnO_2) is also widely used due to its high conductivity and transmissivity [2]. These properties allow its application to solar cells, flat panel displays, optoelectronic devices, and gas sensor application [3-6]. In recent researches, another tin compound, tin monoxide (SnO) has also drawn lot of interests owing to its native p-type property and relative easiness in control, compared with other p-type materials, such as ZnO, NiO. Additionally, tin monoxide was reported to have high hole mobility and charge transport property because 5s orbital of Sn^{2+} ions highly contribute to the conductivity.

Several technologies such as CVD [7-8], sol-gel [9-10], and sputtering [11-12], have been researched to deposit zinc oxide and tin oxide at economic cost and for a wafer scale production with high yields. Among these methods, sputtering have been utilized widely because it is more readily controllable method in achieving desirable chemical and physical property of metal oxide film [13]. In the fabrication of tin oxide and zinc oxide based devices by sputtering, controlling the stoichiometry of metal oxide film was one of challenges, especially from a DC sputtering of metallic targets, in spite of high deposition rate [14-15]. Stoichiometry of ZnO is relatively easy to balance due to thermodynamic stability of ZnO at room temperature [16].

However, nonstoichiometry can be usually observed from the ZnO thin films deposited under oxygen deficient environment. It is one of reason to use ceramic ZnO target by rf sputtering rather than metallic zinc target by dc sputtering even it reveals slow deposition rate [17]. Nonstoichiometry of SnO_2 was arisen from the nature of tin ions, co-existing as multiple compounds, such as SnO, Sn_2O_3 and SnO_2, which are related to the bonding stability in between tin ion and oxygen ion under deposition condition [18-19]. To achieve stoichiometric ZnO, SnO_2 and SnO phases, influence of systematic parameters, such as argon-to-oxygen ratio, deposition temperature, and plasma discharge on the film properties, such as phase formation and its crystallinity have been researched [20-22]. The influence of post annealing on electric, optical property and gas sensing property of SnO_x film were also reported in several literatures [23-27], but interrelationships between post annealing temperature and gas sensing property relating to the change in tin phases was rarely reported.

In this study, ZnO thin films were deposited by rf sputtering and SnO_x thin film sensors were fabricated by rf and dc sputtering ceramic tin dioxide target and metallic tin target. To utilize ZnO thin films for gas sensor application, it is necessary to deposit thin films having least leakage current to avoid other defects causing high resistance to hide resistance change from gas reactions. Electrical conductivity of thin films is reported to be modulated depending on argon to oxygen ratios, power density, and chamber pressure. Leakage current of thin films are measured in between source and drain electrodes. Argon to oxygen ratios, chamber pressures, post annealing were controlled to modulate the electrical property of films. Under the optimized condition, ZnO thin films sensors were fabricated to investigate the gas sensing properties. For SnO_x thin film sensor fabrication, post annealing was performed to investigate its influence on the phase transformation of DC sputtered SnO_x thin films. Then, under appropriate post annealing temperature to achieve apparent portion of SnO phase, SnO_x thin films were prepared by RF/DC co-sputtering and characterized by shifting the position between RF sputtered and DC sputtered regions. Gas sensing properties for SnO_x thin film sensors, representing for three different points, RF, DC, and mixed regions, were compared by recording a resistance profile. The relationship between gas sensing property of SnO_x thin film sensors and structural and phase changes by post annealing temperature and mixing ratio of tin dioxide and monoxide was studied.

4.2 Experiment

ZnO thin film was deposited by rf sputtering on alumina electrode coated silicon dioxide substrate. Initial deposition conditions were referred to other reports utilizing rf sputtering [28]. Power density of rf cathode were 80W (1.76 W/cm^2) and 100W (2.2 W/cm^2), respectively. Argon to oxygen ratios were varied from 20:0 to 20:6 sccm. Chamber pressures were fixed to have around 5 mTorr and 10 mTorr, respectively. Simple TFT (Thin Film Transistor) device was fabricated on silicon dioxide Electrical property of ZnO thin films deposited by sputtering as drawn in figure 4.1. Thickness of SiO2 was 100nm on p$^+$ type silicon. As shown in figure 4.2, different ratio of width and length of aluminum electrodes were deposited by dc sputtering.

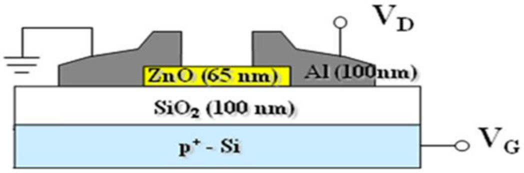

Figure 4.1 Schematic drawing of ZnO thin film TFT device

Experimental conditions are summarized in table 1, 2, and 3 depending on different chamber pressure and argon to oxygen ratio. Two different power densities, 80W and 100W were utilized to investigate the effect on microstructure of ZnO thin films. I-V characteristic of ZnO thin film TFT was measured by Agilent impedance analyzer equipped with a probing station. SnO_x thin film was deposited by RF/DC co-sputtering on silicon dioxide substrate. Power density of DC cathode was 15W (0.33W/cm^2) and 80W (1.76 W/cm^2) for RF, respectively. Deposition time for RF and DC sputtering were determined to have approximately 80nm thickness, respectively and confirmed by observing cross section of SnO_x layers from the interfacial layer on silicon dioxide layer by FE-SEM. Metallic tin target (99.99%, Kurt J. Lesker) was used for DC sputtering and ceramic tin dioxide target (99.99%, Kurt J. Lesker) for RF sputtering. Argon-to-oxygen ratio was controlled to have 20:2 ratios in total 22sccm. Chamber pressure was fixed to be 5 mTorr.

Prior to thin film deposition, interdigitated 100nm thick platinum electrode was deposited by DC sputtering on silicon dioxide substrate, covered with stainless steel shadow mask in 400 μm of finger distance and width. SnO_x thin films were post annealed at four different temperatures, 300 ℃, 450 ℃, 550 ℃, and 650 ℃, respectively, in air atmosphere for 10 hr. X-ray diffractometer (XRD, Bruker D-8) study was carried out to investigate the change in phases and its crystallinity difference. Range of scanning was from 15° to 80° in 2 theta angle. Acceleration voltage and current were 40KV and 40mA, respectively. Scanning was performed to move in the rate of 6.5° per minute. Samples were scanned by increasing 0.05°. Field Emission Scanning Electron Microscopy (FE-SEM, JEOL JSM-7000F) was used to observe the surface morphology of as-deposited and post annealed SnO_x thin films. SnO_x thin film sensors with varying mixing ratios of tin compounds were tested to investigate the sensing properties to three different volatile gases, acetone, ethanol, and ethylene in a closed chamber.

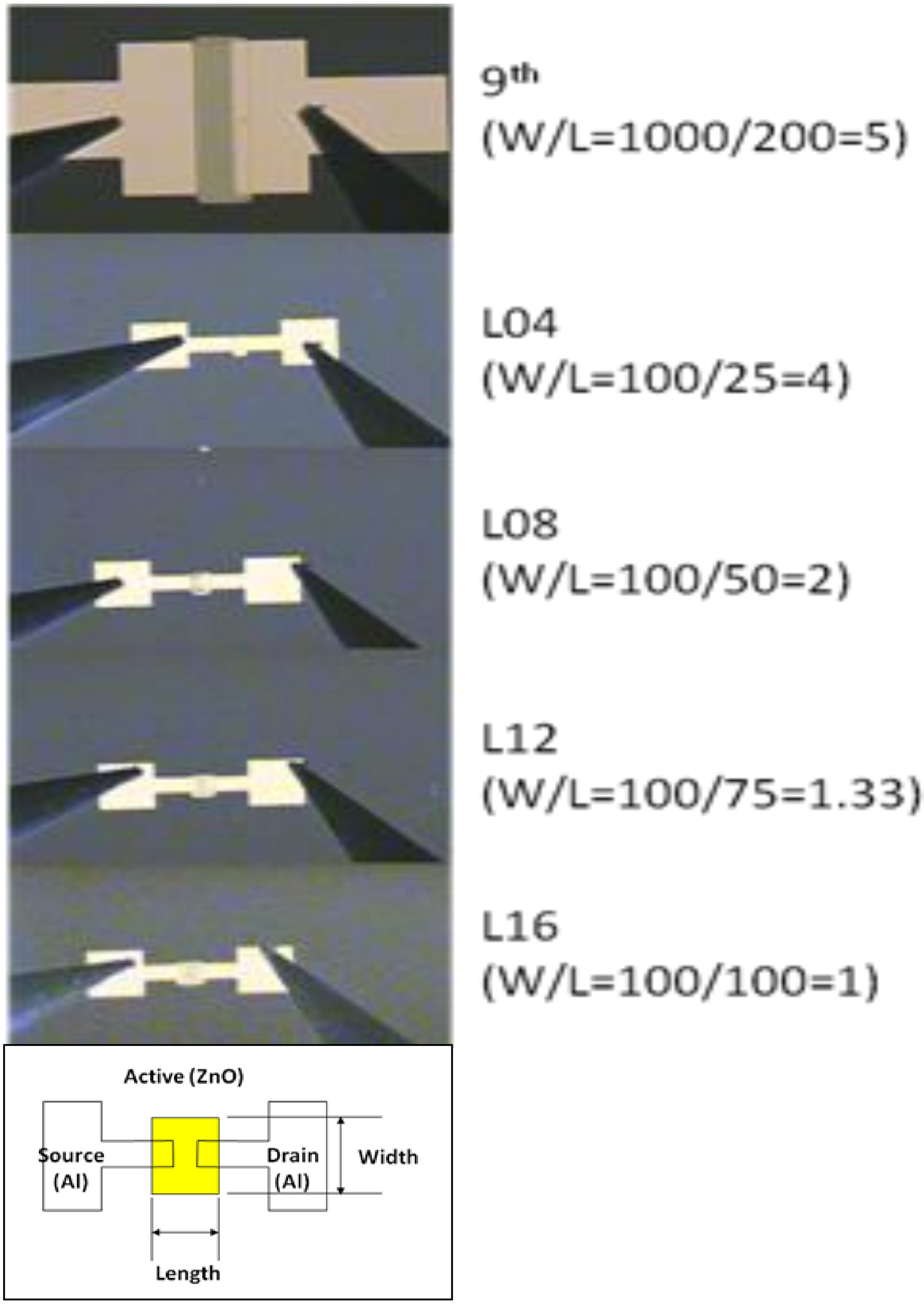

Figure 4.2 Configuration of aluminum source and drain in different geometry of width and length. The ratio of width and length varied from 1 to 5

4.3 Results and discussion

To optimize the electrical property of ZnO thin films for gas sensor application, thin films were deposited under different sputtering conditions. First, power densities of cathode were varied to have 80W and 100W. As shown in figure 4.3, surface morphology of as-deposited ZnO thin films were characterized by FE-SEM. In left side picture, overall grain size of ZnO ranged between 5 to 10nm. ZnO thin films deposited under 100W showed slightly larger grain size with more porosity between grains. Generally, high power density of cathode on plasma generation can cause stress on the deposited film. Oxygen ions with high energy tend to bombard during the deposition. Ions with higher energy induced increased grain size under high power density.

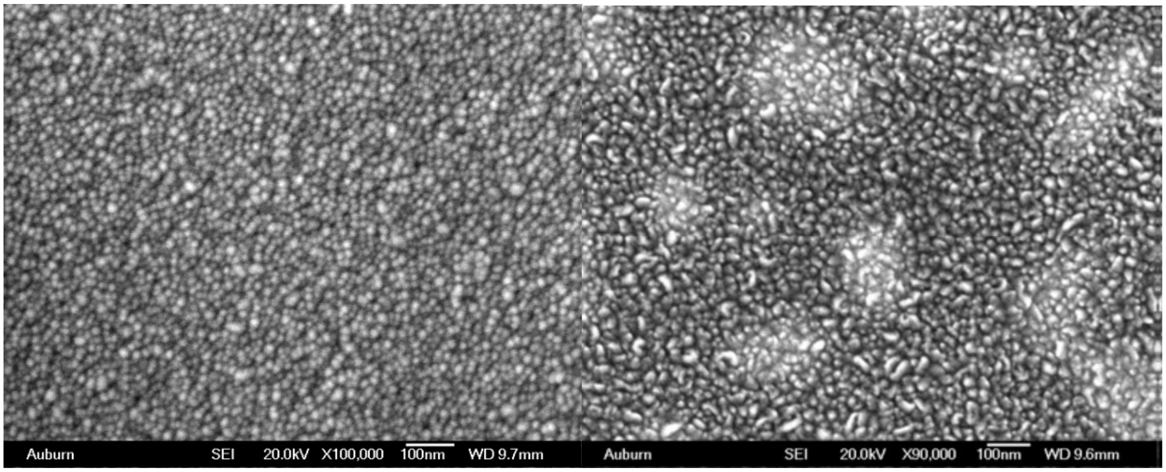

(a) 80W (b) 200W

Figure 4.3 Surface morphology of as-deposited ZnO thin film under (a) 80W and (b) 200W

Electrical property of ZnO thin films depending on deposition pressure was measured by constructing TFT structure. Details of sputtering conditions of ZnO and aluminum electrode were summaried in table 4.1 and 4.2, respectively. Other parameters except chamber pressure was fixed to elucidate the effect of chamber pressure on the film propety. As shown in figure 4.4

and 4.5, drain current IDS are graphed as a function of drain to source voltage according to varing gate voltages from 0V to 10V.

Table 4.1 condition 1 of ZnO thin film TFT device

Active (ZnO)					Electrode (Al)				
Deposition Pressure	Ar:O2	Power	Time	Thickness	Deposition Pressure	Ar:O2	Power	Time	Thickness
10.2 mTorr	20:02	RF 80W	10-20min	~65 nm	4.9 mTorr	20:0	DC 100W	300-435sec	100 nm

Table 4.2 condition 2 of ZnO thin film TFT device

Active (ZnO)					Electrode (Al)				
Deposition Pressure	Ar:O2	Power	Time	Thickness	Deposition Pressure	Ar:O2	Power	Time	Thickness
4.2 mTorr	20:02	RF 80W	10-20min	~65 nm	4.9 mTorr	20:0	DC 100W	300-435sec	100 nm

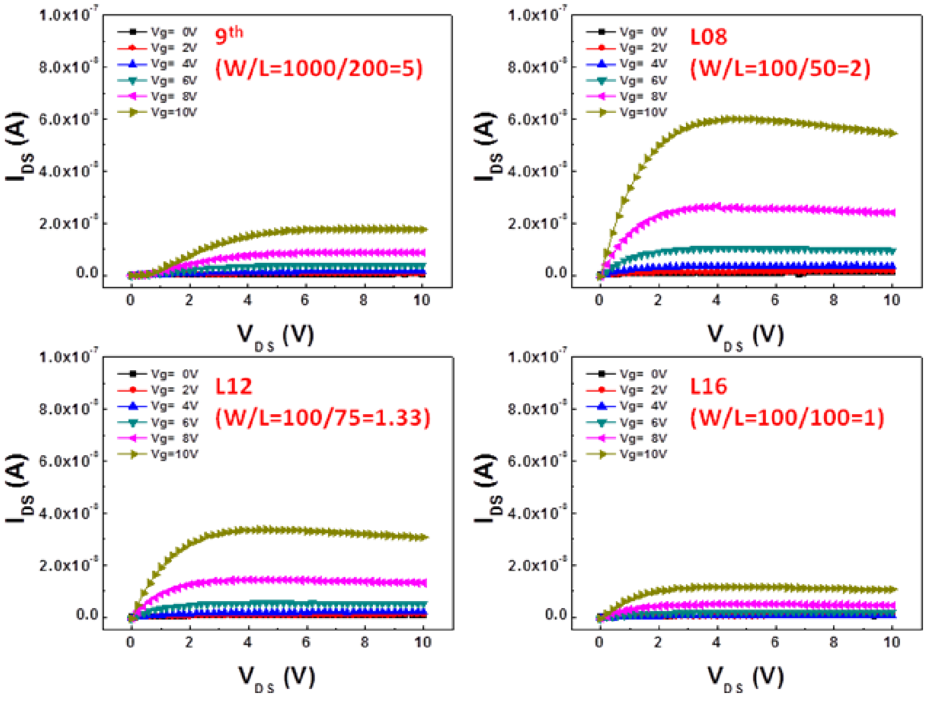

Figure 4.4 Drain current I_{DS} as a function of the drain-to-source voltage V_{DS} for ZnO thin films deposited under condition 1.

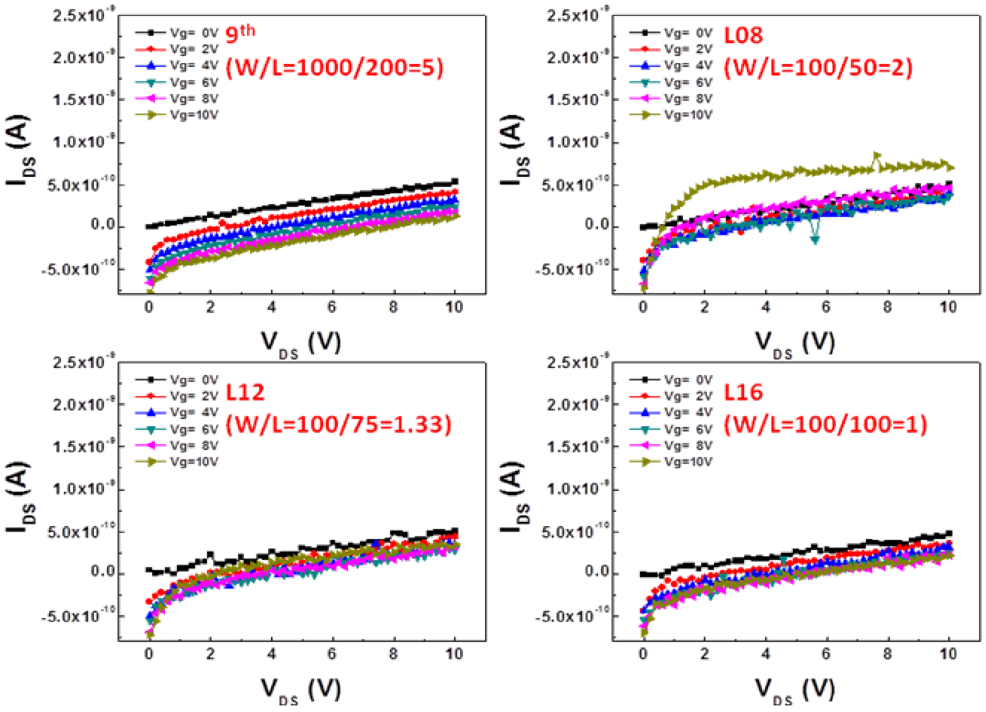

Figure 4.5 Drain current I_{DS} as a function of the drain-to-source voltage V_{DS} for ZnO thin films deposited under condition 2.

Overall TFT properties of ZnO thin films sputtered under high chamber pressure, 10 mTorr, were observed to have an indication of “hard saturation”. It means that pinch-off of the channel is achieved [tin oxide TFT]. However, ZnO thin films deposited under low chamber pressure, 4.2 mTorr, showed relatively poor TFT property and overall drain current ranged lower than 10^{-9}A level. It is attributed that leakage current increased because a mean free path of ion is somewhat increased under low chamber pressure. Argon to oxygen ratios under conditions other parameters are fixed are investigated to modulate the electrical property of ZnO thin film. It was reported that ZnO grain size increases when the amount of oxygen increased. However, the amount of oxygen is more than that of argon, grain size decreased. It can be explained that argon to oxygen ratio that influences the ionized zinc particles and oxygen ions to be reached on the substrate with regard to balanced energies during bombardment to be nucleated. Consequently, different grain sizes are determined according to argon to oxygen ratio [29].

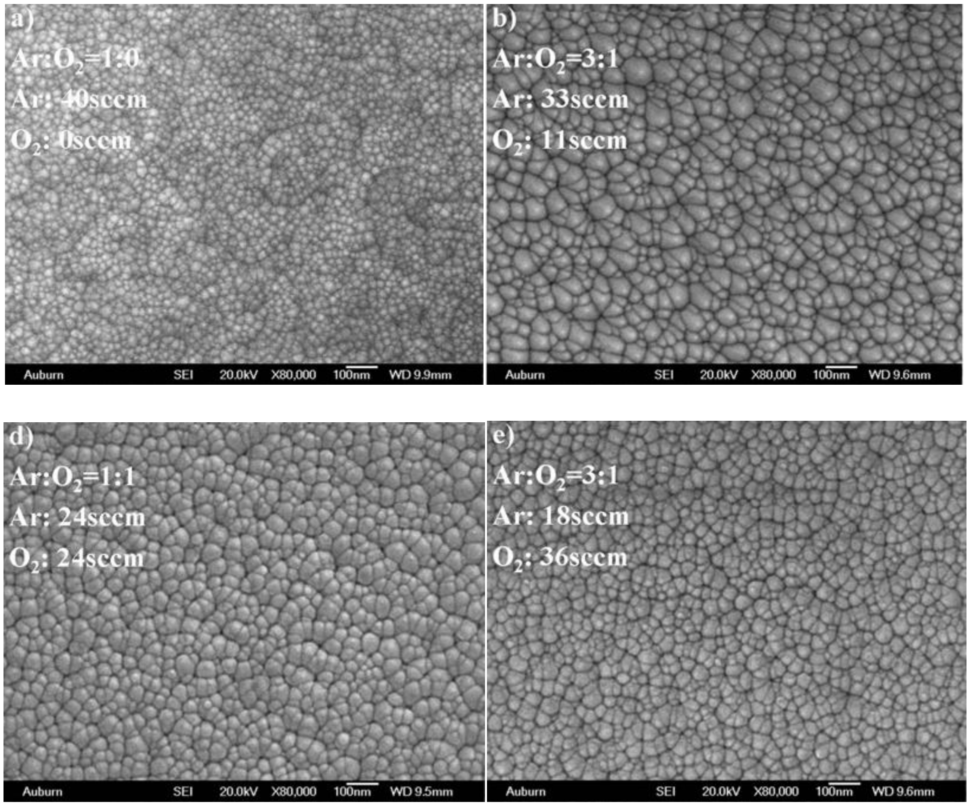

Figure 4.6 Surface morphology of rf sputtered ZnO thin films under different argon to oxygen ratios [30]

To obtain thin film with smaller grain size, argon to oxygen ratios such as 20:0 and 20:2 were selected and thin films were deposited on TFT devices under conditions summarized in table 4.3. TFT property of thin films in terms of drain current and gate voltage were graphed in figure 4.7. Noticeable difference between thin films under argon to oxygen ratios is the range of drain current. As shown in two graphs, current range of thin films deposited under no oxygen is around 10^{-6} level. However, thin films deposited under 20:2 argon to oxygen ratio showed much lower range of drain current as of 10^{-8} level.

Table 4.3 Condition 3. Different argon to oxygen ratios (20:0, 20;2) to deposit ZnO

Active (ZnO)					Electrode (Al)				
Deposition Pressure	Ar:O2	Power	Time	Thickness	Deposition Pressure	Ar:O2	Power	Time	Thickness
10 mTorr	20:0	RF 80W	25min	70 nm	4.9 mTorr	20:0	DC 100W	300-435sec	100 nm
Active (ZnO)					Electrode (Al)				
Deposition Pressure	Ar:O2	Power	Time	Thickness	Deposition Pressure	Ar:O2	Power	Time	Thickness
10 mTorr	20:02	RF 80W	25min	80 nm	4.9 mTorr	20:0	DC 100W	300-435sec	100 nm

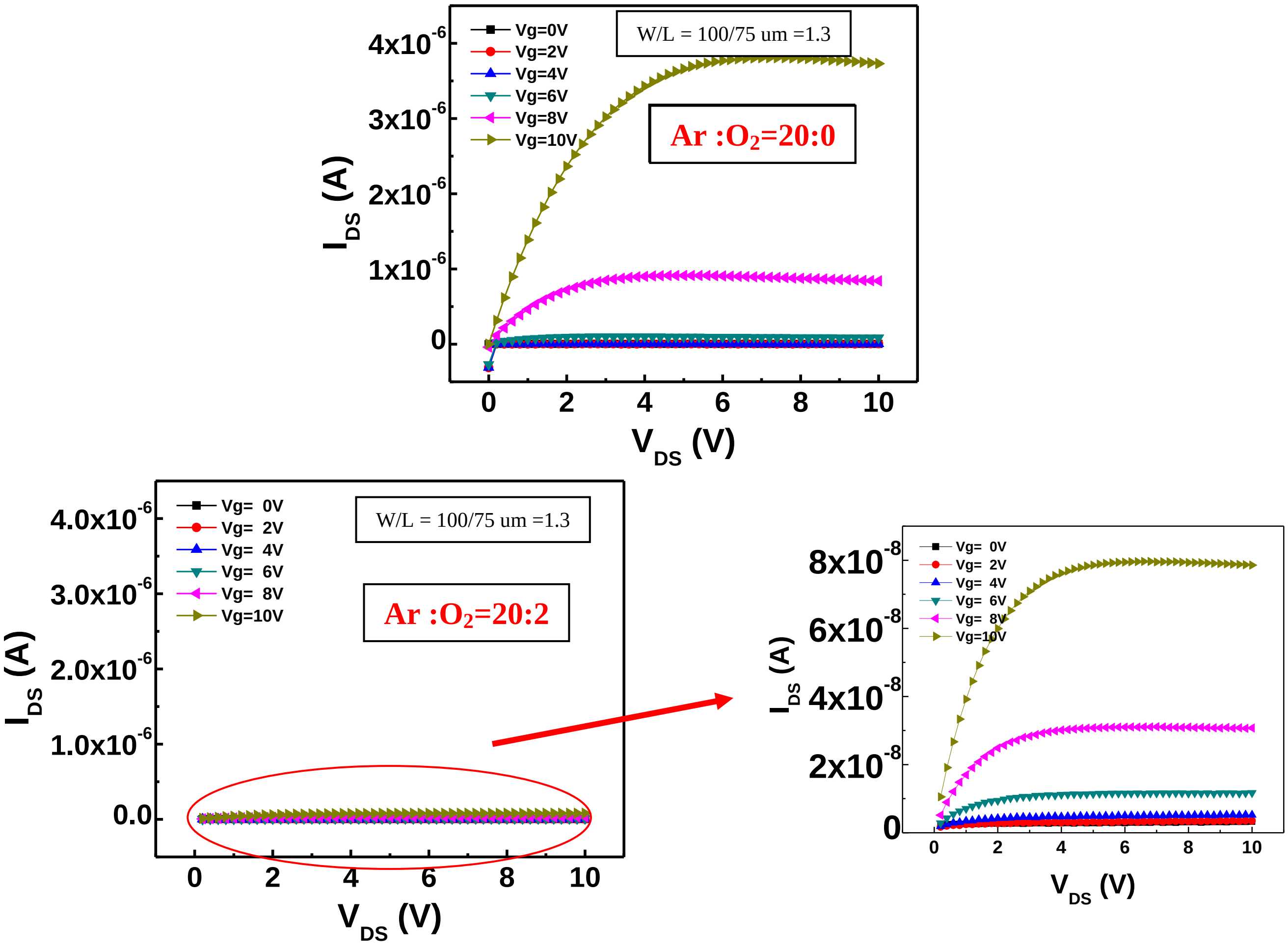

Figure 4.7 Drain current I_{DS} as a function of the drain-to-source voltage V_{DS} for ZnO thin films deposited under Ar:O_2 (20:0, 20:2) ratios

It indicates that charge concentration of ZnO thin films deposited under no oxygen atmosphere is lower than that of thin films deposited under 20:2 ratio of argon to oxygen [31]. Therefore, it can be concluded that process parameters to deposit ZnO thin film suitable for gas sensor fabrication are optimized to have 80W of power, 20:2 ratio of argon to oxygen, and 10 mTorr of chamber pressure, respectively.

For the characterization of SnO_x thin film deposition using dc sputtering, thin films were deposited under conditions described in previous chapter 3. Crystalline structure and phase formation in DC sputtered SnO_x thin films were analyzed by XRD. In figure 4.8, bare silicon dioxide substrate, as deposited SnO_x thin film, 300 ℃ post annealed SnO_x thin film, 450 ℃ post annealed SnO_x thin film, and 650℃ post annealed SnO_x thin film were scanned in $15° < \theta < 80°$.

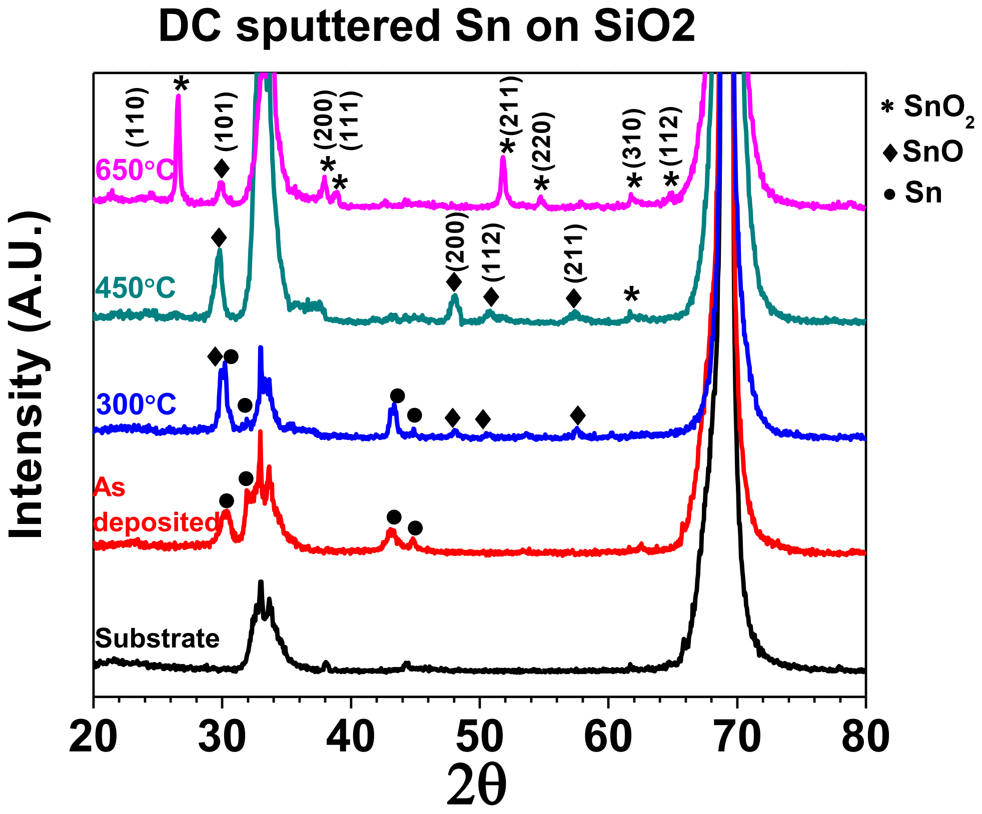

Figure 4.8 XRD graphs of dc sputtered SnO_x thin films on silicon dioxide substrate according to different post annealing temperature for 10hr

For as deposited SnO_x thin film, small peaks indicating metallic Sn phase were observed at 30.3°, 31.9°, 43.2° and 44.8°. This result corresponds well with the peak positions for tetragonal beta Sn phase [32], but no other peaks for tin compounds such as SnO or SnO_2 were observed. It indicates that as deposited thin film by DC sputtering metallic tin target mostly consists of tin phase prior to post-annealing. Minimum temperature for post annealing was set to 300℃ because this temperature is in range of optimum operating temperatures; 300 ~ 500 ℃ for the most metal oxide based sensors to have high sensitivity [33]. In third graph for the 300 ℃ case in figure 4.1, peaks indicating SnO phase was observed at 29.9°, 48°, 50.5° and 57.5°, corresponding to (101), (200), (112), and (211) plane of SnO, respectively. Other peaks for metallic Sn phase were also observed as well. From the result of 450℃ post annealed films in fourth graph, most of peaks for metallic Sn phase disappeared. Instead of that, peaks representing for SnO phase were found to be dominant and small intensity of peak for SnO_2 phase was observed at 61.65°. This explains that metallic Sn phase are transformed mostly into SnO phase by post annealing at 450℃ and might not make a phase transformation into other tin compounds.

In fifth graph for the 650 ℃ post annealed SnO_x thin film, majority of observed peaks stand for SnO_2 phase. One peak for (101) plane of SnO phase was observed at 29.9°,but a relative intensity of SnO phase was much lowered than those of other major peaks for SnO_2 phase. In addition to, peaks for metallic tin phase were not observed any longer, shown until post annealing at 450 ℃. Our results are quite in good agreement with XRD results in other report [34]. The reason for the dominant SnO_2 phase at high post-annealing temperature is attributed to the enhanced oxygen diffusion, inducing to a higher oxidation state [35]. Therefore, it can be concluded that post annealing at 650 ℃ is appropriate temperature to achieve a SnO_2 phase and

450℃ is optimum post annealing temperature to obtain a SnO phase under our experimental conditions.

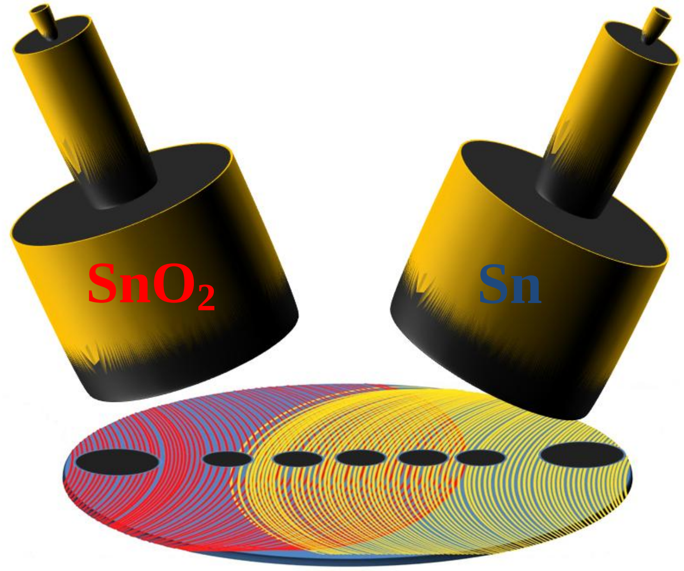

Figure 4.9 Schematic diagram of rf/dc co-sputtering of ceramic SnO_2 target and metallic Sn target on a silicon dioxide substrate. Black dots represent for the selected regions to study the combinatory tin phases depending on distances from each cathode

Based on the previous experimental results, RF/DC co-sputtered SnOx thin films were prepared to investigate the mixing ratio of tin phases on the gas sensing. Post annealing was performed at 450 ℃ and characterized by shifting the positions between the RF cathode and DC cathode as shown in figure 4.9, a schematic figure of co-sputtering. Seven points were selected between SnO_2 and SnO phase. In figure 4.10, XRD characterization was performed to investigate the phase transition in co-sputtered SnO_x films depending on the location. First graph indicates that SnO_x film, deposited closely by DC tin target, was transformed mostly into SnO phase.

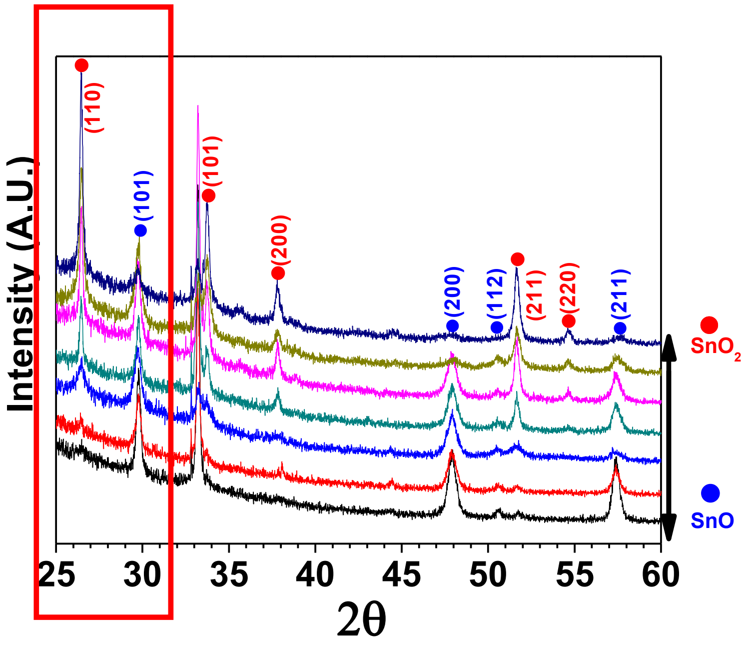

Figure 4.10 XRD graphs of rf/dc co-sputtered thin films with combinatory tin phases. From bottom to top, each graph depicts film deposited closely from Sn target and SnO_2 target, respectively.

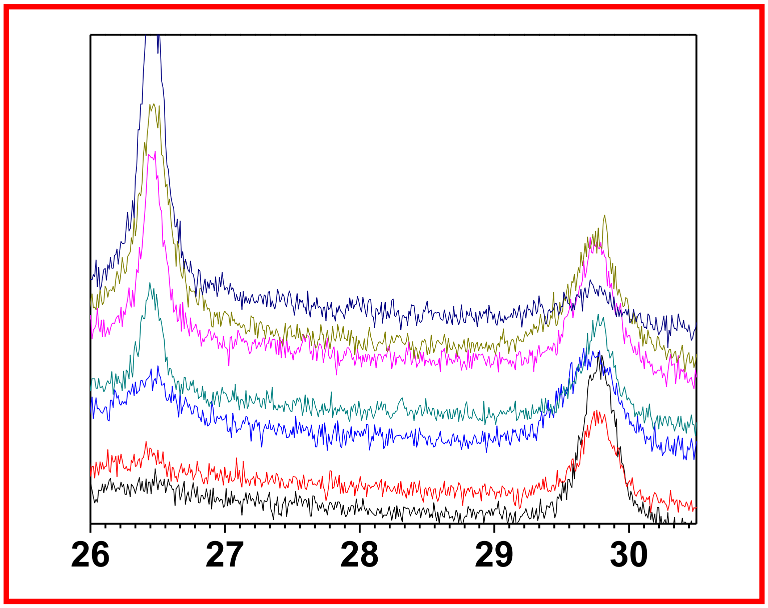

Figure 4.11 Magnified XRD graphs between 26° to 35° to elucidate the shifts in tin phases from tin monoxide (SnO) to tin dioxide (SnO_2)

Whereas, seventh graph shows that SnO_2 are a dominant phase of SnO_x film, deposited closely by RF tin dioxide target. Compared with graphs from first to seventh, especially within the range from 26 to 31, as shown in figure 4.11, it is obvious that relative intensity of peaks at 29.9°, (101) plane of SnO, gradually decrease as the position of films are close to RF SnO_2 cathode, while the intensity of (110) plane of SnO_2 is enhanced at 26.5°. Other peaks for (101) and (200) planes of SnO_2 and (200) and (211) planes of SnO revealed same dependence on the location. It means that gradual change in tin phase from SnO to SnO_2 can be achieved by RF/DC co-sputtering, following with post annealing at 450 ℃. Regarding crystalline phase of SnO_2, post annealed at 450 ℃, It is thought that 450 ℃ is quite enough to favorably stabilize a SnO phase under the sufficient oxygen atmosphere thermadynamically. This result is also in accord with experimental results that SnO_2 thin films, RF sputtered at around 650K showed good polycrystalline phases [36-38].

Surface morphology of SnO_x thin films, depending on the positions between RF/DC cathodes, were studied by FE-SEM. In figure 4.12, four pictures from (a) to (d), each picture represents surface morphology of as deposited SnO_x thin film, post annealed SnO, SnO/SnO_2, SnO_2 thin films at 450 ℃, respectively. As shown in picture (a), surface of as deposited film was fairly uniformly deposited by DC sputtering. Grain size ranged from 5nm to 15nm and no significant defects were observed. Compared with a picture (a) for as-deposited thin film, post annealed films from (b) to (d) revealed apparently different surface morphology. Most of grains were agglomerated together and grown, leaving pores between grains. In spite of change in the mixing ratio of SnO and SnO_2 phases, no significant difference in surface morphology between three thin films was observed. Overall grain size varied approximately within 50nm to 200nm, regardless post annealing temperature.

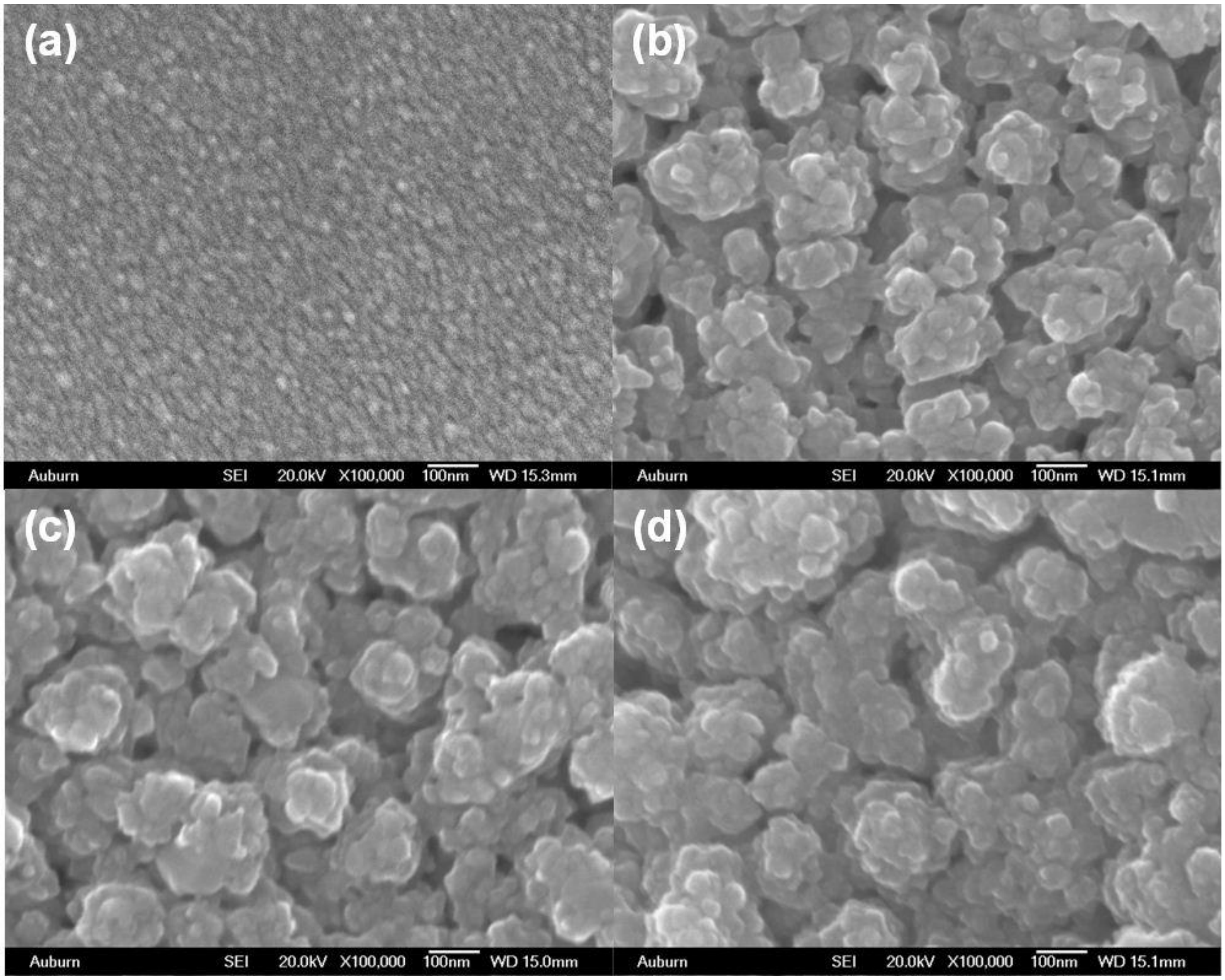

Figure 4.12 Topography of rf/dc co-sputtered SnO_x thin films depending on post annealing temperature (a) as-deposited, (b) 300 ℃ post annealing, (c) 450 ℃ post annealing, (d) 650 ℃ post annealing

Gas sensing property of ZnO thin film sensor was studied by using 800ppm of acetone according to different working temperatures. As described in experimental chapter, ZnO thin films were deposited on alumina substrate with same configuration of 100nm thick platinum electrode with 400 µm finger width and distance, respectively.

R_{air}	R_{gas}	ΔR	$(R_{air}-R_{gas})/R_{air}$	R_{air}/R_{gas}
28169	24830	3339	11.85	1.13
30017	26588	3429	11.42	1.13
31585	27438	4147	13.13	1.15

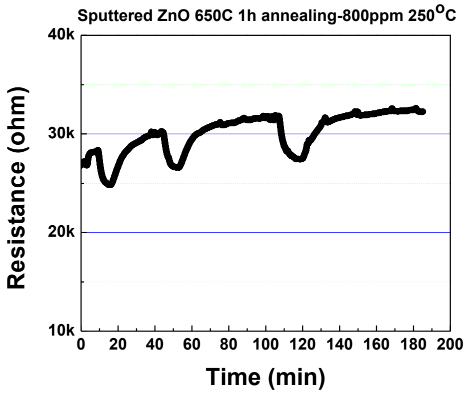

Figure 4.13 Resistance profile of ZnO thin film sensor for 800ppm acetone detection at 250 ℃

R_{air}	R_{gas}	ΔR	$(R_{air}-R_{gas})/R_{air}$	R_{air}/R_{gas}
26277	14425	11852	45.10	1.82
23399	13434	9965	42.59	1.74
22439	13153	9286	41.38	1.71

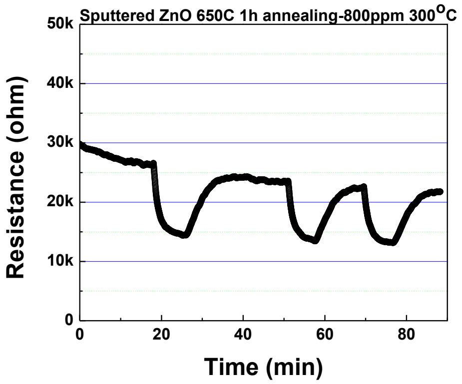

Figure 4.14 Resistance profile of ZnO thin film sensor for 800ppm acetone detection at 300 ℃

R_{air}	R_{gas}	ΔR	$(R_{air}-R_{gas})/R_{air}$	R_{air}/R_{gas}
13449	5350	8099	60.22	2.51
11189	4541	6648	59.42	2.46
10242	4335	5907	57.67	2.36

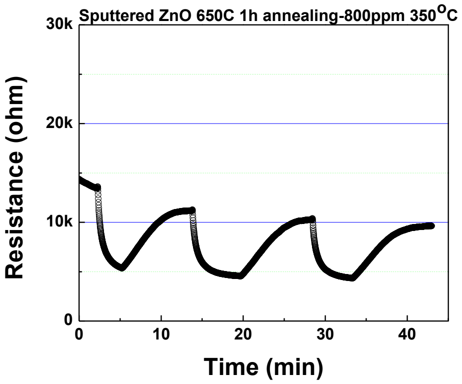

Figure 4.15 Resistance profile of ZnO thin film sensor for 800ppm acetone detection at 350 ℃

Sensing property was studied at three different temperatures such as 250 ℃, 300 ℃, and 350 ℃. As shown in figure 4.13, 4.14, and 4.15, sensitivity and response time for ZnO thin film sensors working at 350 ℃ showed the highest resistance change in a shorter time. Generally, metal oxide sensors working at higher temperature can have more thermal energy to dissociate chemisorbed oxygen and gas molecules. The dissociation mechanism regarding to gas species, however, governs the optimum working temperature to show the highest sensitivity. It was reported that 325 ℃ is the optimum temperature for ZnO acetone sensor to have the highest sensitivity and corresponds well with our experimental data [39].

To investigate the temperature dependence of gas sensing property according to the type of gas species, another volatile organic compound; ethanol was utilized. In figure 4.16 and 4.17, resistance profiles of sputtered ZnO thin film sensor in the detection of ethanol gas varying concentration from 10 ppm to 100 ppm at different working temperatures; 250 ℃, 200 ℃, respectively.

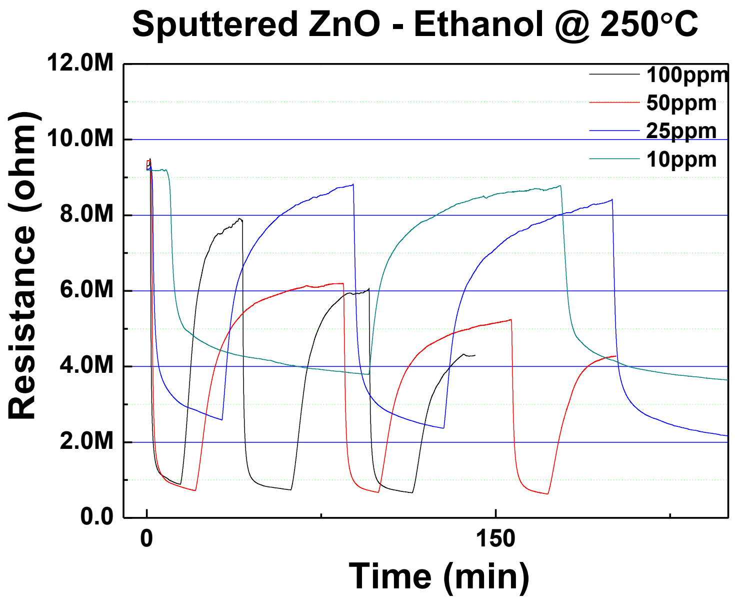

Figure 4.16 Resistance profile of ZnO thin film sensor for ethanol detection at 250 ℃ according to concentrations from 10ppm to 100ppm

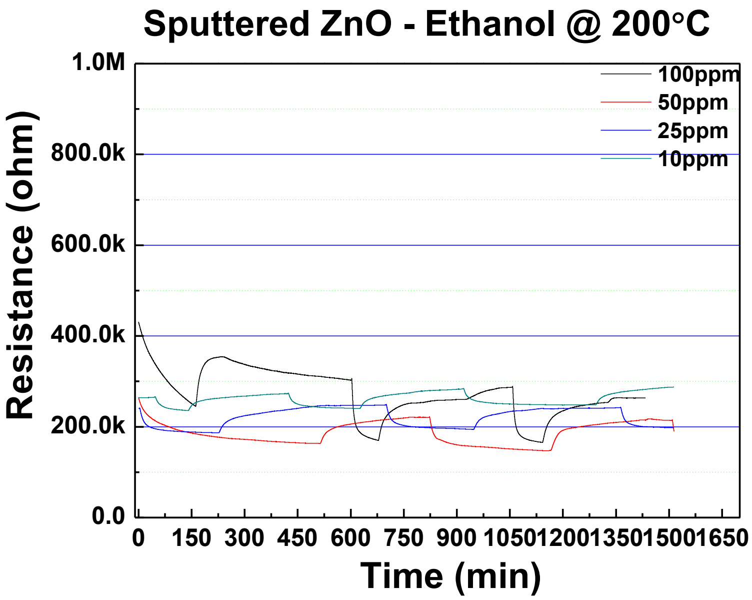

Figure 4.17 Resistance profile of ZnO thin film sensor for ethanol detection at 200 ℃ according to concentrations from 10ppm to 100ppm

Overall sensing properties in terms of sensitivity and response time for ZnO thin film sensors working at 250 ℃ were showed obvious better properties. For ZnO thin film sensors working at 200 ℃ did not recover to the initial resistance after the gas exposure within 450 min. For higher concentration such as 100ppm, even for a longer recovery time, sensor could not have its initial resistance. Detailed sensitivities according to varying concentration of ethanol gas were summarized in table 4.4 and 4.5, respectively. As shown in tables, ZnO thin film sensors working 250 ℃ were observed to have ten times higher sensitivity than sensors working at 200 ℃ regardless of concentration. In figure 4.18, resistance profile of ZnO thin film sensors recorded at 150 ℃. As the sensors were exposed to the lowest concentration of 100ppm, sensor was observed to show the resistance drop but, even after the fresh air exposure, resistance of sensors did not recover back to the initial value. This indicates that 250 ℃ is the minimum working temperature to thermally activate sputtered pure ZnO thin film sensors to detect ethanol gas.

Table 4.4 Sensitivity of rf sputtered ZnO thin film sensors fabricated under 20:2 argon to oxygen ratios in the detection of varying concentrations of ethanol gas at 200 ℃

Type	ppm	R_{air}	R_{gas}	ΔR	$(R_{air}-R_{gas})/R_{air}$ (%)		R_{air}/R_{gas}	
20-2 sputtered 650C 250C- Ethanol	10ppm	266505	235694	30811	11.56	0.64	1.13	0.01
		273697	240217	33480	12.23	-0.03	1.14	0.00
		284934	248447	36487	12.81	-0.61	1.15	-0.01
								1.14
					12.20		1.14	
	25ppm	241582	186559	55023	22.78	-1.53	1.29	-0.02
		249181	194397	54784	21.99	-0.74	1.28	-0.01
		243479	197304	46175	18.96	2.28	1.23	0.04
					21.24		1.27	
	50ppm	263184	163421	99763	37.91	-1.17	1.61	-0.03
		221896	147174	74722	33.67	3.06	1.51	0.07
		214148	131431	82717	38.63	-1.89	1.63	-0.05
					36.74		1.58	
	100ppm	430869	245285	185584	43.07	-0.64	1.76	-0.02
		302779	171397	131382	43.39	-0.96	1.77	-0.03
		287112	169892	117220	40.83	1.60	1.69	0.05
					42.43		1.74	

To investigate the influence of mixing ratio of tin phases on gas sensing property of SnO_x thin film sensors, thin films representing for three domains, SnO, SnO/SnO_2, SnO_2 phases, were fabricated into sensors and were utilized to measure the sensitivity in detection of acetone, ethanol, and ethylene gases. SnO_x thin film sensors, post annealed at 300 ℃, were tested to figure out the feasibility of gas sensors by flowing three different gases. Resistance profiles of thin film sensors were recorded in figure 4.19. Overall resistance profiles seem to be similar with those of thin films, post annealed at 650 ℃. Stability of sensors, however, was not reliable because resistance changes in terms of response time and direction of reaction was different with sensors, fabricated even under same conditions. In figure 4.20, resistance profile of 450 ℃ post annealed SnO thin film sensor was recorded as a function of gas concentration.

Table 4.5 Sensitivity of rf sputtered ZnO thin film sensors fabricated under 20:2 argon to oxygen ratios in the detection of varying concentrations of ethanol gas at 250 ℃

Type	ppm	R_{air}	R_{gas}	ΔR	$(R_{air}-R_{gas})/R_{air}$ (%)		R_{air}/R_{gas}	
20-2 sputtered 650C 250C-Ethanol	10ppm	3977001	1647523	2329478	58.57	1.71	2.41	0.11
		3787319	1561537	2225782	58.77	1.51	2.43	0.10
		3556657	1298135	2258522	63.50	-3.22	2.74	-0.21
								2.53
					60.28		2.53	
	25ppm	4831858	1360961	3470897	71.83	1.53	3.55	0.22
		4603849	1249422	3354427	72.86	0.51	3.68	0.08
		4399439	1081950	3317489	75.41	-2.04	4.07	-0.30
					73.37		3.77	
	50ppm	13560580	1378261	12182319	89.84	-0.95	9.84	-0.79
		11510140	1248568	10261572	89.15	-0.27	9.22	-0.17
		9684556	1195310	8489246	87.66	1.22	8.10	0.95
					88.88		9.05	
	100ppm	11038650	1051891	9986759	90.47	-0.51	10.49	-0.48
		9275373	879319	8396054	90.52	-0.56	10.55	-0.53
		7103844	788316	6315528	88.90	1.06	9.01	1.01
					89.96		10.02	

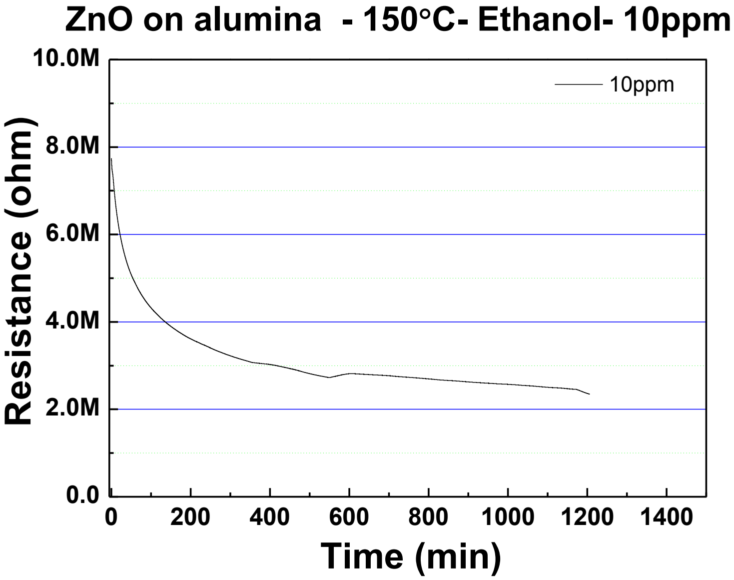

Figure 4.18 Resistance profile of ZnO thin film sensor for 10 ppm ethanol detection at 150 ℃

Six graphs represent the resistance profile in the detection of 200ppm and 100ppm of three different gases at 300 ℃. Initial resistance of sensor in synthetic air was in 30KΩ ~ 35KΩ ranges. After exposure to gases, resistance of thin film sensors all increased to 40KΩ ~ 50KΩ ranges. Generally, most metal oxide based gas sensors having intrinsic n-type semiconductor property show the resistance decrease when exposed to reducing gases, such as acetone, ethanol, and ethylene [40]. However, the reaction of SnO thin film sensor to reducing gases indicates that the property of SnO thin film is intrinsic p-type semiconductor. As studied in XRD characterization, dominant phase of SnO_x thin film at the location close to DC cathode, post annealed at 450 ℃, was SnO phase. SnO phase was reported in several literatures that it has p-type property of semiconductor [41-43]. Sensitivity, in terms of $|R_{air}/R_{gas}|$, was calculated to 1.29, 1.48, and 1.23 for 200ppm of acetone, ethanol, and ethylene, respectively. Response time, time to recover to initial resistance, was measured to be around 42min, 25min, and 23min, for acetone, ethanol, and ethylene, respectively.

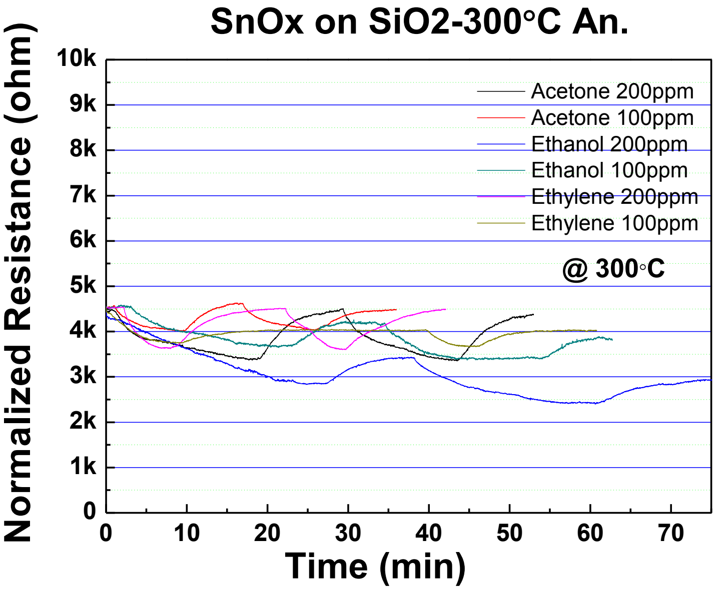

Figure 4.19 Resistance profiles of SnO$_x$ thin film sensors, post annealed at 300 °C according to 200 and 100ppm of acetone, ethanol, and ethylene, respectively

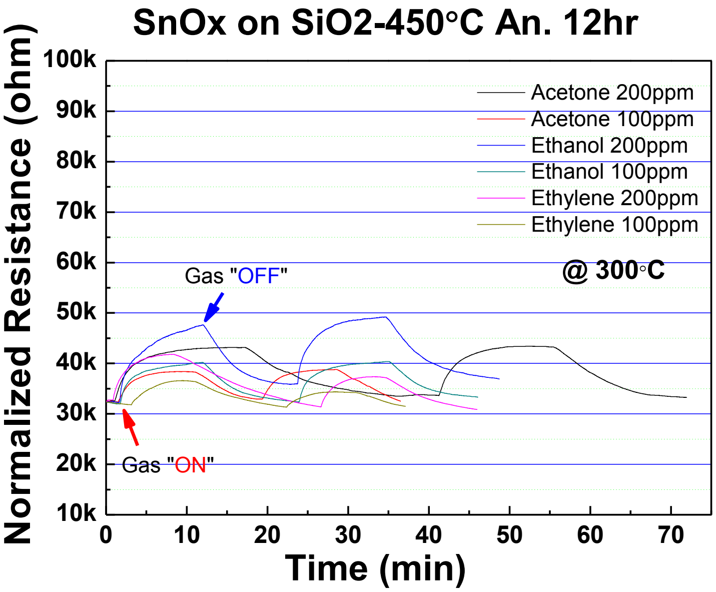

Figure 4.20 Resistance profiles of SnO$_x$ thin film sensors, post annealed at 450 °C according to 200 and 100ppm of acetone, ethanol, and ethylene, respectively

SnO_2 thin film sensors were also tested to study the gas sensing property to reducing gases. In figure 4.21, resistance profiles of SnO_2 thin film sensors were drawn as a function of gas concentration for acetone, ethanol, and ethylene. Gas concentration varied from 50ppm to 200ppm. Initial resistance of SnO_2 thin film sensors was in approximately 2.8MΩ. Compared with the initial resistance of SnO thin film sensors in air, initial resistance of SnO_2 thin film sensors was about one hundred times higher. It is thought that band gap of SnO, 0.7ev, is much smaller than band gap of SnO_2, 3.6ev, and is attributed to higher conductivity for SnO thin films [44-45]. In terms of direction of resistance change, SnO_2 thin film sensors, consisting of mainly SnO_2 phase, showed a typical n-type property of semiconductor material. Similarly to other metal oxide based sensors, resistance of sensor decreased when sensors were exposed to reducing gases. As the concentration of gases increased, the more resistance of sensor dropped. Sensitivity for acetone varied in 1.06~1.41, 1.12~1.39 for ethanol, and 1.10~1.26 for ethylene.

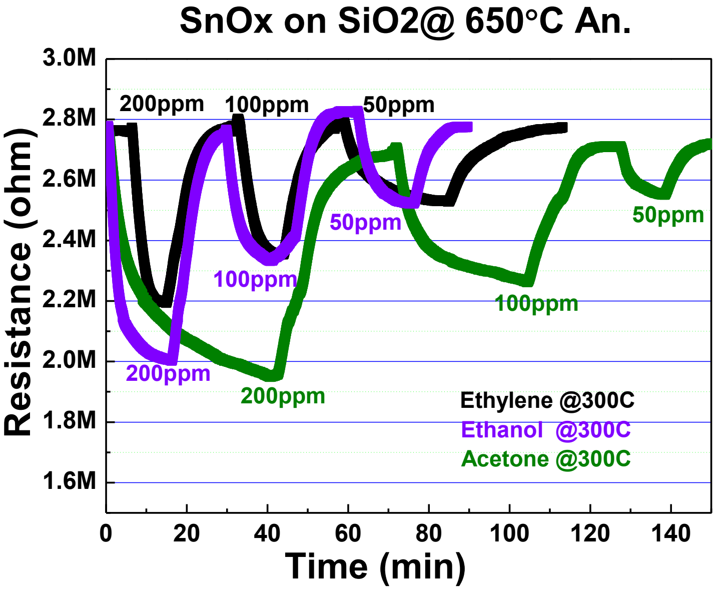

Figure 4.21 Resistance profiles of SnOx thin film sensor, post annealed at 650 °C, according to different concentrations of ethylene, ethanol, and acetone

Response time for ethanol was similar with that of ethylene, but it took much longer for acetone detection. It is due to the influence of post annealing temperature on direction of reaction between reducing gases and SnO_x thin film sensors, post annealed at 450 ℃, were graphed in figure 4.22 as a function of dominant phase of tin compound.

For better comparison in direction of reaction, initial resistances of sensors were normalized into averaged resistance value. All recorded resistance values were divided by initial resistance and redrawn in the range of -2 to 2. Negative value represents the resistance decrease after gas exposure and the resistance increase indicates for positive value. When sensors were operated at 300 ℃ by flowing 200ppm of ethanol in synthetic air, SnO thin film sensor responded in positive direction as described in previous chapter. Apparent unstable response, fluctuating in resistance change to reducing gas was observed for mixed SnO/SnO_2 sensor. Typical behavior of resistance change was measured for SnO_2 sensor. In the case of mixed SnO/SnO_2 thin film sensor, overall direction of reaction was similar with that of SnO thin film sensor, but slight decrease and increase of resistance was observed continuously during the gas reaction and recovery. It appears that competition between co-existing SnO phase and SnO_2 phase is attributed to mixed direction in response during the gas reaction and recovery. It is obvious that the reverse shift in the direction of response during volatile gas reaction can be controllable as a function of tin phase transition from SnO to SnO_2. Therefore, it is our thought that SnO thin films can be utilized for the future electronic nose applications as one of approaches to distinguish the gas in mixtures.

In table 4.6, sensitivity was expressed to the value of $S=R_a/R_g$. Here, R_a represents the resistance in air and R_g shows the resistance in volatile gas, respectively. To display the opposite direction in gas reactions, sensitivity for n-type semiconducting sensor was shown in positive value and negative value for p-type semiconducting sensor. Sensitivities for three volatile gases, acetone, ethanol and ethylene were measured by using SnO and SnO_2 thin film sensors.

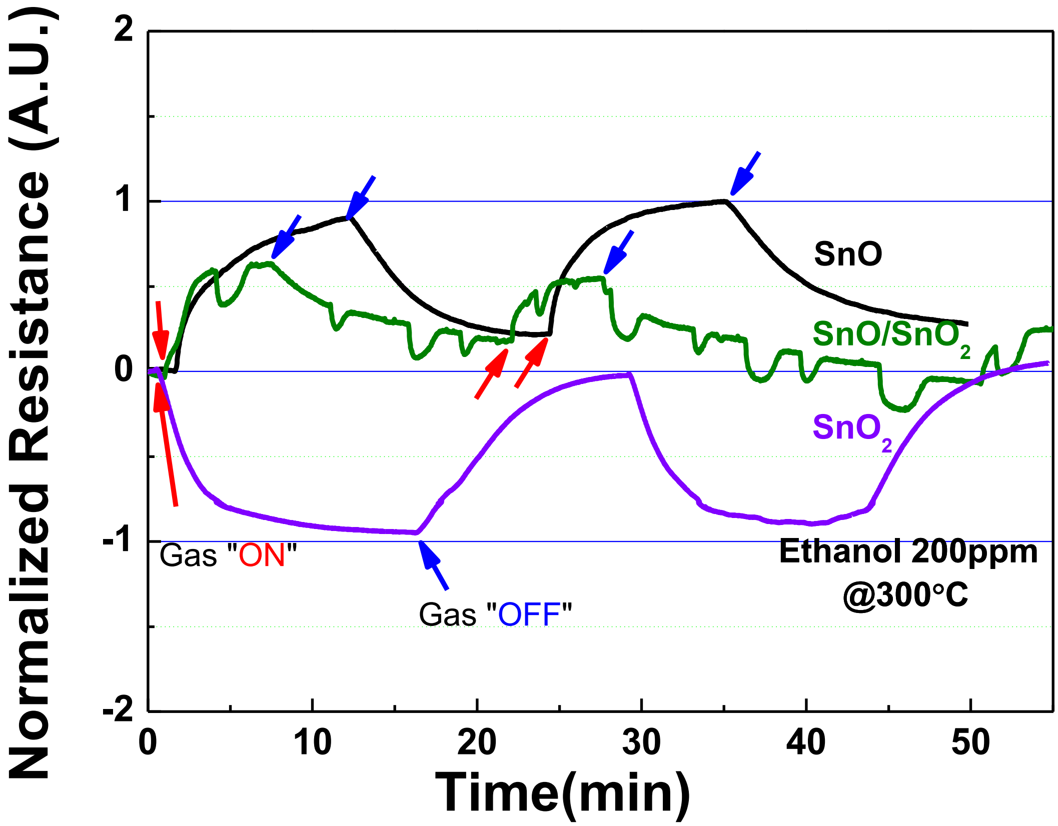

Figure 4.22 Comparisons of resistance profiles of SnO, SnO_x, and SnO_2 thin film sensors in detection of 200ppm of ethanol gas at 300 °C

Table 4.6 Sensitivity comparisons for SnO and SnO2 thin film sensors in detection of 200 ppm of acetone, ethanol, and ethylene. Resistance drop after gas exposure was expressed to positive value and vice versa for resistance increase

	Acetone	Ethanol	Ethylene
SnO thin film sensor	-1.29	-1.48	-1.23
SnO_2 thin film sensor	1.41	1.37	1.26

In the comparison of sensitivities between three volatile gases, it was observed for SnO thin film sensor that sensitivity for ethanol was relatively higher than those for acetone and ethylene gases, meanwhile, SnO_2 thin film sensor revealed similar sensitivity for acetone and ethanol. It is thought that improved selectivity for SnO thin film sensor in detection of ethanol gas might be due to a relative small band gap energy and high charge transport property of SnO. Dipole moment of acetone (2.91D) is somewhat higher than that of ethanol (1.69D). On SnO_2 thin films with higher band gap energy, ethanol could not correspond properly due to a lower dipole moment, which contributes to the resistance change; even it has a small molecular weight that allows easy gas reactions. However, on SnO thin films, participating ethanol species can fully contribute to the resistance change [46].

Ethylene was detected with similar sensitivity for both SnO and SnO_2 thin film sensors to have -1.23 and 1.26, respectively, but overall sensitivities were lower than those of acetone and ethanol gases. This might be due to the difference in nature of volatile gases. It was reported that acetone and ethanol has a polarity in chemical structure due to a carbonyl group, which is directly related to the charge transfer [47-48]. On the contrary, chemical structure of ethylene is combination of nonpolar molecules [49]. It appears that this nonpolar property of ethylene gas induced a relatively lower sensitivity.

4.4 Summary and Conclusions

Several parameters in sputtering which influence the ZnO thin film property were studied to find out the optimum conditions to fabricate the thin film VOC sensors. 80W, 20:2 ratios of argon to oxygen, and 10 mTorr of chamber pressure were found to be the optimum for the fabrication. Based on these conditions, rf sputtered ZnO thin film sensors were tested in two different gas atmospheres such as acetone and ethanol. In detection of acetone gas, 350 ℃ was observed to be the optimum condition. However, in the detection of ethanol gas, ZnO thin film sensors working 300 ℃ was observed to show better sensitivity and shorter response time. This can be explained that dissociation and chemisorption mechanism of metal oxide based sensors depending on gas species are somewhat different to have the optimum working temperature.

RF/DC co-sputtered SnO_x thin film sensors were fabricated on silicon dioxide substrate by post annealing at 450℃. Depending on the location, different mixing ratio of SnO and SnO_2 phases were obtained. In terms of direction of response, SnO and SnO_2 thin film sensors responded in an obvious opposite direction and mixed phases of SnOx thin film sensor revealed unstable response to the volatile gases. From the film characterization, it is concluded that a dominant phase in SnO_x thin film determine the gas sensing property of SnO_x thin film sensors. P-type SnO thin film sensor was found that it can be utilized to gas sensor application with reliable sensitivity and response time, comparable to n-type SnO_2 thin film sensors. It is believed that a difference in direction of reaction will contribute to the future electronic nose development both for the enhanced selectivity by combining with other n-type semiconducting materials, ZnO, WO_3 and In_2O_3 and doping.

References

1. J. Hammer, "Low-loss epitaxial ZnO optical waveguides," *Appl. Phys. Lett.,* **21**[8] 358 (1972).
2. T. D. Senguttuvan and L. K. Malhotra, "Sol gel deposition of pure and antimony doped tin dioxide thin films by non alkoxide precursors," *Thin Solid Films,* **289**[1-2] 22-28 (1996).

3. G. Boschloo and D. Fitzmaurice, "Spectroelectrochemistry of Highly Doped Nanostructured Tin Dioxide Electrodes," *The Journal of Physical Chemistry B,* **103**[16] 3093-98 (1999).
4. J. Dominguez, "Epitaxial nanocrystalline tin dioxide thin films grown on (0001) sapphire by femtosecond pulsed laser deposition," *Appl. Phys. Lett.,* **79**[5] 614 (2001).
5. M. Kunst, T. Moehl, F. Wünsch, andH. Tributsch, "Optoelectronic properties of SnO2 / TiO2 junctions," *Superlattices and Microstructures,* **39**[1-4] 376-80.
6. J. Tamaki, T. Maekawa, N. Miura, andN. Yamazoe, "CuO-SnO2 element for highly sensitive and selective detection of H2S," *Sensors and Actuators B: Chemical,* **9**[3] 197-203 (1992).
7. T. Riemann, J. Christen, G. Kaczmarczyk, A. Kaschner, A. Hoffmann, A. Zeuner, D. Hofmann, andB. K. Meyer, "Microscopic Analysis of High Quality Thick ZnO CVD Layers: Imaging of Growth Domains, Strain Relaxation, and Impurity Incorporation," *physica status solidi (b),* **229**[2] 891-95 (2002).
8. J. Jeong, S.-P. Choi, C. I. Chang, D. C. Shin, J. S. Park, B. T. Lee, Y.-J. Park, andH.-J. Song, "Photoluminescence properties of SnO2 thin films grown by thermal CVD," *Solid State Communications,* **127**[9-10] 595-97 (2003).
9. M. Ohyama, H. Kouzuka, andT. Yoko, "Sol-gel preparation of ZnO films with extremely preferred orientation along (002) plane from zinc acetate solution," *Thin Solid Films,* **306**[1] 78-85 (1997).
10. C. Cobianu, C. Savaniu, P. Siciliano, S. Capone, M. Utriainen, andL. Niinisto, "SnO2 sol–gel derived thin films for integrated gas sensors," *Sensors and Actuators B: Chemical,* **77**[1-2] 496-502 (2001).

11. B. Khuri-Yakub, "Reactive magnetron sputtering of ZnO," *J. Appl. Phys.*, **52**[7] 4772 (1981).
12. R. Cavicchi, "Layer by layer growth of epitaxial SnO2 on sapphire by reactive sputter deposition," *Appl. Phys. Lett.*, **61**[16] 1921 (1992).
13. J. Lu, Y. Zhang, Z. Ye, L. Wang, B. Zhao, andJ. Huang, "p-type ZnO films deposited by DC reactive magnetron sputtering at different ammonia concentrations," *Materials Letters,* **57**[22-23] 3311-14 (2003).
14. R. Snyders, M. Wautelet, R. Gouttebaron, J. P. Dauchot, andM. Hecq, "Correlation between the gas composition and the stoichiometry of SnOx films prepared by DC magnetron reactive sputtering," *Surface and Coatings Technology,* **142-144**[0] 187-91 (2001).
15. A. Martel, F. Caballero-Briones, P. Bartolo-Pérez, A. Iribarren, R. Castro-Rodríguez, A. Zapata-Navarro, andJ. L. Peña, "Chemical and phase composition of SnOx:F films grown by DC reactive sputtering," *Surface and Coatings Technology,* **148**[2-3] 103-09 (2001).
16. A. Martel, F. Caballero-Briones, P. Quintana, P. Bartolo-Pérez, andJ. L. Peña, "X-ray study of tin oxide films obtained by reactive DC sputtering from a metallic tin target in pure oxygen plasma," *Surface and Coatings Technology,* **201**[8] 4659-65 (2007).
17. M. Tadatsugu, "Transparent conducting oxide semiconductors for transparent electrodes," *Semiconductor Science and Technology,* **20**[4] S35 (2005).
18. A. Martel, F. Caballero-Briones, J. Fandiño, R. Castro-Rodríguez, P. Bartolo-Pérez, A. Zapata-Navarro, M. Zapata-Torres, andJ. L. Peña, "Discharge diagnosis and controlled deposition of SnOx:F films by DC-reactive sputtering from a metallic tin target," *Surface and Coatings Technology,* **122**[2-3] 136-42 (1999).

19. D. Vlachos, "Dependence of sensitivity of SnOx thin?film gas sensors on vacancy defects," *J. Appl. Phys.*, **80**[10] 6050 (1996).
20. M. Di Giulio, G. Micocci, A. Serra, A. Tepore, R. Rella, andP. Siciliano, "SnO2 thin films for gas sensor prepared by r.f. reactive sputtering," *Sensors and Actuators B: Chemical,* **25**[1-3] 465-68 (1995).
21. G. Beensh-Marchwicka, L. Kròl-Stępniewska, andA. Misiuk, "Influence of annealing on the phase composition, transmission and resistivity of SnOx thin films," *Thin Solid Films,* **113**[3] 215-24 (1984).
22. B. Alterkop and et al., "Effect of air annealing on opto-electrical properties of amorphous tin oxide films," *Journal of Physics D: Applied Physics,* **36**[5] 552 (2003).
23. A. De and S. Ray, "A study of the structural and electronic properties of magnetron sputtered tin oxide films," *Journal of Physics D: Applied Physics,* **24**[5] 719 (1991).
24. T. Suzuki and T. Yamazaki, "Effect of annealing on the gas sensitivity of tin oxide ultrathin films," *Journal of Materials Science Letters,* **9**[7] 750-51 (1990).
25. J.-L. Huang, D.-W. Kuo, andB.-Y. Shew, "The effects of heat treatment on the gas sensitivity of reactively sputtered SnO2 films," *Surface and Coatings Technology,* **79**[1-3] 263-67 (1996).
26. J. Kaur, S. C. Roy, andM. C. Bhatnagar, "Highly sensitive SnO2 thin film NO2 gas sensor operating at low temperature," *Sensors and Actuators B: Chemical,* **123**[2] 1090-95 (2007).
27. D. E. Williams, "Semiconducting oxides as gas-sensitive resistors," *Sensors and Actuators B: Chemical,* **57**[1-3] 1-16 (1999).

28. H. Ahn, J. H. Noh, S.-B. Kim, R. A. Overfelt, Y. S. Yoon, andD.-J. Kim, "Effect of annealing and argon-to-oxygen ratio on sputtered SnO2 thin film sensor for ethylene gas detection," *Materials Chemistry and Physics,* **124**[1] 563-68 (2010).
29. K. B. Sundaram and A. Khan, "Characterization and optimization of zinc oxide films by r.f. magnetron sputtering," *Thin Solid Films,* **295**[1-2] 87-91 (1997).
30. S. Yoon, Dissertation, Graduate school, Auburn University (2009)
31. D. Kang, "Amorphous gallium indium zinc oxide thin film transistors: Sensitive to oxygen molecules," *Appl. Phys. Lett.,* **90**[19] 192101 (2007).
32. JCPDS #04-0673
33. J. Kong, N. R. Franklin, C. Zhou, M. G. Chapline, S. Peng, K. Cho, andH. Dai, "Nanotube Molecular Wires as Chemical Sensors," *Science,* **287**[5453] 622-25 (2000).
34. C. Nayral, E. Viala, P. Fau, F. Senocq, J.-C. Jumas, A. Maisonnat, andB. Chaudret, "Synthesis of Tin and Tin Oxide Nanoparticles of Low Size Dispersity for Application in Gas Sensing," *Chemistry – A European Journal,* **6**[22] 4082-90 (2000).
35. X. Pan, "Oxidation and phase transitions of epitaxial tin oxide thin films on (012) sapphire," *J. Appl. Phys.,* **89**[11] 6048 (2001).
36. L. Y. Liang, Z. M. Liu, H. T. Cao, Z. Yu, Y. Y. Shi, A. H. Chen, H. Z. Zhang, Y. Q. Fang, andX. L. Sun, "Phase and Optical Characterizations of Annealed SnO Thin Films and Their p-Type TFT Application," *Journal of The Electrochemical Society,* **157**[6] H598-H602 (2010).
37. L. Y. Liang, Z. M. Liu, H. T. Cao, andX. Q. Pan, "Microstructural, Optical, and Electrical Properties of SnO Thin Films Prepared on Quartz via a Two-Step Method," *ACS Applied Materials & Interfaces,* **2**[4] 1060-65 (2010).

38. X. Liu, "Preparation and characterization of p-jour semiconducting tin oxide thin film gas sensors," *J. Appl. Phys.,* **107**[6] 064309 (2010).

39. P. P. Sahay, "Zinc oxide thin film gas sensor for detection of acetone," *Journal of Materials Science,* **40**[16] 4383-85 (2005).

40. J. X. Wang and et al., "Hydrothermally grown oriented ZnO nanorod arrays for gas sensing applications," *Nanotechnology,* **17**[19] 4995 (2006).

41. W. Guo, "Microstructure, optical, and electrical properties of p-jour SnO thin films," *Appl. Phys. Lett.,* **96**[4] 042113 (2010).

42. X. Pan, "Oxidation and phase transitions of epitaxial tin oxide thin films on (012) sapphire," *J. Appl. Phys.,* **89**[11] 6048 (2001).

43. H.-N. Lee, H.-J. Kim, andC.-K. Kim, "p-Channel Tin Monoxide Thin Film Transistor Fabricated by Vacuum Thermal Evaporation," *Japanese Journal of Applied physics,* **49** (2010).

44. J. M. Themlin, R. Sporken, J. Darville, R. Caudano, J. M. Gilles, andR. L. Johnson, "Resonant-photoemission study of SnO2: Cationic origin of the defect band-gap states," *Physical Review B,* **42**[18] 11914-25 (1990).

45. Y. Ogo, "p-channel thin-film transistor using p-jour oxide semiconductor, SnO," *Appl. Phys. Lett.,* **93**[3] 032113 (2008).

46. J. Li, Y. Lu, Q. Ye, M. Cinke, J. Han, andM. Meyyappan, "Carbon Nanotube Sensors for Gas and Organic Vapor Detection," *Nano Letters,* **3**[7] 929-33 (2003).

47. K.-S. Chen, T.-C. Wei, M.-S. Li, H.-M. Wu, T.-P. Tang, C.-Y. Wang, andY.-C. Tu, "Chemical characterization of plasma-polymerized films from acetylene and nitrogen-

containing mixtures and their ethanol vapor sensitivity," *Radiation Physics and Chemistry,* **76**[6] 941-50 (2007).

48. T. N. Obee and S. O. Hay, "Effects of Moisture and Temperature on the Photooxidation of Ethylene on Titania," *Environmental Science & Technology,* **31**[7] 2034-38 (1997).
49. D. Jadsadapattarakul, C. Thanachayanont, J. Nukeaw, andT. Sooknoi, "Improved selectivity, response time and recovery time by [0 1 0] highly preferred-orientation silicalite-1 layer coated on SnO2 thin film sensor for selective ethylene gas detection," *Sensors and Actuators B: Chemical,* **144**[1] 73-80 (2010).

CHAPTER 5 EFFECT OF ARGON-TO-OXYGEN RATIO DURING RF SPUTTERING AND POST ANNEALING ON GAS SENSING PROPERTY OF SNO$_2$ THIN FILM

5.1 Introduction

Having artificial control over fruit ripening is very important in producing a high-value commercial product in the agricultural industry. Ethylene has been utilized as an artificial treatment in controlling the ripening process, especially in tomato and banana production [1]. Ethylene is also reported as one of the distinctive gases emitted when certain plants are infected by pathogens. *Botrytis cinerea*, one of the most well-known pathogens, emits ethylene gas from the reaction between plants and the pathogen. Tomatoes infected by bacteria are known to generate small amounts of ethylene [2]. For such applications as monitoring plant conditions or plant health, fast, simple, and reliable detection of ethylene is required [3]. Several approaches have been explored to detect ethylene gas in air. A detection system through a CO2 laser combined with a photoacoustic cell was utilized to observe whether ethylene gas is produced from *B. cinerea* contamination [4]. A mid-infrared filter spectrometer was used to determine ethylene gas. It was able to precisely recognize ethylene from other mixed gases with a detection limit of less than 20ppm; however, the system consisted of bulky components such as an IR-emitter, optical chopper, and coupling optics [5]. Alternative techniques for miniaturized sensors designed to detect ethylene gas were reported. Porous silicon-based heterodiode was fabricated with a hydrocarbon layer that is sensitive to ethylene gas [3]. I-V characteristics of the heterodiode are modified by the adsorption of the gas. Color changeable films based on SiO_2 nanoparticles with palladium and ammonium molybdate were fabricated on filter papers [6]. Different colors were observed due to the oxidation of ethylene by Pd reduction. These methods, however, showed limited sensitivity or long operation times.

An inexpensive and simple method of utilizing metal oxide semiconductors has been attempted. Thick film SnO_2 fabricated by a screen printing technique was used for ethylene gas detection [7-9]. A SnO_2 sensor with about 20–30 μm thickness was able to measure the concentration of several ppm of ethylene [2]. WO_3 was mixed with SnO_2 to improve the sensitivity, and a strong dependence of the WO_3 amount on the sensitivity was observed. A 10 μm thick film with SnO_2-0.3%wt WO_3 showed the best sensitivity [8]. Recently, 5 μm thick SnO_2 was deposited on micromachined silicon substrate to obtain a low-cost gas sensing microsystem. By forming a multiple sensor array, the selective detection of ethylene gas was improved [7]. SnO_2 thick films have demonstrated the measurement of ethylene gas with several ppm sensitivities. Approaches via thin film SnO_2 have been reported to detect oxidizing gases such as CO, O_3, and C_2H_5OH with higher sensitivity and more accurate control of microstructure compared to thick film-type sensors [10-14]. However, no literature of thin film SnO_2 for ethylene gas detection is available to understand the relationship between the thin film process, structure of sensing material, and ethylene sensing characteristics for developing an integrated microsensor.

In this study, R.F. sputtered SnO_2 thin films were fabricated, and their ethylene-sensing characteristics were investigated. Processing conditions during R.F. sputter deposition, such as post annealing and the argon-to-oxygen ratio, were systematically examined to find the optimal process conditions and to understand ethylene sensing mechanism in thin film SnO_2.

5.2 Experiment

Tin oxide film was deposited on an alumina substrate. A SnO_2 ceramic target (99.99%) was used for R.F. sputtering at 80W for 25 minutes. The total amount of gas mixture was fixed to 30 sccm for all argon-to-oxygen ratios. Different argon-to-oxygen ratios were tested through R.F. sputtering, including 27.3:2.7, 23:7, 20:10, and 15:15. To compare samples prepared at different argon-to-oxygen ratios, all samples in this study have the same film thickness of 120 nm. Post annealing was performed at 650 ℃ for 1hr by using a tube furnace in an air atmosphere. A Pt electrode with 100 nm thickness was coated on alumina substrate prior to SnO_2 deposition by DC sputtering at 100W. An interdigitated structure was fabricated by using a shadow mask, and the distance between electrodes and width of electrode was 4 mm. Configuration of thin film sensor is drawn in figure 5.1.

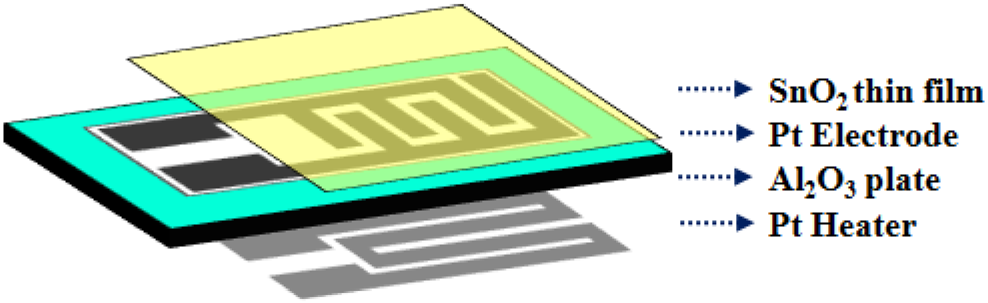

Figure 5.1 Configuration of rf sputtered SnO2 thin film ethylene sensor

5.3 Results and discussion

To investigate the effects of the argon-to-oxygen ratio and post-annealing on SnO_2 phase formation, XRD analysis was performed. Figure 5.2 shows the XRD scans for the as-deposited thin films prepared by sputter deposition at four different argon-to-oxygen ratios of 15:15, 20:10, 23:7, and 27.3:2.7. SnO_2 phases were not observed in all as-deposited films. Only peaks of alumina substrate and platinum electrode were found. The films were post-annealed at 650 °C for 1hr and were characterized as shown in Figure 5.3. Apparently, the films annealed at 650 °C show the presence of three SnO_2 peaks corresponding mainly to (110) at 26.5°, (101) at 33.8°, and (211) at 55.7° for all different argon-to-oxygen ratios. SnO peaks that are often observed during oxidation of sputtered Sn film are not characterized in this experiment probably due to the use of an oxide target [15]. It appears that relative intensity of peak indicating SnO_2 (110) plane at 26.5° is slightly higher compared with peaks of (101) and (211) as the amount of oxygen in Ar/O_2 gas mixture increases. Similar results on promoting (110) peak at higher oxygen pressure are reported in Sb-doped SnO_2 films by sputter deposition [16]. The formation of the lowest energy surface of SnO_2 seems to be enhanced with the increase of oxygen pressure during sputter deposition.

The surface morphology of sputtered SnO_2 at different argon-to-oxygen ratios was characterized by FE-SEM analysis as shown in Figure 5.4 and 5.5. SEM observation reveals that differences in surface morphology as a function of the argon-to-oxygen ratio for both as-deposited and post-annealed films are not significant. However, the overall grain size of post-annealed films apparently become larger than that of as-deposited films, which indicates distinguishable changes in morphology and grain structure as a result of high-temperature annealing.

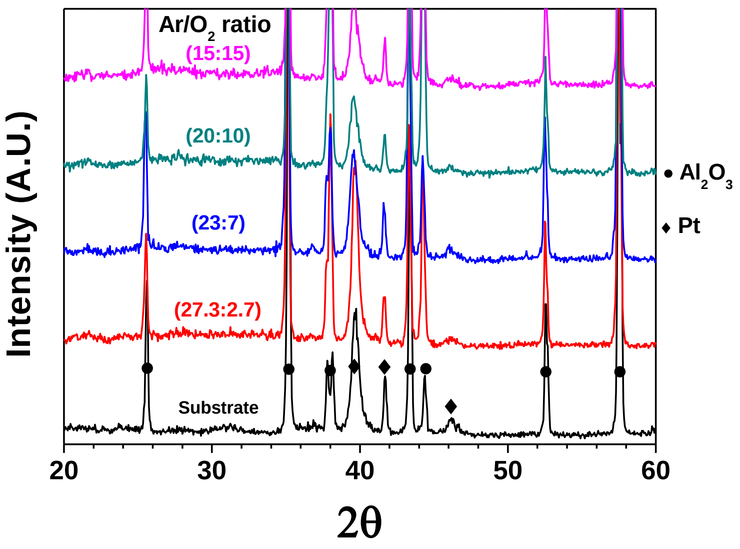

Figure 5.2 XRD graphs of as-deposited rf sputtered SnO_2 thin films on platinum coated alumina substrate under four different argon-to-oxygen ratios (from top to bottom, 15:15, 20:10, 23:7, 27.3:2.7 and peak for pt coated substrate)

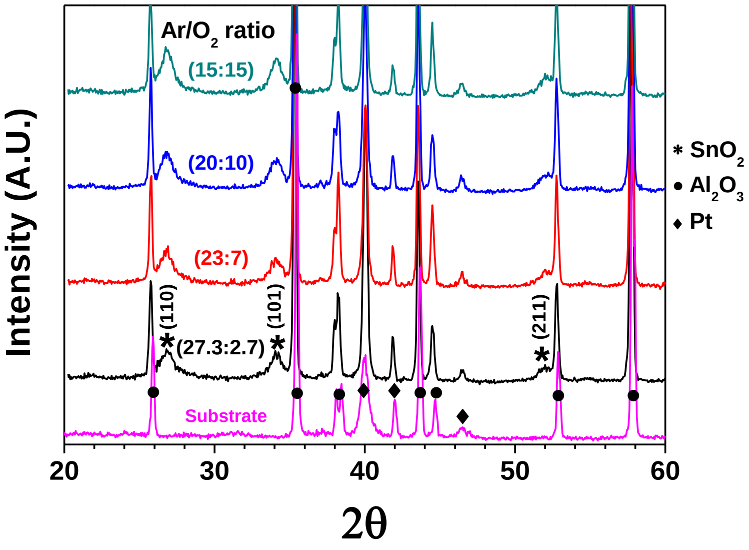

Figure 5.3 XRD graphs of 650 °C post annealed rf sputtered SnO_2 thin films on platinum coated alumina substrate under four different argon-to-oxygen ratios (from top to bottom, 15:15, 20:10, 23:7, 27.3:2.7 and peak for pt coated substrate)

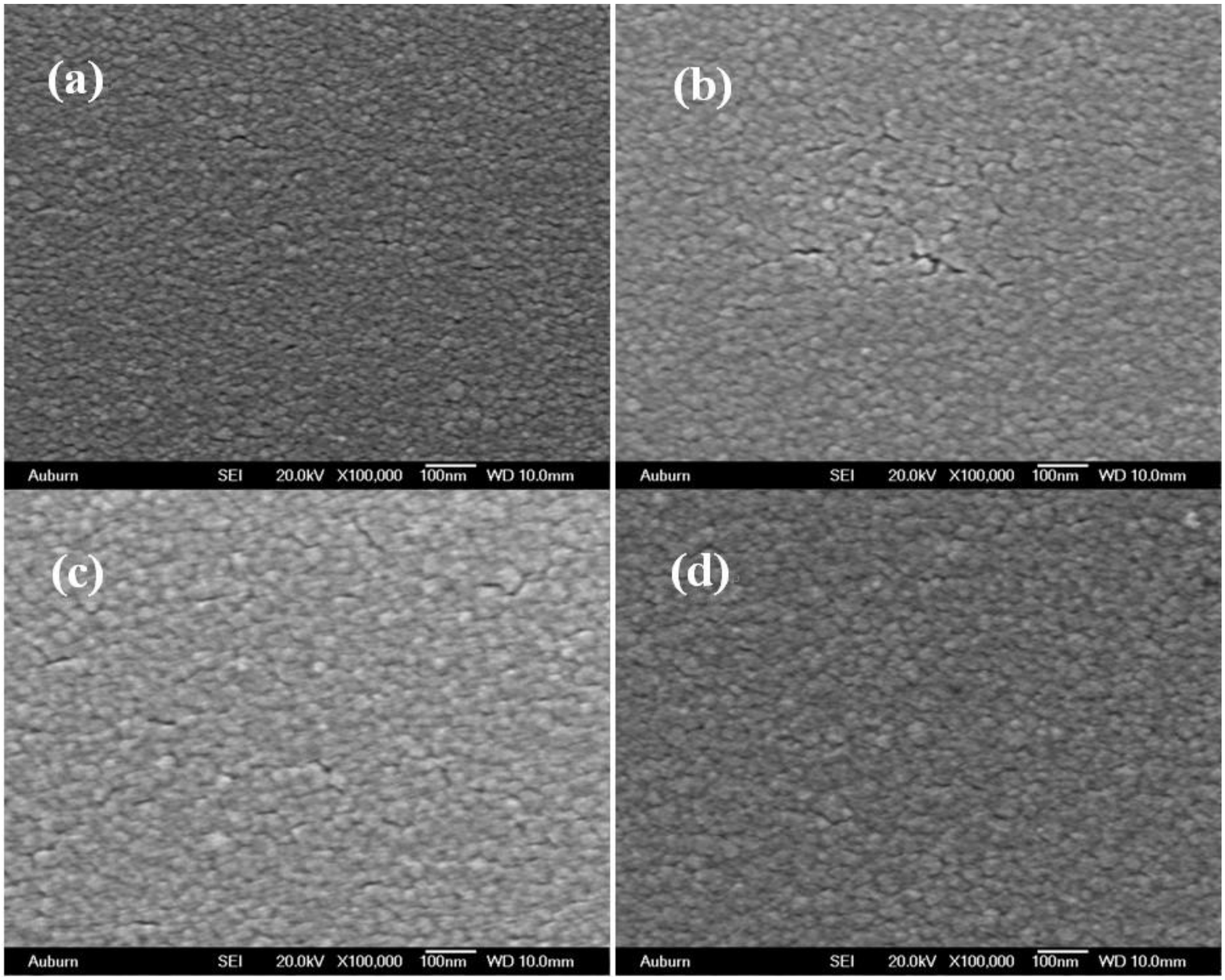

Figure 5.4 As-deposited SnO_2 thin film under different argon-to-oxygen ratios (a) 15:15 (b) 20:10 (c) 23:7 (d) 27.3:2.7

The ethylene gas sensing characteristics of SnO_2 thin films were studied by measuring resistance change by time and by calculating sensitivity that is defined as the ratio of resistance measured in air (R_{air}) to that of the detecting gas (R_{gas}). Figure 5.6 shows the resistance change of as-deposited and post-annealed SnO_2 films. Both samples were deposited at a 20:10 argon-to-oxygen ratio, and measurement was performed at 25ppm of ethylene concentration in air. The sensitivity values of post-annealed and as-deposited films are calculated as around 6.5 and 2.7,

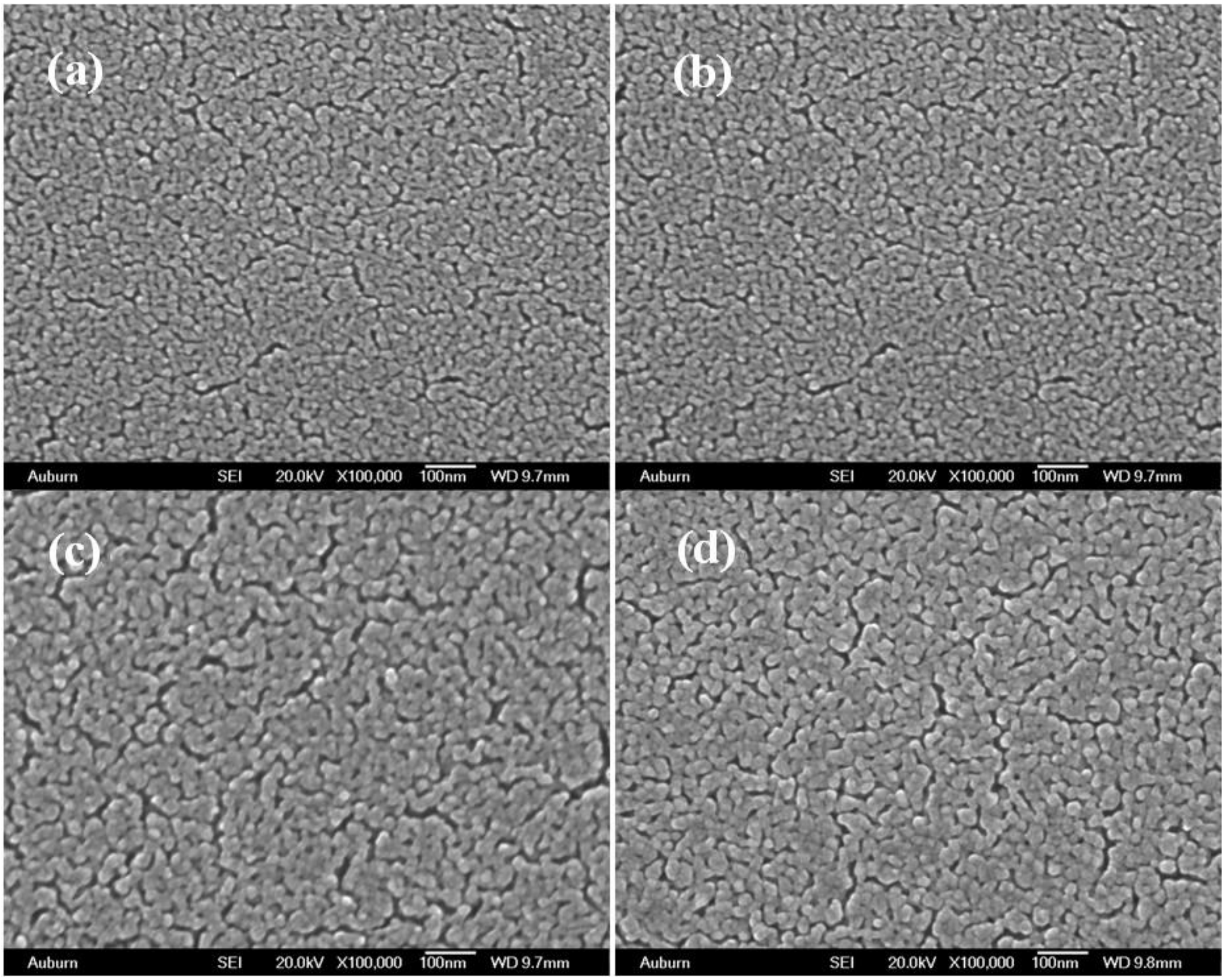

Figure 5.5 650 ℃ post annealed SnO_2 thin film under different argon-to-oxygen ratios (a) 15:15 (b) 20:10 (c) 23:7 (d) 27.3:2.7

respectively. For the as-deposited tin oxide film, the response time for sensing 25ppm of ethylene gas was approximately 14.3 min until the resistance drop was saturated. The recovery time was determined to be 25.7 min by measuring the time back to the saturated initial resistance. After post-annealing at 650 ˚C for 1hr, the response time and recovery time become 4.5 min and 11.3 min, respectively.

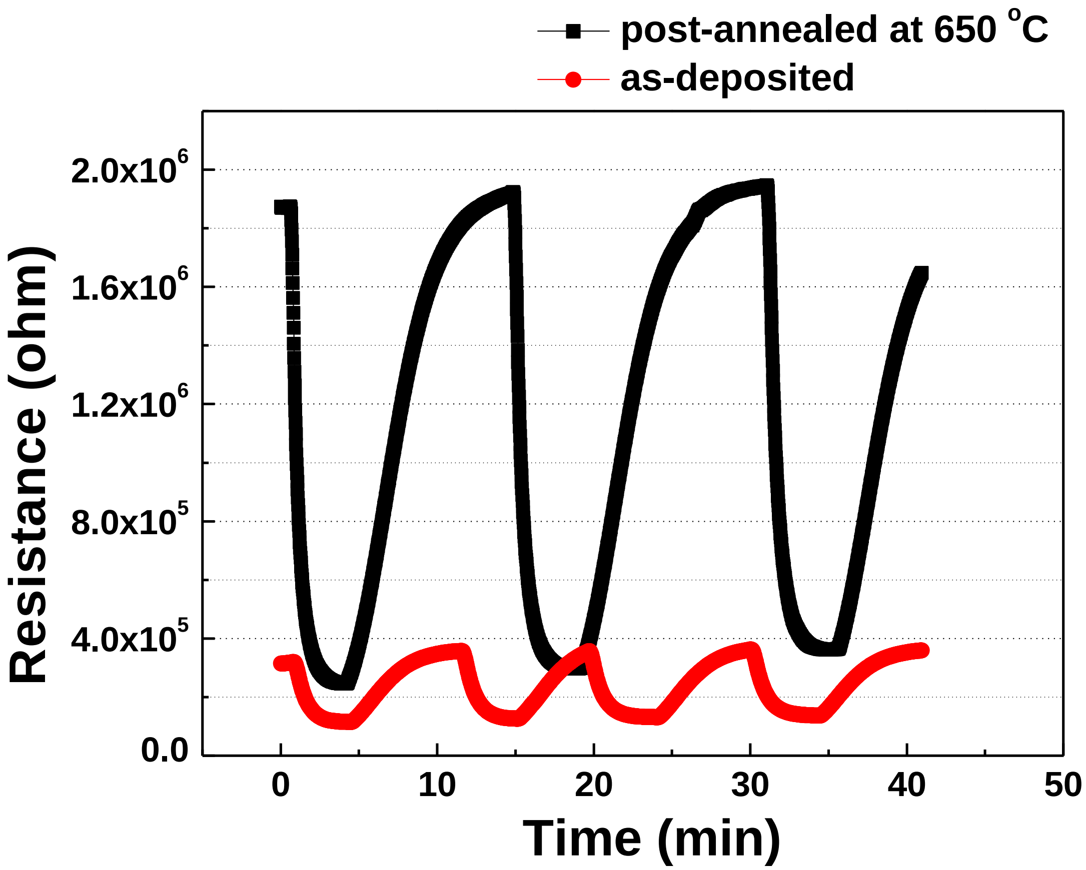

Figure 5.6 Resistance profiles of as-deposited SnO_2 thin film sensor and 650 ℃ post annealed SnO_2 thin film sensor prepared under 20:10 argon-to-oxygen ratio. Ethylene concentraion was 25 ppm in total 100 sccm of gas flow

The sensitivity values are higher than reported values measured by SnO_2 thick films. Ivanov et al. reported that undoped SnO_2 films showed the sensitivity of around 1.5, and doped SnO_2 reached 4.2 at 10 ppm ethylene and 300 ℃ sensing temperature [6]. Pimton-Ngam et al. also reported the best sensitivity of 1.7 from 0.3 wt% WO_3 doped SnO_2 at 6 ppm ethylene concentration and at 300 ℃ sensing temperature [8]. Our undoped SnO_2 films show the sensitivity of 4.1 from post-annealed film and 2.0 from as-deposited film at 10 ppm and 300 ℃ conditions. Apparently, the resistance change due to gas exposure is higher in post-annealed

SnO_2 than in as-deposited due to the formation of the SnO_2 phase. Besides a signal change, initial resistance values between as-deposited and post-annealed films were typically different. Initial resistance of SnO_2 thin films prior to ethylene exposure was recorded at approximately 380K ohm for as-deposited film and 1.8M ohm for post-annealed SnO_2 as shown in figure 5.6. From the SEM observation, the surface morphology of post-annealed SnO_2 exhibits marked grain boundary or voids, which is believed to increase resistance. Similar effects of annealing on the resistance increase of SnO_2 by thermal oxidation of Sn film are also reported by S. Laghrib et al. [15]. Another possible reason may be due to the stoichiometry of the film. As-deposited film may be a non-stoichiometric form due to oxygen deficient sputtering conditions, and such nonstoichiometry usually makes it more conductive [18]. FE-SEM/EDS characterization was carried out to examine the quantitative composition of both the as-deposited and post-annealed thin films. The values of x, in SnO_x were measured to be around 1.6 ± 0.2 for the as-deposited films, and about 1.9 ± 0.1 for post-annealed thin films within the detection limit.

Ethylene gas sensitivity of films depending on an argon-to-oxygen ratio during sputter deposition was compared in figure 5.7. The working temperature and concentration of ethylene gas were fixed at 300℃ and 25ppm, respectively, in air. As expected from XRD and SEM results, the effect of the argon-to-oxygen ratio on the gas sensitivity is not evident, while post-annealing improves sensitivity probably due to increased crystallinity of annealed films. Scrutiny of post-annealed SnO_2 films reveals that the film deposited at a higher oxygen ratio shows slightly higher sensitivity. It may be due to the increased (110) orientation from the XRD result. It is reported that the (110) plane in SnO_2 exhibits the shortest Sn interatomic distance [9]. It could be estimated that dissociative chemisorptions of oxygen is facilitated by the decrease of Sn interatomic distance. Reducing gas, such as ethylene gas molecule, can easily react with adsorbed negatively charged oxygen ions on the (110) plane.

The ethylene gas concentration was varied to investigate sensitivity changes for both as-deposited and post–annealed films. The four different ethylene concentrations included 100ppm, 50ppm, 25ppm, and 10ppm. Resistance change, average value, and their deviations are summarized in Table 1. Annealed thin films reveal approximately 10 percent higher sensitivity compared with as-deposited thin films at a high concentration of ethylene gas. The difference in sensitivity became larger up to about 20% as ethylene concentration decreases down to 10ppm. An ethylene gas sensing mechanism was considered as illustrated in figure 5.8. It is thought that the reaction between adsorbed O^- ion and ethylene caused oxidation of ethylene into ethylene oxide similar to alcohol detection by SnO_2 [16]. Free electrons released during the reaction can be responsible for the resistance drop in gas measurement [11].

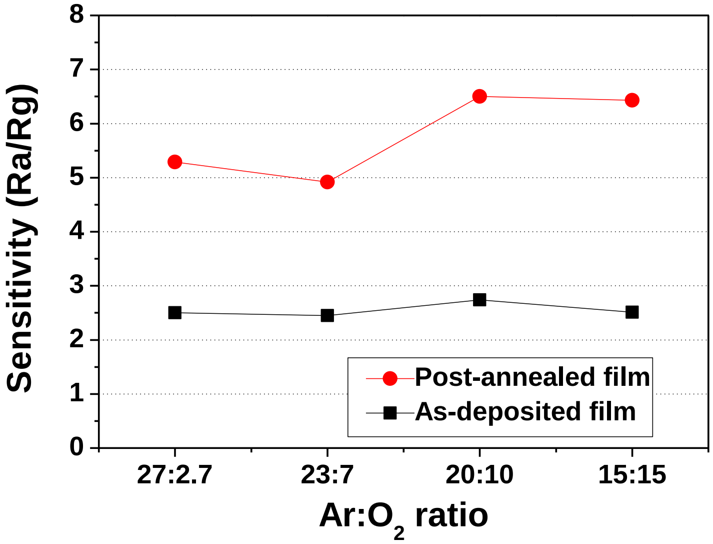

Figure 5.7 Sensitivities of as-deposited and post-annealed SnO_2 thin films as a function of argon to oxygen ratio at ethylene concentration of 25 ppm

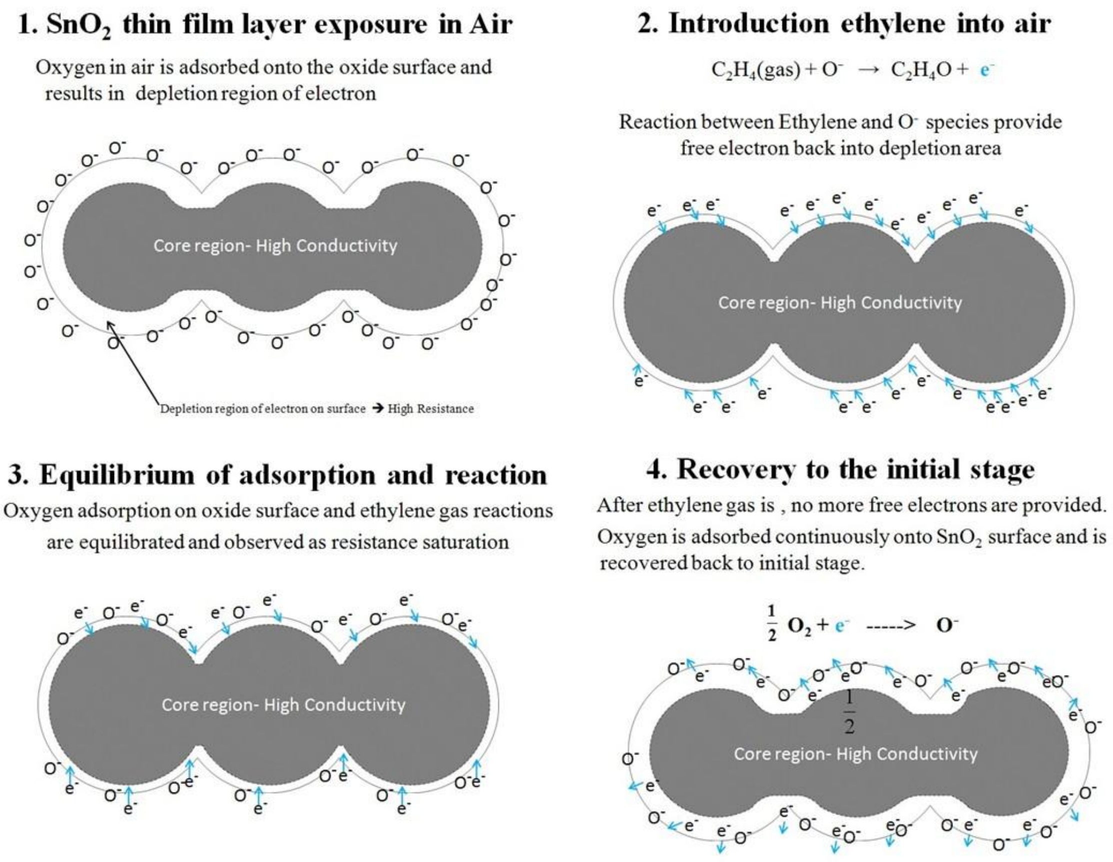

Figure 5.8 the proposed ethylene sensing mechanism with SnO_2 thin film

5.4 Summary and Conclusions

SnO2 thin films were fabricated by R.F. magnetron sputtering to fabricate ethylene gas sensors. Ethylene gas ranging from 100ppm to 10ppm level in synthetic air was measured by a SnO2 thin film sensor with higher sensitivity compared with bulk SnO2. In sputter parameters, the argon-to-oxygen ratio during SnO2 sputtering negligibly influenced the sensing properties of ethylene gas, while post-annealing at 650℃ obviously enhanced sensitivity. Post-annealed films showed improved sensitivity to ethylene gas up to 30% compared with that of the as-deposited films. However, the change of sensitivity in SnO2 films as a function of the argon-to-oxygen gas ratio was measured to be less than 10%. It is believed that the sensitivity improvement after post-annealing is mainly due to the formation of the SnO2 phase. The sensitivity change in SnO2 films prepared at different argon-to-oxygen ratios may result from slightly enhanced (110) orientation in the SnO2 films after annealing.

References

1. C. S. Barry and J. J. Giovannoni, "Ethylene and Fruit Ripening," *Journal of Plant Growth Regulation,* **26** 143–59 (2007).
2. A. Giberti, M. C. Carotta, V. Guidi, C. Malagù, G. Martinelli, M. Piga, andB. Vendemiati, "Monitoring of ethylene for agro-alimentary applications and compensation of humidity effects," *Sensors and Actuators B,* **103** 272-76 (2004).
3. S. Belhousse, H. Cheraga, N. Gabouze, andR. Outamzabet, "Fabrication and characterisation of a new sensing device based on hydrocarbon groups (CHx) coated porous silicon," *Sensors and Actuators B,* **100** 250-55 (2004).
4. S. M. Cristescu, D. D. Martinis, S. t. L. Hekkert, D. H. Parker, andF. J. M. Harren, "Ethylene Production by Botrytis cinerea In Vitro and in Tomatoes," *Applied and Environmental Microbiology,* **68**[11] 5342-50 (2002).
5. J. W. l. J. Hildenbrand , S. Hartwig, A. Eberhardt, B. Halford ,M. Moreno, J. Fonollosa , L. Fonseca , J. Santander , R. Rubio,I. Gra`cia, C. Cane1187, "A compact optical multichannel system for ethylene monitoring," *Microsystem Technology,* **14** 637-44 (2008).
6. P. Ivanov, E. Llobet, A. Vergara, M. Stankova, X. Vilanova , J. Hubalek, I. Gracia, C. Can´e, andX. Correig, "Towards a micro-system for monitoring ethylene in warehouses," *Sensors and Actuators B,* **111-112** 63-70 (2005).

7. Jin-Ho Kim and S. Shiratori, "Fabrication of Color Changeable Film to Detect Ethylene Gas," *Japanese Journal of Applied Physics,* **45**[5A] 4274-78 (2006).
8. Y. Pimtong-Ngam, S. Jiemsirilers, andS. Supothina, "Preparation of tungsten oxide–tin oxide nanocomposites and their ethylene sensing characteristics," *Sensors and Actuators A,* **139** 7-11 (2007).
9. M. Batzill and U. Diebold, "The surface and materials science of tin oxide " *Progress in Surface Science,* **79** 47-154 (2005).
10. V. V. Kissine, S. A. Voroshilov, andV. V. Sysoev, "Oxygen flow effect on gas sensitivity properties of tin oxide film prepared by r.f. sputtering," *Sensors and Actuators B,* **55** 55-59 (1999).
11. K. N. Yu, Yonghong Xiong, Yulong Liu, andC. Xiong, "Microstructural change of nano-SnO 2 grain assemblages with the annealing temperature," *Physical Review B,* **55**[4] 2666-71 (1997).
12. G. Korotcenkov, "Gas response control through structural and chemical modification of metal oxide films: state of the art and approaches," *Sensors and Actuators B,* **107** 209–32 (2005).
13. G. Korotcenkov, I. Blinov, M. Ivanov, andJ. R. Stetter, "Ozone sensors on the base of SnO2 films deposited by spray pyrolysis," *Sensors and Actuators B,* **120** 679-86 (2007).
14. G. Korotcenkov and B. K. Cho, "Thin film SnO2-based gas sensors: Film thickness influence," *Sensors and Actuators B,* **142** 321–30 (2009).
15. S. Laghrib, H. Amardjia-Adnani, D. Abdi, andJ. M. Pelletier, "Tin oxide thin layers obtained by vacuum evaporation of tin and annealing under oxygen flow," *Vacuum,* **82** 782–88 (2008).

16. H.-C. Lee, W.-S. Hwang, G.-B. Lee, andY.-M. Lu, "Effects of O2/Ar flow ratio on the alcohol sensitivity of tin oxide film," *Applied Surface Science,* **252** 3502–08 (2006).
17. J. Lee, "Effects of oxygen concentration on the properties of sputtered SnO2:Sb films deposited at low temperature," *Thin Solid Films,* **516** 1386–90 (2008).
18. V. Matol´in, I. Matol´inova, T. Mori, andM. Yoshitake, "Study of palladium interaction with magnetron sputtered SnO2 films," *Journal of Surface Science and Nanotechnology,* **4** 497-503 (2006).

CHAPTER 6 GEOMETRIC EFFECT OF ZNO NANORODS ON ETHANOL SENSING PROPERTY: THE RELATIVE ROLE OF THICKNESS OF SEED LAYER

6.1 Introduction

Nanostructured ZnO has attracted a high amount of interest due to its high band gap energy and wide exciton binding energy [1], which has led to a variety of applications including solar cells, high power LEDs and gas sensors [2-3]. Various technologies such as MOCVD [4-6], sol-gel spin coating [7-9], electrospinning [10-11] and chemical solution method [12-14] have been used to synthesize nanostructured ZnO. Among these, the chemical solution method is a simple and economic way to synthesize nanostructured ZnO at low temperatures (75 ~ 95 ℃) and on a large array of substrates [15]. Furthermore, such low temperature process permits the use of flexible substrates to develop low cost and practical sensor fabrication techniques [16-17]. For ZnO nanorod growth by the chemical solution method, it has been reported that a seed layer plays an important role in vertically aligning the nanorods and selectively patterning them on the substrate [18-24]. The influence of ZnO thin film thickness on electrical and optical properties such as field emission properties, optical transmittance and photo-conducting properties has been reported in several publications. Yu et al. [25] reported the linkage between electrical and optical properties of ZnO thin film and the crystallinity due to film thickness. Hao et al. [26] showed that a change in the optical transmittance due to density and resistivity of Al-doped ZnO films was driven by film thickness. Mridha et al. [27] also investigated the photoconducting properties as a function of ZnO film thickness. Although there are many reports to investigate thickness effects on the electrical and optical properties of ZnO thin films, few studies have been conducted to link the growth of nanostructures with the properties of the seed layer. Liu et al. [28] investigated an approach to modulate the field emission properties of ZnO nanowires grown on various seed layer thicknesses. The nanowire density, determined by the seed layer thickness, affected the field emission properties of the ZnO nanowires. Similarly, gas sensing properties depending on film thickness and comparisons between thin film sensors and nanostructured sensors have been reported. Kim et al. demonstrated a thickness dependence on ethanol sensing performance of a ZnO thin film sensor and further enhancement by aluminum doping [29]. Hydrogen sensing properties of platinum coated ZnO thin film sensors of varying thickness were compared with ZnO nanorods sensors by Tien et al [30]. Liewhiran et al. investigated the influence of film thickness of ZnO thick films (5 to 15 µm) made by flame spray pyrolysis on ethanol sensing properties [31]. No systematic investigation has been conducted, however, to determine the significance of the seed layer thickness on the sensitivity of a nanostructured ZnO gas sensor.

In this study, different thicknesses of ZnO thin films were prepared by a radio frequency (rf) sputter deposition method and used as a seed layer for the growth of ZnO nanorods by a thermolysis-assisted chemical solution method. Structural properties of the seed layers and nanorods were characterized by scanning electron microscopy and X-ray diffraction. Two types of sensors, i.e. seed layer only and nanorods on a seed layer, were utilized to examine the influence of seed layer on gas sensing properties. A quantitative analysis was also performed to determine the relative role of the seed layer on the sensitivity.

6.2 Experiment

6.2.1 Fabrication of ZnO seed layer

Top side interdigitated electrodes (IDE) and bottom side heaters were patterned in platinum on a nominally 0.25 mm thick polyimide film (Cirlex, Fralock, Valencia, CA, USA) via shadow masks. The width and spacing of the IDE fingers were 400 μm. ZnO seed layers ranging in thickness from 8 to 160 nm were deposited on the top side IDEs by rf sputtering of a ceramic ZnO target (99.99%, Kurt J. Lesker, Pittsburgh, PA, USA). The thickness of the seed layer was controlled with the deposition time and confirmed by observing the film cross section with FE-SEM. Other processing parameters included argon-to-oxygen ratio, chamber pressure and plasma generation power that were fixed at 20:2, 5 mTorr and 80 W, respectively. The deposition rate for these conditions was approximately 3.2 nm per minute.

6.2.2 Synthesis of ZnO nanorods

ZnO nanorods were grown on top of the ZnO seed layer in the manner described by Vayssieres [32]. A mixture of 0.01 mol of crystalline zinc nitrate hexahydrate (ACS Certified, Fisher Scientific, Pittsburgh, PA, USA) and 0.01 mol of hexamethylenetetramine (99%, Sigma-Aldrich, St. Louis, MO, USA) were dissolved in 400 ml of deionized (DI) water. The aqueous solution was stirred at room temperature for 12 hr until all chemicals were completely dissolved. A hot water bath (IsoTemp 202, Fisher Scientific) was used to accurately maintain a synthesis temperature of 85 °C. Previously seeded substrates were placed into the solution with the seed layer pointing down and ZnO nanorods allowed growing for 4 hr. The sensors were washed with DI water immediately upon removal from the solution.

6.3 Results and discussion

6.3.1 Characterization of ZnO

The crystallinity and morphology of both the ZnO seeded substrates and the nanorod structures were examined using X-ray diffraction (XRD) and field emission scanning electron microscopy (FE-SEM). XRD samples were scanned from 20° to 80° 2-theta at the rate of 5° per minute under 40 kV and 40 mA power with a CuK-alpha radiation source (D/MAX B, Rigaku, Tokyo, Japan). Surface morphology was observed with FE-SEM (JSM-7000F, JEOL, Tokyo, Japan)

6.3.2 Crystal structure and morphology of ZnO seed layer and ZnO nanorods

The XRD scans of substrates with different thickness ZnO seed layers are shown in figure 6.1. For 80 and 160 nm thick ZnO seed layers, a reflection peak at 34.2° indexed to the (002) plane was observed. Thinner samples did not show ZnO peaks due to the poor sensitivity of XRD. The highest peak, representing the polyimide substrate, was observed at 38.15°. Generally, rf sputtered ZnO thin films prefer to orient along the c-axis due to lower surface energy in the (00*l*) planes, a result similar to our previous observations on a semi-crystalline polyimide substrate [33-35]. XRD results for the ZnO nanorods grown on seeded substrates are shown in figure 6.2. The highest intensity reflection peak occurred at 34.2°, corresponding to the (002) plane of ZnO. Two other peaks indexed to (100) and (101) planes of ZnO were also observed at 31.5° and 36.05°, respectively. These XRD results indicate that ZnO nanorods grown on different thickness seed layers were vertically well aligned with the ZnO seed layer. The degree of (002) texture of the seed layer determines the vertical alignment of the nanorods [36-37]. Surface morphology of the different thickness ZnO seed layers deposited on a silicon dioxide substrate was characterized by FE-SEM as shown in figure 6.3. First, the surface of the silicon dioxide substrate (a) was observed to compare with those of ZnO sputtered thin films.

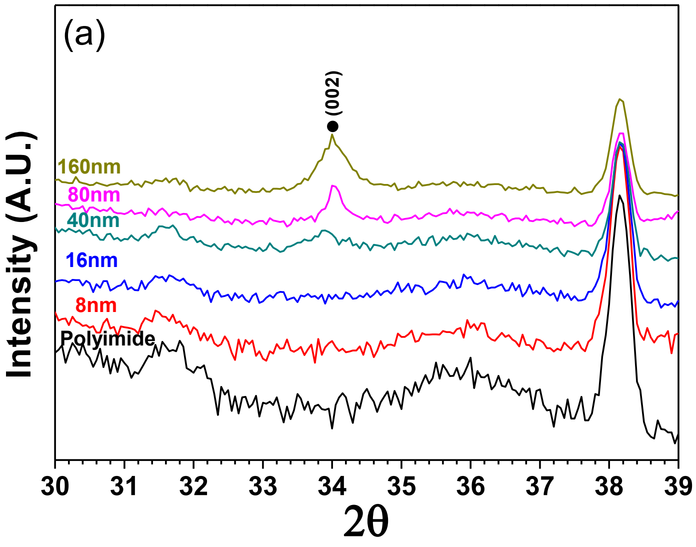

Figure 6.1 XRD graphs of rf sputtered ZnO seed layers varying thicknesses from 8 nm to 160 nm on polyimide film

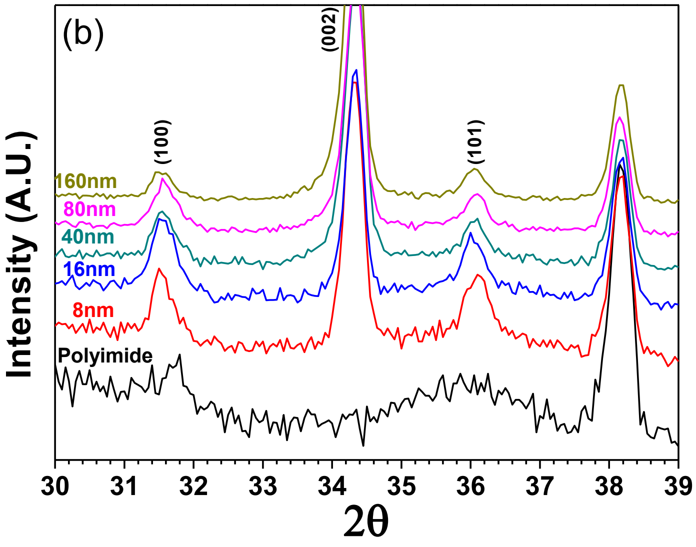

Figure 6.2 XRD graphs of ZnO nanorods grown on varying thicknesses of seed layer from 8 nm to 160 nm on polyimide film

For the thinner seed layers, 8 nm (b) and 16 nm (c), ZnO grains and the underlying substrate were visible. As the seed layer became thicker, 40 nm (d), 80 nm (e), and 160 nm (f), ZnO grains became more distinct and were observed more clearly with greater contrast. These images indicate that ZnO grains are uniformly distributed on the substrate surface regardless film thicknesses in the range of 8 nm to 160 nm. The diameter of the grains was approximately 5 nm. The influence of seed layer thickness on the microstructure of the grown ZnO nanorods was also investigated as shown in figure 6.4. Most ZnO nanorods appear to grow vertically on the ZnO seeded polyimide films regardless of the seed layer thickness. No noticeable morphological difference was observed for the ZnO nanorods as a function of seed layer thickness. It has been reported that the density of nanostructured ZnO does not critically depend on the thickness of the seed layer if the seed layers are thick enough to form a continuous ZnO film [25]. Once the substrate is uniformly covered with a seeding ZnO layer, no additional nuclei for the promotion of ZnO nanorod growth may be observed. The strongest influence on the morphology of the ZnO nanorods was the growth conditions for nanorod formation. The length, density, and diameter of the ZnO nanorods continuously increased with increasing growth time. As will be discussed in next section, the height of ZnO nanorods has an approximately linear relationship with the growth time for our experimental conditions.

6.3.3 Ethanol sensing properties

The two-wire resistance of the ZnO thin film and nanorod sensors as a function of the thin film (i.e. seed layer) thickness was measured across the platinum electrodes in both synthetic air and 100 ppm ethanol environments. The substrate temperature was held at 300 ℃.

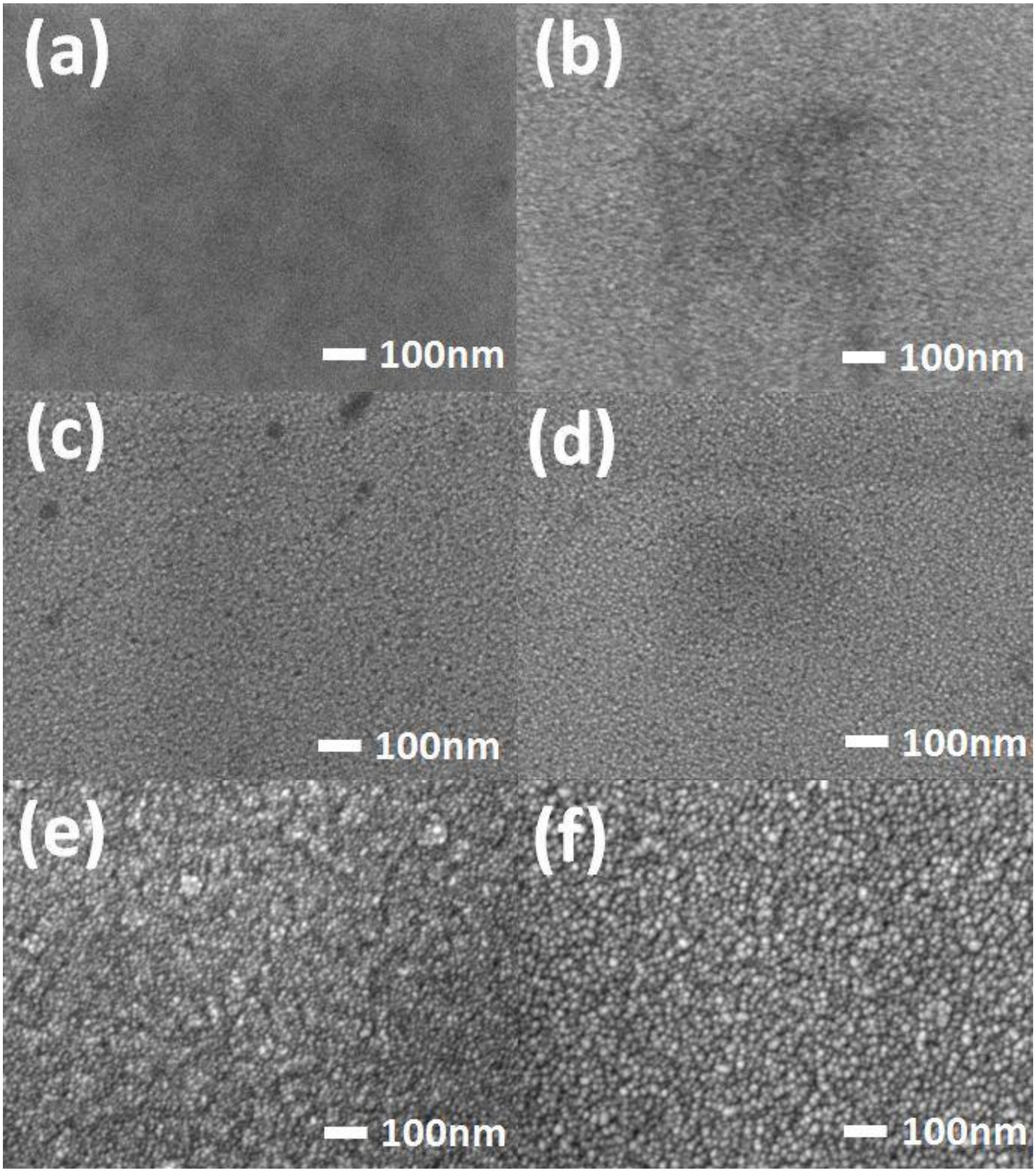

Figure 6.3 SEM pictures of rf sputtered ZnO seed layers varying thicknesses with (a) 0 nm (silicon dioxide surface), (b) 8 nm, (c) 16 nm, (d) 40 nm, (e) 80 nm, (f) 160 nm on the substrates

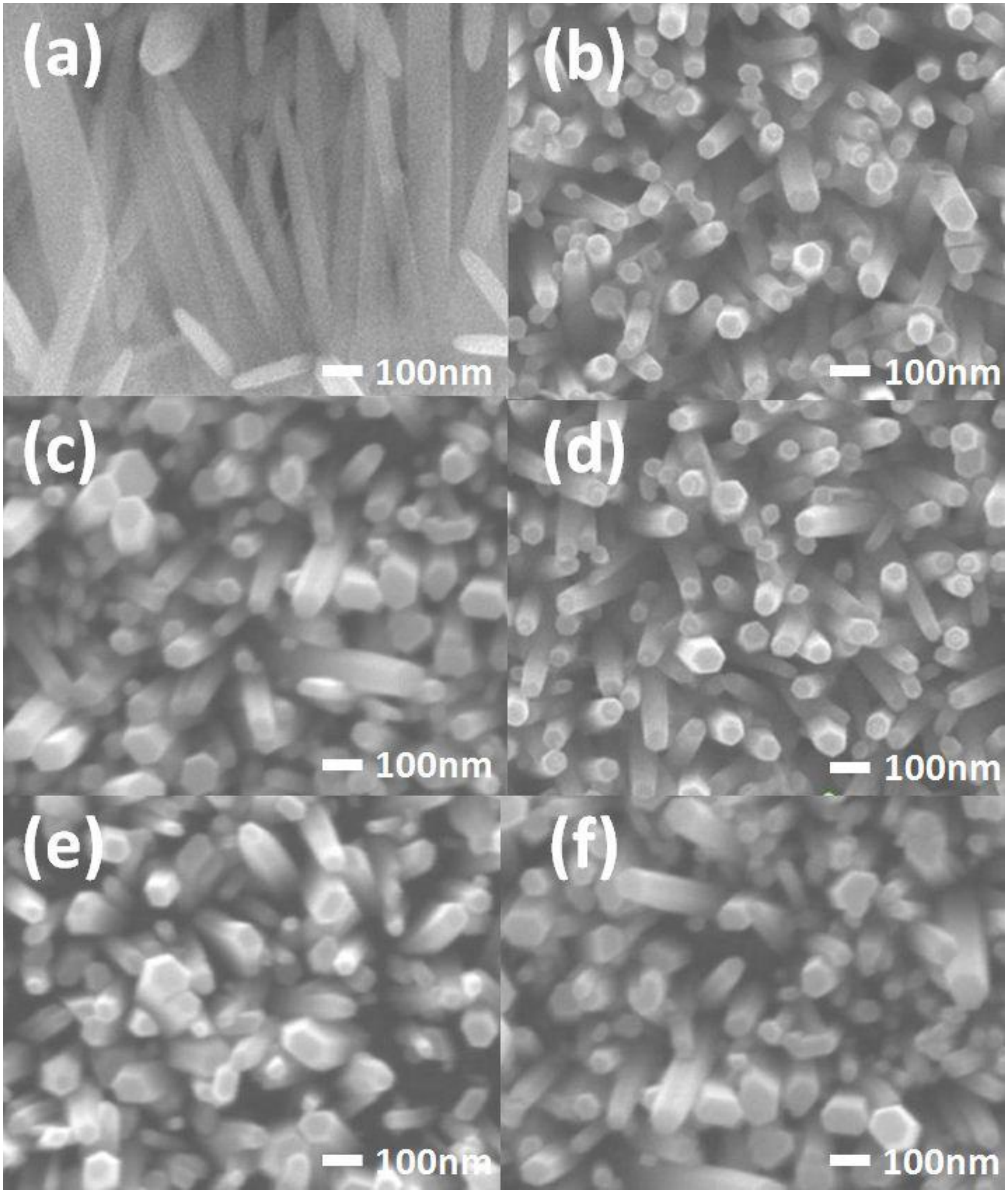

Figure 6.4 SEM pictures of surface of ZnO nanorods grown on (a) bare substrate (no seed layer) and varying thicknesses of seed layers (b) 8 nm (c) 16 nm, (d) 40 nm, (e) 80 nm, (f) 160 nm on polyimide film

The resistance was recorded once the signal stabilized to within ±1% for at least 30 min. Sensitivity was defined as the ratio of resistance in air (R_{air}) to the resistance in ethanol (R_{gas}): $S=R_{air}/R_{gas}$. In synthetic air, the resistance of the ZnO thin films dropped significantly as the film thickness increased as shown in figure 6.5. The resistance fell below 200 MΩ when the thickness of the seed layer exceeded 40 nm. Such a resistance change with film thickness is commonly observed in oxide thin films. Generally, the higher resistance of thinner films is due to decreased mobility and concentration of charge carriers as the thickness decreases [38-42].

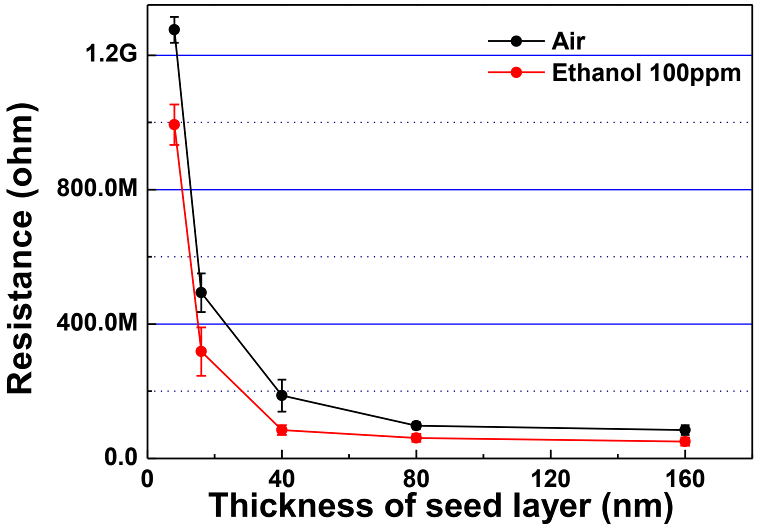

Figure 6.5 Initial resistance of rf sputtered ZnO thin film sensors on polyimide film as a function of thickness of seed layer under synthetic air and 100 ppm of ethanol at 300 ℃

The resistance in synthetic air of ZnO nanorod sensors grown on different thickness seed layers was also measured as shown in figure 6.6. After ZnO nanorod growth, the resistance is similar irrespective of the seed layer thickness, as expected. Most resistance values for the ZnO nanorod sensors were below 500 kΩ regardless of the seed layer thickness. ZnO nanorod sensor resistance was primarily a consequence of the increased surface area of the nanorods allowing greater adsorption of oxygen molecules thereby increasing charge carrier concentration over the ZnO thin film [43].

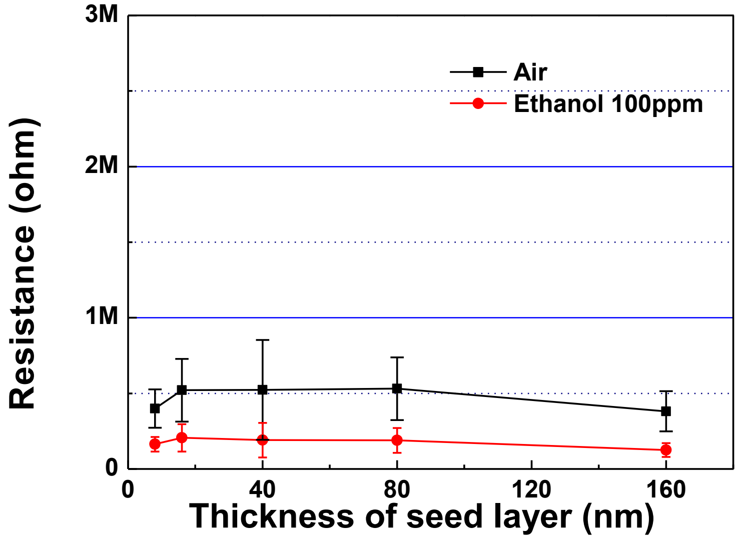

Figure 6.6 Initial resistance of a ZnO nanorod sensors as a function of thickness of seed layer under synthetic air and 100 ppm of ethanol at 300 °C

In 100 ppm ethanol, the ZnO sensors showed a similar, though lower magnitude, response as in synthetic air. For the ZnO thin film sensors, the sensitivities to 100 ppm ethanol gas ranged from 1.29 for 8 nm film thickness to 2.23 for 40 nm film thickness as shown in figure 6.7. The highest sensitivity for the ZnO thin film sensor was observed at the 40 nm thickness, which is near the Debye length for the ZnO thin film at 300 °C [44].

Below 40 nm, ZnO thin film showed decreased sensitivity. This result may be due to the reduced number of gas reaction sites on the thin film when the film thickness becomes similar in scale to the grain size. In addition, reduced mobility of the charge carriers may occur when the film is thinner than the Debye length. Similar scaling effects on gas sensing properties are reported in the literature [29, 38-89].

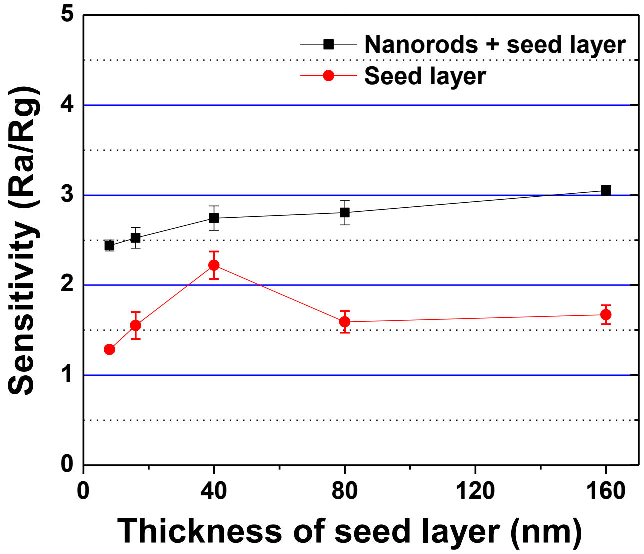

Figure 6.7 Comparison between ZnO thin film sensor and ZnO nanorods sensor for the detection of 100 ppm of ethanol at 300 °C as a function of thickness of seed layer

For the ZnO nanorod sensors, grown on different thickness seed layers, the sensitivity to 100 ppm ethanol exhibits only a slight monotonic increase in sensitivity with film thickness as shown in figure 6.7. Overall, the sensitivity difference was less than 10% over the entire range of seed layer thicknesses investigated. It appears that the seed layer thickness for the growth of ZnO nanorods does not noticeably influence the gas sensing properties. Similar in reasoning for the ZnO nanorod response in air, it can be deduced that charge carriers responsible for ethanol gas sensing reactions are derived principally from ZnO nanorods. Therefore, the thickness of the seed layer does not influence gas sensing properties of the ZnO nanorod structure.

To determine the detection limit of ZnO thin film and nanorod sensors, sensitivities were obtained as a function of ethanol gas concentration. The substrate temperature was held at 300 °C. In figure 6.8, the resistance profile of a 40 nm thick ZnO thin film sensor, which displayed the highest sensitivity based on the previous measurements, is shown as a function of the ethanol gas concentration from 10 to 200 ppm. Calculating sensitivity as before (R_a/R_g), the sensitivity for the 40 nm thin film sensor ranged from 1.57 for 10 ppm of ethanol to 2.98 for 200 ppm.

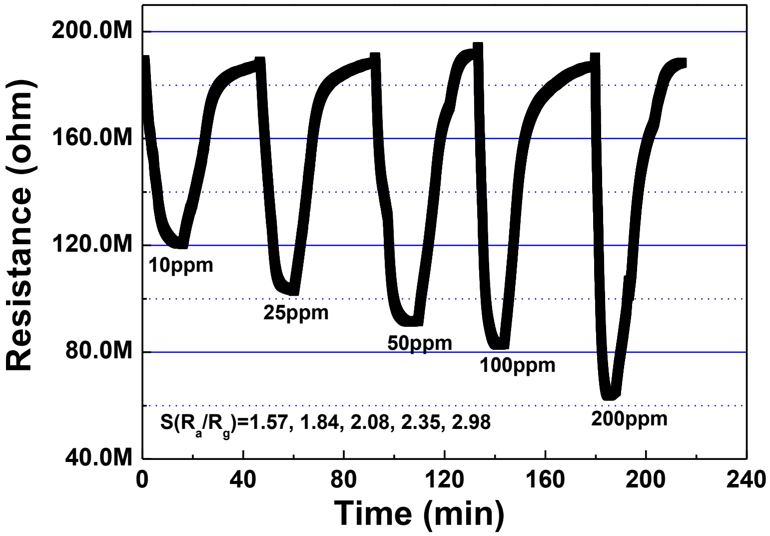

Figure 6.8 Resistance profile of 40 nm thick ZnO thin film sensor in detection of ethanol as a function of ethanol concentration (10 ppm to 200 ppm) at 300 ℃

The resistance profile of a ZnO nanorod sensor, grown on 40nm thick seed layer, was also measured as shown in figure 6.9. Compared to the thin film sensor, sensitivity improved to 1.78 for 10 ppm and 3.85 for 200 ppm ethanol, respectively, as shown in figure 6.10. However, in our study, ZnO nanorods sensors revealed limited enhancement of sensitivity compared with the thin film sensor in contrast to other reports in the literature. Chou et al. reported that an Al doped ZnO sputtered film showed approximately 2.7 in sensitivity value from 100 ppm of ethanol at 250 ℃ [45]. Feng et al. fabricated a ZnO nanoflowers that had a diameter of individual rods of around 150 nm giving a sensitivity of 14.6 for 100ppm of ethanol at 300 ℃ [46].

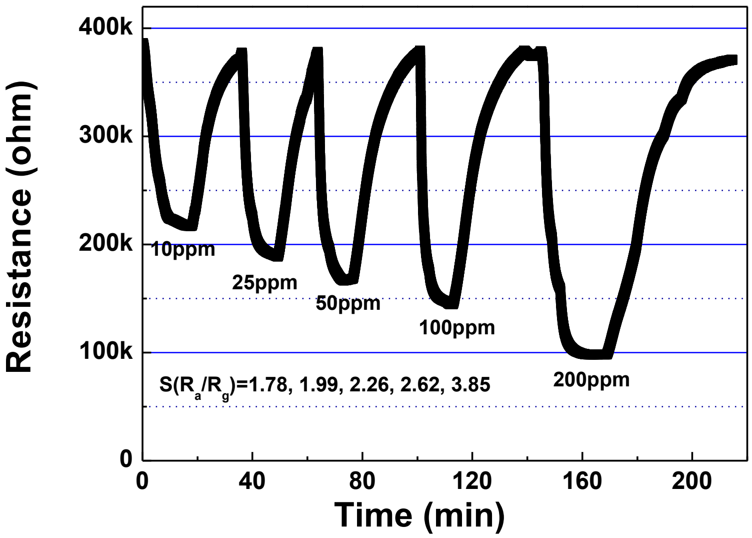

Figure 6.9 Resistance profile of ZnO nanorod sensor with 40 nm thick seed layer in detection of ethanol as a function of ethanol concentration (10 ppm to 200 ppm) at 300 °C

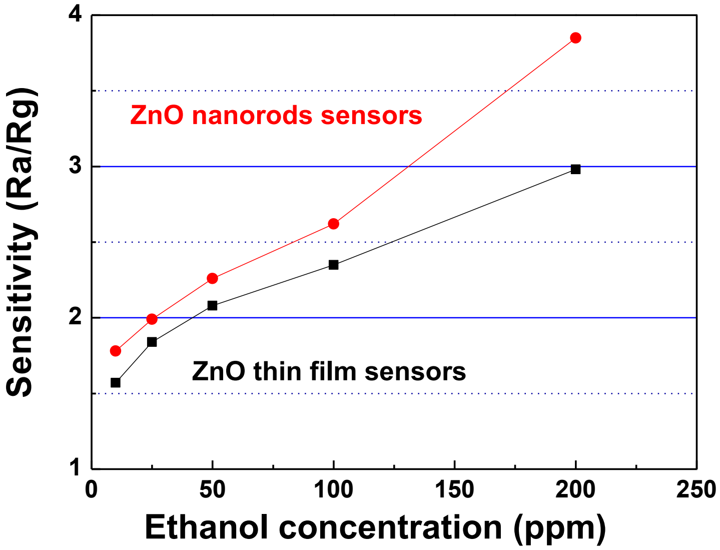

Figure 6.10 Calculated sensitivities are shown corresponding to each ethanol concentration from 10 to 200 ppm for ZnO nanorods sensors and ZnO thin film sensors, respectively

Sonochemically synthesized ZnO nanotube-based sensors were also reported with a sensitivity of approximately 14.6 for the detection of 100 ppm of ethanol at 300 °C [47]. In comparison with other reported sensitivities for ethanol gas, our nanorod sensors did not show substantial improvement in sensitivity while the sensitivity of our thin film sensors was comparable. Due to this point, it is assumed that control of nanostructure geometry may be more influential on sensing properties rather than the thickness of seed layer. Thus the geometric dimension of ZnO nanorods was investigated further.

First, ZnO nanorod density was modulated by controlling the growth time. Seed layer thickness was held constant at 80 nm and the nanorod growth time varied from 1 to 4 hr with 1 hr intervals. Qualitatively, both the density and diameter of the nanorods increase with growth time as shown in the FE-SEM micrographs of figure 6.11. The length of the ZnO nanorods was measured as a function of growth time by examining cross sections of the ZnO coatings with FE-SEM and the results shown in figure 6.12. After 1 hr growth, approximately 400 nm long nanorods were obtained and the nanorod length increased to around 1.5 μm after 4 hr growth. For our experimental conditions, the ZnO nanorods length showed an almost linear relationship with growth time.

The resistance of ZnO nanorods grown on an 80 nm thick seed layer over a 4 hr period was also measured and the results shown in figure 6.13. The environment was synthetic air and the substrate temperature was 300 °C. The initial resistance of a bare 80 nm ZnO thin film sensor was above 120 MΩ. The resistance decreased as ZnO nanorod growth time increased. The ethanol gas sensing properties of these ZnO nanorod sensors were also characterized and the results shown in figure 6.14. Enhanced sensitivity to ethanol with increasing nanorod growth time was observed. In 100 ppm ethanol, the sensitivity of a bare ZnO seed layer, before the growth of nanorods, showed a sensitivity of 1.59 and it increased to 2.75 for the nanorods grown for 4 hours, nearly a 73% increase. The nanorod volumetric parameters density, diameter, and length modulate the charge carrier density and thus directly influence the sensitivity of the ZnO nanorod sensor. Both initial resistance and the resistance change clearly depend on these volumetric parameters of the ZnO nanorod sensors. Therefore, it appears that the charge carrier density rather than the seed layer thickness is the primary factor determining the sensing properties of the ZnO nanorod sensors.

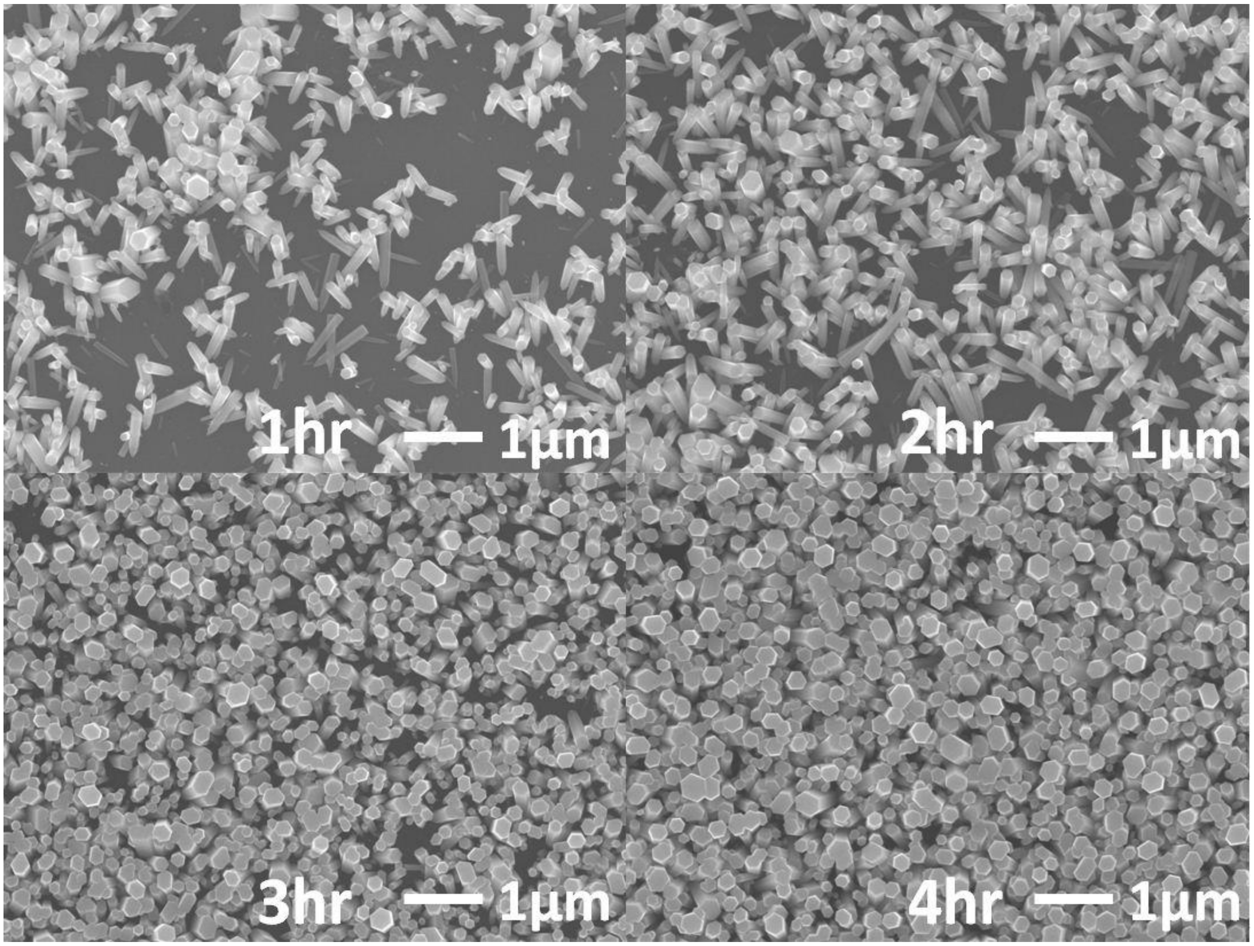

Figure 6.11 SEM pictures of surface of ZnO nanorods grown on polyimide film with 80 nm thick seed layer as a function of growth time from 1 hr to 4 hr

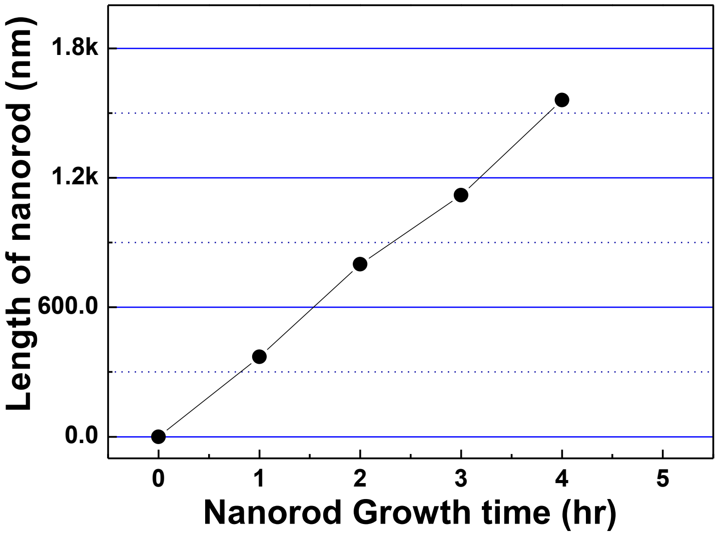

Figure 6.12 Average length of ZnO nanorod grown on polyimide film with 80 nm thick seed layer as a function of growth time

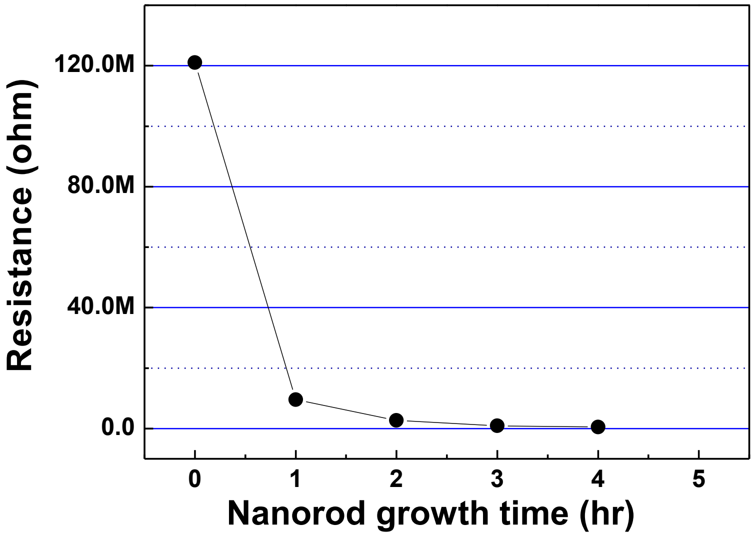

Figure 6.13 Initial resistances of ZnO nanorod sensors on polyimide film as a function of growth time

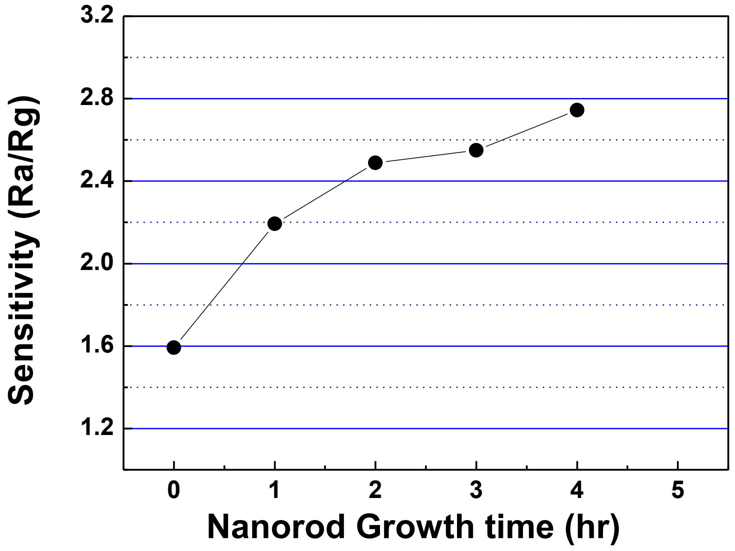

Figure 6.14 Sensitivity of ZnO nanorod sensors in detection of 100 ppm of ethanol as a function of growth time

6.3.4 Sensing mechanism

To validate the strong effect of the nanorod volumetric parameters on the gas sensitivity, a quantitative equation to explain the gas sensing mechanisms of ZnO-based sensors was developed. In developing a gas sensing mechanism, most open literature report a relationship between the sensitivity and gas concentration [48]. Many modifications to this type of equation have been proposed for a more accurate prediction and corroboration of experimental data [49-50]. There has not been, however, any attempt to quantitatively isolate and describe the effects of the seed layer and nanorods structure on the gas sensitivity. To explain the individual contributions of the seed layer and nanorods, an equation to describe the sensitivity, *S*, as a function of gas concentration can start with eq. (1) [51]:

$$S = aC^{b} + 1 \qquad \text{.. (1)}$$

where C is the ethanol concentration, b is a charge parameter for the oxygen ion species (1 for O^-, 0.5 for O^{2-}) and a is given by:

$$a = e \cdot \left(\frac{D^2}{(D - 2L_d)^2}\right) \qquad \text{.. (2)}$$

where D is the diameter of nanorod or thickness of film, L_d is the Debye length of ZnO, and e is a material constant, $e = \frac{1}{n_o}(\sigma_o * \Phi)^b$. Here, n_o and σ_o, are electron concentration under synthetic air and number of chemisorbed oxygen ions per unit area, respectively. Φ is the ratio of surface area per volume of material.

The constant a can be separated into two parts: the contributions from seed layer, a_1, and the contributions from the nanorods, a_2,

$$a_1 = \alpha \cdot (\Phi_{seed})^b \left(\frac{T_{seed}{}^2}{(T_{seed} - 2L_d)^2}\right), \qquad a_2 = \alpha \cdot (\Phi_{nanorods})^b \left(\frac{D_{nanorod}{}^2}{(D_{nanorod} - 2L_d)^2}\right) \qquad \text{............. (3)}$$

where α is a material constant, $\alpha = \frac{1}{n_o}(\sigma_o)^b$.

Then for the ZnO seed layer, eq. (1) can be expressed as

$$\log(S - 1) = \log a_1 + b \log C \qquad \text{………..…………………...… (4)}$$

and for ZnO nanorods grown on a seed layer, eq. (1) becomes

$$\log(S-1)=\log(a_1+a_2)+b\log C \quad \text{……………..………..... (5)}$$

The surface area to volume of the seed layer and nanorods was calculated for our experimental conditions giving: $\Phi_{seed}=2.500\times10^{7}m^{-1}$ and $\Phi_{nanorods}=4.686\times10^{7}m^{-1}$.

When the thickness of the seed layer (T_{seed}) is 40 nm and $2L_d$ and b are assumed to about 30 nm and 0.5, respectively. For ZnO nanorods grown on the seed layer, it is also assumed that $2L_d$ is approximately 30 nm and b is 0.5. The average diameter of ZnO nanorod ($D_{nanorod}$) is 100 nm. a_1 and a_2 are calculated to be 0.1600 and 0.1879, respectively. When the constant α is $2.0X10^{-6}$, the sensitivity of ZnO seed layer becomes

$$\log(S-1)=\log[0.16]+0.5\log C \quad \text{…..…............................ (6)}$$

Then, ZnO nanorods on seed layer becomes

$$\log(S-1)=\log[0.1879]+0.5\log C \quad \text{.................................... (7)}$$

Our experimental results were compared with these derived equations and the results are shown in figure 6.15. The calculated sensitivity values from eq. (6) and (7) appear to closely match to the experimentally measured sensitivities. Since the derived equations mainly consider geometrical dimensions of the ZnO sensor structure, i.e. the change of surface area and the diameter of the nanorod, the contribution from increased surface area of nanorods can be responsible for the enhanced sensitivity of ZnO nanorod sensor. Sensitivity can be maximized when the nanorod diameter is about twice the Debye length corresponding to the surface area contribution from the nanorods when the diameter of nanorods is close to $2L_d$ (eq. (3)).

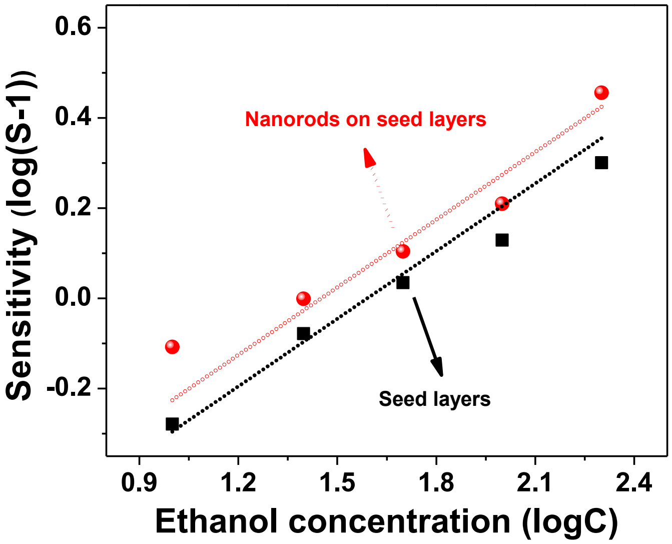

Figure 6.15 Sensitivity in log scale of 40 nm ZnO thin film sensor and ZnO nanorod sensor with 40 nm thick seed layer as a function of ethanol concentration in log scale (10 ppm to 100 ppm) at 300 °C (Solid dot line: calculated sensitivity of ZnO nanorods on seed layers or ZnO seed layer. Marker: measured sensitivity of ZnO nanorods on seed layers or ZnO seed layers.)

6.4 Summary and Conclusions

The effects of seed layer thickness on the morphology and gas sensing properties of ZnO nanorods were investigated. ZnO nanorods were grown on ZnO seed layers, i.e. thin films deposited on flexible polyimide substrates. The thickness of the seed layer varied from 8 nm to

160 nm, and ZnO nanorods were grown on seed layers of different thicknesses. Although the seed layers showed distinct differences in microstructure and gas sensing properties, the results obtained with ZnO nanorods on various seed layer thicknesses did not present any structural changes or significant variation of the gas sensing properties. No effect of seed layer thickness on gas sensitivity of ZnO nanorods was observed, which indicates that the charge carrier density from ZnO nanorods is primarily responsible for gas sensing properties. A quantitative equation to predict the ethanol sensitivity of ZnO nanorod and thin film sensors confirms the dominant influence of the increased surface area to volume ratio for ZnO nanorods on gas detection. The results suggest more emphasis should be placed on modulation of the nanostructure geometry for gas sensing applications.

References

1. Z. Tao, X. Yu, X. Fei, J. Liu, Y. Zhao, H. Wu, G. Yang, S. Yang, andL. Yang, "Synthesis and optical properties of halogen-doped ZnO phosphor," *Materials Letters,* **62**[17-18] 3018-20 (2008).
2. E. Galoppini, J. Rochford, H. Chen, G. Saraf, Y. Lu, A. Hagfeldt, andG. Boschloo, "Fast Electron Transport in Metal Organic Vapor Deposition Grown Dye-sensitized ZnO Nanorod Solar Cells," *The Journal of Physical Chemistry B,* **110**[33] 16159-61 (2006).
3. S. J. An, "Enhanced light output of GaN-based light-emitting diodes with ZnO nanorod arrays," *Appl. Phys. Lett.*, **92**[12] 121108 (2008).
4. S.-K. Kim and J.-Y. Son, "Epitaxial ZnO Thin Films for the Application of Ethanol Gas Sensor: Thickness and Al-Doping Effects," *Electrochemical and Solid-State Letters,* **12**[2] J17-J19 (2009).

5. L. C. Tien, "Hydrogen sensing at room temperature with Pt-coated ZnO thin films and nanorods," *Appl. Phys. Lett.*, **87**[22] 222106 (2005).
6. C. Liewhiran and S. Phanichphant, "Influence of Thickness on Ethanol Sensing Characteristics of Doctor-bladed Thick Film from Flame-made ZnO Nanoparticles," *Sensors,* **7**[2] 185-201 (2007).
7. K. Black, A. C. Jones, P. R. Chalker, J. M. Gaskell, R. T. Murray, T. B. Joyce, andS. A. Rushworth, "MOCVD of ZnO thin films for potential use as compliant layers for GaN on Si," *Journal of Crystal Growth,* **310**[5] 1010-14 (2008).
8. W. Lee, M.-C. Jeong, andJ.-M. Myoung, "Catalyst-free growth of ZnO nanowires by metal-organic chemical vapour deposition (MOCVD) and thermal evaporation," *Acta Materialia,* **52**[13] 3949-57 (2004).
9. D. C. Kim, B. H. Kong, S. O. Jun, H. K. Cho, D. J. Park, andJ. Y. Lee, "Pressure dependence and micro-hillock formation of ZnO thin films grown at low temperature by MOCVD," *Thin Solid Films,* **516**[16] 5562-66 (2008).
10. S. Yoon, D. Liu, D. Shen, M. Park, andD.-J. Kim, "Effect of chelating agents on the preferred orientation of ZnO films by sol-gel process," *Journal of Materials Science,* **43**[18] 6177-81 (2008).
11. M. Ohyama, H. Kouzuka, andT. Yoko, "Sol-gel preparation of ZnO films with extremely preferred orientation along (002) plane from zinc acetate solution," *Thin Solid Films,* **306**[1] 78-85 (1997).
12. J.-H. Lee and B.-O. Park, "Transparent conducting ZnO:Al, In and Sn thin films deposited by the sol–gel method," *Thin Solid Films,* **426**[1-2] 94-99 (2003).

13. W. Wang, Z. Li, L. Liu, H. Zhang, W. Zheng, Y. Wang, H. Huang, Z. Wang, andC. Wang, "Humidity sensor based on LiCl-doped ZnO electrospun nanofibers," *Sensors and Actuators B: Chemical*, **141**[2] 404-09 (2009).
14. W. Wang, Z. Li, W. Zheng, H. Huang, C. Wang, andJ. Sun, "Cr2O3-sensitized ZnO electrospun nanofibers based ethanol detectors," *Sensors and Actuators B: Chemical,* **143**[2] 754-58 (2010).
15. Z. Wang, X.-f. Qian, J. Yin, andZ.-k. Zhu, "Large-Scale Fabrication of Tower-like, Flower-like, and Tube-like ZnO Arrays by a Simple Chemical Solution Route," *Langmuir,* **20**[8] 3441-48 (2004).
16. H. Zhang and et al., "Arrays of ZnO nanowires fabricated by a simple chemical solution route," *Nanotechnology,* **14**[4] 423 (2003).
17. J. Huang, Y. Wu, C. Gu, M. Zhai, K. Yu, M. Yang, andJ. Liu, "Large-scale synthesis of flowerlike ZnO nanostructure by a simple chemical solution route and its gas-sensing property," *Sensors and Actuators B: Chemical,* **146**[1] 206-12 (2010).
18. L. E. Greene, M. Law, J. Goldberger, F. Kim, J. C. Johnson, Y. Zhang, R. J. Saykally, andP. Yang, "Low-Temperature Wafer-Scale Production of ZnO Nanowire Arrays," *Angewandte Chemie International Edition,* **42**[26] 3031-34 (2003).
19. H. Ahn, J.-H. Park, S.-B. Kim, S. H. Jee, Y. S. Yoon, andD.-J. Kim, "Vertically Aligned ZnO Nanorod Sensor on Flexible Substrate for Ethanol Gas Monitoring," *Electrochemical and Solid-State Letters*, **13**[11] J125-J28 (2010).
20. A. E. Rakhshani, "Thin ZnO films prepared by chemical solution deposition on glass and flexible conducting substrate," *Applied Physics A: Materials Science & Processing,* **81**[7] 1497-502 (2005).

21. J. Cheng, X. Zhang, andZ. Luo, "Aligned ZnO nanorod arrays fabricated on Si substrate by solution deposition," *Physica E: Low-dimensional Systems and Nanostructures*, **31**[2] 235-39 (2006).
22. L. W. Ji, "Ultraviolet photodetectors based on selectively grown ZnO nanorod arrays," *Appl. Phys. Lett.*, **94**[20] 203106 (2009).
23. W.-S. Wang and et al., "A ZnO nanorod-based SAW oscillator system for ultraviolet detection," *Nanotechnology*, **20**[13] 135503 (2009).
24. J. Joo, D. Lee, M. Yoo, andS. Jeon, "ZnO nanorod-coated quartz crystals as self-cleaning thiol sensors for natural gas fuel cells," *Sensors and Actuators B: Chemical*, **138**[2] 485-90 (2009).
25. M. Guo, P. Diao, andS. Cai, "Hydrothermal growth of perpendicularly oriented ZnO nanorod array film and its photoelectrochemical properties," *Applied Surface Science*, **249**[1-4] 71-75 (2005).
26. A. S. Gonçalves, M. R. Davolos, andA. F. Nogueira, "Efficient Dye-Sensitized Solar Cells Based on the Combination of ZnO Nanorods and Microflowers," *Journal of Nanoscience and Nanotechnology*, **10**[10] (2010).
27. H. Zhang, X. Li, andG. Chen, "Fabrication of Photoelectrode Materials Electrochemistry for the Environment," pp. 473-513. in**.** Edited by C. Comninellis and G. Chen. Springer New York, 2010.
28. X. Yu, J. Ma, F. Ji, Y. Wang, C. Cheng, andH. Ma, "Thickness dependence of properties of ZnO:Ga films deposited by rf magnetron sputtering," *Applied Surface Science*, **245**[1-4] 310-15 (2005).

29. X. Hao, J. Ma, D. Zhang, T. Yang, H. Ma, Y. Yang, C. Cheng, andJ. Huang, "Thickness dependence of structural, optical and electrical properties of ZnO:Al films prepared on flexible substrates," *Applied Surface Science,* **183**[1-2] 137-42 (2001).
30. S. Mridha and D. Basak, "Thickness dependent photoconducting properties of ZnO films," *Chemical Physics Letters,* **427**[1-3] 62-66 (2006).
31. J. Liu, J. She, S. Deng, J. Chen, andN. Xu, "Ultrathin Seed-Layer for Tuning Density of ZnO Nanowire Arrays and Their Field Emission Characteristics," *Journal of physical chemistry. C, nanomaterials and interfaces* **112**[31] 6 (2008).
32. L. Vayssieres, "Growth of Arrayed Nanorods and Nanowires of ZnO from Aqueous Solutions," *Advanced Materials,* **15**[5] 464-66 (2003).
33. K. H. Kim, K. C. Park, andD. Y. Ma, "Structural, electrical and optical properties of aluminum doped zinc oxide films prepared by radio frequency magnetron sputtering," *Journal of Applied Physics,* **81**[12] 7764-72 (1997).
34. K. Tominaga, M. Kataoka, H. Manabe, T. Ueda, andI. Mori, "Transparent ZnO:Al films prepared by co-sputtering of ZnO:Al with either a Zn or an Al target," *Thin Solid Films,* **290-291** 84-87 (1996).
35. A. C. Lua and J. Su, "Effects of carbonisation on pore evolution and gas permeation properties of carbon membranes from Kapton® polyimide," *Carbon,* **44**[14] 2964-72 (2006).
36. L. E. Greene, M. Law, D. H. Tan, M. Montano, J. Goldberger, G. Somorjai, andP. Yang, "General Route to Vertical ZnO Nanowire Arrays Using Textured ZnO Seeds," *Nano Letters,* **5**[7] 1231-36 (2005).

37. W. I. Park, D. H. Kim, S.-W. Jung, andG.-C. Yi, "Metalorganic vapor-phase epitaxial growth of vertically well-aligned ZnO nanorods," *Applied Physics Letters*, **80**[22] 4232-34 (2002).
38. X. Du and S. M. George, "Thickness dependence of sensor response for CO gas sensing by tin oxide films grown using atomic layer deposition," *Sensors and Actuators B: Chemical*, **135**[1] 152-60 (2008).
39. Y.-S. Choe, "New gas sensing mechanism for SnO2 thin-film gas sensors fabricated by using dual ion beam sputtering," *Sensors and Actuators B: Chemical*, **77**[1-2] 200-08 (2001).
40. X. Yu, J. Ma, F. Ji, Y. Wang, C. Cheng, andH. Ma, "Thickness dependence of properties of ZnO:Ga films deposited by rf magnetron sputtering," *Applied Surface Science*, **245**[1-4] 310-15 (2005).
41. G. G. Mandayo, E. Castaño, F. J. Gracia, A. Cirera, A. Cornet, andJ. R. Morante, "Strategies to enhance the carbon monoxide sensitivity of tin oxide thin films," *Sensors and Actuators B: Chemical*, **95**[1-3] 90-96 (2003).
42. M. Öztas and M. Bedir, "Thickness dependence of structural, electrical and optical properties of sprayed ZnO:Cu films," *Thin Solid Films*, **516**[8] 1703-09 (2008).
43. Y. Zhang, A. Kolmakov, Y. Lilach, andM. Moskovits, "Electronic Control of Chemistry and Catalysis at the Surface of an Individual Tin Oxide Nanowire," *The Journal of Physical Chemistry B*, **109**[5] 1923-29 (2005).
44. J. Goldberger, D. J. Sirbuly, M. Law, andP. Yang, "ZnO Nanowire Transistors," *The Journal of Physical Chemistry B*, **109**[1] 9-14 (2004).

45. S. Chou, L. Teoh, W. Lai, Y. Su, andM. Hon, "ZnO:Al Thin Film Gas Sensor for Detection of Ethanol Vapor," *Sensors,* **6**[10] 1420-27 (2006).
46. P. Feng, Q. Wan, andT. H. Wang, "Contact-controlled sensing properties of flowerlike ZnO nanostructures," *Applied Physics Letters,* **87**[21] 213111 (2005).
47. Y.-J. Chen, C.-L. Zhu, andG. Xiao, "Ethanol sensing characteristics of ambient temperature sonochemically synthesized ZnO nanotubes," *Sensors and Actuators B: Chemical,* **129**[2] 639-42 (2008).
48. D. E. Williams, "Semiconducting oxides as gas-sensitive resistors," *Sensors and Actuators B: Chemical,* **57**[1-3] 1-16 (1999).
49. Q. Yuan, Y.-P. Zhao, L. Li, andT. Wang, "Ab Initio Study of ZnO-Based Gas-Sensing Mechanisms: Surface Reconstruction and Charge Transfer," *The Journal of Physical Chemistry C,* **113**[15] 6107-13 (2009).
50. C. C. Li, Z. F. Du, L. M. Li, H. C. Yu, Q. Wan, andT. H. Wang, "Surface-depletion controlled gas sensing of ZnO nanorods grown at room temperature," *Applied Physics Letters,* **91**[3] 032101 (2007).
51. N. Hongsith, E. Wongrat, T. Kerdcharoen, andS. Choopun, "Sensor response formula for sensor based on ZnO nanostructures," *Sensors and Actuators B: Chemical,* **144**[1] 67-72 (2010).

CHAPTER 7 SYNTHESIS OF ZNO AND SNO$_2$ NANORODS AND TRANSITION METAL DOPING BY ELECTRODEPOSITION

7.1 Introduction

Transition metal ions such as nickel, cobalt, and copper have attracted much interest that those were reported to modulate the electrical and optical properties of ZnO [1]. Doping nickel ions into the ZnO lattice can create the additional acceptor or donor level in the energy band of ZnO. Nickel doped ZnO was observed to have a red shift in the band edge by photoluminescence characterization. Additionally, a band tailing to the lower energy level was combined. Due to these factors, the thickness of the surface depletion layer of ZnO is reduced and therefore, the sensing property of doped ZnO can be enhanced [2]. The photocatalytic effect of transition metal ions was also studied in terms of doping concentration. Choi et al. did a photoluminescence measurement by changing concentrations of various metal ions and it was revealed that photocatalytic effect was dependent on both concentration and type of metal ions [3]. In water splitting by ZnO, an additional donor or acceptor level is created above the valence band edge and under the conduction band edge as a result of creating photo induced electrons or holes due to the unique d-orbital of transition metals [4]. Several technologies to dope transition metal ions into ZnO efficiently have been tried. Large-scale nickel was doped into ZnO nanowire arrays by using a metal vapor vacuum arc source doping method to modify the electrical conductivity of pure ZnO nanowires [5]. In this method, $2\times10^{17}\text{cm}^{-2}$ of nickel ions were spread on the vertically aligned nanowires with a 5° angle in the similar way of sputtering as shown in figure 7.1. Post annealing at 950 ℃ for 2hr was followed in oxygen ambient to reduce the physically induced defects during doping. From the photoluminescence and electrical conductivity measurements, obvious red shift and increased conductivity were observed [5]. However, it requires post annealing process at high temperature to fairly distribute nickel ions, which can limit its applications and might cause structural deformation.

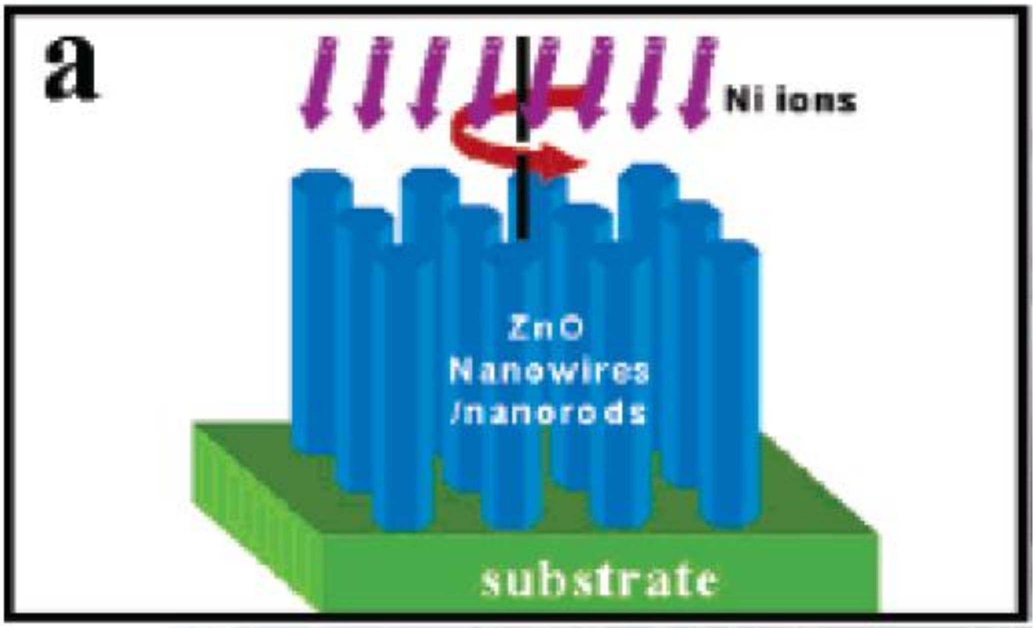

Figure 7.1 schematic diagram of metal vapor vacuum arc source doping method [5]

Nickel, copper, and cadmium were doped on ZnO thin films by Gonzalez et al using SILAR (Successive Ion Layer Adsorption and Reaction) method [6]. In this study, $ZnSO_4$ solution with $NH_4(OH)$ were prepared by adding nickel chloride, copper chloride, and cadmium chloride, respectively. One immersion of glass substrate in a heated solution to 95 ℃ could deposit approximately 25Å thin film and repeated continuously to obtain the target thickness. Post annealing was performed at 450 ℃ for 2hr In case of nickel and copper, initial amount of elements were observed to comparably be doped in ZnO films. Cadmium, however, was rarely detected in XRF characterization due to a size difference in ionic radius between zinc and cadmium. Although this method could dope copper and nickel ions, its deposition rate is very slow and also required post annealing treatment to enhance the influence of transition metal ions.

In terms of processing temperature, low temperature chemical solution method has advantages either in using various substrates or preventing unexpected structural defect at economic costs. Doping of transition metal ions in aqueous solutions were studied by simply adding raw materials in forms of chloride or nitrate. Mn and Co were doped into ZnO nanorods in aqueous solution by panigrahy et al. [7]. 5 mol% of Mn and Co were mixed with zinc salts, but only 1 to 2 at% of Mn and Co were observed from ZnO nanorods. Additionally, shifts in both XRD and Raman studies revealed that it was induced a lattice distortion from the doping.
However, transition metal ions in aqueous solution prefer to stay in a solution as aquo complex rather than incorporating into zinc lattices [8].

To overcome this preference of transition metal ions, electric potential to favor growth of incorporation of ions on the substrate was applied. Cui et al [9] suggested an electrodeposition method to dope transition metal ions, nickel and cobalt in aqueous solution for the first time in 2005. Less than 3 at% of nickel and cobalt were successfully doped into ZnO nanowire arrays during the synthesis without a significant shape change. -0.8V negative potential was applied on a silicon substrate using gold wires. Initial concentration of cobalt and nickel in zinc nitrate solution was 2 mol%, respectively. From the EDS study, similar concentrations of nickel and cobalt were detected from ZnO nanowires to have 1.7 and 2.2 at%, respectively with maintaining aligned ZnO nanowires. From these results, dc filed can be a dominant driving force to dope transition metal ions into ZnO nanostructure in aqueous solution.

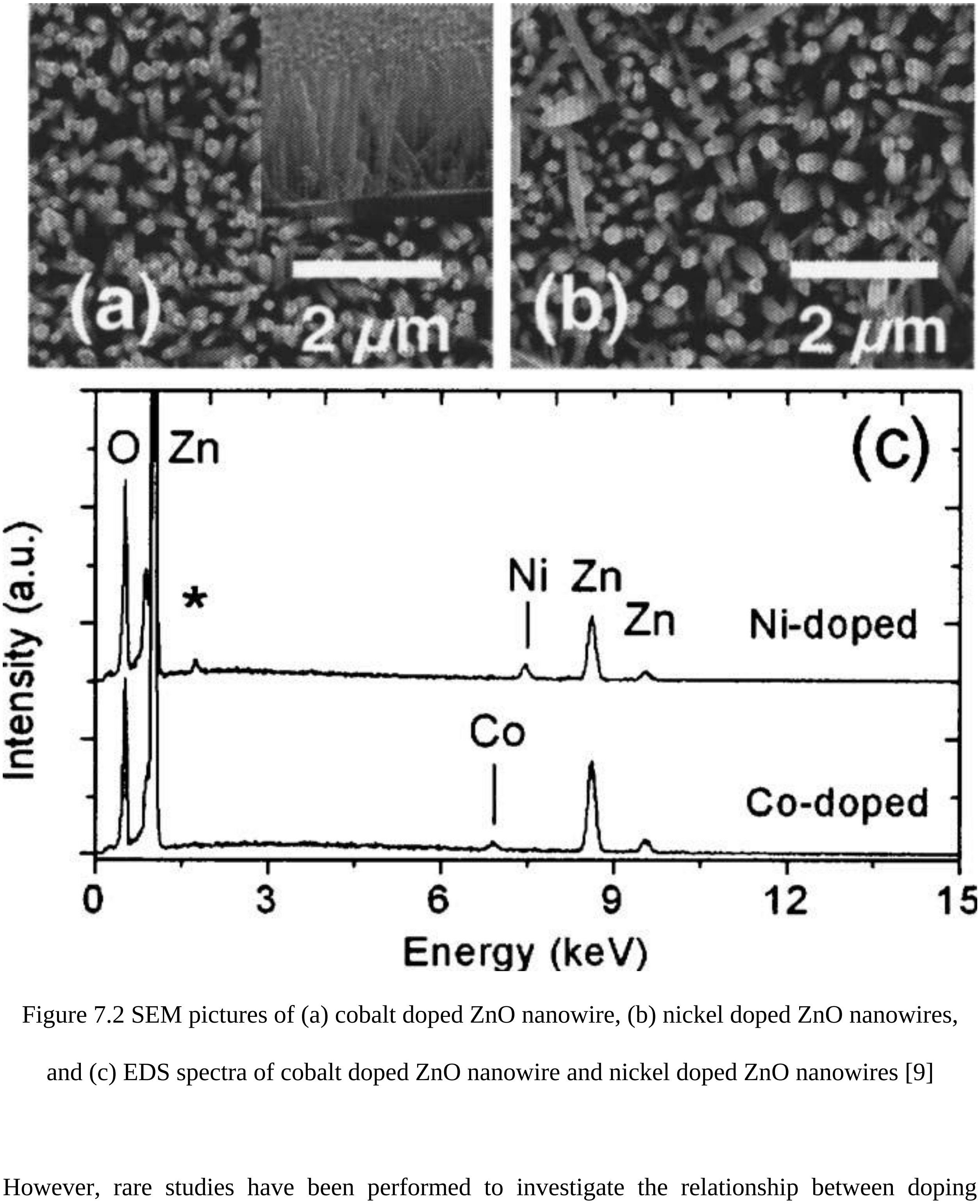

Figure 7.2 SEM pictures of (a) cobalt doped ZnO nanowire, (b) nickel doped ZnO nanowires, and (c) EDS spectra of cobalt doped ZnO nanowire and nickel doped ZnO nanowires [9]

However, rare studies have been performed to investigate the relationship between doping concentration and structural change of ZnO in aqueous chemical solution method. Additionally, voltage dependence of allowable doping concentration in ZnO nanostructure is not studied yet.

In this chapter, structural change depending on applied dc voltage is studied by FE-SEM and XRD in terms of geometry of ZnO nanorods. Limit of the amount of incorporated transition metal ions, nickel and cobalt, according to applied voltage were studied by FE-SEM and EDS. Sensing property dependence on structure and doping concentration of transition metal doped ZnO nanorods will be discussed in next chapter.

7.2 Experiment

As explained in previous chapter, polyimide Cirlex® films were cleaned with acetone to remove the dust and residual grease. Cleaned surface was dried using pure nitrogen gas. First, 100nm thick platinum was coated by dc sputtering with stainless steel shadow mask. Another sample was coated without a shadow mask. Pt-coated polyimide films, patterned one and nonpatterned one, were used as anodes to compare the difference on SnO_2 and ZnO nanorods growth. For SnO_2 nanorod growth, SnO_2 thin film was deposited by R.F sputtering as a seed layer under 20:10 ratio of argon to oxygen, which showed the best sensitivity to reducing gases. Expected thickness of sputtered film is 120nm. For the comparison with similar structure of ZnO and SnO_2 nanostructure, this approach was chosen for our study. Following is the details of SnO_2 synthesis.

100ml D.I. water (if 600ml)
0.034g of $SnCl_4.5H_20$ (0.204g)
0.920 of $(NH_2)2CO$ (5.52g)

R.F. sputtered SnO_2 substrate
heating @95 ℃ for 2 days

washing with D.I. water

Figure 7.3 chart flow to growth the SnO_2 nanorods on a sputtered seed layer

For ZnO nanorods growth, 80nm thick ZnO thin films were rf sputtered on both pt-coated films. Stainless steel sheet was used as cathodes. To maintain the distance between anode and cathode to be 1cm, ZnO thin film coated polyimide film as anode was hang on the Teflon bar and stainless steel cathode was located under the samples. Portable dc power supplier (18V/3A, GPS-1830D, Instek) was connected to substrate and stainless steel cathode. DC voltage varied from 1V to 5V to find the optimum voltage to incorporate doping elements into ZnO nanorods. Nickel, cobalt, and copper were mixed to zinc nitrate hexahydrate in the molar ratio of 1 to 10 %. Nickel nitrate hexahydrate, cobalt nitrate hexahydrate (97.7%, Aldrich), and copper nitrate hemi(pentahydrate) were used as source materials. All chemical solutions were stirred for at least 1hr to resolve all chemicals completely.

To fix other parameters influencing geometry of ZnO nanorods, growth time, deposition temperature, and molar ratio of zinc nitrate hexahydrate and HMT were controlled to have same as 4hr, 85 ℃, and 0.01mol, respectively.

7.3 Results and discussion

7.3.1 Synthesis and morphology of SnO_2 nanorods

SnO_2 nanorods were tried to grown on a sputtered SnO_2 thin film. In figure 7.4, both SnO_2 thin films (left) and SnO_2 nanorods (right) were observed by FE-SEM. As shown in figures, dense thin films were deposited on polyimide film and it shows some agglomerated grains which are in somewhat larger size.

On above the thin films, SnO_2 nanorods were grown but it did not grow into nanorods. Initial nucleation on the thin film was observed partially and did not cover the whole areas. It might be due to the problem during deposition in heated water. It was hard to maintain initial amount of water until the end of experiment because water continuously evaporated. So, synthesis was usually performed as stored in autoclave inside the oven. Even if the closed bottle to maintain its water level, other factors such as bottle pressure and growth time was failed to growth the SnO_2 nanorods.

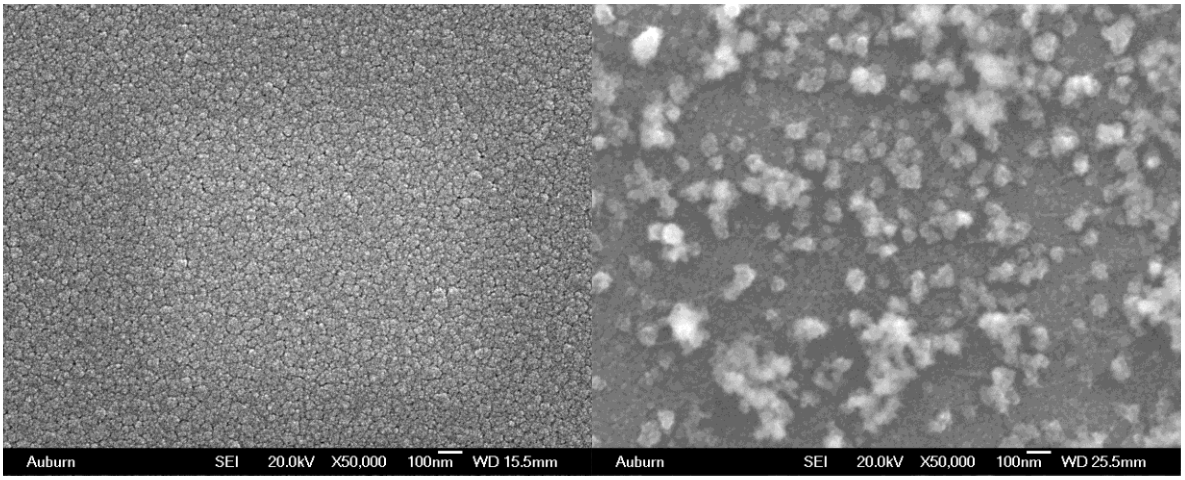

(a) R.F sputtered SnO_2 on PI film (b) SnO_2 nanoparticles on PI film

Figure 7.4 surface morphology of rf sputtered SnO_2 thin film on polyimide film and synthesized SnO_2 nanoparticles on polyimide film. It was intended to grown nanorods but nanoparticles were nucleated instead due to improper process conditions

7.3.2 Morphology of transition metal doped ZnO nanorods grown without dc field

In-situ doping of transition metal ions was tried during growing ZnO nanorods at elevated temperature. Among transition metal ions such as nickel, cobalt, and copper, nickel was selected to test the feasibility of in-situ doping in chemical solution growth. Nickel salts in molar concentration in zinc nitrate solution were varied from 2% to 100% if nickel ions can be incorporated into ZnO nanorods after the growth. As shown in figure 7.1, six pictures represent morphologies of ZnO nanorods taken in vertical direction. Regardless of nickel concentration up 10%, no significant difference in shape of ZnO nanorods was observed.

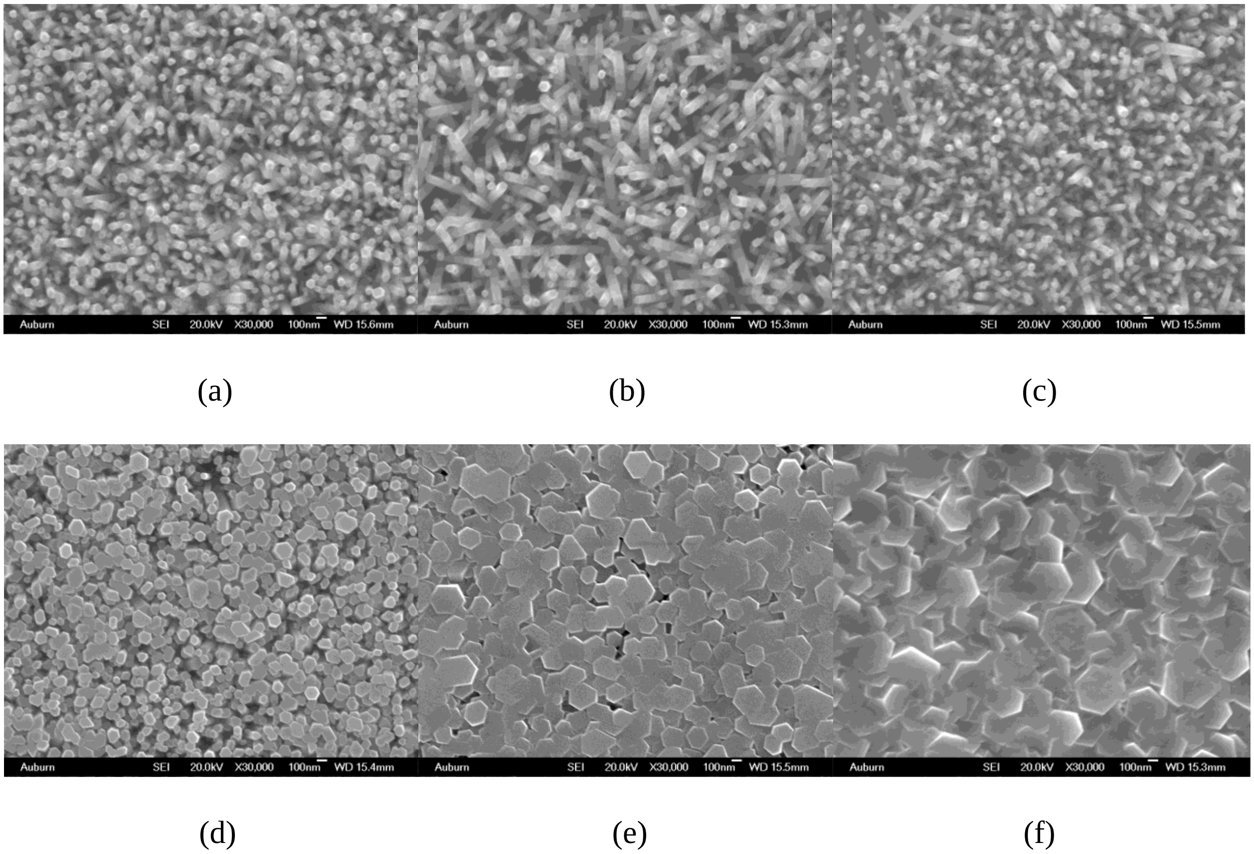

(a) (b) (c)

(d) (e) (f)

Figure 7.5 Surface topography of ZnO nanorods grown in chemical solution with different nickel salts in the molar ratio of zinc salts (a) 2% nickel, (b) 6% nickel, (c) 10% nickel, (d) 30% nickel, (e) 50% nickel, (f) 100% nickel

In cases of high doping concentrations such as 30%, 50%, and 100%, diameter of nanorod increases as concentrations increase. As the diameter become enough large to occupy spaces between nanorods, it was observed that connection between nanorods initiated. It is very similar with the phenomena observed in pure ZnO nanorods growth and based on the same principles.

Chemical balances in between salts including zinc and nickel and HMT is highly deviated from the 1:1 initial ratio. Higher concentration of cat ions than hydroxyl ions from HMT induced increased diameter of nanorods and its density [10]. The feasibility of in-situ doping of transition metal ions under no dc field was characterized compositionally by EDS by measuring the atomic % of doping elements on ZnO nanorods. EDS results are shown in figure 7.5. Specific measured concentrations of nickel are summarized as at % in table 7.1. Maximum doping concentration of nickel, measured in ZnO nanorods were less than 2 at % even the amount of initial concentration of nickel salts varied from 2% to 100% in molar ratio. This means that nickel doping in aqueous solution without external filed is limited to 2 at% due to the nature of transition metal ions preferring to stay in a solution.

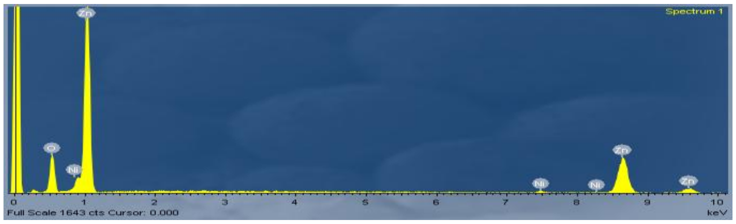

(a) 2% nickel

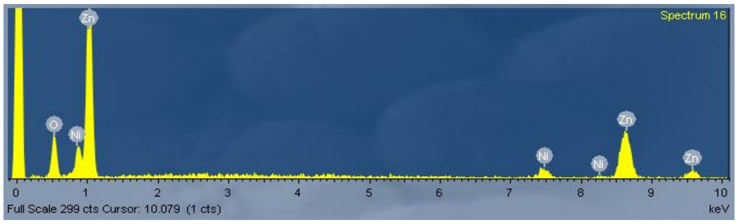

(b) 4% nickel

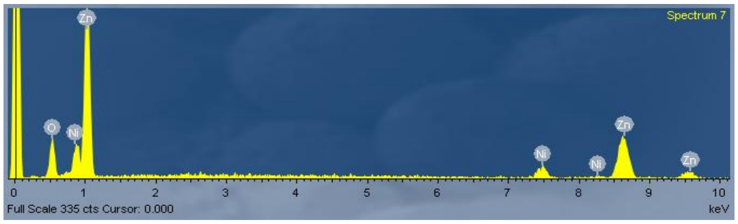

(c) 6% nickel

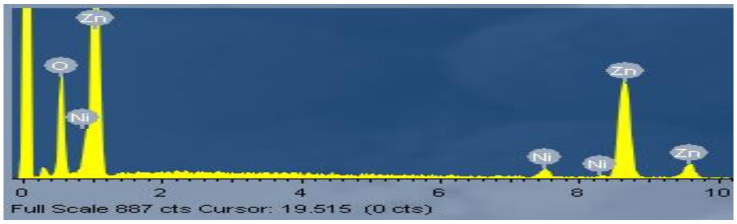

(d) 10% nickel

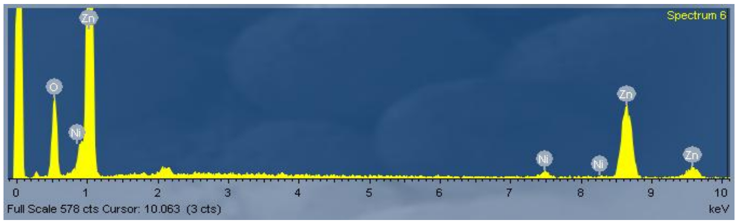

(e) 30% nickel

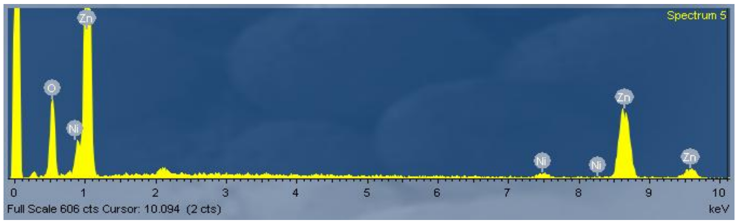

(f) 50% nickel

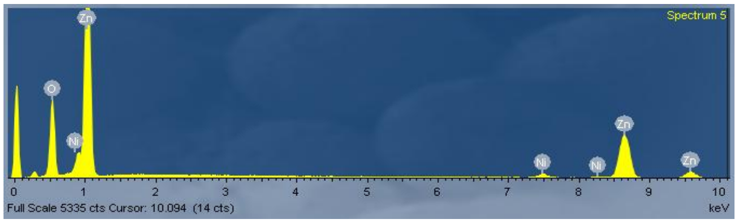

(g) 100% nickel

Figure 7.6 EDS graphs of nickel doped ZnO nanorods grown in aqueous solution without dc field according to six different nickel concentrations

To confirm the existence of doping element in ZnO nanorods, structural characterization was performed by XRD. In figure 7.7, pure ZnO nanorods grown on 80 nm thickness of thin film deposited polyimide substrate was studied first as a standard.

Table 7.1 EDS results of atomic % of dopants in nickel doped ZnO nanorods

Doping Concentration	Nickel (at %)
0.0002mol (2%)	0.91
0.0006 mol(6%)	1.02
0.001 mol(10%)	1.78
0.003 mol(30%)	1.58
0.005 mol(50%)	1.35
0.010 mol(100%)	1.25

The peak representing for (002) plane of ZnO nanorods was observed at around 34.3° in 2 theta angle. Nickel dopants varied from 2% to 10% in molar ratio to zinc salts. Other peaks representing for (100) and (101) were observed at 31.5° and 36.05°, respectively. Relatively intensity of peaks for (100) and (101) planes was much weak compare to that of (002) plane. In cases of nickel doped ZnO nanorods, peak for (002) did not show any noticeable shift in angle. Overall intensities of XRD graphs lowered than that of pure ZnO nanorods. In figure 7.8, XRD results for same experiments, performed for cobalt doped ZnO nanorods, was represented. Similarly with the previous results, no significant differences for cobalt doped ZnO nanorods were observed. Therefore, it can be explained that in-situ doping of transition metal ions in aqueous solution without additional driving force is not a practical method based on the EDS and XRD studies. However, one noticeable point in topography of ZnO nanorods in SEM picture, up to 10% of nickel salt in the molar ratio of zinc salt do not influence the growth of ZnO nanorods in conserving its natural anisotropic property. Based on these factors, in next chapter, dc filed was applied in the synthesis of ZnO nanorods containing various concentrations of nickel and cobalt up to 10 % in molar ratio of zinc salt.

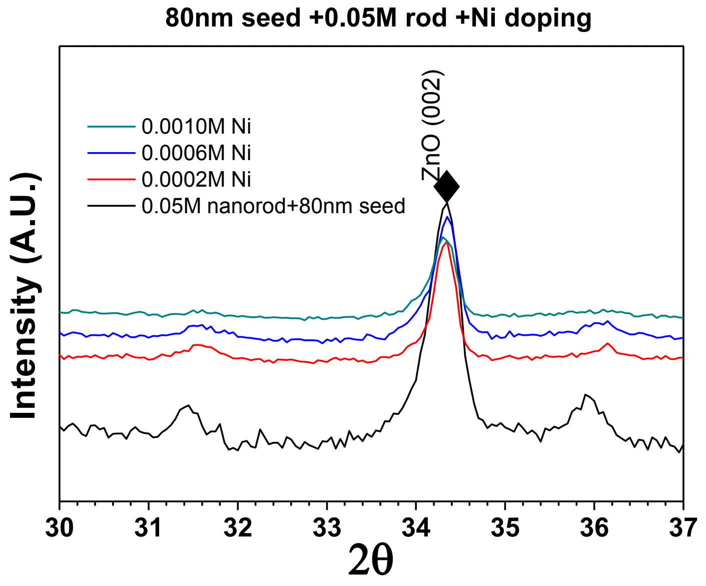

Figure 7.7 XRD graphs of nickel doped ZnO nanorods according to doping concentration

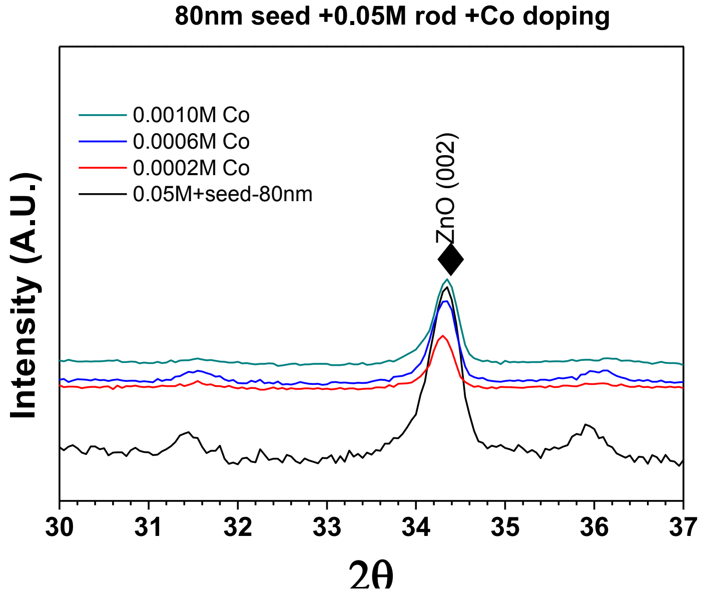

Figure 7.8 XRD graphs of cobalt doped ZnO nanorods according to doping concentration

7.3.3 Voltage dependence of morphology of ZnO nanorods

Prior to the transition metal doping during ZnO nanorods` growth, influence of dc field on the morphology of ZnO nanorods was studied in terms of diameter and length of ZnO nanorods using SEM. In figure 7.9, surface morphology of ZnO nanorods grown in chemical solution by applying different dc voltage 1.75V, 5V, respectively for 4hr. Pictures were taken under low magnification to describe the size difference in diameter and uniformity of nanorods. As compared in two picture. Left side picture shows well-distributed and vertically grown nanorods, which has diameters in 100 ~ 200nm range. On the contrary, right-side picture reveals much larger nanorods and some randomly grown nanorods grown under 5V dc. Overall diameters of nanorods in between 1 μm and 5 μm were observed, approximately 10 to 20 times larger than those grown under 1.75V dc. In figure 7.10, higher dc voltage; 5V was applied and nanorods grown under 5V dc were compared with other previous results. At lower magnification in left side pictures, it was obvious that morphology of nanorods dramatically changed as the applied dc voltage increased. Especially, ZnO nanorods grown under 5V dc seems to have randomly grown additional layers on vertically grown nanorods as shown in second picture for 3V dc case. It can be explained that the rate of ZnO nucleation increases as high dc voltage applies.

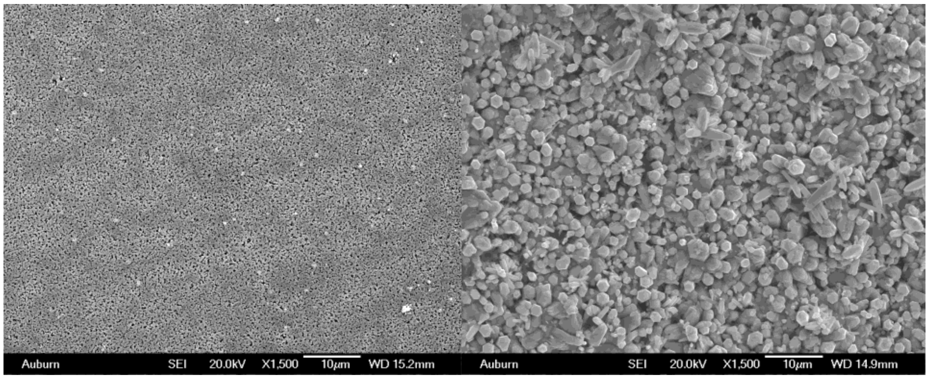

X1500

1.75V 3V

Figure 7.9 Surface morphology of ZnO nanorods depending on dc voltage to show the overall size difference in diameter under X1500

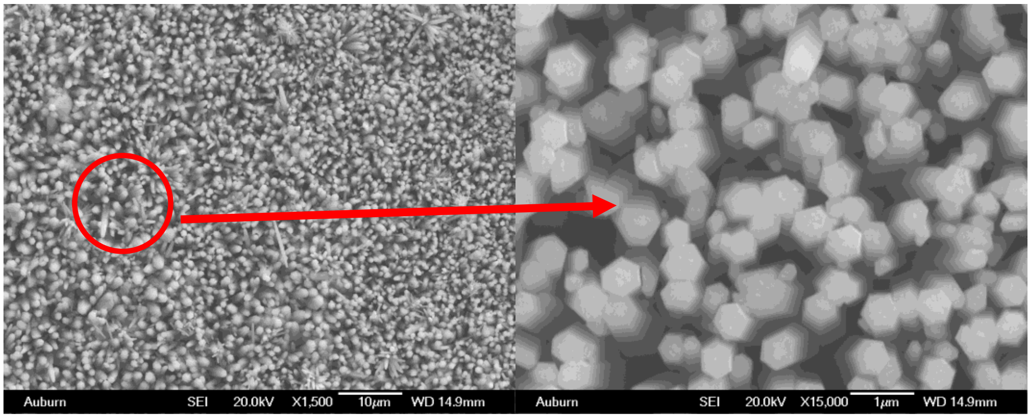

DC 2.25V

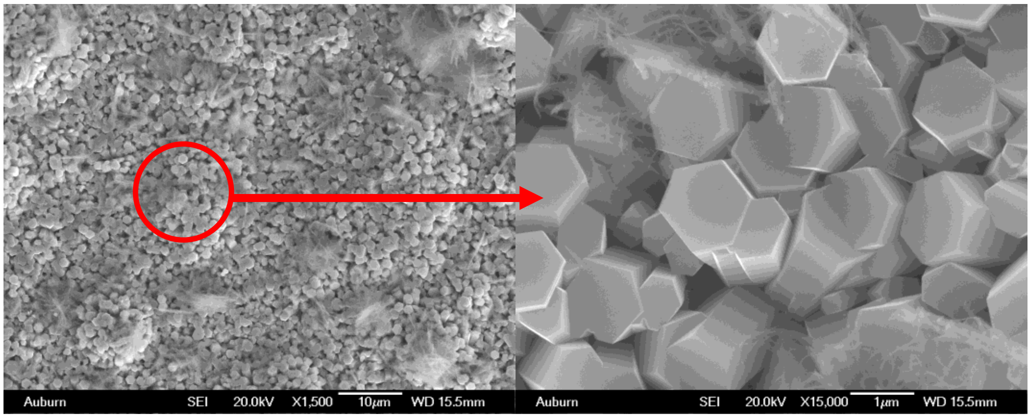

DC 3V

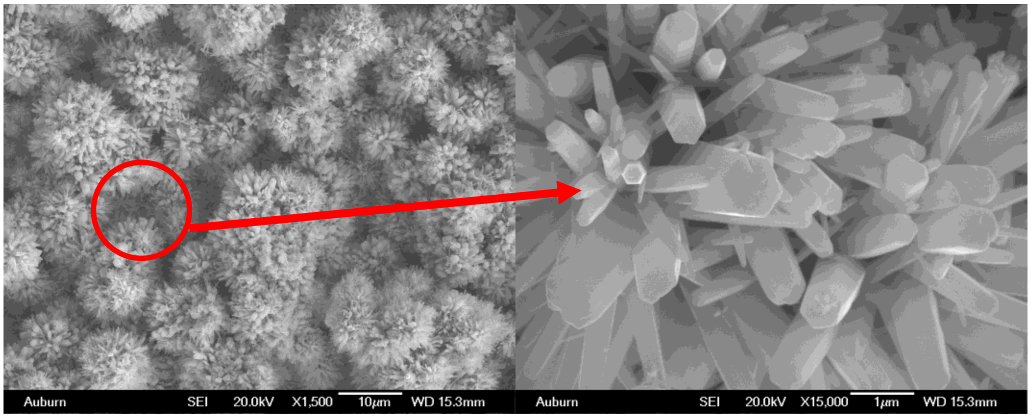

DC 5V

Figure 7.10 surface morphology of ZnO nanorods depending on dc voltages to represent the size difference and growth direction

High nucleation rate under high current make a transition of preferred nucleation on ZnO seed layer, which play a heterogeneous nucleation site, to other sites, not on the seed layer. Growth mechanism is also influenced as the current density increases. Crystal growth in lateral direction as well as vertical direction is enhanced. Consequently, randomly grown ZnO nanorods on second layer are thought to be observed in third picture. Additionally, EDS characterization was carried out to measure the nickel concentration on ZnO nanorods grown under two different dc voltages. As shown in figure 7.11, nickel amount in ZnO nanorods were different depending on applied dc voltage. To compare the applied voltage only, initial amount of nickel salt was fixed to have 2%. In case of 1.75V, even 2% of nickel salt was added in a solution, detected amount of nickel in ZnO nanorods was less than 0.5%. Meanwhile, ZnO nanorods synthesized under 5V dc voltage revealed 3.86% of nickel, more than initial amount of nickel. It is thought that 3V was quite enough to incorporate both zinc salt and nickel salt in ZnNiO nanorods growth and induced somewhat large size of nanorods as shown in SEM picture by modifying the nucleation rate.

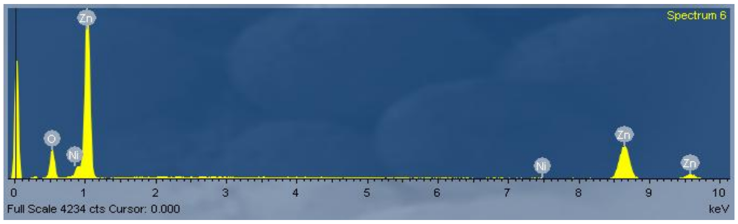

1.75V

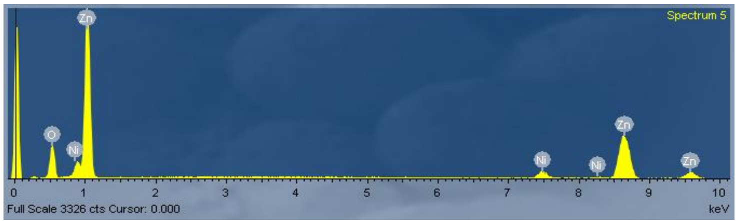

3V

Figure 7.11 EDS results of 1.75V and 3V DC applied ZnO nanorod with 0.0002mol of nickel

To take advantage of a nanostructured ZnO to a have high surface to volume ratio, optimum dc voltage to conserve the pure nanostructure of ZnO and draw transition metal ions sufficiently into zinc sites in aqueous solution is required. Therefore, dc voltage between 1.75V and 3V were tested by stepping 0.25V from 1.75V to 3V. Various concentrations of nickel salts also will be tested under dc voltages between 1.75V and 3V in next chapter.

Table 7.2 EDS results of atomic % of dopants in nickel doped ZnO nanorods at 1.5V and 3V dc voltages

Doping Concentration, dc voltage	Nickel (at %)
0.0002 mol(2%), 1.75V	0.10
0.0002 mol(2%), 3V	3.86

7.3.4 Voltage dependence of nickel doping in ZnO nanorods

In previous chapter, voltage dependence of ZnO nanorods growth and detected amount of nickel in synthesized ZnO nanorods was studied. From the SEM, EDS results, voltage range between 1.75V and 3V was thought to be reasonable starting points to more narrow down the range to find out the optimum dc voltage. After the several repeated synthesis, 2.25V was found to be the optimum condition to achieve both anisotropic property of ZnO nanorods and designed concentration of transition metal ions from raw materials. In figure 7.12, nickel doped and cobalt doped ZnO nanorods were characterized according to different concentration of nickel and cobalt from 2% to 6%.

In left side pictures, nickel doped ZnO nanorods were observed to maintain vertically aligned shape of pure ZnO nanorods. Somewhat modified shape, however, was seen especially at endpoint of nanorods and induced increased specific surface area than pure ZnO nanorods. It may be attributable to the chemical balance change in molar ratio of solution. A similar result is reported in elsewhere [11]. In right side pictures, cobalt doped ZnO nanorods were characterized in a same way. 6% cobalt doped ZnO nanorods, however, did not show the amount of cobalt as much as added in solution.

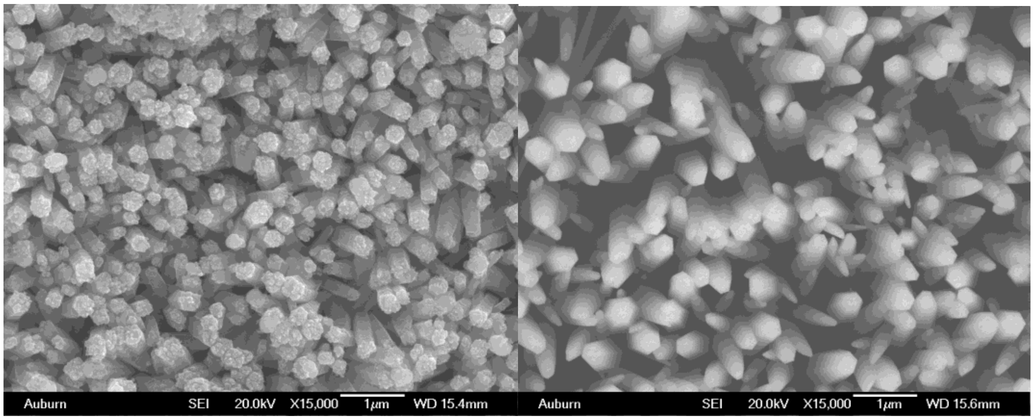

Ni 0.0002 mol (2.15%) Cobalt 0.0002 mol (1.94%)

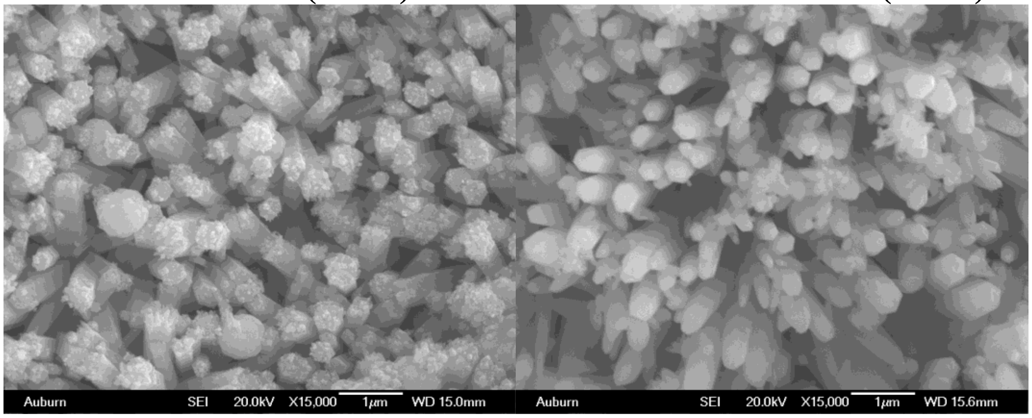

Ni 0.0004 mol (3.80%) Cobalt 0.0004 mol (3.75%)

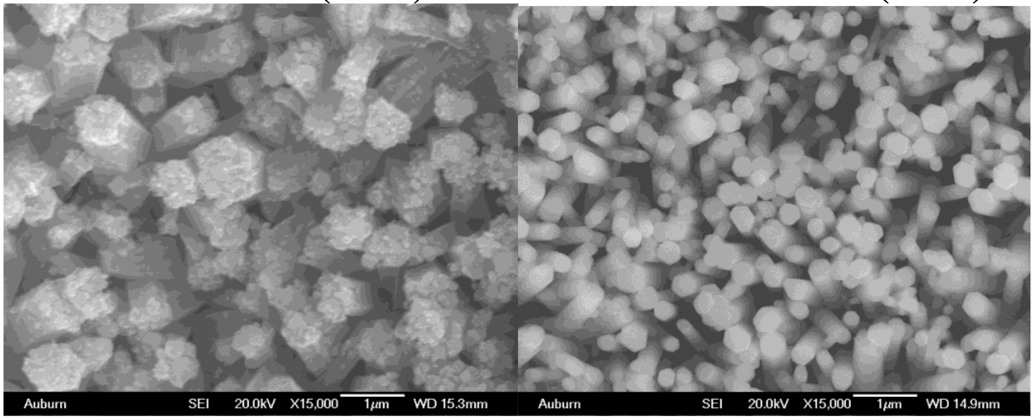

Ni 0.0006 mol (5.42%) Cobalt 0.0006 mol (1.04%)

Figure 7.12 SEM pictures of nickel doped ZnO nanorods (left column), cobalt doped ZnO nanorods (right column). All pictures were taken at X15000

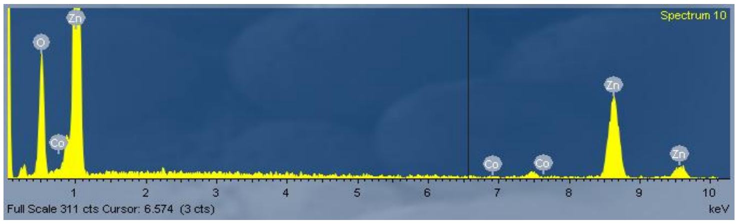

(a) 6% cobalt doped ZnO nanorods

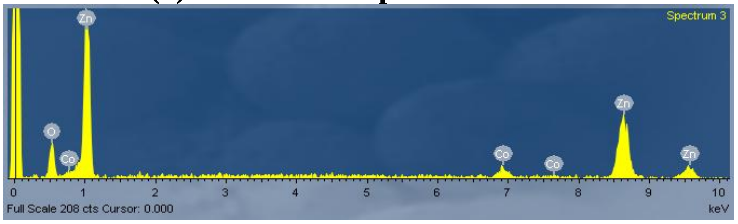

(b) 4% cobalt doped ZnO nanorods

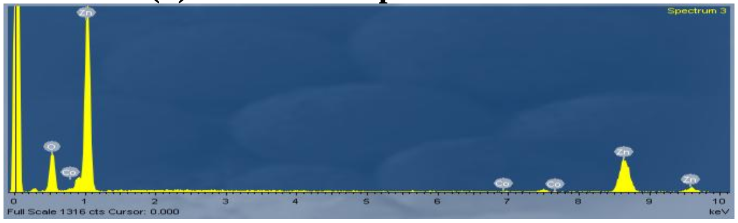

(c) 2% cobalt doped ZnO nanorods

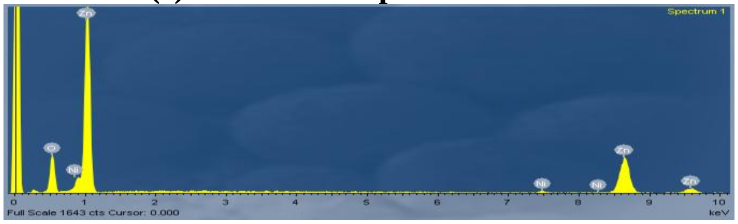

(d) 2% nickel doped ZnO nanorods

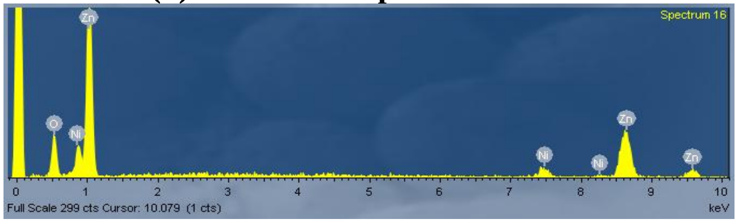

(e) 4% nickel doped ZnO nanorods

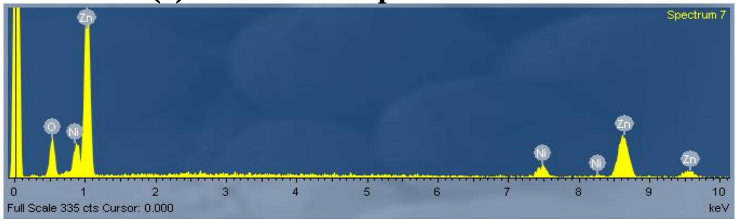

(f) 6% nickel doped ZnO nanorods

Figure 7.13 EDS results of 2.25V DC applied ZnO nanorod with nickel, cobalt, and copper

(a) 6% cobalt, (b) 4% cobalt, (c) 2% cobalt, (d) 2% nickel, (e) 4% nickel, (f) 6% nickel

This might be due to the ionic radius difference in between zinc and cobalt [12]. Additionally, electronegativity of nickel and cobalt compared with zinc are different and thought to influence the incorporation of doping ions [13]. In figure 7.13, EDS spectrum of nickel and cobalt doped ZnO nanorods varying concentration from 2% to 6%. As shown in spectrum, up to 6 at % of nickel and cobalt was measured to be doped into ZnO nanorods successfully under our experimental conditions by electrodeoposition.

7.4 Summary and Conclusions

Transition metal ions, nickel, cobalt, and copper were doped by electrodeposition during the synthesis of ZnO nanorods in aqueous solution. Optimum conditions such as distance between electrode, dc voltage, and chemical balance between zinc salts including transition metal materials and HMT, releasing counter ion, hydroxyl ion, were investigated to obtain both doping concentration and nanostructured ZnO. Under the optimized experimental conditions, nickel, cobalt, and copper were tried to in-situ dope into ZnO nanorods. Only 4% of cobalt was successfully doped into ZnO nanorods. In case of copper, corrosion occurred on the substrate working as a negative electrode. In future study, more experiments to resolve these issues will be performed. Consequently, nickel was successfully doped into ZnO nanorods with varying concentrations from 2 at% to 10 at% for the sensing layer. Gas sensing property of nickel doped ZnO nanorods sensor will be studied in next chapter.

References

1. C.-H. Chien, S. H. Chiou, G. Y. Guo, andY.-D. Yao, "Electronic structure and magnetic moments of 3d transition metal-doped ZnO," *Journal of Magnetism and Magnetic Materials,* **282**[0] 275-78 (2004).
2. S. Polarz, A. Roy, M. Lehmann, M. Driess, F. E. Kruis, A. Hoffmann, andP. Zimmer, "Structure–Property–Function Relationships in Nanoscale Oxide Sensors: A Case Study Based on Zinc Oxide," *Advanced Functional Materials,* **17**[8] 1385-91 (2007).
3. W. Choi, A. Termin, andM. R. Hoffmann, "The Role of Metal Ion Dopants in Quantum-Sized TiO2: Correlation between Photoreactivity and Charge Carrier Recombination Dynamics," *The Journal of Physical Chemistry,* **98**[51] 13669-79 (1994).
4. Z. Zou, J. Ye, K. Sayama, andH. Arakawa, "Direct splitting of water under visible light irradiation with an oxide semiconductor photocatalyst," *Nature,* **414**[6864] 625-27 (2001).
5. J. H. He, C. S. Lao, L. J. Chen, D. Davidovic, andZ. L. Wang, "Large-Scale Ni-Doped ZnO Nanowire Arrays and Electrical and Optical Properties," *Journal of the American Chemical Society,* **127**[47] 16376-77 (2005).
6. A. E. Jiménez-González, "Modification of ZnO Thin Films by Ni, Cu, and Cd Doping," *Journal of Solid State Chemistry,* **128**[2] 176-80 (1997).
7. B. Panigrahy, M. Aslam, andD. Bahadur, "Aqueous Synthesis of Mn- and Co-Doped ZnO Nanorods," *The Journal of Physical Chemistry C,* **114**[27] 11758-63 (2010).
8. L. E. Greene, B. D. Yuhas, M. Law, D. Zitoun, andP. Yang, "Solution-Grown Zinc Oxide Nanowires," *Inorganic Chemistry,* **45**[19] 7535-43 (2006).
9. J. B. Cui, "Electrodeposition and room temperature ferromagnetic anisotropy of Co and Ni-doped ZnO nanowire arrays," *Appl. Phys. Lett.,* **87**[13] 133108 (2005).

10. Y. Tak and K. Yong, "Controlled Growth of Well-Aligned ZnO Nanorod Array Using a Novel Solution Method," *The Journal of Physical Chemistry B,* **109**[41] 19263-69 (2005).
11. J. Qiu, X. Li, W. Yu, X. Gao, W. He, S.-J. Park, Y.-H. Hwang, andH.-K. Kim, "Morphology transformation from ZnO nanorod arrays to ZnO dense film induced by KCl in aqueous solution," *Thin Solid Films,* **517**[2] 626-30 (2008).
12. R. Shannon, "Revised effective ionic radii and systematic studies of interatomic distances in halides and chalcogenides," *Acta Crystallographica Section A,* **32**[5] 751-67 (1976).
13. S. Ricote and N. Bonanos, "Enhanced sintering and conductivity study of cobalt or nickel doped solid solution of barium cerate and zirconate," *Solid State Ionics,* **181**[15-16] 694-700 (2010).

CHAPTER 8 GAS SENSING PROPERTY OF NICKEL DOPED ZNO NANORODS UNDER UV IRRADIATION AT ROOM TEMPERATURE

8.1 Introduction

Nanostructured ZnO has been widely exploited a lot due to good semiconducting and electronic properties. These properties drive microdevice applications such as thin film transistors, high power LED, gas sensors, and spintronic devices [1-4]. Due to its high surface area, nanostructured ZnO was able to detect the sub ppm range of volatile gases such as acetone and ethanol in gas sensor applications [5-6]. Room temperature sensing can expand the application of metal oxide based gas sensors to areas such as explosive and flammable gas detection, and the biomedical field [7]. Nevertheless, metal oxide gas sensors are commonly operated at an elevated temperature to overcome the energy required for the chemisorptions between gas molecules, which allows for high sensitivity with a short response time. To overcome the limits of high operating temperature, noble metals such as platinum, palladium, and gold have been doped. This has improved sensing properties at relatively lower temperatures by enhancing interactions between dopants and gas molecules [8-10]. Additionally, UV illumination of metal oxide has been attempted to achieve room temperature sensing. When ZnO is illuminated with an UV light with the energy equal or larger than its band gap (3.4 eV), the photocarriers are generated in ZnO. Such photo carriers play a key role in the adsorption/desorption of surface molecules by altering the depletion layer width and the barrier height between grains [7, 11]. A number of previous reports have shown that ZnO nanostructures could operate at room temperature by utilizing either noble metal dopants or UV illumination. However, to this point, there has been no clear demonstration of improved gas sensitivity by combining UV illumination and doping transition metals in ZnO nanostructure. Doping of transition metals in ZnO has been mostly investigated in modifying ferroelectric properties [12-14], but few studies have focused on transition metal doping for enhancing gas sensing properties. In this paper, we report on the demonstration of enhanced sensitivity by combined UV illumination and transition metal doping in ZnO nanorods. Nickel was chosen as a dopant for ZnO nanorods because of similar ionic radius with zinc ions [15] and facile incorporation of Ni into ZnO without altering ZnO morphology during electrodeposition. Different concentrations of nickel doped ZnO nanorods are examined and the mechanism of enhanced UV activation for room temperature sensing due to doped Ni is proposed.

8.2 Experiment

Ni-doped ZnO nanorods were fabricated by solution from zinc nitrate hexahydrate (0.01mol), hexamethylenetetramine (0.01mol), nickel nitrate hexahydrate (0.0001mol to 0.001 mol), and deionized (D.I.) water (400ml). Nickel concentration in the solution was varied from 0 at% to 10 at%. The completely mixed solution was elevated to 85℃ for 4hr. To promote Ni doping into ZnO nanorods during growth, 2.25V DC voltage was applied between electrodes on polyimide film and reference electrode with 1 cm distance. Polyimide films patterned by platinum interdigitated electrodes were used as substrates. The Pt electrodes were deposited by DC sputtering, and the finger size and distance of the interdigitated electrodes were both 400µm. An 80nm thick ZnO film prepared by RF sputtering was used as a seed layer, i.e. nucleation sites for vertical growth of ZnO nanorods. ZnO nanorods were characterized by FE-SEM (field emission scanning electron microscopy, JEOL JSM-7000F) to observe the surface morphology of samples. At % (Atomic percent) of nickel in ZnO nanorods after the synthesis was characterized by EDS (energy dispersive spectroscopy) equipped to FE-SEM. Structural change and phase difference according to nickel concentrations were studied by XRD (x-ray diffractometer, Rigaku D/MAX B with $Cu_{K\alpha}$) and Raman spectroscopy (He-Cd laser, 80mW, Kimmon Electric with 441.6 nm line). Acetone gas sensing measurement was performed in a closed chamber by flowing dry synthetic air and acetone gas by mass flow controller [16]. To investigate the effects of UV, an array of five 2.2mW of Bulb type UV LED (365nm, Nichia Corp, Japan) was located facing normal to the sensing layer with a distance of 0.5 mm between UV LED and ZnO nanorods.

8.3 Results and discussion

Figure 8.1 presents the surface topography of ZnO nanorods according to nickel concentration. From (a) 0 at%, to (f) 10 at%, concentration of nickel in solutions for growing ZnO nanorods is increased by 2 at%. Pure ZnO nanorods were grown to be vertically aligned to the substrate corresponding to hexagonal structure along [002] direction. With Ni doping, overall morphology of nanorods was similar to that of pure nanorods, but the end points of nanorods in the top view of the SEM picture appear to be slightly modified. The shape modification at the end of ZnO nanorods occurred more clearly as the Ni concentration increased. At higher Ni concentration such as 8 at% and 10 at%, the end points of nanorods seem to connect with each other, probably due to segregation of nickel-related secondary phase and/or relatively fast growth rate of nickel ions [17]. Most transition metal ions are known to stay preferably in aqueous

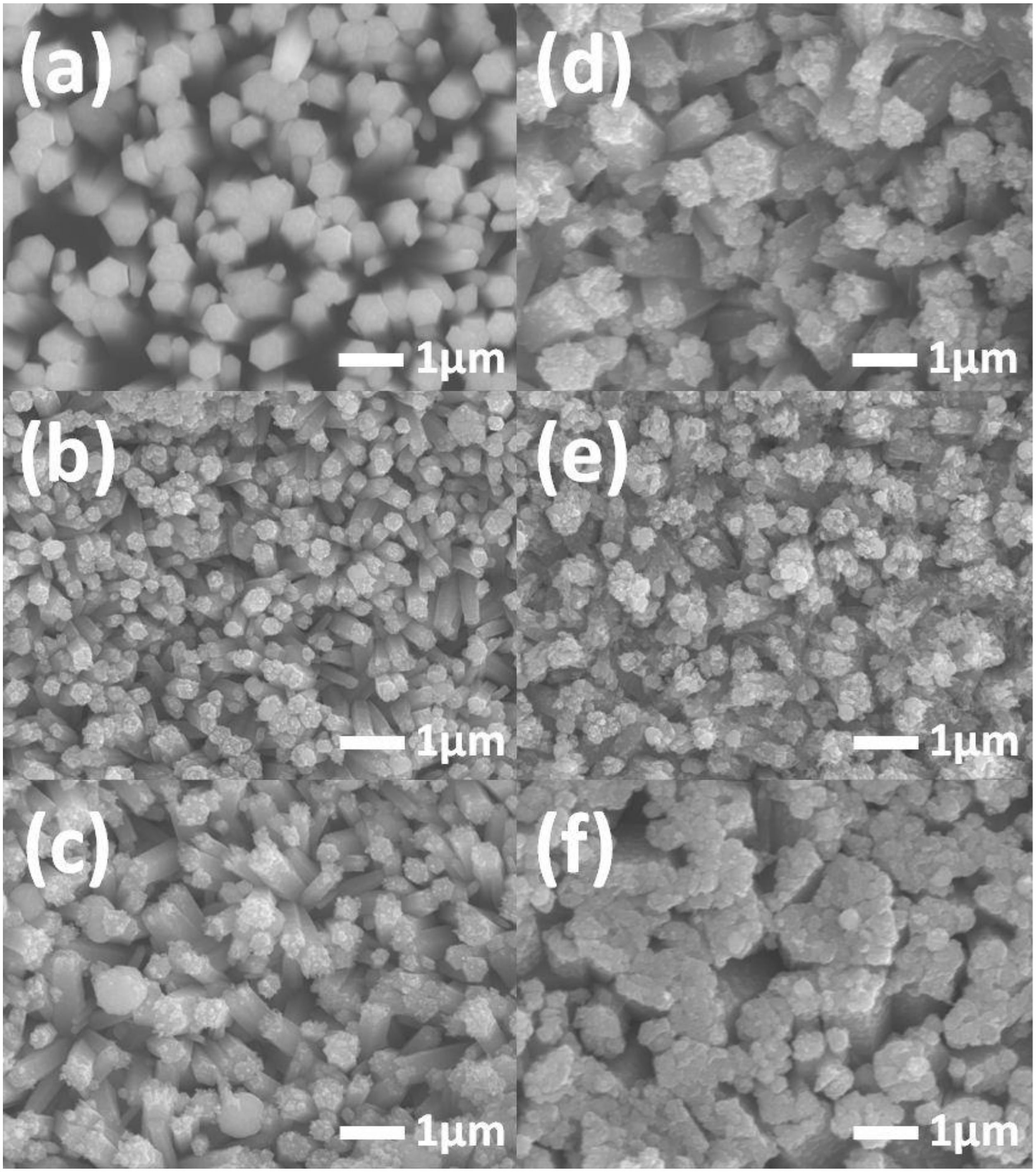

Figure 8.1 SEM pictures of nickel doped ZnO nanorods depending on nickel concentrations (a) pure, (b) 2%, (c) 4%, (d) 6%, (e) 8%, (f)10%

solutions as stable complexes, not to incorporate into the zinc site [18] and the formation of secondary phases related to transition metal ions or variation can result in the change of morphology [19-20].

In the ZnO quantum dots synthesis by doping nickel ions, electronic absorption spectra study showed that Ni^{2+} could suppress the nucleation and growth of ZnO, resulting in spatial distribution of Ni dopants [21]. Although slight modification in the shape of the rod tip was observed with Ni doping, overall anisotropic growth of ZnO was maintained. The doped concentration was measured by EDS as shown in figure 8.2 of 6 at% Ni-doped ZnO. The table inserted in the figure shows the relationship between Ni concentration in the solution and nanorods. Nickel ions in the precursor solution seem to be well incorporated into ZnO nanorods. Peaks representing nickel ions at 0.855keV, 7.475keV and 8.21keV were increased as the Ni concentration increases.

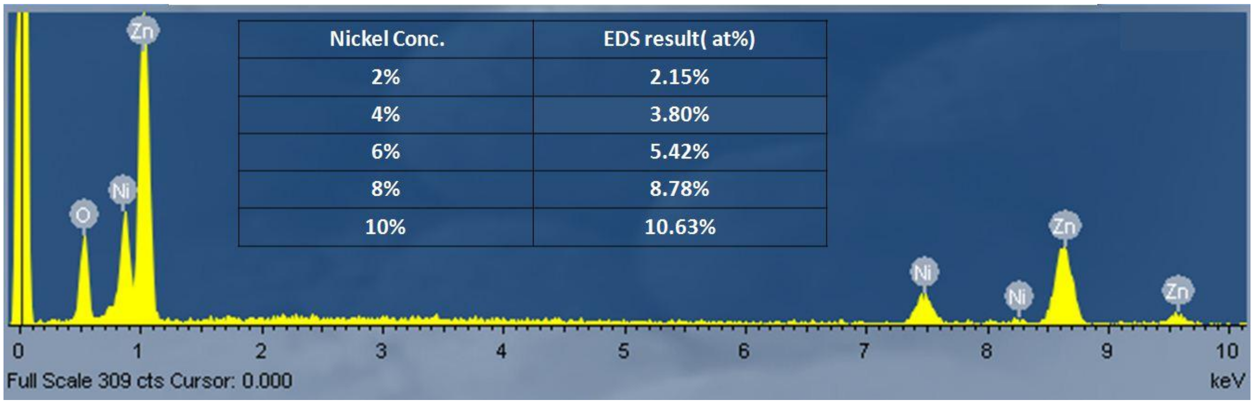

Nickel Conc.	EDS result(at%)
2%	2.15%
4%	3.80%
6%	5.42%
8%	8.78%
10%	10.63%

Figure 8.2 EDS spectrum of 6 at% nickel doped ZnO nanorods. Insert table summarizes doped concentration of nickel in ZnO nanorods according to molar concentration of nickel salt

The effect of the Ni dopants on the structural change was characterized by XRD. Figure 8.3 shows peaks corresponding to the (100) plane, (101) plane, and (102) plane of ZnO nanorods at around 31.5°, 36.1°, and 47.5°. But the relative intensity of those peaks was much lower than that of the peak representing (002) plane at 34.3° irrespective of Ni doping concentration. The result means that preferred c-axis growth of ZnO nanorods was maintained even at higher concentration of Ni dopant. When observing peak position, a slight shift in 2 theta angles to a higher angle region can indicate substitutional doping of Ni ions into the Zn sites due to a similar ionic radius (0.55nm) of Ni ion with that of Zn ion (0.6nm) [22-24]. However, the excessive Ni doping such as 8 at% and 10 at% resulted in the formation of a secondary NiO phase.

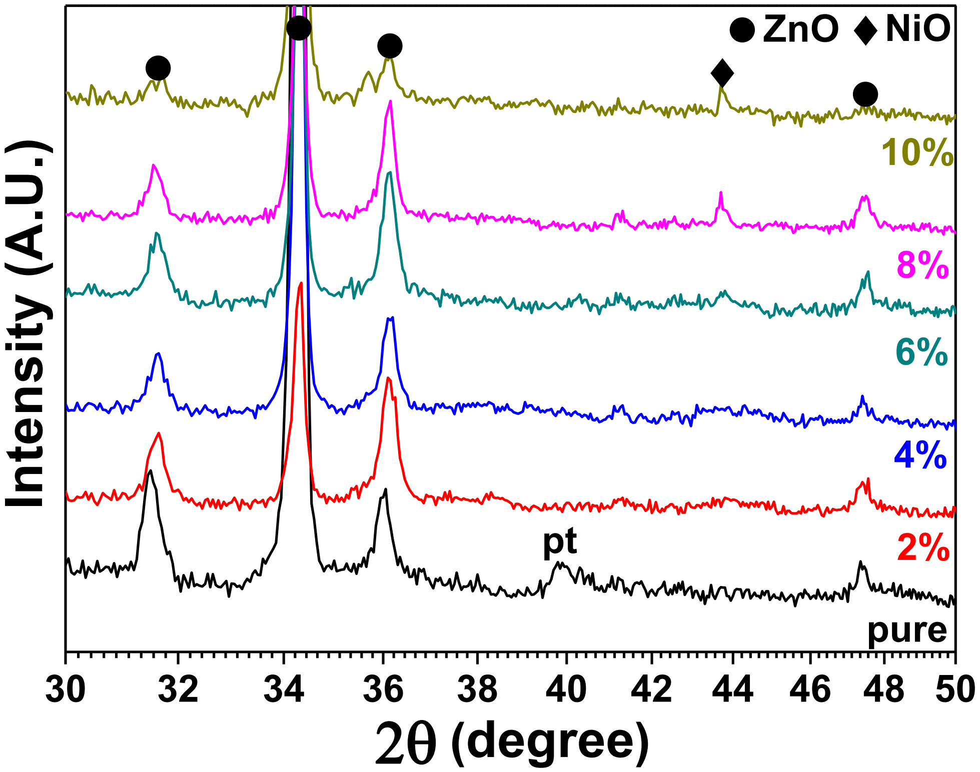

Figure 8.3 XRD graphs of ZnO nanorods containing varying concentrations of nickel from 0 at% to 10 at%

Raman spectroscopy was also used to analyze the secondary phases as shown in figure 8.4. Two modes, A_1 (Transverse Optical) and E_1 (Longitudinal Optical), were used to study changes in Ni-doped ZnO nanorods. ZnO single crystal grown to c-axis direction was used for calibration, and 437cm^{-1} for E_1 mode and 583cm^{-1}for A_1 mode were measured. For ZnO nanorods, E_1 mode was observed in the range of 426~432 cm^{-1}. The frequency for A_1 mode varied from 574 to 567 cm^{-1} with slightly increasing Ni concentration. A more obvious shift in frequency was observed for A_1 mode, especially from 6 at%-doped ZnO nanorods. The results can be explained by the presence of dopants in Zn lattices [25].

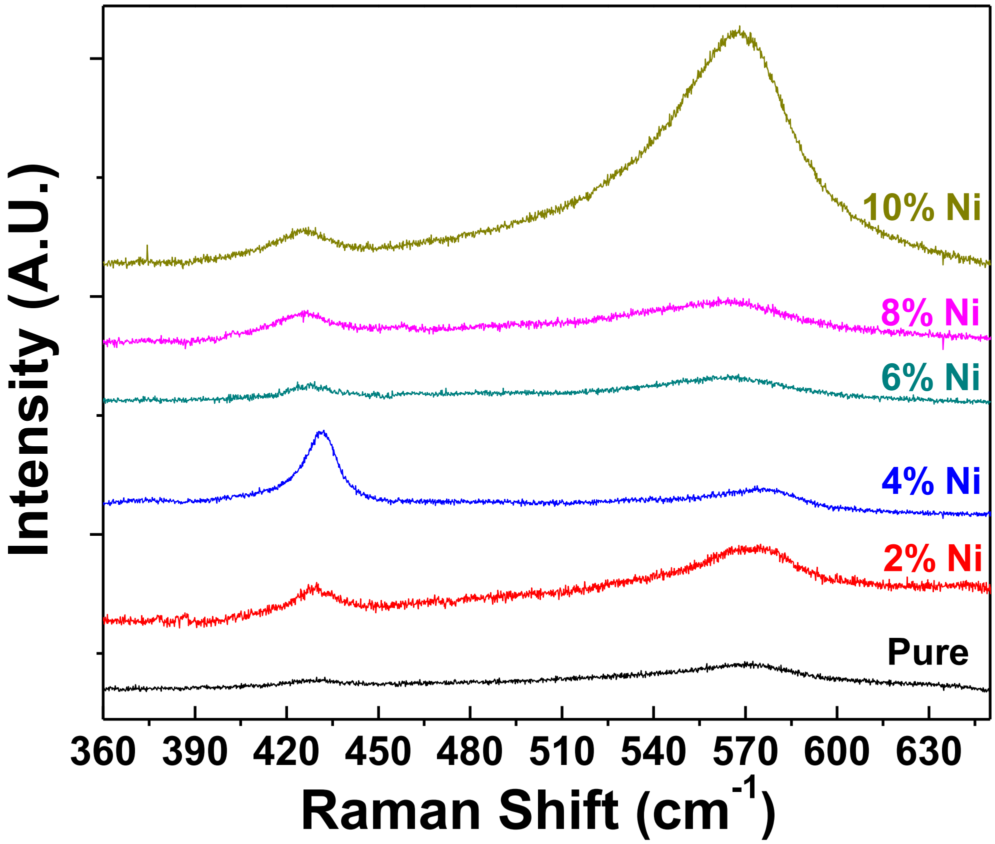

Figure 8.4 Raman spectroscopy results of ZnO nanorods depending on nickel concentrations

It is thought that the incorporation of smaller nickel ions into zinc ions can distort ZnO lattices and induce tensile stress [26]. At the highest doping concentration of 10 at%, peak intensity became significantly increased and the peak was broaden around at 567~569 cm^{-1}, which might be attributed to the overlap from the secondary NiO phase.

Gas sensing properties of doped ZnO nanorods were characterized using acetone gas. Normalized room temperature resistance profiles of pure ZnO nanorods and 6% Ni-doped ZnO nanorods under UV illumination, and pure ZnO nanorods without UV illumination was shown in figure 8.5. Initial resistance was quite different depending on the samples and UV illumination.

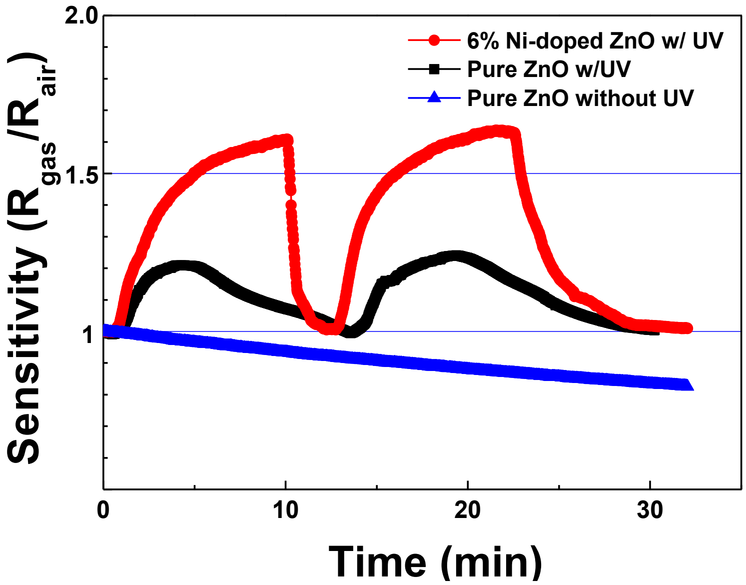

Figure 8.5 Comparisons of resistance profiles of ZnO nanorods sensors between nickel doped ZnO nanorods, pure ZnO nanorods under UV illumination, and pure ZnO nanorods under dark atmosphere

Resistance of Ni-doped ZnO nanorods under UV illumination shows around 9kΩ whose value is quite lower than that of the sample without UV illumination. Lowered initial resistance can result from the prolific amount of photo-induced charge carriers under UV illumination and the reduction of the energy barrier of ZnO by nickel ion [27-28]. Upon exposure of 100ppm of acetone gas to Ni-doped ZnO nanorods, the resistance of the device increased up to around 15kΩ. The sensitivity ($S=R_g/R_a$), defined by resistance of air (R_a) over resistance of acetone (R_g), was roughly 1.61 for 6 at% Ni-doped ZnO nanorods and 1.34 for pure ZnO nanorods. Compared with reported UV activated chemical sensors, sensitivity enhanced by nickel doping was determined to be comparable to sensitivity improvement using 254nm UV light [7] and nanostructure modulation [11].

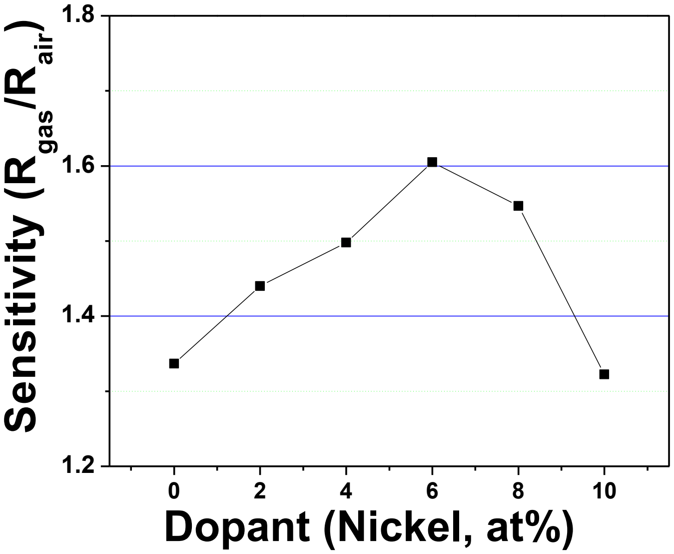

Figure 8.6 Acetone sensitivity comparisons under UV light according to nickel doping concentration

Neither doped nor undoped ZnO nanorods showed clear response without UV illumination at room temperature. The acetone gas sensitivity of ZnO nanorods as a function of nickel concentration was determined as shown in figure 8.6. The sensitivity to acetone increased continuously up to 6 at% Ni-doped ZnO, but the samples with the excess Ni concentrations such as 8 and 10 at% deteriorated with worse sensitivity. Such deteriorated sensitivity at higher Ni concentration would occur due to a secondary phase, p-type NiO that has an interference with n-type ZnO from the gas reactions. A slight increase of the surface area with nickel concentration is thought to influence the sensitivity in doped ZnO nanorods. However, highly doped ZnO nanorods deteriorated sensitivity although the surface area was increased. This result indicates that the dominant factor for sensitivity enhancement of nickel-doped ZnO nanorods is mainly due to the interaction between nickel ions and UV induced photons.

It is well known that the reaction between chemisorbed oxygen molecules and gas molecules is primary gas sensing mechanism by metal oxides. When UV is illuminated to the metal oxide, the reaction between photo-induced oxygen ions and gas molecules can be additionally involved by UV energy, which is larger than the band gap energy of ZnO. Charge carrier transfer between photo-induced oxygen and gas molecules is easily promoted even at room temperature due to its relatively weak bonding [29]. However, the enhancement mechanism of UV activation on gas sensing properties by doped transition metals, however, has not yet been reported. We suggest an acetone gas sensing mechanism under UV illumination of Ni-doped ZnO nanorods based on the modification of existing gas sensing mechanisms [7, 11]. First, electron hole pairs are created by UV illumination and photo-induced holes interact with chemisorbed oxygen ions on ZnO nanorods (reaction 1) and resulting in desorbed oxygen (reaction 2):

$$hv \rightarrow h^{+} + e^{-} \quad \text{……………………..………………........ (1)}$$

$$h^{+} + O_2^{-}(chemisorbed) \rightarrow O_2(gas) \quad \text{……….…………....……….. (2)}$$

A charge transfer transition of Ni ion by UV illumination leads to additional holes (reaction 3), and the holes react with chemisorbed oxygen ions to desorb oxygen (reaction 4) as the following scheme:

$$Ni^{2+} + hv \rightarrow Ni^{+} + h^{+} \quad \text{……..……..……………...……….. (3)}$$

$$h^{+} + O_2^{-}(chemisorbed) \rightarrow O_2(gas) \quad \text{…………………...………......... (4)}$$

Meanwhile, photo-induced electrons [$e^{-}(hv)$] by UV react with the ambient oxygen molecules, creating photo-induced oxygen ions (reaction 5). While the chemisorbed oxygen ions are strongly bound to the ZnO surface, the photo-induced oxygen ion [$O_2^{-}(hv)$] are weakly attached to the ZnO surface:

$$O_2 + e^{-}(hv) \rightarrow O_2^{-}(hv) \quad \text{………………………………….... (5)}$$

Photo-induced oxygen ions interact with acetone gas (reaction 6) and carbon monoxide that is also the resultant of acetone gas reactions (reaction 7 & 8) [30]. The reactions release free electrons on the ZnO surface:

$$CH_3COCH_3 + O_2^-(hv) \rightarrow CH_3CO^+ + CH_3O^- + e^- \tag{6}$$

$$CH_3CO^+ \rightarrow CH_3^+ + CO \tag{7}$$

$$CO + O_2^-(hv) \rightarrow CO_2 + e^- \tag{8}$$

The photo-induced free electrons released from the surface of ZnO nanorods due to the above reactions result in the resistance increase of ZnO nanorods, i.e. an improved sensitivity. Schematic drawing of sensing mechanism mentioned above is shown in figure 8.7.

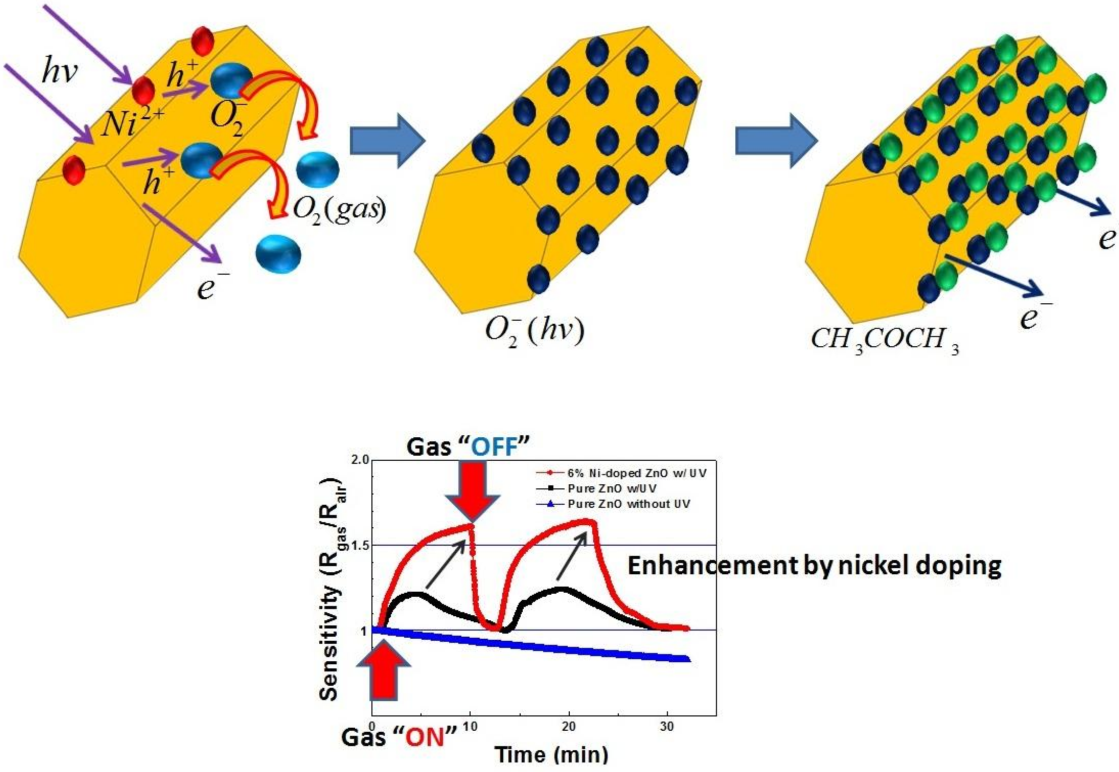

Figure 8.7 Schematic drawing of suggested mechanism of gas sensing of nickel doped ZnO nanorods under UV light illumination

8.4 Summary and Conclusions

In conclusion, doped Ni in ZnO nanorods shows improved room temperature gas sensing through the UV illumination. The formation of a secondary NiO phase at higher Ni concentration deteriorates the gas sensitivity by reducing UV activation. The suggested mechanism can explain the promoted sensitivity based on the involvement of weakly bound photo-induced oxygen ions upon the exposure of acetone gas. It is our expectation that transition metal doped nanostructured ZnO can be a potential pathway to achieving room temperature gas sensing with better sensing performance.

References

1. P. F. Carcia, R. S. McLean, M. H. Reilly, andG. Nunes, "Transparent ZnO thin-film transistor fabricated by rf magnetron sputtering," *Applied Physics Letters*, **82**[7] 1117-19 (2003).
2. J. H. Lim, C. K. Kang, K. K. Kim, I. K. Park, D. K. Hwang, andS. J. Park, "UV Electroluminescence Emission from ZnO Light-Emitting Diodes Grown by High-Temperature Radiofrequency Sputtering," *Advanced Materials,* **18**[20] 2720-24 (2006).
3. M.-W. Ahn, K.-S. Park, J.-H. Heo, J.-G. Park, D.-W. Kim, K. J. Choi, J.-H. Lee, andS.-H. Hong, "Gas sensing properties of defect-controlled ZnO-nanowire gas sensor," *Applied Physics Letters*, **93**[26] 263103 (2008).
4. C. Ronning, P. X. Gao, Y. Ding, Z. L. Wang, andD. Schwen, "Manganese-doped ZnO nanobelts for spintronics," *Applied Physics Letters*, **84**[5] 783-85 (2004).

5. Q. Wan, Q. H. Li, Y. J. Chen, T. H. Wang, X. L. He, J. P. Li, andC. L. Lin, "Fabrication and ethanol sensing characteristics of ZnO nanowire gas sensors," *Applied Physics Letters,* **84**[18] 3654-56 (2004).
6. Q. Qi, T. Zhang, L. Liu, X. Zheng, Q. Yu, Y. Zeng, andH. Yang, "Selective acetone sensor based on dumbbell-like ZnO with rapid response and recovery," *Sensors and Actuators B: Chemical,* **134**[1] 166-70 (2008).
7. J. Gong, Y. Li, X. Chai, Z. Hu, andY. Deng, "UV-Light-Activated ZnO Fibers for Organic Gas Sensing at Room Temperature," *Journal of Physical Chemistry C,* **114**[2] 1293-98 (2009).
8. Z. Zhou, K. Kato, T. Komaki, M. Yoshino, H. Yukawa, M. Morinaga, andK. Morita, "Effects of dopants and hydrogen on the electrical conductivity of ZnO," *Journal of the European Ceramic Society,* **24**[1] 139-46 (2004).
9. N. Hongsith, C. Viriyaworasakul, P. Mangkorntong, N. Mangkorntong, andS. Choopun, "Ethanol sensor based on ZnO and Au-doped ZnO nanowires," *Ceramics International,* **34**[4] 823-26 (2008).
10. X. Wang, J. Zhang, Z. Zhu, andJ. Zhu, "Effect of Pd2+ doping on ZnO nanotetrapods ammonia sensor," *Colloids and Surfaces A,* **276**[1-3] 59-64 (2006).
11. S.-W. Fan, A. K. Srivastava, andV. P. Dravid, "UV-activated room-temperature gas sensing mechanism of polycrystalline ZnO," *Applied Physics Letters,* **95**[14] 142106 (2009).
12. C. Cheng, G. Xu, H. Zhang, andY. Luo, "Hydrothermal synthesis Ni-doped ZnO nanorods with room-temperature ferromagnetism," *Materials Letters,* **62**[10-11] 1617-20 (2008).

13. G. Huang, J. Wang, X. Zhong, G. Zhou, andH. Yan, "Synthesis, structure, and room-temperature ferromagnetism of Ni-doped ZnO nanoparticles," *Journal of Materials Science,* **42**[15] 6464-68 (2007).

14. H. Wang, Y. Chen, H. B. Wang, C. Zhang, F. J. Yang, J. X. Duan, C. P. Yang, Y. M. Xu, M. J. Zhou, andQ. Li, "High resolution transmission electron microscopy and Raman scattering studies of room temperature ferromagnetic Ni-doped ZnO nanocrystals," *Applied Physics Letters,* **90**[5] 052505 (2007).

15. R. Shannon, "Revised effective ionic radii and systematic studies of interatomic distances in halides and chalcogenides," *Acta Crystallographica Section A,* **32**[5] 751-67 (1976).

16. H. Ahn, J.-H. Park, S.-B. Kim, S. H. Jee, Y. S. Yoon, andD.-J. Kim, "Vertically Aligned ZnO Nanorod Sensor on Flexible Substrate for Ethanol Gas Monitoring," *Electrochemical and Solid-State Letters,* **13**[11] J125-J28 (2010).

17. J. Bang, "Enhanced and stable green emission of ZnO nanoparticles by surface segregation of Mg," *Nanotechnology,* **17**[4] 973 (2006).

18. L. E. Greene, B. D. Yuhas, M. Law, D. Zitoun, andP. Yang, "Solution-Grown Zinc Oxide Nanowires," *Inorganic Chemistry,* **45**[19] 7535-43 (2006).

19. N. S. Norberg, K. R. Kittilstved, J. E. Amonette, R. K. Kukkadapu, D. A. Schwartz, andD. R. Gamelin, "Synthesis of Colloidal Mn2+:ZnO Quantum Dots and High-TC Ferromagnetic Nanocrystalline Thin Films," *Journal of the American Chemical Society,* **126**[30] 9387-98 (2004).

20. E. Liu, P. Xiao, J. S. Chen, B. C. Lim, andL. Li, "Ni doped ZnO thin films for diluted magnetic semiconductor materials," *Current Applied Physics,* **8**[3-4] 408-11 (2008).

21. X. Qiu, L. Li, J. Zheng, J. Liu, X. Sun, andG. Li, "Origin of the Enhanced Photocatalytic Activities of Semiconductors: A Case Study of ZnO Doped with Mg2+," *Journal of Physical Chemistry C,* **112**[32] 12242-48 (2008).
22. X. Liu, F. Lin, L. Sun, W. Cheng, X. Ma, andW. Shi, "Doping concentration dependence of room-temperature ferromagnetism for Ni-doped ZnO thin films prepared by pulsed-laser deposition," *Applied Physics Letters,* **88**[6] 062508 (2006).
23. J.-J. Wu, S.-C. Liu, andM.-H. Yang, "Room-temperature ferromagnetism in well-aligned Zn[sub 1 - x]Co[sub x]O nanorods," *Applied Physics Letters,* **85**[6] 1027-29 (2004).
24. C. J. Cong, J. H. Hong, Q. Y. Liu, L. Liao, andK. L. Zhang, "Synthesis, structure and ferromagnetic properties of Ni-doped ZnO nanoparticles," *Solid State Communications,* **138**[10-11] 511-15 (2006).
25. T. L. Phan and et al., "Raman scattering in Me-doped ZnO nanorods (Me = Mn, Co, Cu and Ni) prepared by thermal diffusion," *Nanotechnology,* **19**[47] 475702 (2008).
26. B. Panigrahy, M. Aslam, andD. Bahadur, "Aqueous Synthesis of Mn- and Co-Doped ZnO Nanorods," *Journal of Physical Chemistry C,* **114**[27] 11758-63 (2010).
27. M. Yang, T. Xie, L. Peng, Y. Zhao, andD. Wang, "Fabrication and photoelectric oxygen sensing characteristics of electrospun Co doped ZnO nanofibres," *Applied Physics A,* **89**[2] 427-30 (2007).
28. D. A. Schwartz, N. S. Norberg, Q. P. Nguyen, J. M. Parker, andD. R. Gamelin, "Magnetic Quantum Dots: Synthesis, Spectroscopy, and Magnetism of Co2+- and Ni2+-Doped ZnO Nanocrystals," *Journal of the American Chemical Society,* **125**[43] 13205-18 (2003).

29. L. Peng, T.-F. Xie, M. Yang, P. Wang, D. Xu, S. Pang, andD.-J. Wang, "Light induced enhancing gas sensitivity of copper-doped zinc oxide at room temperature," *Sensors and Actuators B: Chemical*, **131**[2] 660-64 (2008).
30. S.-J. Chang, T.-J. Hsueh, I.-C. Chen, S.-F. Hsieh, S.-P. Chang, C.-L. Hsu, Y.-R. Lin, andB.-R. Huang, "Highly Sensitive ZnO Nanowire Acetone Vapor Sensor With Au Adsorption," *IEEE TRANSACTIONS ON NANOTECHNOLOGY,* **7**[6] 754-59 (2008).

CHAPTER 9 CONCLUSION AND FUTURE WORK

9.1 Conclusion of Dissertation

Nanostructured ZnO and SnOx have been synthesize and deposited by various technologies such as rf/dc sputtering, thermolysis assisted chemical solution method, and electrodeposition. The modulation of structure, composition, and phase was a primary goal to investigate those effects under high temperature and UV illumination at room temperature on the gas sensing properties of ZnO and SnO_x based VOC sensors. In this study, improvement of the specific surface area through the nanostructure synthesis was carried out to investigate the effect on the resistance change for higher sensitivity. UV energy was employed to activate metal oxide based sensor at room temperature. Transition metal doping was attempted to enhance the room temperature gas sensing properties under UV illumination. For higher selectivity, the approach by combinatory phase of SnO_x was attempted to discriminate the sensing properties of gas species among gas mixtures of acetone, ethanol, and ethylene.

For the first time, ethylene sensing behavior of rf sputtered SnO_2 thin film sensor was studied in terms of post annealing temperature and argon-to-oxygen ratio. Four different argon-to-oxygen ratios ranged from 27:2.7, 23:7, 20:10, and 15:15 to have total 30 sccm of gas in plasma generation. Depending on different amount of oxygen, deposition rate of sputtering was varied. Therefore, thicknesses of films were controlled to have in similar range. SnO_2 thin films deposited under high oxygen concentrations such as 15:15 and 20:10 showed improved crystalline phase of (110) orientation. The shortest distance between Sn atoms are thought to attribute somewhat higher sensitivity for ethylene detection. Thin film sensors, however, post annealed at 650 ℃ showed 30% enhanced sensitivities than as-deposited thin film sensors regardless of argon-to-oxygen ratios. It means that post annealing is more influencing to film property than argon-to-oxygen ratio on ethylene detection. Ethylene gas sensing mechanism was proposed based on the experimental results. Ethylene reacts with chemisorbed oxygen ion on the SnO_2 surface. Then, ethylene oxide is produced by releasing free electrons and released free electrons are supplied to the metal oxide surface, which induces the resistance decrease. After the gas is off, no more free electrons are provided and resistance of SnO_2 is back to initial resistance.

Combinatory phase of SnO_x thin film sensors were developed to investigate the influence of crystalline phase of tin compound on the improved gas sensing property in gas mixtures. Three different gases, such as acetone, ethanol, and ethylene were utilized. To deposit combinatory phase of tin compound, rf/dc co-sputtering using metallic tin target and ceramic SnO_2 target was employed. Following post annealing were carried out at different temperatures ranging from 300 ℃ to 650 ℃. Depending on temperature, obvious crystalline phase difference was observed along the substrate according to the distance from dc and rf cathode. Stable tin monoxide (SnO) was achieved on the dc sputtered SnO_x thin film post annealed at 450 ℃ and tin dioxide (SnO_2) was observed from 450 ℃ and stabilized both on rf sputtered SnO_x thin film post annealed at 650 ℃. To fabricate the SnO_x sensors with combinatory tin compound phases, cosputtered SnO_x thin film were post annealed at 450 ℃. In XRD and EDS study, obvious transition in crystalline phase from SnO to SnO_2 was observed along the substrate. Dominant phase of SnO was observed around the films deposited by dc sputtering. SnO_2 phase was mostly observed at the films deposited by rf sputtering. Center region of films was found to have mixed SnO, SnO_2, and Sn_2O_3 phases. SnO_x thin film sensors with combinatory phase were tested to investigate the gas sensing property. Obvious noticeable difference in gas sensing property in terms of direction of reaction were observed for SnO_x thin films according to dominant crystalline phase such as SnO, SnO_2 and mixed phases. It was attributed that SnO and SnO_2 have intrinsic p-type and n-type semiconducting properties, respectively. In addition to, somewhat difference in sensitivity among three VOC gases were observed. It was thought that difference in band gap energy and charge carrier mobility between SnO and SnO_2 induced sensitivity difference corresponding to dipole moment and molecular weight of gases.

For the highly sensitive flexible VOC sensor development, ZnO ethanol nanorods sensors were fabricated on polyimide film. To grown vertically aligned ZnO nanorods for the improved sensitivity, ZnO thin film was sputtered to a seed layer. ZnO nanorods was grown on seed layer by the thermolysis assisted chemical solution method at low temperature; 85 ℃. Ethanol sensing was successfully monitored by ZnO nanorods flexible sensor at 300 ℃. Working temperature, however, was still high for flexible device operation. It was thought that other energy sources replaceable thermal energy need to be considered for flexible VOS sensor working at room temperature.

To activate metal oxide based sensor, UV-LED was employed due to its low power consumption and suitability to be embedded in flexible device. By following same procedure performed to fabricate ZnO nanorods sensor on flexible substrate, sensing property of ZnO nanorods sensor under UV illumination was studied by using acetone gas. To study the improvement in sensing properties by nanorods, both ZnO thin film sensors and ZnO nanorods sensors were tested and compared in terms of sensitivity and response time. Noticeably, ZnO nanorods showed improved sensing property than ZnO thin films sensor under UV illumination. Sensitivity for 100ppm acetone, however, was still poor that thermally activated ZnO nanorods sensors. Transition metal doping was considered to improve the sensing property of ZnO nanorods sensors. It was reported that transition metal ions can be substitutionally doped into ZnO nanorods and modulate the photocatalytic property as well as electrical property. Nonetheless, it was quite hard to control doping ions during the nanorods synthesis in aqueous solution due to a nature of transition metal ions to stay in solutions as forming aquo complex.

To overcome the technical challenge, electrodeposition was applied to efficiently dope transition metal ions into ZnO nanorods. Three transition metal ions such as nickel, cobalt, and copper were tried to dope into ZnO nanorods but, nickel ions revealed the optimum results without much changing in nanostructure. It was due to the similar ionic radius of zinc and nickel ions. Doping concentration of nickel varied from 0 at% to 10 at% and characterized by SEM, XRD, EDS, and Raman spectroscopy. For highly doped ZnO nanorods such as 8 and 10 at% revealed somewhat modified nanorods and were observed to have secondary phase; nickel oxide. In study of gas sensing properties under UV illumination, it was found that 6 at% nickel doped ZnO nanorods showed the best sensing property because highly doped ZnO nanorods sensors were deteriorated by NiO phase having p-type semiconducting property. Based on these experimental results, acetone sensing mechanism under UV illumination and role of nickel doping to enhance the room temperature gas sensing properties were suggested. Photo-induced holes by UV light made weakly-bound oxygen ions on metal oxide. This oxygen mainly participates in gas reactions with acetone molecules relatively easily at room temperature. Doped nickel ions contributed by releasing additional holes from the UV activation and subsequently induced additional photo—induced oxygen which can reacts with more acetone molecules.

9.2 Future Work

Thus far, nanostructured metal oxides have been researched to improve the sensitivity. In terms of the specific surface area, hierarchical nanostructure should be applied to VOC sensor device. By utilizing preferred nucleation and growth mechanism, hierarchical nanostructure can be achieved. Compared with simple two dimensional nanostructure, hierarchical nanostructure provide the more specific surface area in same volume. In terms of selectivity, combination of crystalline phase as well as material will be one approach to detect specific gas molecule from gas mixtures. Furthermore, it would be interesting to construct nanostructured p-n junction device to maximize both surface to volume ratio and energy barrier for the gas reactions.